EXPERIMENTAL INVESTIGATION AND THEORETICAL ANALYSIS OF PASSIVE DRAG REDUCTION OVER SURFACES OF VARIOUS DEGREES OF WETTABILITY

by

© Ahmed Faraj Alarbi Alsharief

A Thesis submitted to the School of Graduate Studies in partial fulfillment of the requirements for the degree of

Doctor of Philosophy

Department of Mechanical Engineering

Faculty of Engineering and Applied Science

Memorial University of Newfoundland

December 2023

St. John's Newfoundland and Labrador Canada

Abstract

In recent years, researchers have focused on studying skin drag reduction through surface modification, with nanocoating technology playing a significant role. Various techniques, such as chemical etching, solution immersion, laser electrodeposition, and coating, have been employed to modify surfaces. Critical parameters in the manufacturing process include simplicity, speed, cost-effectiveness, and versatility. Commercially available superhydrophobic/oleophobic coatings, introduced in April 2016, operate by reducing surface energy to minimize the contact area between liquid and solid surfaces. The impact of superhydrophobic surfaces on flow is characterized by slip length and wetting degree parameters. However, many of these parameters related to drag reduction remain poorly understood, and relevant data is scarce in the literature.

An experimental and theoretical study of Taylor-Couette (TC) flows and open channel flows were performed to investigate the passive viscous drag reduction using various randomly fabricated SHSs. Three different commercial SH coatings were used to fabricate the tested surface. In the TC flow study, the experiments were carried out in a small-scale facility using the MCR-301 Rheometer, along with concentric disposal cups (CDCs) as TC cells purchased from Anton Paar Instruments. The tested liquids were water, 5 cSt silicone oil and 10 cSt silicone oil. An open channel was modified to use a replaceable test surface with constant water depth in the second phase. The test surface will be painted with three commercial superhydrophobic coatings. A laser Doppler velocimetry (LDV) system was used to measure the velocity over the modified test surface at seven locations to investigate the shear stress when the test surface is in both coated and uncoated states.

In the first part of the Taylor-Couette (TC) study, slippage was demonstrated over three fabricated SHSs in laminar and low turbulent flow. The investigation explored how slip length increased with rising Reynolds (Re) numbers over the tested SHSs, employing a viscous model to study the generated plastron thickness. The mean skin friction coefficient (C_f) was fitted to a modified semiempirical logarithmic law in the Prandtl–von Kármán coordinate. An effective slip length was estimated within the 35-41 μm range, resulting in a drag reduction (DR) of RMS value between 7-11% for the surfaces. This highlights the proportional relationship between b^+, δ^+, and the Re number. Statistical analysis, including regression modelling, was applied to experimental data, yielding an R^2 of 0.87 and strong agreement with the experimental results. The regression model indicated that b+ and Re numbers exerted a greater influence on δ^+ than the wetting degree, emphasizing minimal differences in the wetting degree among the three tested surfaces. The second part of the Taylor-Couette (TC) cell study investigates the impact of surface wettability on drag reduction using three hydrophobic coatings—FlouroPel Coating (FPC-800M), Superhydrophobic Binary Coating (SHBC), and Ultra-Ever Dry (UED)—applied to curved aluminum surfaces. The study employs three liquids with different viscosities to characterize wettability and flow features. Static and dynamic contact angles on the surfaces were measured, and a rheometer-equipped Taylor-Couette flow cell was used to evaluate drag reduction. Static contact angle measurements revealed superhydrophobic behaviour for water (maximum static contact angle (SCA) of 158°) and oleophilic behaviour for the 10 cSt silicone oil (SCA of 13°). Water rheometer measurements demonstrated a maximum drag reduction of 18% for UED-coated surfaces. Interestingly, oleophilic surfaces exhibited a maximum drag reduction of 6% and 7% in the silicone oils with low static contact angles. The observed drag reduction is attributed to an increase in plastron thickness, influenced by an elevation in Reynolds number and dynamic pressure, coupled with a decrease in static pressure normal to the superhydrophobic wall.

The open channel study explores the effectiveness and sustainability of commercial superhydrophobic coatings in reducing skin friction drag. Three distinct SHSs applied through a spray coating technique on an acrylic flat plate are investigated for their drag reduction (DR) properties. The SCA of water on these surfaces measure 145°, 147°, and 155°. Turbulent flow measurements are conducted using a two-dimensional Laser Doppler Velocimetry (LDV) system in an open channel flow facility, with experiments performed at an approaching Reynolds number of 34200. A unique aspect of this study is the characterization of drag reduction along the entire span of the fabricated surface in the streamwise flow direction. Velocity measurements are taken in a spanwise direction at each selected plane, and a theoretical prediction model for slip velocity and slip length is evaluated. The results show that the slip length equals the coating thickness as the plastron depletes. The SHSs enhance turbulence intensity and streamwise normal shear stress, particularly near the wall. As one moves away from the wall, the impact of turbulence diminishes, indicating the existence of an interface region near the wall due to the SHSs. Overall, the study demonstrates average drag reductions of 11%, 7%, and 18% for the tested SHSs. Importantly, it provides compelling evidence for the consistent reduction of viscous drag across the entire span of the plate, from the leading edge to the trailing edge.

Acknowledgments

I would like to dedicate this thesis to my family in appreciation for putting up with my long hours and supporting my efforts from start to finish.

I am grateful and wish to express my deepest gratitude to my supervisors, Prof. Xili Duan and Prof. Yuri S. Muzychka, for their continuing advice, useful suggestions, guidance, and interest through all stages of this work. This dissertation would not have been possible without their direction and constant assistance.

In addition, I would express my sincere gratitude to Prof. Anand Yethiraj and Prof. Baafour Nyantekyi-Kwakye (Nana), who contributed to constructing my experimental knowledge.

Moreover, I wish to thank all my brilliant Interfacial Thermofluids and Energy colleagues.

Table of Contents

List of Tables

List of Figures

Nomenclature

Greek symbols

ΔA	The interface area	m^2
$\Delta\theta$	Contact angle hysteresis	Degree
ΔW_{int}	The interfacial energy	mN/m
λ	The fluid's mean free path	µm
ρ	Liquid density	Kg/m^3
Γ	The aspect ratio	
γ_{sv}	The surface tension (energy per unit surface) of the solid–vapour interface	N/m
γ_{lv}	The surface tension of the liquid-vapour interface	N/m
γ_{ls}	The surface tension of the solid-liquid interface	N/m
ω	The angular velocity	rad/s
η	The radius ratio	
θ_E	Equilibrium contact angle	degree
θ^*	Static contact angle	degree
θ^*_{adv}	Advancing dynamic contact angle	degree
θ^*_{rec}	Receding dynamic contact angle	degree
θ^*_t	Tilt Angle	degree
δ	depicts the effective plastron layer thickness	µm
δ_l	specifies the half-channel height	mm
δ_l	specifies the half-channel height	mm
$\delta_{CA\text{-}sd}$	The standard deviation	
$\delta_{\tau s}$	Shear stress with SH coating	N/m
$\delta_{\tau c}$	Shear stress without SH coating	N/m
δ_ν	The viscous length scale	mm
δ_{CA-Re}	The image resolution error	
δ^+	Dimensionless plastron layer thickness	
τ_s	Time-average shear stress over the smooth surface	N/m
τ_c	Time-average shear stress over coated surfaces	N/m
τ_w	Time-averaged wall shear stress	N/m

τ_w^+	Dimensionless wall shear stress	
μ_L	Microliter	
μa	Dynamic viscosity of air	Pas
μw	Dynamic viscosity of water	Pas
ν	kinematic viscosity	m^2/s
σ	Surface tension	N/m
σ_o	the error to uncertainty in the determination of the beam-crossing angle	
σ_u	Uncertainty streamwise mean velocity	
$\sigma_{\langle uu \rangle}$	Uncertainty Streamwise Normal Shear stress	
α	Torque exponent	

Latin symbols

b	Slip length	μm
b_{eff}	Effective slip length	μm
b^+	Dimensionless effective slip length	
C_L	End effect correction factor	
C_f	Skin friction coefficient	
d	Gap distance	mm
E	Substrate energy	mN/m
H	The channel height	mm
G	The non-dimensional toque	
κ	von Kármán-Prandtl constant	
L	Cylinder length	mm
N	Constant	

n	Rotational speed	rpm
M	Constant	
r	Roughness ratio	
r_i, r_o	The inner and outer cylinder radius	mm
Re	Reynolds number	
S	Spreading Parameters	
u_b	The mean bulk velocity of the flow over the Baseline surface	m/s
u_{be}	The mean bulk velocity of the flow over SHS	m/s
U_m	The mean streamwise velocity component	m/s
u_m	Mean flow velocity	m/s
u_τ	Friction velocity	m/s
u_s	Slip velocity	m/s
u_s^+	Dimensionless slip velocity	

Abbreviations

ADCA	Advancing contact angle
CA	Contact Angle
CAH	Contact Angle Hysteresis
DCA	Dynamic contact angle
DR	Drag reduction
LDV	Laser Doppler velocimetry
CCF	Circular Couette flow regime

TVF	Taylor vortex flow regime
WVF	Wavey vortex flow regime
MWVF	Modulated wavy vortex flow regime
TTVF	Taylor turbulent vortex flow regime
UED	Ultra Ever Dry
FT-MW	FlouroThane-MW
FPC-800M	fluoroacrylic solution with fluorinated nanoparticles
LDV	Laser Doppler velocimetry
RDCA	Receding contact angle
SCA	Static contact angle
SH	Superhydrophobic
SO	Superoleophobic
SOS	Superoleophobic surfaces
SHS	Superhydrophobic surfaces

Subscripts

g	Gas
l	liquid
ls	Liquids-Solid
lv	Liquid-vapour
s	Solid
vs	Vapour-solid

CHAPTER I

Chapter 1 Introduction

1-1 Introduction

The flow friction and the accompanying drag forces can occur in either laminar or turbulent confined flows in many applications, such as oil pipelines, floodwater drainage systems, firefighting systems, and water heating and cooling systems [1]. The drag forces of the pipe's walls can reduce the momentum of fluid flow, which leads to reduced efficiency of the designed system.

Moreover, viscous shear drag forces exerted on marine vessels, where roughly 50% of a ship's and 60% of a submarine's drag results from skin friction [2], can increase fuel consumption and CO_2 emissions, contributing to global warming. Several active, interactive and passive techniques for reducing viscous skin friction have been explored in the past, with varying degrees of success. The passive techniques include structured and unstructured superhydrophobic surfaces (SHSs) that change the surface topography. The studies reported the governing laws of the slip length (b) over the SHSs experimentally, theoretically, and numerically.

1-2 Drag Reduction and Techniques

The overall drag in internal flows can be classified into three main categories: pressure form drag, pressure interaction drag, and skin friction or viscous shear drag, as shown in Figure 1-1 [3], [4]. Pressure form drag is caused by the drag associated with the energy, which needs to move fluid from behind an object to the front of the object through the flow stream and then back to a location behind it, resulting in a drag force on the object [5]. In other words, it is an asymmetrical pressure field between a moving object's upstream and downstream sides. The techniques for its reduction are well understood. Pressure interaction drag occurs when a pressure field is projected onto a surface topography. Its understanding is limited due to the unpredictable changes in the pressure gradient and flow vortices. Skin friction/viscous shear drag results from the interactions between a fluid and a surface parallel to the flow stream; the attraction between the fluid and wall surface is known as skin friction or shear viscous drag [5]. Skin friction drag reduction (DR) in turbulent flows, which forms a significant part

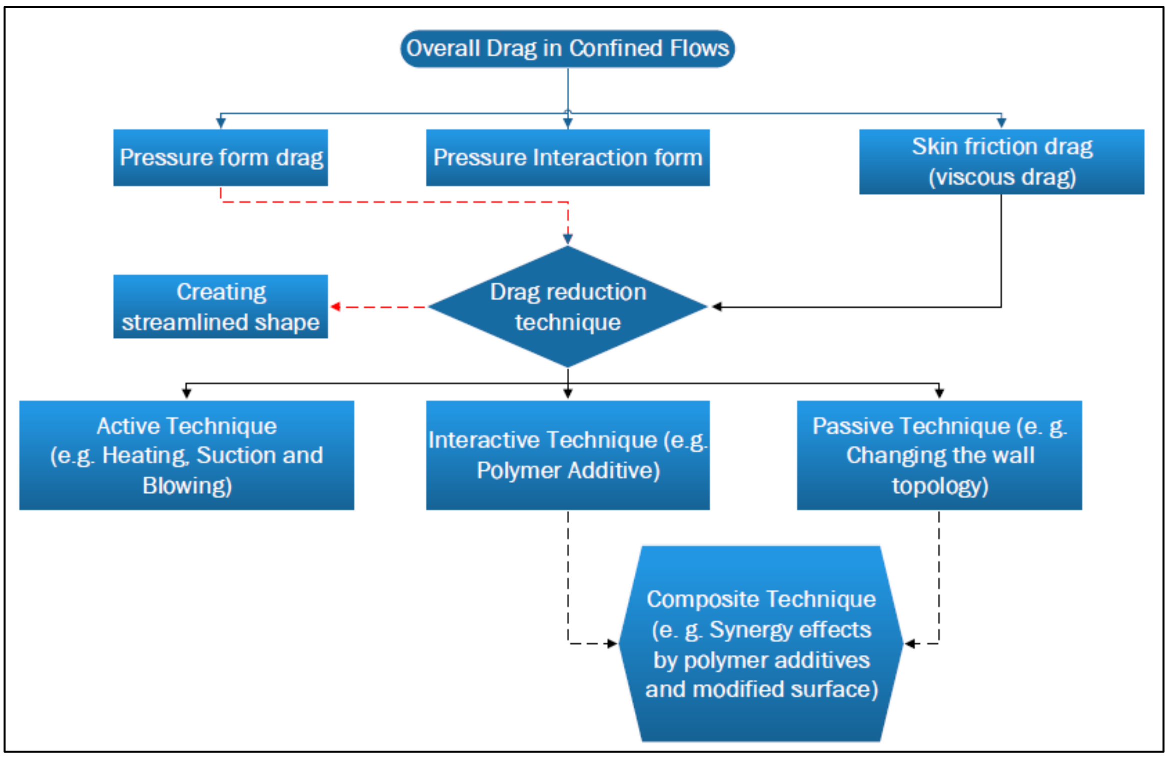

Figure 1-1 General categorization of overall drag of confined flows and its reduction techniques

of overall drag forces, has received considerable attention due to the tremendous economic and ecological interest in such flows over the last few decades.

The reduction of overall viscous shear drag can be classified into three main categories: active techniques, interactive drag-reduction techniques, and passive techniques [6]–[8]. It is crucial for internal flows to reduce the drag in order to save the pumping power or enhance the turbulent mixing. The active drag reduction includes suction, blowing, bionic jet surface, air bubbles, and heating wall drag reduction. However, in most of these techniques, extra gas-providing devices or energy are essential for an effective active drag reduction, raising costs and limiting their applications. Interactive drag reduction through the addition of polymer has been extensively studied, but this mechanism remains a complicated task. Due to the presence of the nano-long chains of polymer additives, steady-flowing conditions can be covered in the boundary layer.

Different speeds at the nano-long chain ends will be achieved with the polymer additive nano-long chains in turbulence, and the nano-long chains will rotate to decrease the difference in speed. Ultimately, to realize the drag-reducing feature, the chains achieve a balance at positions parallel to the pipe flow. This method can be regarded as a rotation-redirection effect. Passive drag-reduction techniques can be classified into two main approaches, as shown in Figure 1-2 [4]. The first method relies on the so-called superhydrophobic effect using unstructured surfaces [9]. It results from a combination of the hydrophobicity of the surface material (chemically hydrophobic) and surface topography (physically rough) [10]. Many biological surfaces exhibit remarkable non-wetting features, particularly in certain plant leaves (see Figure 1-3) [6], [11]. The superhydrophobicity of lotus leaves is well known. Much attention has been drawn to the well-known superhydrophobicity of lotus leaves, which has created great interest in fundamental research and industrial applications. A lotus leaf's static contact angle and hysteresis are around 164° and 3°c). Many biological surfaces exhibit remarkable non-wetting features, particularly in certain plant leaves [6], [11]. By mimicking the lotus leaf structure, superhydrophobic coating works to reduce surface energy. Surface energy quantifies the disruption of intermolecular bonds that occurs when a surface is created. When reducing the surface energy, the contact area fraction between liquid and solid surfaces also becomes a minimum.

The second approach is structured superhydrophobic surfaces, which have two categories. The first category is the compliant wall drag reduction related to rearranging the bulk flow into properly formed surface grooves, which could be longitudinal or transverse microgrooves. Alternately, the use of extremely thin grooves with friction decreases the flow velocity inside such grooves, thus reducing the shear to which the bounding wall is exposed [6], [11], [12] [2][7][8]. The challenge with this technique is that the compliant wall work is difficult to sustain over a long period. It will lose its drag-reduction efficiency if compliant wall hardness is achieved [6]. The second category uses riblet micro-post surfaces associated with grooves specially structured to create small separation bubbles where the fluid slows down, exposing the bounding wall to a reduced shear [6], [11], [12]. Although the riblet posts surfaces approach has a limited application, many researchers have proven that this method reduces frictional drag up to about 10% in water [6], [11]. The last two passive DR methods are active in single-fluid systems [12]. All characteristics of the methods described above use distinctive surface topography, leading to the formation of the desired flow structures. Many examples of their applications include water repellency, self-cleaning, anti-icing, anti-biofouling, anti-corrosion, desalination, and drag reduction [13], [14].

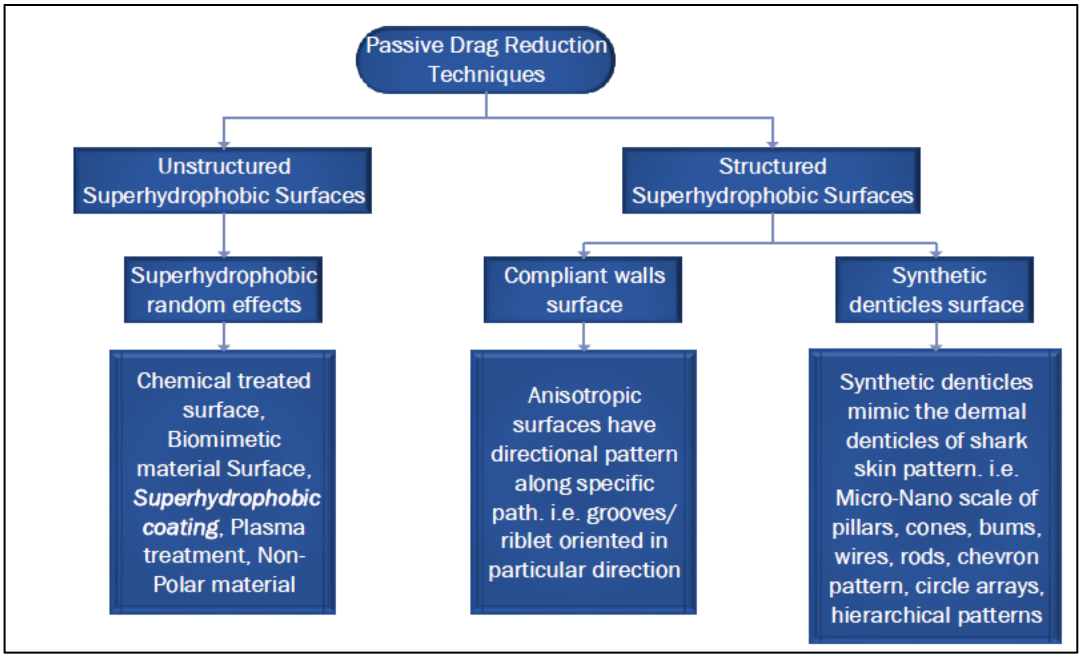

Figure 1-2 Passive drag reduction techniques

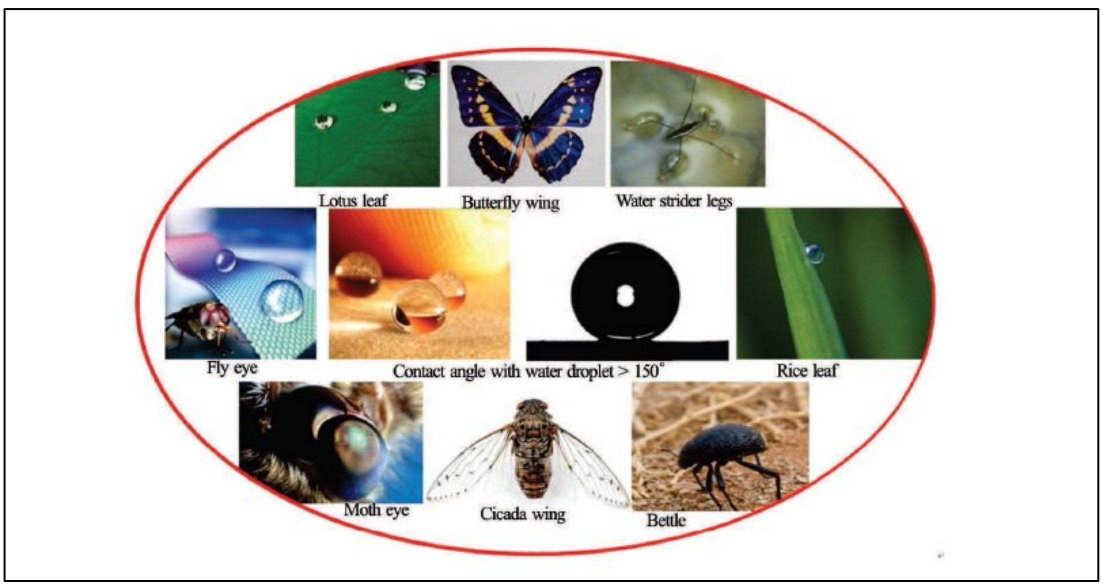

Figure 1-3 Different superhydrophobic biological functional surfaces [11].

1-3 Flow Slip and Slip Length

Slip length is another parameter used to describe the surface slippage velocity. The slip can be interpreted as the depth into the boundary at which the velocity profile can extrapolate to zero [15]. A slip boundary condition concept was first proposed by Navier (1823) [9]. In his model, Navier proposed that the magnitude of the slip velocity, u_{slip}, is directly proportional to the magnitude of the shear rate experienced by the fluid at the wall, as follows [9]:

$$U_S = u_{slip} = b\left|\frac{\partial u}{\partial y}\right| \tag{1-1}$$

where *b* is the slip length.

In 1879, Maxwell was the first to quantify the slip length of gas flow passing a solid surface. He claimed that a slip length is on the order of the fluid's mean free path, λ. This hypothesis was later thoroughly investigated and corroborated by other researchers, such as Tolstoi (1952) and Blake (1990) [16]. Therefore, for nearly all macroscopic flows of simple fluids, the value of slip length is considerably small, $b = 1$ nm. It can be neglected, and the no-slip boundary condition can be used without loss of accuracy. The slip phenomenon refers to any situation in fluid dynamics where the velocity tangential component's value appears to be different from that of the one that is in immediate contact with the solid surface, as shown in Figure 1-4 [17].

Slip length is a property of the fluid/solid interface and can, in principle, vary in space. Many factors can affect slip, such as surface roughness, shear rate (which is equal to the slope of the velocity profile), poor interfacial wettability (weak surface energy), and nucleation of nanobubbles on hydrophobic and superhydrophobic surfaces [16]. Some references claim that slip classification depends on many conditions, as shown in Figure 1-5 [18], [19], [20].

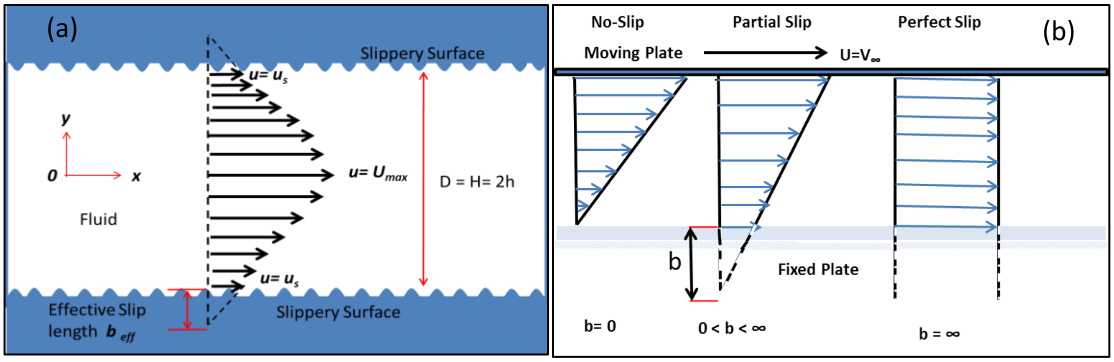

Figure 1-4 Schematic diagram of effective slip analysis

in (a) Poussile and (b) in Taylor-Couette flows.

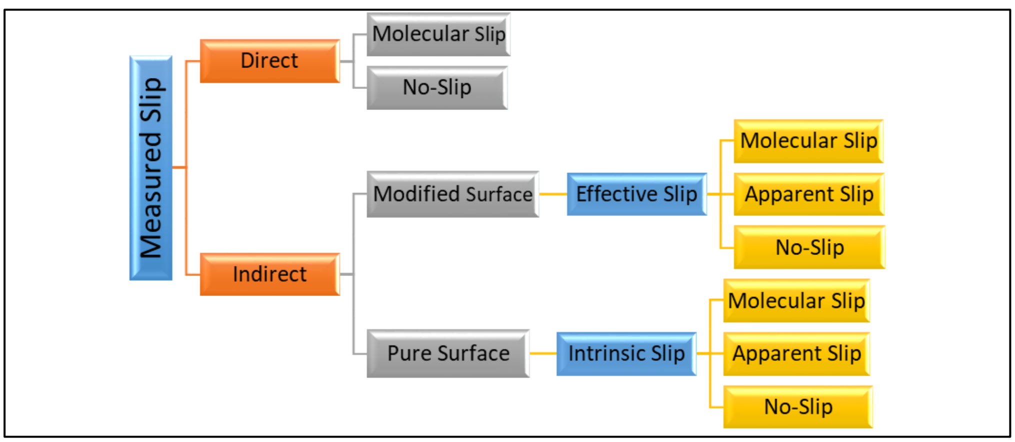

Figure 1-5 Hierarchical distribution of the measured slip length.

There is no direct experimental observation method of molecular slip; molecular dynamic simulation (MDS) has been used to observe the direct molecular slip [20]. Nonetheless, the term slip length must be tackled carefully, as there are two different notations of slip length (local slip and global slip). The local or intrinsic slip refers to the possibility of fluid molecules slipping against solid molecules. The global slip refers to the macroscopic effect of the local slip on the fluid in the far field, which is the effective slip in this case [21]. The impact of a superhydrophobic surface on flow, as mentioned earlier, is parametrized by slip length.

1-4 Surface Energy, Wettability and its Characterization

1-4-1 Surface Energy and Wettability

The contact between two separate phases gives rise to a phase boundary; the contact area is named the interface. The unusual properties of surfaces and interfaces are due to unbalanced intermolecular interaction forces (or energies) across surfaces or interfaces, such as liquid-liquid, liquid-gas, liquid-solid, gas-solid, and finally solid-solid (there is no gaseous-gas interface because all gasses are miscible). The term surface usually applies to solid-gaseous and liquid-gaseous interfaces. Molecules in a fluid feel a mutual attraction. When this attractive force is overcome by thermal agitation, the molecules enter a gaseous phase. Let us first consider a free surface, for example, between gas and liquid (refer to Figure 1-6). Attractive neighbours surround a water molecule in the fluid bulk, while a molecule at the surface has a reduced number of such neighbours and is, therefore, in an energetically-unfavourable state. Creating a new surface is energetically costly, and a fluid system will minimize surface areas, thereby facilitating small fluid bodies to evolve into spheres. In order to bring a molecule to the interface, the molecule must use its internal "potential energy" to resist this force. Hence, an increase in the interface area by ΔA requires an energy ΔW_{int}. The interfacial energy is defined as the ratio:

$$\gamma = \frac{\Delta W_{int}}{\Delta A}; \left[\frac{J}{m^2}\right] \quad or\ \Delta W = \gamma \cdot \Delta A\ \ and\ \Delta W \sim \Delta A \tag{1-2}$$

The interfacial energy (γ) can be defined as work done on (energy put into) a system for enlargement of the interfacial area between two phases by a unit area Δ A. It is more common to use the term surface tension for a liquid surface (liquid-gas interface). Surface tension is the elastic tendency of a liquid surface, making it acquire the smallest surface area possible. Note that surface tension increases as the intermolecular attraction increases and the molecular size decreases. It refers to the force per unit length required to stretch the surface (interface) with a unit of N/m. With surface tension, the liquid surface behaves like a stretched elastic membrane, having a contractive tendency.

Similarly, interfacial tension refers to the tension that exists at the interface between two non-miscible liquids. Surface tension σ has the units of force/length or equivalently energy/area. It may be thought of as negative surface pressure or, equivalently, as a line tension acting in all directions parallel to the surface, as illustrated in Figure 1-7.

Surface energy and surface tension refer to essentially the same physical phenomena, as well as the same dimensional quantity. The latter can be shown in the dimensional analysis below. Furthermore, the two terms share the same symbol (γ) in the literature, though some texts use γ for surface energy and σ for surface tension.

Surface energy (γ) =

$$= \left[\frac{Energy}{Area}\right] = \frac{J}{m^2} = \frac{N \cdot m}{m^2} = \frac{N}{m} = \left[\frac{Force}{Length}\right] = \text{Surface tension } (\sigma) \qquad (1\text{-}3)$$

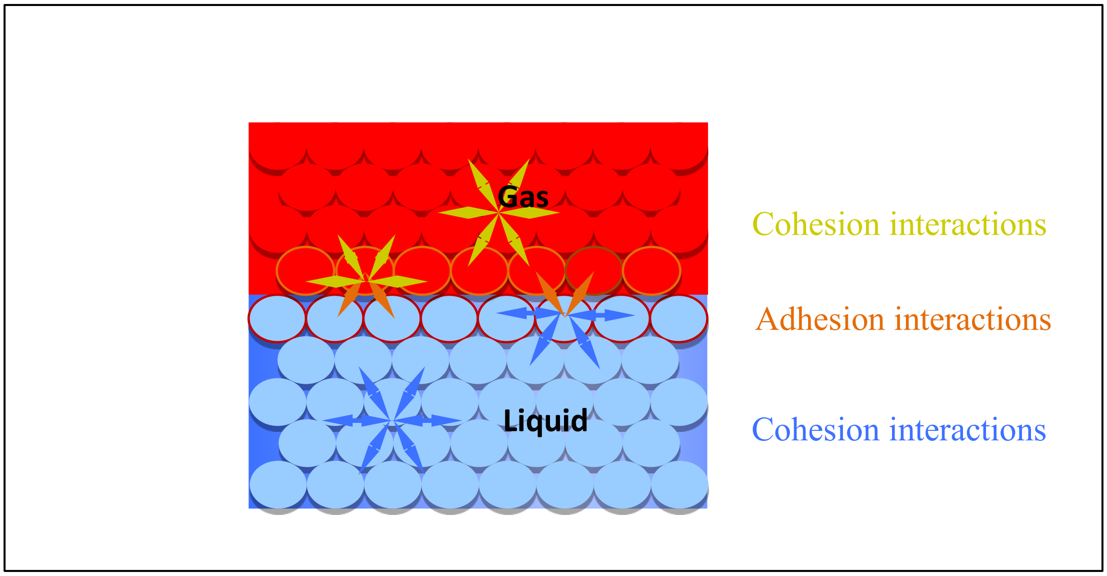

Figure 1-6 Free surface between a gas and a liquid at a molecular scale [22]

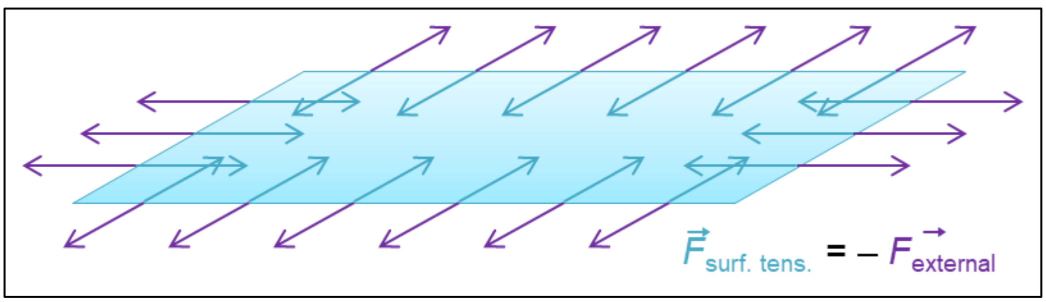

Tensile force tangential to the area

Figure 1-7 Surface tension force is analogous to negative surface pressure force [22]

The main effect of surface tension on a liquid is its change in shape to minimize the interfacial area, while on a solid, it is wetting with liquid. More generally, wetting occurs at fluid-solid contact.

1-4-2 Surface wettability characterization

The recent rapid developments in the manufacturing of superhydrophobic coating created a wide range of engineering applications [17]. As mentioned earlier, the effect of a superhydrophobic surface on flow is parametrized by slip length. Recent studies show that increasing slip length values up to the order of 100 µm have been measured on a variety of SHSs [22]. Based on these measurements, the drag-reduction application of superhydrophobic surfaces is still confined to microfluidic devices, which is a promising trend. In addition, SHSs have the future potential to reduce drag at macroscopic scales [23].

Wetting refers to the phenomenon of liquid contacting a solid or another liquid surface. Two possibilities exist (partial wetting or total wetting), depending on the three interfaces' surface energies, as shown in Figure 1-8. Now, let us consider that $\sigma_l = \gamma_{lg}, \sigma_s = \gamma_{sg}\ and\ \gamma_{sl}$, as shown in Figure 1-6. The degree of wetting is determined by spreading parameters S:

$$S = [E_{substraite}]_{dry} - [E_{substraite}]_{wet} = \gamma_{sg} - (\gamma_{sl} + \gamma_{lg}) \qquad \text{(1-4)}$$

The main effect of surface tension on liquid is its change in shape to minimize the interfacial area, while on the solid, it is wetting with liquid. More generally, wetting occurs at fluid-solid contact. Wettability, which indicates the degree of wetting, refers to a solid surface's ability to allow a liquid to contact and spread over it. A force balance between adhesive and cohesive forces determines the wettability. Contact angle CA, which is the measure of the wettability (or degree of wetting of a solid by a liquid), can be used to illustrate the hydro/oleophobicity of a surface [24]. The contact angle can be measured and calculated based on Young's Equation, as presented in Equation (1-5) [25];

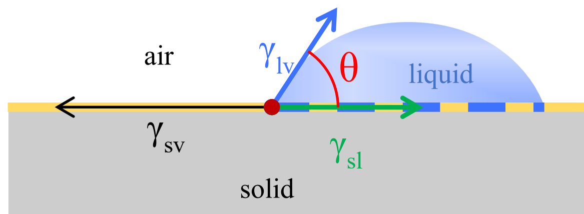

Figure 1-8 Three-phase contact line

$$Cos\theta_E = \frac{\gamma_{sv} - \gamma_{lv}}{\gamma_{ls}} \tag{1-5}$$

Where θ_E is the equilibrium contact angle, γ_{sv} is the surface tension (energy per unit surface) of the solid–vapour interface, γ_{sl} is the surface tension of the solid–liquid interface, and $\gamma_{lv}$is the surface tension of the liquid-vapour interface.

Young's Equation is a fundamental and classical wetting model for an ideal surface (smooth, homogeneous, isotropic, inelastic, chemically inert, flat/unstructured surface). However, Young's Equation can be invalid in the actual circumstance of surface construction and surface topography [24], [25] because rare solid surfaces are quite homogenous [26]. When the surface contains some roughness in nano or micro-scales, the tangential direction at the three-phase contact line is not parallel to the apparently solid surface (see Figure 1-9) [26]. Both rough and nano-microstructured surfaces inherently increase the hydrophobicity of hydrophobic surfaces through two different models [27]. The first model is the Wenzel state, where the hydrophobicity can be enhanced by increasing the surface roughness; if the liquid is non-wetting on the homogenous surface, the presence of surface roughness can render this type of substrate even more non-wetting [24]–[27]. Wenzel derived the equilibrium condition for the surface with a roughness r:

$$\cos \theta_W = r \cos \theta_E \tag{1-6}$$

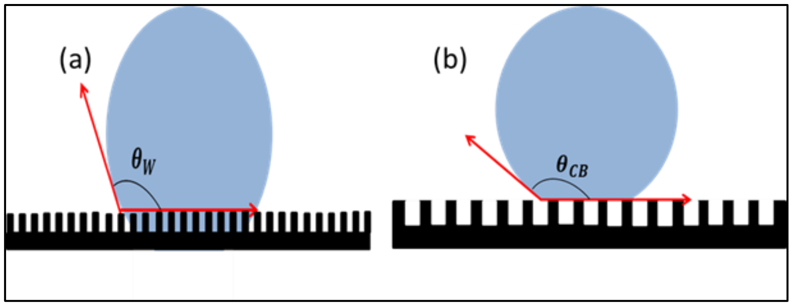

Figure 1-9 (a) Wenzel model; and (b) Cassie-Baxter Model

Where θ_W represents the apparent contact angle, r is the roughness factor, which equals to:

$$r = \frac{\text{(actual surface area)}}{\text{(geometric surface area)}} \tag{1-7}$$

The roughness factor r is a dimensionless parameter. As illustrated, if r remains greater than the unity, the actual surface area must be higher than the geometric area. Therefore, when r increases, the total surface/interfacial area also increases, leading to an increase in interfacial energy [24]–[27]. The second model is the Cassie-Baxter state, where a composite interfacial impact resulting from an air-water interface causes air to be trapped between microstructural features of the advancing wetting front [24]–[27], as illustrated in Figure 1-9b. These models represent the homogenous and heterogeneous surfaces, respectively. Both models are derived from changes in the interfacial energy of the solid-liquid or solid-vapour phases [27]. The wettability of a surface can be characterized by the contact angle (CA); the hydrophilic surface has a contact angle below 90º. A surface with a CA of above 90º is known as a hydrophobic surface; a surface with a CA above 150º and a rolling angle below 5º is defined as a superhydrophobic surface [1], as outlined in Figure 1-10.

The static contact angle, advancing contact angle, receding contact angle, roll-off or sliding angle can be used to characterize the surface wettability [28].

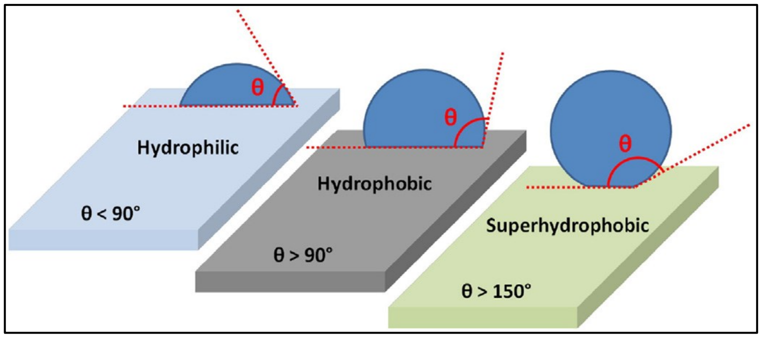

Figure 1-10 The static contact angle over hydrophilic, hydrophobic and superhydrophobic surfaces

Superhydrophobic surfaces are extremely water-repellent surfaces. They are characterized by their extremely low surface energy and the presence of micro- or nanostructures on their surface that cause water droplets to bead up and roll off rather than spreading out and wetting the surface. This property can be useful in a variety of applications, such as preventing ice formation on aircraft wings, reducing drag on ships, and keeping buildings and other structures dry and free of dirt and other contaminants.

There are several ways to characterize superhydrophobic surfaces, including:

1- Contact angle measurement: The contact angle is the angle at which a droplet of water touches the surface. A superhydrophobic surface will have a contact angle greater than 150 degrees, indicating that the surface almost completely repels the water droplet.

2- Surface energy measurement: The surface energy of a material is a measure of its ability to wet other materials. Materials with low surface energy are more likely to be superhydrophobic.

3- Scanning electron microscopy (SEM): SEM is a technique that uses a beam of electrons to produce detailed images of the surface of a material. It can be used to visualize the micro-or nanostructures on a superhydrophobic surface and understand how they contribute to its water-repellent properties.

4- Surface roughness measurement: Superhydrophobic surfaces are often characterized by their roughness, which can be measured using techniques such as atomic force microscopy (AFM).

To sum up, passive drag reduction is the most applicable, durable and low-cost technique among other techniques since it depends on the surface morphology change. Structured and non-structured textures can fabricate a surface's morphology. The superhydrophobic coating technique is the practical method to fabricate non-structured surfaces. Its mechanism depends on reducing the surface energy and creating a nano-micro roughness that traps an air layer. This air layer works as a lubricator between the fluid and the surface to reduce friction and increase the slip velocity. The slip velocity can be measured by the slip length, a property of the fluid/solid interface. The wettability or wetting degree, which is defined as the surface repellency to wet, is used to characterize the superhydrophobic surface. The static contact angle of a fabricated surface greater than 150° will be considered a superhydrophobic surface. Among other techniques, this work will consider two methods to characterize surface wettability: contact angle measurements and SEM technique.

1-5 Motivation

Effective flow drag reduction with superhydrophobic surfaces has attracted many researchers. Most previous works examined their own SH coatings. Recently, the SH coating has become available commercially with a wide range of SCAs. The SCA does not sufficiently characterize the surface wettability. Dynamic CA, CA hysteresis, and rolling CA are other parameters that have been used to characterize surface wettability. Most commercial superhydrophobic coatings have their painting procedure, whether spray, dipping or/and spinning. Some applications cannot be easily applied by following the recommended coating procedure due to complications with the geometry dimensions. The phenomenon of flow enhancement, i.e., flow drag reduction, by modifying the pipeline's inner surface has attractive benefits to fluids transportation. Surfaces coated with superhydrophobic/superoleophobic coatings may significantly improve flow capacity or reduce operating costs. Some of the applications of SHS coatings are outlined in Figure 1-11. The literature results revealed that a significant drag reduction could be achieved in laminar and microfluidic flows. The turbulent flows have been debated extensively with contrasting results both numerically and experimentally. From an engineering perspective, we can say that there is a close analogy of the Taylor-Couette flow with pipe flow, whereby many flow configurations were used to study this flow. Most previous studies used cone, plate or disc setup, while others used cylindrical configurations. The small flow field in the Taylor-Couette flows encourages researchers to investigate the achieved drag reduction and slip length. Friction in confined flows is manifested by the phenomenon of drag through the inner walls. Several recent studies examined drag reduction in confined flows by using SH coatings to engineer large slip flows. Most studies were conducted in rectangular ducts or open water channels with transparent walls, allowing non-intrusive measurement techniques such as particle image velocimetry (PIV) or similar in rare studies using Laser Doppler Velocimetry (LDV).

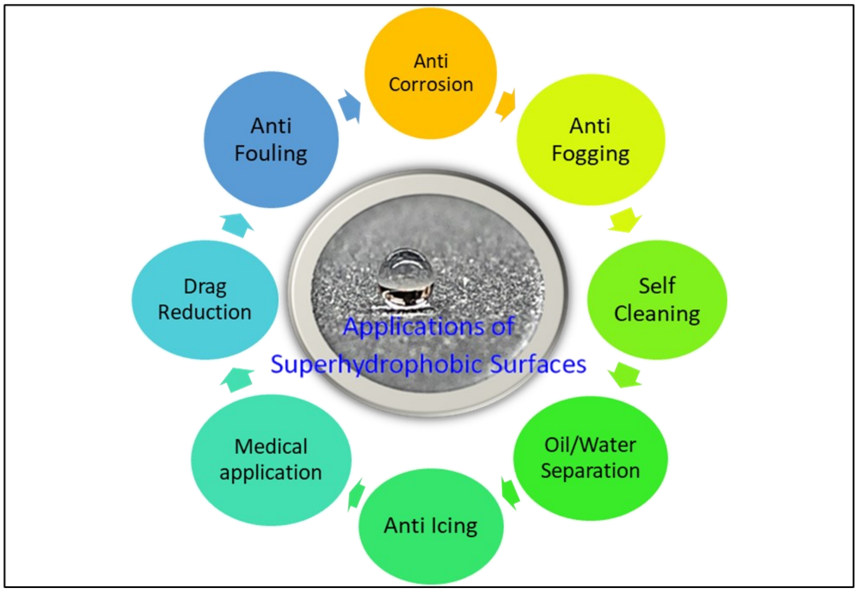

Figure 1-11 Potential applications of superhydrophobic surfaces in various fields

On the other hand, the pipe flow studies used intrusive measurement techniques such as hot film and pressure or differential pressure sensors. However, the DR results in confined turbulent flows showed a contrasting trend between reduction and enhancement. Some high SCA showed high drag reduction with the same level of drag enhancement, while others showed low drag reduction despite their high water-repellant degrees. These contrasts refer to the used surface geometry/fabrication and the measurement tools. Although advanced flow visualization techniques have been used in the experimental works, the limitations of those experimental works prevent drawing a whole picture of the studied phenomena. All previous numerical studies used structured surfaces as boundary layer flow patterns in both confined and TC flows. A vanishing air layer between the flowing fluid and the structured surface is largely responsible for the contrast in the achieved DR.

In the literature, neither slip length nor plastron thickness correlates with the wetting degree of the surface. It is known that the flow behaviour has a critical Re number where the plastron disappears, and drag enhances in both Taylor-Couette and Poiseuille flows. An experimental study is performed to acquire the required data to correlate the wetting degree effect on both slip length and plastron thickness. Such an investigation would significantly contribute to our knowledge, as it is widely assumed that a high SCA results in a high DR ratio. Further investigations will result in additional understanding, which will lead to the promising futuristic use of SHS technology.

1-6 Research Objectives

Skin-friction drag caused by turbulent boundary layer flows accounts for a significant portion of the energy consumed by many industrial applications (i.e., marine vessels/fluid transportation). As a result, a significant reduction in frictional drag would significantly reduce cost and environmental impacts. In small-scale applications, superhydrophobic surfaces (SHSs), which trap a layer of air underwater, have shown promise in decreasing drag. All proposal works are concerned with developing an empirical correlation for predicting the achieved drag based on the surface wettability and the nature of the flow. A comprehensive literature review revealed that no general or empirical correlation had been developed for predicting the achieved drag and its relationship with characteristics of the surface wettability (i.e. static contact angle SCA, dynamic contact angle DCA, contact angle hysteresis CAH, or tilt angle TA). This study will conduct a series of experimental investigations of Taylor-Couette (TC), and open channel flows over several SHSs or superoleophobic surfaces (SOSs). Moreover, a numerical study will be carried out to determine how the coating materials will behave while undergoing drag reduction tests. Briefly, the major research points to be addressed are as follows:

- The effect of surface wettability on drag will be studied in small-scale experiments involving the flow of water and silicone oils with different viscosities in a TC configuration.
- A viscous model will be used to investigate the trapped air (plastron) thickness for SHSs.
- The defect theory will be used to derive the inverse skin friction, including the slip length effect for the outer wall of the used TC cell. The mean skin friction coefficient (Cf) can be fitted to a modified semi-empirical logarithmic law expressed in the Prandtl–von Kármán coordinate.
- A statistical tool (e.g. SPSS) will be used to develop a regression model between the achieved drag, slip length, flow parameters and surface wettability parameters (e.g. SCA, DCA, CAH or TA).
- In the experiments of an open channel water flow, the laser Doppler velocimetry (LDV) system will be used to measure the velocity profile over three different SHS and one smooth (no-coating) surface. These measurements will confirm how these modified surfaces reduce the shear drag near the wall.
- Experimentally scrutinize the modifying turbulent structures in channel flows using three commercial superhydrophobic surfaces and the impact of free-stream velocity on each superhydrophobic surface performance.

These fundamental data will provide insight into the flow enhancement mechanism and determine the initial and boundary conditions, which are helpful for further numerical model development.

1-7 Dissertation Outline and Structure

Figure 1-12 illustrates the connection between these distinct elements and the structure of the thesis. The thesis is divided into eight chapters and six appendices. The main content of the thesis is organized as follows:

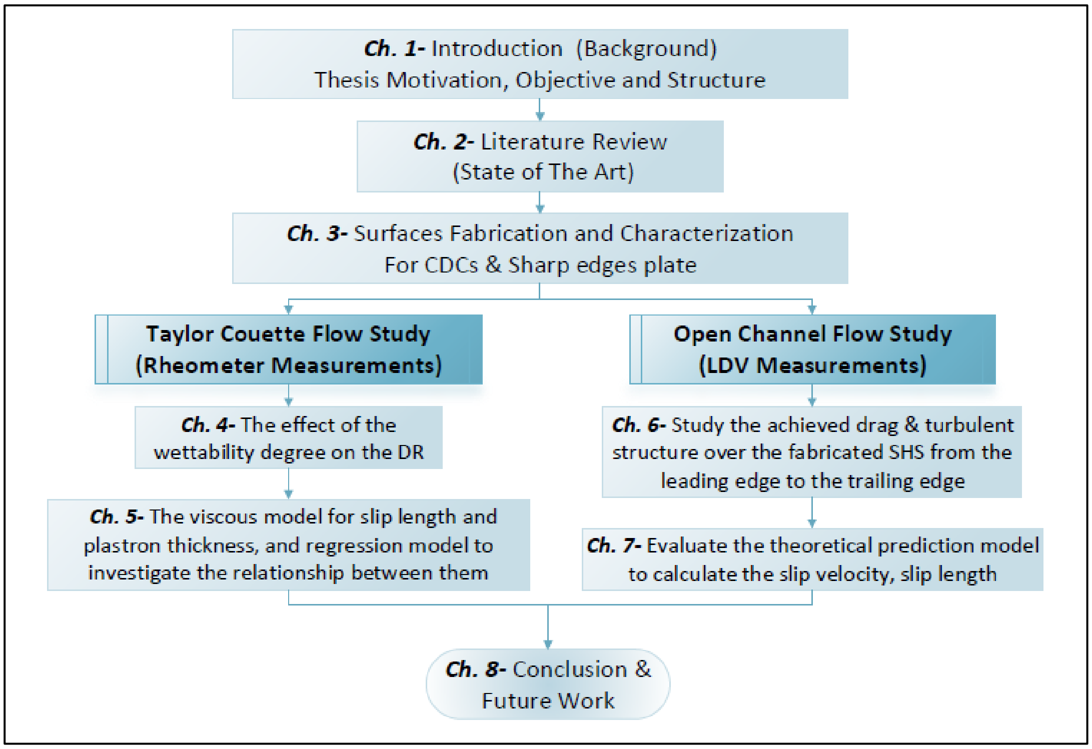

Figure 1-12 Thesis structure flowchart

Chapter 1 (Background): introduces the concept of using superhydrophobic surfaces with the slip boundary condition as a passive method to reduce drag, motivation, objective and the structure of this thesis.

Chapter 2 (Literature Review): reviews the existing literature on passive techniques for reducing viscous friction drag in Taylor Couette Flows and confined flows.

Chapter 3 (Surfaces Fabrication and Characterization): provides details on the fabrication and characterization procedures of the tested surfaces of CDCs used in the rheometer study and the sharp edges flat plate surfaces used in the open channel flow.

Chapter 4 (Experimental Rheometer Measurements): The effect of the wettability degree on the drag reduction of water and different viscosities oils in the Taylor Couette cell flows.

Chapter 5 (Theoretical Model for slip length/ Regression Model): A viscous model is used to calculate the plastron thickness; Prandtl–von Kármán model is modified to calculate the effective slip length; Statistical analysis is used to develop a regression model from the experimental data to investigate the parameters impacts on the drag reduction.

Chapter 6 (Experimental Laser Doppler Velocimetry Measurements): Study the achieved drag and turbulent structure over the fabricated SHSs from the leading edge to the trailing edge of the sharp edge flat plate.

Chapter 7 (Fundamental research about the validation of the slip velocity proposed theoretical model): Experimental data are used to evaluate the theoretical prediction model to calculate the slip velocity and slip length. An improved check procedure slip length is then proposed.

Chapter 8 (conclusions and recommendations for future work): The conclusions drawn from preceding chapters are briefly summarized, and recommendations for future work are presented.

CHAPTER II

Chapter 2 Literature Review

2-1 Introduction

The most significant advances in the techniques for nanofabrication surfaces throughout the last two decades were reported in this chapter. A literature survey of the previous experimental and numerical works will be conducted for both Taylor-Couette flows (wall-driven flow) and Poiseuille flows (pressure-gradient flow).

2-2 Superhydrophobic Coating Limitations, Development Phases and the Recent Situation

The superhydrophobic coating materials industry has significantly advanced over the last two decades, making the product commercially available. It faced many challenges during all development steps and passed many phases, and each phase can have limited applicability and durability. The recent widespread superhydrophobic technologies open doors to many applications, from personal to very complex industrial applications. Simpson et al. [13] classified the stages into four phases. The first phase improved engineered disordered nanotextured surfaces to provide a maximum CA of 178°. The main disadvantage of these surfaces is that these polymer strands are easily matted down, thus reducing the contact angle to below 130°. In the second phase, a micrograph of diatomaceous earth (DE) was treated with hydrophobic silane. It becomes superhydrophobic due to its hydrophobic surface chemistry and the amplification impact of its texture and nano-porosity. This SH nanoporous powder is called SH diatomaceous earth, or simply SHDE, and provides a typical contact angle in the range of 160° to a maximum of 175°.

The third phase is volumetric superhydrophobic coatings and includes paints, epoxies, silicones, and other SH products. It is superhydrophobic throughout the coating's entire volume, from its outer surface to the underlying substrate. This development makes SH coatings much more durable and expands their capabilities in new ways, such as reducing or eliminating impingement issues. In the fourth phase, polyurethane (or a hydrophobic sol-gel process) is used to generate a superhydrophobic thin optical clarity film when applied on a transparent substrate (e.g., glass or plastic). The main obstacle to making it applicable is that the film can easily remove only a small amount of abrasion. The fourth generation of superhydrophobic coating pioneered a new manufacturing era, presenting this coating as a commercial product in the summer of 2016.

The coating drag-reduction mechanism focuses primarily on smooth surface drag reduction and low surface energy drag reduction [29]. Recent studies have shown that the transition from the laminar boundary layer to the turbulent boundary layer can be avoided by spraying the compatible coating on the desired surface. For drag reduction of low surface energy, spraying a compatible coating changes the pipe wall's wettability because the hydrophobicity of the coating reduces the velocity gradient of the fluid on the tube wall; it leads to a decrease in the shear force on the wall, which can, in turn, reduce the drag [29]. In their review, Simpson et al. [13] mentioned that the above-named superhydrophobic materials were unavailable commercially for many reasons. However, they have been available commercially for various applications since April 2016. Many examples of their applications include water repellency, self-cleaning, anti-icing, anti-biofouling, anti-corrosion, desalination, and drag reduction [13], [14]. Based on the most recent research on superhydrophobic coating and its composite materials, characterizations, and applications, it can be seen that the produced SH coatings have a wide range of SCA (from 137° to 168°) with different substrate materials and coating techniques. This diversity makes it possible to apply coatings for specific applications, as shown in Figure 2-1.

Although remarkable progress has been made in manufacturing SH polymer nanocoatings over the past two decades, many challenges still need to be addressed for large-scale industrial applications. The present era demands the production of green, eco-friendly, superhydrophobic, low-level polymer nanocoatings with volatile organic emissions (VOCs), longer shelf life, and strong adhesion qualities [14], [30], [31]. Thus, it can be claimed that with ever-increasing interest and scientific focus in this field, a great deal of advancement could be achieved, leading to large-scale production and industrial marketing [30], [31].

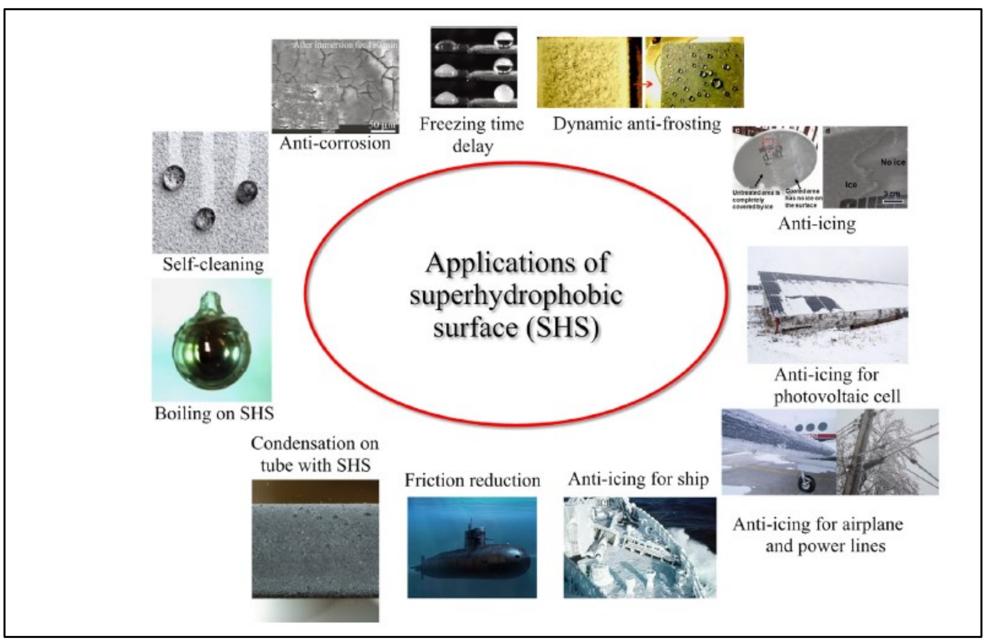

Figure 2-1 13 Applications of superhydrophobic surfaces [15]

Table I (Appendix A) summarizes the most recent research on superhydrophobic coating and its characterizations. It can be seen that the produced SH coatings have a wide range of SCA from 137º to 168º with different substrate materials and coating techniques. This diversity makes it possible to apply coatings for specific applications.

2-3 Taylor- Couette Flows – (Driven-Wall)

The flow friction combined with drag forces can present in either laminar or turbulent flow of many applications such as oil pipelines, flood water disposal, firefighting systems, water heating and cooling systems and marine vehicles [1]. In the gap between two independently-rotating coaxial cylinders, as shown in Figure 2-2, the Taylor-Couette (TC) flow facilitates molecular and convective propagation of azimuthal momentum between these two cylinders. It results in a net loss of angular momentum in one of the cylinders powered externally, which can be measured as torque (T) [32].

It is our reliance on the cylinders' rotational frequencies of interest that helps us understand the flow's gross characteristics, which include the curved streamwise flow, wall-normal pressure gradient due to centrifugal force, and the finite streamwise extent constraint [32], [33]. As the TC flow is a closed system and can be very easily controlled, it is appropriate to study turbulence interaction with superhydrophobic surfaces [34], [35].

As shown in Figure 2-2, this problem was first tackled by M. Couette (1890) and G.I. Taylor (1923) [36]. The main parameters describing the TC system are the inner and outer cylinder radius (r_i and r_o, respectively), the corresponding gap width $d = r_o - r_i$, and the cylinder's length L. In a dimensionless form, these parameters are given via the radius ratio (η) and the aspect ratio (Γ), where $\Gamma = L/d$. The system can be driven through the rotation of the inner and outer cylinders or through either one of them. This is quantified in dimensional form by the angular velocity (ω), as well as in dimensionless form by the respective Reynolds number, as follows [37]:

$$Re_{i,o} = \frac{r_{i,o} \cdot \omega_{i,o} \cdot d}{\nu} \qquad (2\text{-}1)$$

where ν is the kinematic viscosity of the fluid between the cylinder's gap [37]. Re_i is always positive in TC flow, whereas $Re_o > 0$ stands for a corotating outer cylinder and $Re_o < 0$ for a counter-rotating outer cylinder [37]. There are several explanations for the success of the TC system. It is well defined mathematically by equations put forth by Navier-Stokes with their boundary conditions; it is experimentally accessible with high precision due to its simple geometries and high symmetries. It is an ideal system to study the interaction between the boundary layers and the bulk flow. Moreover, there is a close analogy of the TC flow with pipe flow [38], [37].

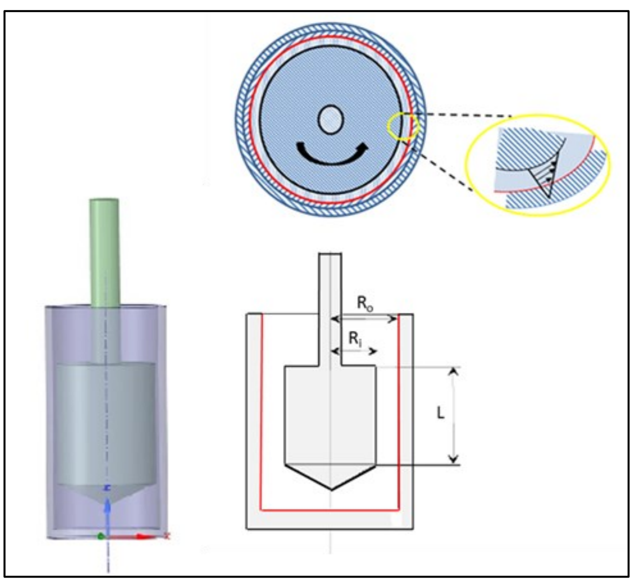

Figure 2-2 Cylindrical geometry system used in Taylor-Couette flow rheometer (CC-27 Setup)

2-3-1 Experimental Works

There have been several attempts to discover the drag reduction in the wall-driven (TC) flows with superhydrophobic surfaces. The science of rheology has undergone remarkable improvement in the wake of advances in modern and more precise technologies; hence, most TC studies were conducted by using rheometer devices with various setup geometries. The previous works elaborate on using the cone and disk geometries more than other geometries in these TC flow studies. Table 1 summarizes previous work to measure slip length and estimate the drag reduction using different rheometer geometries, bulk Reynolds numbers, and the surface characterized by both static contact angle **θ^*** and contact angle hysteresis **$\Delta\theta$**. Figure 2-3 compares the measured effective slip lengths in Table 1 with their uncertainties. One SH surface produced a slip length higher than 100 μm, while others were around 50 μm and even less than 20 μm in some cases. This discrepancy is due to many reasons, such as the variety of geometrical setup and operating conditions (i.e., Re, gap distance (d), fluid viscosity, and surface wettability). Figure 2-3 illustrates the measured drag reduction in TC flows, as Table 1 shows that glycerin produced the highest drag reduction compared to water among all results. However, the degree of oleophobicity must be smaller than the degree of hydrophobicity for the same surface used by Choi and Kim [39]. There is a disparity in the performed drag reduction results, as presented in Figure 2-4, due to several factors such as the surface's hydrophobicity, TC flow setup configuration, the contact area of liquid on the testing surface (i.e., SHS), and operating conditions (i.e., torque or shear rate applied).

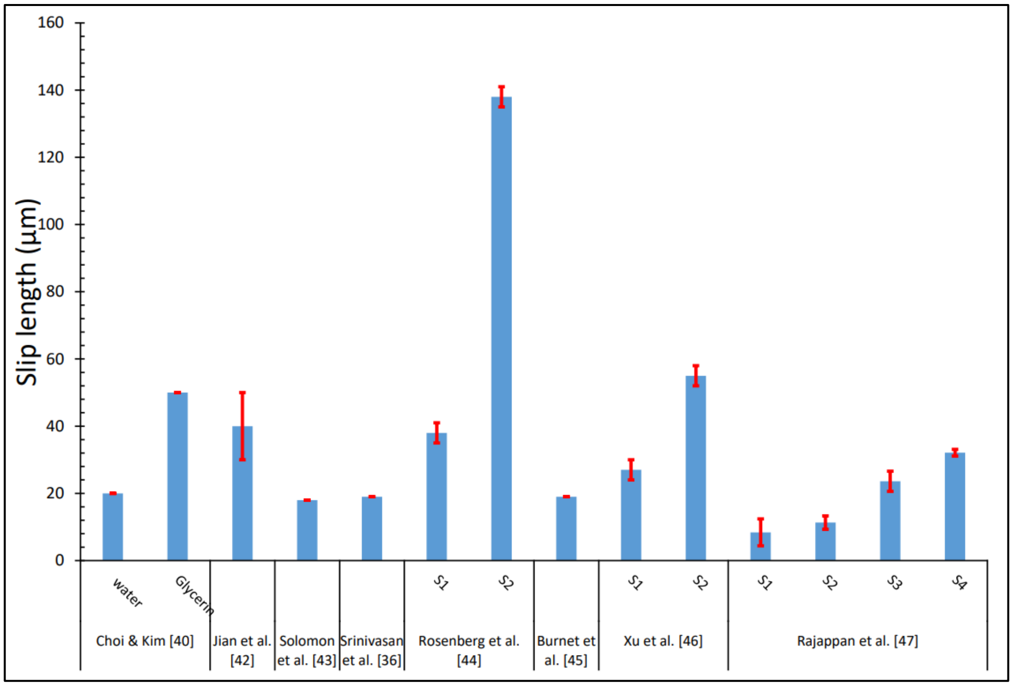

Figure 2-3 Comparison of the slip length measured by previous studies in different TC flows

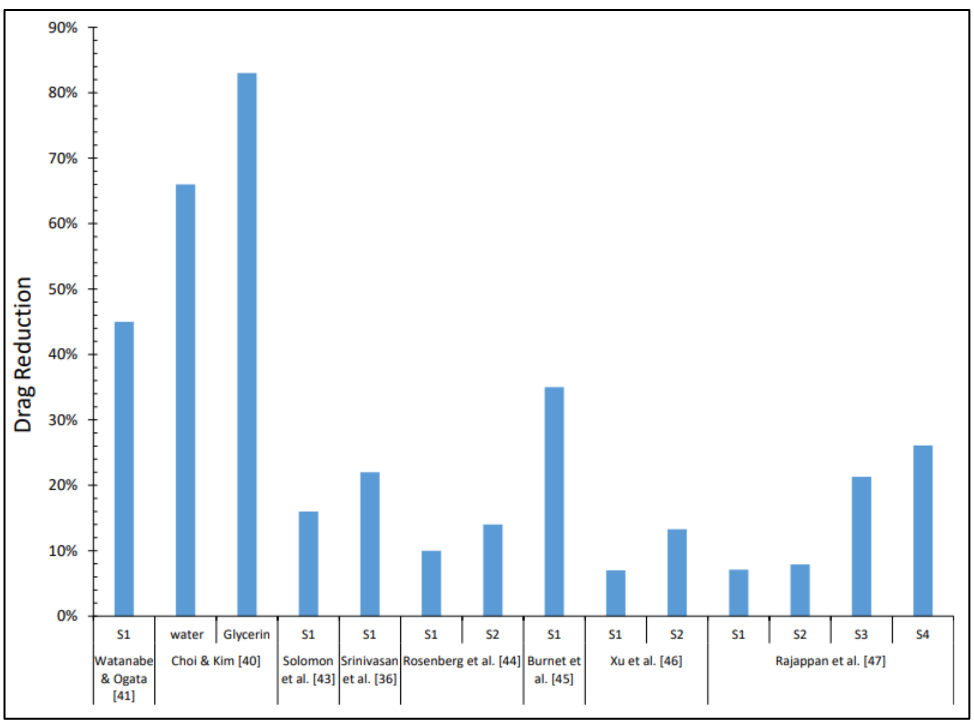

Figure 2-4 Drag reduction of TC flows performed by SHS in previous studies

Table 2-1 Drag reduction of TC flows performed by SHS in previous studies.

Author	Geometry Setup	Type of SHS	Re_b (Re_τ)	θ*	Δθ
Watanabe & Ogata [40]	Disc and plate	Random (coating)	$8*10^4$,$2*10^5$	163°	-
Choi & Kim [39]	Cone and plate	Random	$10>Re_b<10^3$	>175°	-
Jian et al. [41]	Disc and plate	Stripe structure	-	157° +/-4	
Solomon et al. [42]	Cone and Plate	Laser ablated posts	-	163°	-
Srinivasan et al. [35]	Cylinder system	Depositing sprayable SH-coating	$8*10^4$	160°	-
Rosenberg et al. [43]	Cylinder system	Structured SHS	($100<Re_\tau<140$)	-	-
Buren et al. [44]	Cylinder system	Structured square microscale grooves	10500	-	-
Xu et al. [45]	Cone and plate	PTFE, TiO_2 spray coating	-	145°, 165°	16°, 6°
Rajappan et al. [46]	Cylinder system	Four random SHSs	$10^4< Re < 10^5$	-	2°, 3°, 4°, 4°

2-4 Poiseuille flows – (Pressure gradient)

Over the past two decades, the superhydrophobic surfaces and their drag-reducing potential have attracted many researchers by affecting essential applications such as microfluidic devices, fluid transfer through pipes in oil industries, marine vessels, and large crude carriers. The industrial world is seeking to increase the energy efficiency of devices in light of rising energy costs and increased public awareness around energy conservation. In confined flows, drag reduction has been an important topic because it reduces energy loss and increases overall system efficiency. This subsection will summarize experimental and numerical studies using SHS to identify the research gaps and lack of knowledge in drag reduction.

Despite the difficulties in characterizing and scaling up SHS features, both regularly patterned surfaces and random SH surfaces have attracted many researchers. Table III summarizes the previous attempts to characterize drag reduction of SH surfaces in turbulent flow with a corresponding geometry of surfaces, apparent contact angle θ* and contact angle hysteresis Δθ when reported, where Δθ is equal to the difference between θ^*_{adv} and θ^*_{rec}. Although various geometries were studied, most previous research was conducted in rectangular channels with one or two modified SHS to measure slip velocity. Figure 2-5 illustrates the previous studies, which showed drag reduction in the range of -90% as a minimum to a maximum of +90%. In addition, some studies showed no drag reduction achieved from used SHSs (i.e., the Peguero and Breuer case) [47]. In the case of Gogte et al. [48], the measured drag reduction ranged between 3% and 18%. The negative sign in some studies indicates a drag enhancement rather than a reduction. This lack of consistency opens the door for debate regarding the high drag reduction provided in certain other SHSs using different flow geometries and experimental measurement tools. Table III lists critical parameters in these studies, including the lengths of the experimental surfaces, range of friction or shear Reynolds numbers evaluated

$$Re_\tau = \frac{H}{2\delta_v} = \frac{\delta}{\delta_v} = \frac{u_\tau .\ \delta_l}{v} \tag{2-2}$$

where H is the channel height, δv indicates the viscous length scale, δ depicts the effective boundary layer thickness, u_τ represents the shear wall velocity, δ_l specifies the half-channel height, and ν is kinematic viscosity.

Table 2-2 Previous work characterizations of SHS used in a drag reduction of Poiseuille flows

Reference	Surface Geometry	θ*	$\Delta\theta$	Length (cm)	Slip Velocity us(m/s)	Re_τ (Re_b)
Gogte et al. [48]	random	156°	-	4.3	0.005-0.014	40-288
Henoch et al. [49]	posts, ridges	-	-	20	-	150-600
Zhao et al. [50]	random	-	-	80	-	(1700-3300)
Daniello et al. [51]	ridges	-	-	100	0.4	100-300
Woolford et al. [52]	rib/cavity	160°	-	0.82	-	3-100
Peguero and Breuer [47]	Grooves, random, nanograss	180°	-	43	-	200 (6000)
Jung & Bhushan [53]	posts	173°	1°	6	-	0-18
Aljallis et al. [54]	random	164°	5°	122	-	(520-5170)
Bidkar et al. [55]	random	155°	-	15	-	(1000-5000)
Park et al. [56]	ridges	-	-	2.7	-	250
Srinivasan et al. [34]	random	161°	0°	60	-	(480-3810)
Zhang et al. [57]	random	161°	0.9°	30	-	-
Hokmabad & Ghaemi [58]	random	165°	-	50	-	(2530)
Ling et al. [32]	random	159°	-	15	0.3-0.75	(693-4496)
Gose et al. [59]	random	>161°	<5°	120	-	215-950
Abu Rowin & Ghaemi [60]	riblet surfaces with random	-	-	57	0.023	(144-4360)
Abu Rowin & Ghaemi [61]	random	152°	-	4	0.27	217 (7000)

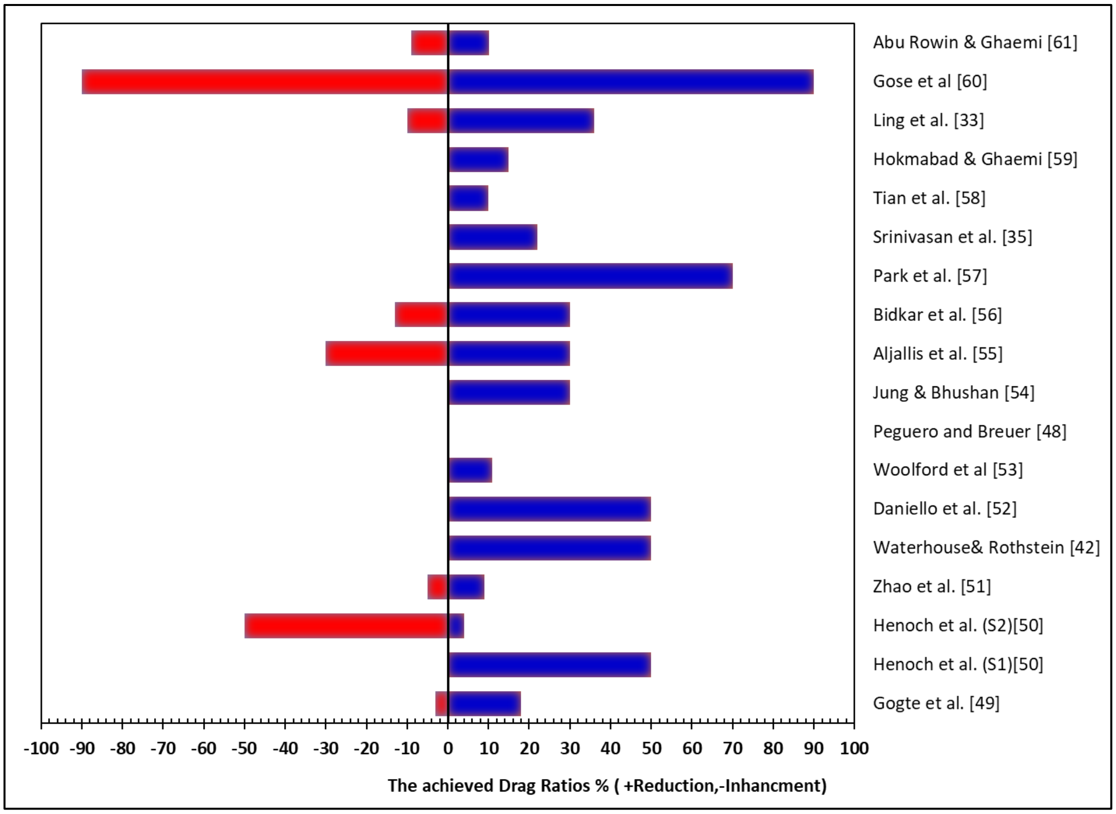

Figure 2-5 Conflicts in the drag are performed using SHS
in different confined flow setups

2-5 Summary

This chapter reviewed the present state of the art in terms of the experimental work conducted to study passive drag reduction using SHSs in wall-driven and pressure gradient flows and available in the open literature. The wall-driven flow studies were conducted using rheometer devices with many setups, i.e. disk and plate, cone and plat, and cylindrical system (TC cell). The readings from some of these apparatuses were debated and criticized as their results are inconclusive since the achieved slip length is within the experiment uncertainty range. The experiments with SH coating in the cylindrical system (TC cell) used the inner surface where the pressure is low in this region compared with the outer wall. All the Taylor Couette flow measurements generally showed drag reduction from 5% to 80%. The overview of the vibrant field of drag reduction with mimetics of superhydrophobic surfaces in closed and open channels is provided in this review. Non-intrusive techniques such as PIV and LDV are used with a limited field of view, which does not present the complete picture of the flow over the entire studied SHS. Other studies used intrusive techniques such as pressure sensors to measure the achieved drag with limited information about the flow behaviour. This limitation rises the question of how long the unstructured SHS will sustain in a highly turbulent flow. The controversial and conflicting findings on this side still have attracted many researchers to investigate further since SHS technology has developed; that can help to understand what factors lead to this conflict in the investigated results.

CHAPTER III

Chapter 3 Surface Fabrication and Characterization

3-1 Introduction

Characterizing the wettability of the SHS is crucial for predicting its drag-reduction capability. A liquid droplet of tested fluid mounted on curved or flat, homogeneous surfaces has an inherent contact angle (θ) along the three-phase contact axis. The contact angle CA (θ) is determined by the equilibrium between the surface tension of the liquid droplet, the surface energy of the solid, and the interfacial tension between the liquid and the solid. The superhydrophobic surface is chemically heterogeneous. The air plastron is commonly referred to as the air layer captured between the SH surface and the water. This air plastron is generally linked with a non-wetted state Cassie-Baxter. The air plastron is affected by the topography of the superhydrophobic surfaces. The scanning electron microscope (SEM) photographs of coatings' surface morphology were used to investigate the surface topography that generates water/oil repellant using the commercial SH nano-coatings and to closely depict how the SH nano-coating is in this microscale step. In this chapter, the prepared surfaces used in the two experimental parts of this work had investigated. The investigation includes static and dynamic contact angle measurements and SEM images that to report the wettability of surfaces and surface morphology. The examined surface preparation methods are presented in detail.

3-2 Coating Materials

Superhydrophobic coatings were selected based on their compatibility and resistance to solvents and chemicals, durability, adhesion, and suitability for large-scale applications were considered, along with cost considerations. All of the selected products are for industrial use, not for cosmetic use. The primary factor guiding the choice of commercial superhydrophobic coatings was their extensive range of wetting capabilities, and the selected coatings offer a static contact angle for water ranging from 140° to 171° and for oil ranging from >100° to 140°. All surfaces in this work are fabricated using four commercial superhydrophobic coatings, which are FPC-800M Cythonix, Fluothane-MW Cytonix, Ultra-Ever Dry, and SHBC-Nasiol. The FPC-800M and Fluorothane-MW are monolayers, while UED and SHBC are binary-layer (bottom-top) coatings. The first layer is the base coat, which binds the substrate and the second layer of a superhydrophobic top coating. The chemical composition of the coating ingredients of FPC-800M contains ethyl nonafluoroisobutyl ether, ethyl nonafluorobutyl and fluoropolymer. The Fluorothane-MW is a composition of Solvent naphtha (petroleum), light aliphatic and Fluorocarbons. The SHBC consists of perfluorooctanoic acid, perfluorooctanesulfonic acid and nontoxic, ultra-SiO_2 nanoparticles. In comparison, the UED in its bottom layer comprises xylene, tret-butyl acetate, acetone propane-2-one, and propane, while the top layer contains acetone and silica (SiO_2).

3-3 Curved Surfaces

The schematic diagram of the Taylor-Couette (TC) cell used in this work is presented in Figure 3-1. The TC consists of concentric disposal cups (CDC) used for the CC27 cylindrical setup of the rheometer MRC302 from Anton-Paar GmbH. The CDC is made from an aluminum sheet thickness of 1 mm, as shown in Figure 3-1. This section will detail the CDC surfaces' superhydrophobic surfaces fabrication, morphology and wettability characterization methods.

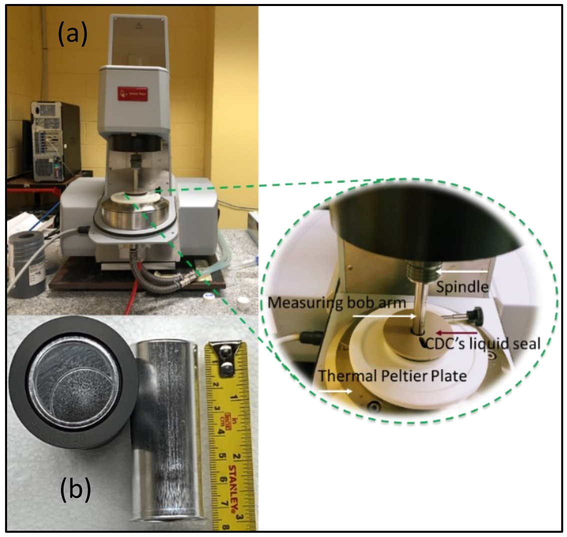

Figure 3-1The modular compact Rheometer -MCR 301 (a), which uses the concentric disposal cups with its base for measuring system CC27 (b) as the Taylor-Couette cell used in the present work

3-3-1 Surfaces Preparation and coating layer thickness

The inner surface of each cup was treated with the dipping and spinning technique, as shown in Figure 3-2. This technique was used instead of the recommended spray technique because the inner diameter of CDCs is small. A new CDC was used for each SH coating to prevent errors in the torque measurements due to the impurities of other products. The CDC cups were cleaned using water and acetone first, then thoroughly dried by air. To get a homogenous coating layer, the cup was, after being dipped in the coating, immediately spanned at a fixed rotating speed using a center lathe machine at 100 r/min. All surfaces were cured at room temperature for more than 72 Hrs. Some SH coatings are recommended to be used after seven days when the surfaces show high superhydrophobicity.

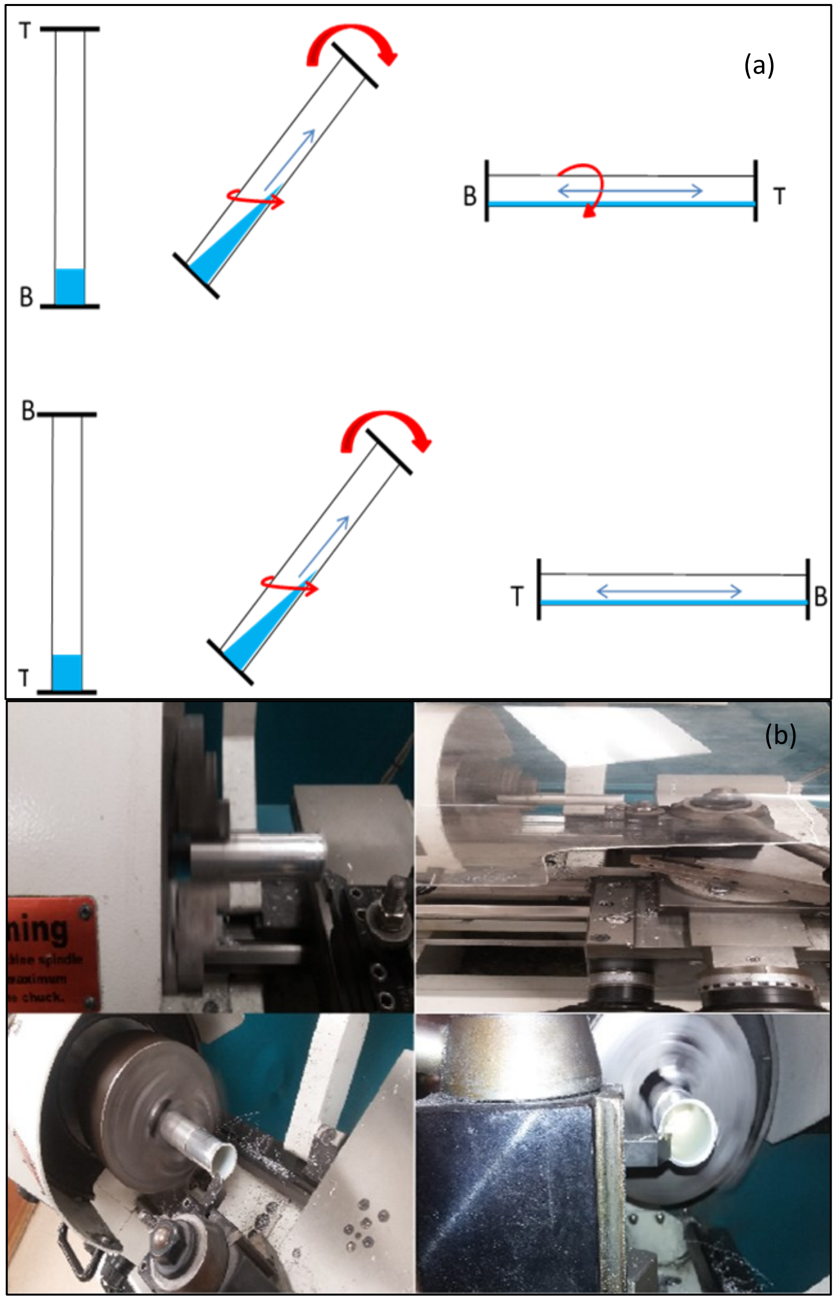

Figure 3-2 (a) Dipping and (b) spinning technique used to prepare the SHS of the CDC sample used in the rheology study

As illustrated in Figure 3-1, the coating layer changes the gap between the measuring bob and CDC inner surface, which is important for the rheometer tests. For this reason, the thickness of the coating layers was measured using an ultrasonic coating thickness gauge

(Elcometer 456 Model), as shown in Figure 3-3. The thickness gauge and non-ferrous probe were calibrated on an uncoated base CDC surface (this will be termed the smooth surface in the rest of this paper) with foils of verified thickness. The probe has a resolution of ± 0.1 µm. The coating thickness was measured by gently touching the probe tip to the sample surface and holding it there until the gauge displayed the thickness measurement. More than 70 points were measured for each sample. The average was taken to calculate the coating thickness for each sample, as presented in Figure 3-4, and a measurements output sample is presented in Appendix B. The coating layer resulted in a slight change in the inner-cylinder radius and the radial gap, which were taken into account for the experimental conditions. Table 3-1 illustrates each used sample's average coating thickness value. However, slight variations in the thickness of a superhydrophobic coating may occur due to factors like the application process or gradual wear and tear. Nonetheless, these variations are usually insignificant and do not substantially impact the overall superhydrophobic properties. In this study, we conducted three repetitions of the experiment for each sample to assess the coating's durability and ensure the reproducibility of the results.

Table 3-1 Summary of the average value of the SH coating layer thickness for each sample:

Used liquids	The thickness of the SH Coating Layer (µm)		
	FPC-800M	UED	SHBC
Water	5 ±0.2	13.4 ±0.4	18.1 ±0.5
Silicone Oil (5 cSt)	4.5 ±0.14	17.3 ±0.5	18.1 ±0.5
Silicone Oil (10 cSt)	3.9 ±0.1	16 ±0.5	24.4 ±0.7

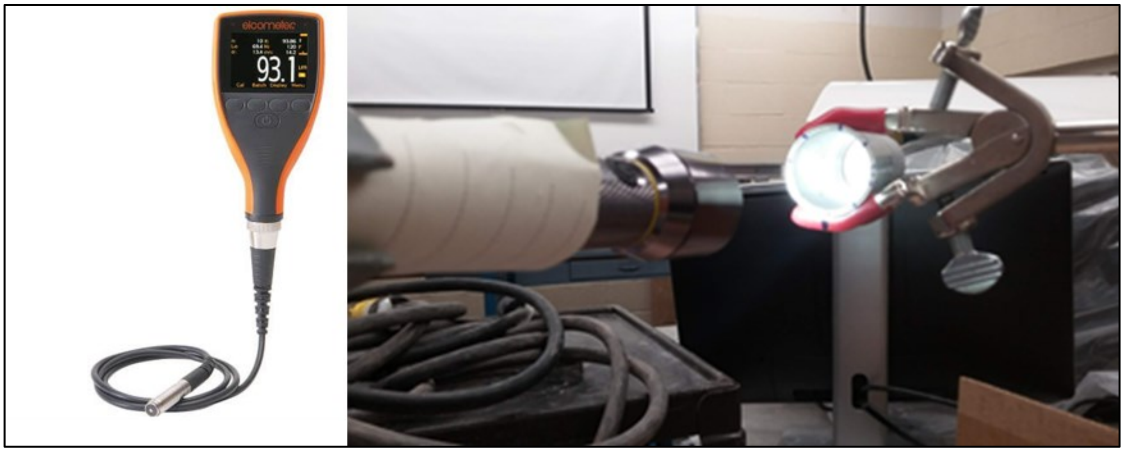

Figure 3-3 Elcometer thickness gauge used to measure the SH coating layer of the used CDCs and sample preparation to measure the coating thickness.

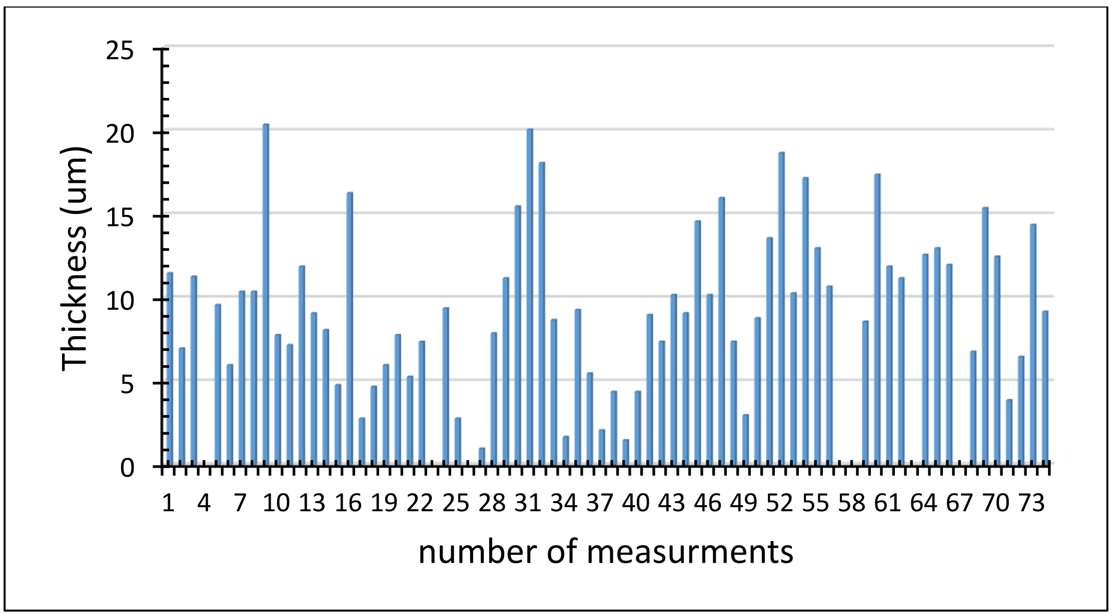

Figure 3-4 Coating thickness measurements were taken over the whole surface for one sample to calculate the average value.

3-3-2 Surfaces Characterization

A droplet of 20 μL of each used liquid was used to characterize the curved surface samples prepared for this purpose, as presented in Figure 3-5. The measurements were averaged over ten fresh spots for samples. The goniometer of the OCA15 optical contact angle measurements (DataPhysics, GMBH Germany) was used to measure the static and dynamic contact angles, as shown in Figure 3-6. The SCA20 software (DataPhysics) was used for droplet analysis and control operating parameters. The contour of the droplet was calculated based on the polynomial fitting model for deionized water and the circle fitting model for silicone oils; these overcame the curvature of the substrates and gave accurate measurements compared to the other available models.

Moreover, the surface morphology, which describes the surface topography, is discussed in this section. The technical report of each SH coating used in the present work, as mentioned earlier in subsection 3-1, indicated the low static and dynamic angles using mineral oils. The tested silicone oils have higher viscosities than the mineral oils. Silicone oils often have larger and more flexible molecular chains than mineral oils. This enhanced molecular size and flexibility allow silicone oils to readily diffuse and spread across surfaces, making them appear more oleophilic at stationery. The high oleophilicity makes the measurements of the dynamic contact angles (very low values) more difficult with the tested oils.

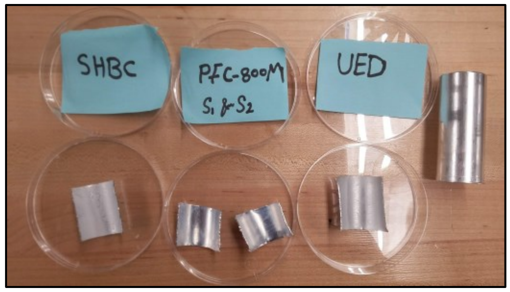

Figure 3-5 The samples of CDCs painted by three different superhydrophobic coatings

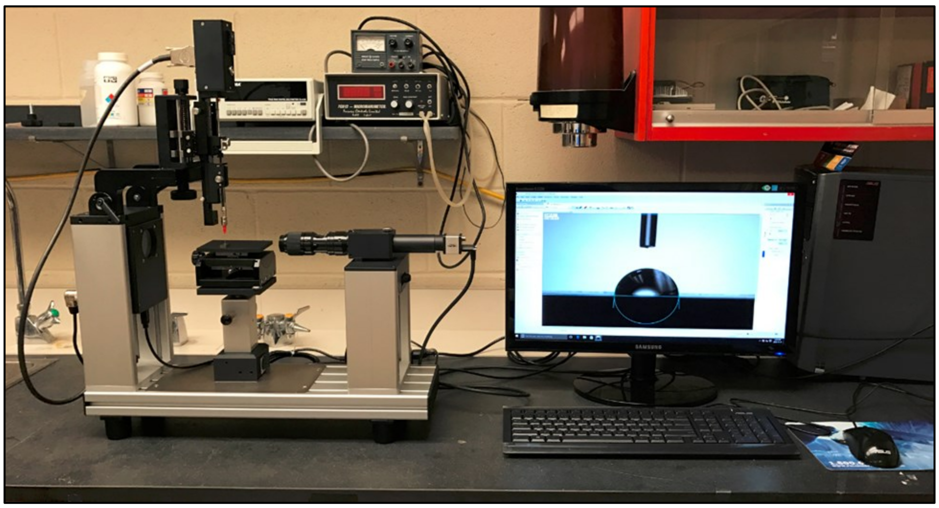

Figure 3-6 Contact angle measurement device (The goniometer of the OCA15 from DataPhysics, GMBH Germany)

3-3-2-1 Static Contact Angle

The wettability of coated surfaces was evaluated based on the values of static contact angle, receding and advancing dynamic contact angles, and contact angle hysteresis. Table 3-2 summarizes the static and dynamic contact angles for all surfaces used in this work, measured under ambient laboratory conditions. The contact angle measurements led us to estimate the wettability state of the fabricated surfaces with the used fluids. Overall, the fabricated surfaces reacted with water as a SH surface, indicating deionized water's high surface tension. The FPC-800M sample is defined as a hydrophobic surface by the producers' specifications (140°), producing a higher θ_s of 150°. Both UED and SHBC showed θ_s of 158° and 152°, respectively, which are less than the producers' specifications of 170°. The coating procedure used in this work caused the obtained low θ_s, which was contrary to the producers' recommendation. Figures 3-7 and 8 illustrate all SCA measurements over the tested surfaces, ten random measurements at different locations on the same sample to take the average value of the SCA and some images for the measurements.

3-3-2-2 Dynamic Contact Angles and Contact Angle Hysteresis

The measurements of the dynamic contact angles of all SH surfaces using water showed that the SHBC had a higher contact angle hysteresis with 6°. In contrast, the other two surfaces had 1o and 2° for UED and FPC-800, respectively. Fluid viscosities were increased 5 and 10 times greater than water to measure the fabricated surfaces' oleophobicity. Silicone oils of 5 and 10 cSt were used for this purpose. For 5 and cSt oils, the low θs of all samples produced a perfect wetting state for UED and SHBC samples, and this created difficulty in measuring the dynamic contact angles. The FPC-800M showed a high contact angle hysteresis of 11°, describing the prepared surfaces' oleophobicity state. Table 3-2 summarizes the static and dynamic contact angles for all surfaces and liquids used in this work, measured under ambient laboratory conditions.

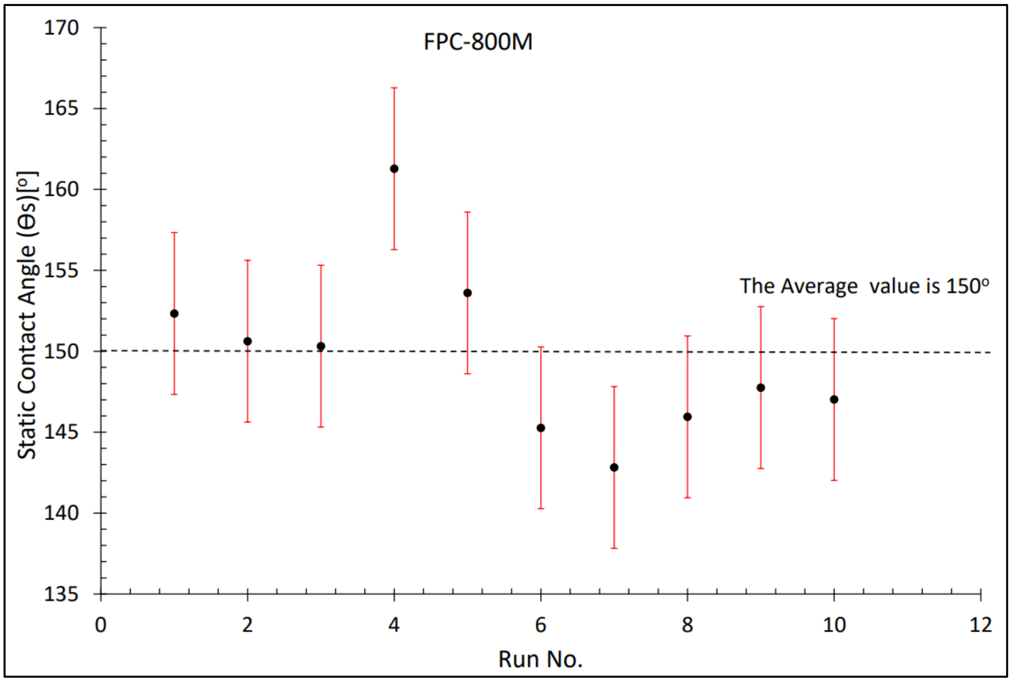
FPC-800M
The Average value is 150º
Static Contact Angle (Ɵs)[º]
Run No.

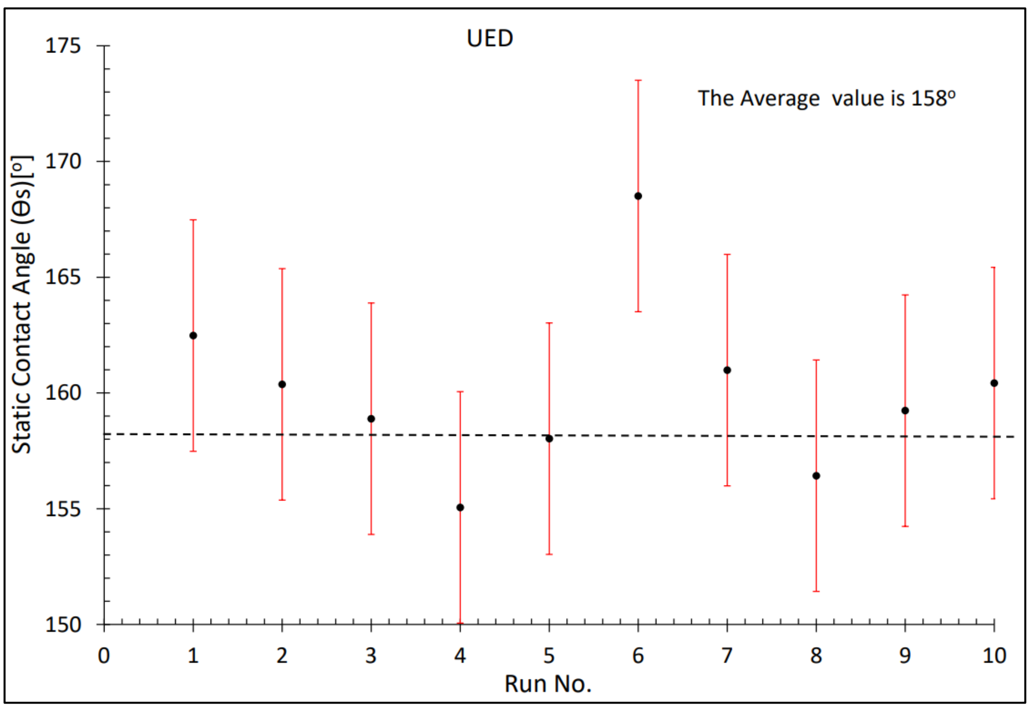
UED
The Average value is 158º
Static Contact Angle (Ɵs)[º]
Run No.

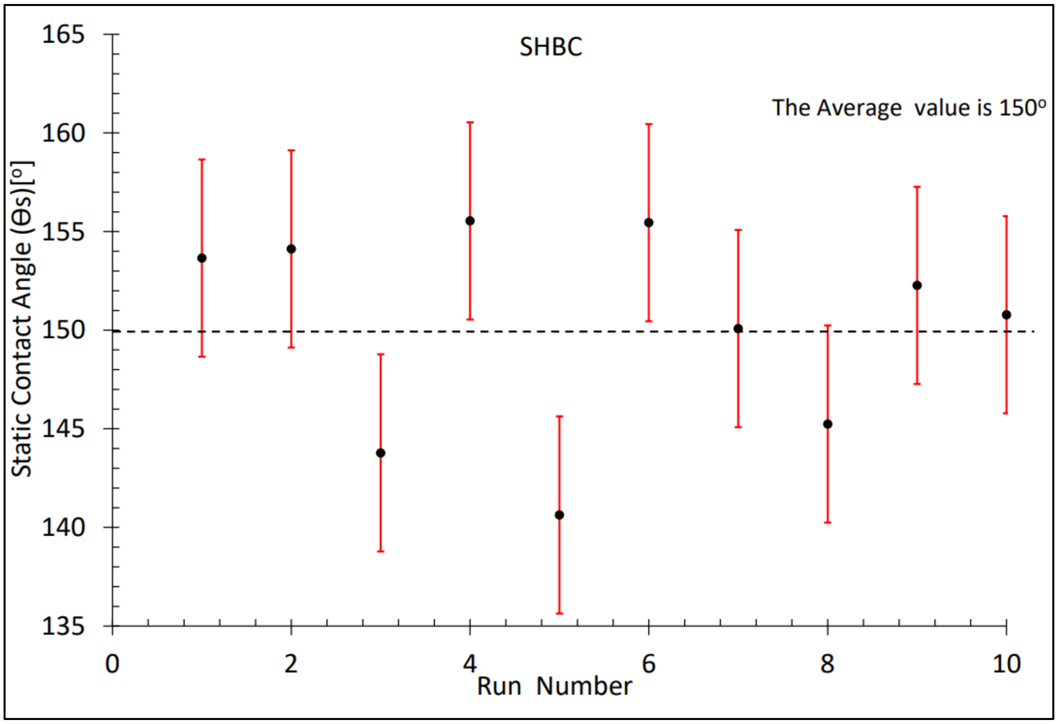

Figure 3-7 The Static contact angle measurements for all used curved surfaces, the error bars for RMS error which is ±5∘ for each measurement

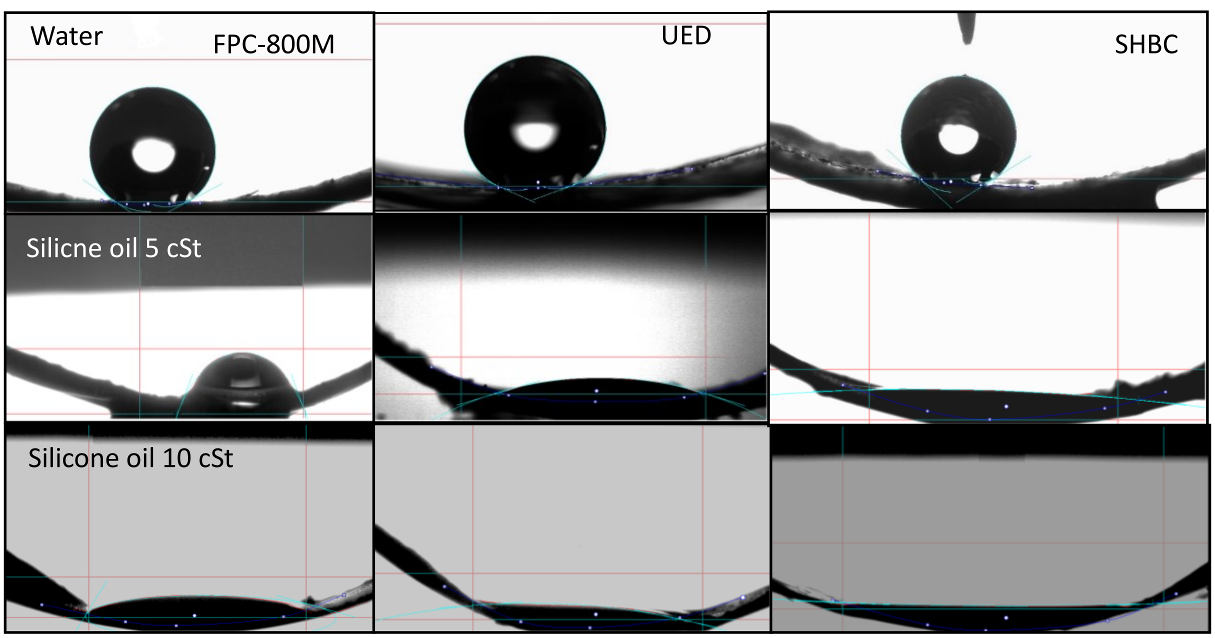

Figure 3-8 Some static contact angle (θs) measurements for the fabricated samples of FPC-800M, UED and SHBC, respectively, in each column and the tested liquid in each row

Table 3-2 Summary of surface wettability parameters for all tested liquids and surfaces; the reported errors are the standard deviations of measurements that were taken at different locations on each tested curved sample.

	Water			Silicone Oil 5 cSt			Silicone Oil 10 cSt		
	FPC-800M	UED	SHBC	FPC-800M	UED	SHBC	FPC-800M	UED	SHBC
Static Contact Angle	150± 5 °	158± 5 °	152± 5 °	59± 5 °	33.5± 1 °	16.5± 1°	27± 1 °	22.1± 5 °	13± 1 °
Advancing Contact Angle	155± 5 °	156± 5 °	154± 5 °	84± 10°	-	-	-	-	-
Receding Contact Angle	153± 5 °	155± 5 °	148± 5 °	73± 5 °	-	-	-	-	-

3-3-2-3 Curved Surfaces Morphology

The superhydrophobic surface is chemically heterogeneous. The air plastron is commonly referred to as the air layer captured between the SH surface and the water. This air plastron is generally linked with a non-wetted Cassie-Baxter state. The air plastron is affected by the topography of the superhydrophobic surfaces. SEM images of the coating surfaces' morphology were employed to examine the surface topography responsible for creating water/oil repellency with the commercial superhydrophobic nano-coatings. These images offer a detailed depiction of the microscale structure of the superhydrophobic nano-coating. Using an MLA 650 FEG model (FEI co.), the scanning electron microscope (SEM) images were taken for samples from the SH-coated of CDCs. The SEM images of the coated surface morphology were used to characterize the surface topography and investigate the coating's durability that generates water/oil repellant using the commercial SH nano-coatings. Furthermore, the SEM images provided a detailed representation of the microscale structure of the superhydrophobic nano-coating. At magnifications ranging from 1200X to 22000X, these images produced clear and well-defined depictions of the surface topography.

Figure 3-9 shows the SEM images; it depicts the geometry of hills (the brighter region) and valleys (the darker region) in the micrometre range. A closer inspection revealed that the particles were densely compacted. The SEM images of FPC-800M started from the magnification of 1200X and 11000X and ended with a final magnification of 22000X. This was conducted to zoom in and take a deep insight into the topography structure of the prepared surfaces. The FPC-800M surface showed a nonisotropic sponge-like structure that made up the nano-coating layers. The cross-section resembled the top and bottom surfaces of the nano-coating. The SEM images for the FPC-800M inspected the large pore sizes of 1-5 μm with surfaces of nano roughness structure.

The SHBC surface showed an isotropic sponge-like structure. A zoom-in SEM image for a spot not covered by SHBC coating was investigated to see the surface structure. Contrary to the FPC-800, the SHBC had pores of nano-porous length scale, and the images could not provide that scale in the large magnification. The UED is similar to the SHBC as both are applied using a binary layer to create a superficial layer with finely textured geometry. This top surface consists of patterns of geometric shapes and billions of interstitial spaces based on the structure of a nanotextured surface. The created random structure helped generate low surface energy, which caused droplets of the used liquid to be in contact with a meagre percentage of the coating. The SEM images of the UED could not investigate the nanostructure of the interfacial coating layer, and they focused on two air bubble spots that were generated during the applied coating process. The SEM zoom-in image in Figure 3-9c with final magnification could not capture any detail in the nanostructure of the sample surface, which was difficult to see with the used SEM device. Although dependent on the Re number, the multi-scale roughness length scales of the surfaces played a significant role in influencing the flow behaviour [62]. The SEM images can clearly show that the mutable length scales are present on all tested samples. Moreover, it is clear from all the SEM images of all samples that the coating technique is crucially important in tamping the effect and coating formation due to insufficient compaction and lack of dense aggregations and agglomerations between nanoparticles.

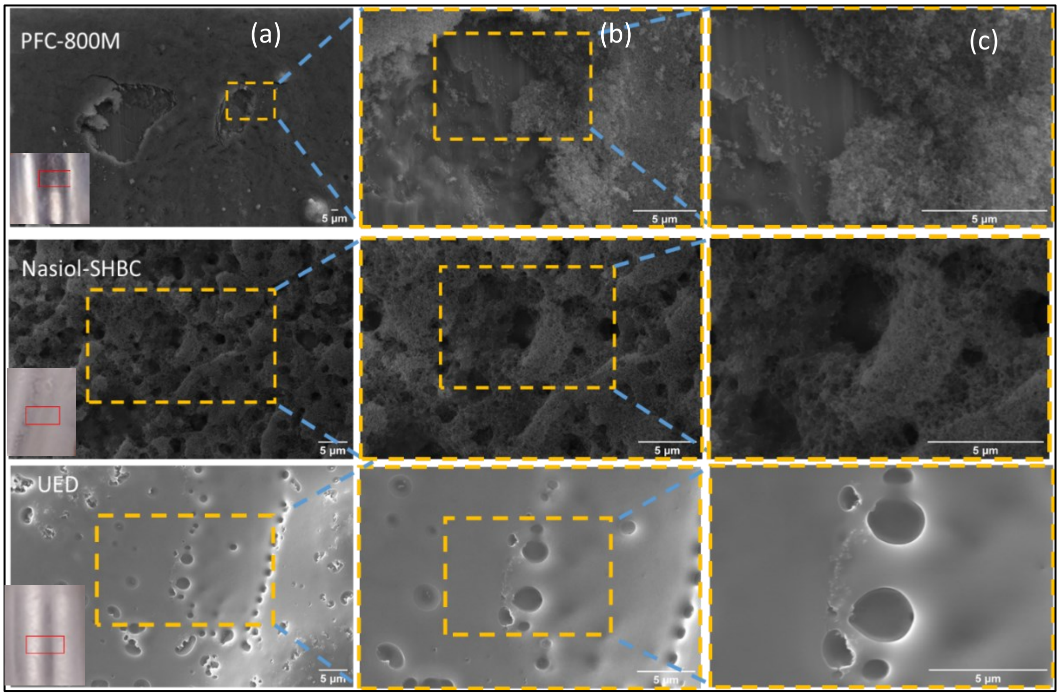

Figure 3-9 SEM images of the surface topography of the random roughness of coating surfaces that are exposed to the flow. The highlighted area magnified scale from 1200X in (a), 11000X(b) to 2000X in (c). The scale bar of 5 μm appears in all magnification step

3-4 Flat Surfaces

The second part of the experimental study is to investigate drag reduction over a large flat plate. An open channel is used in this study, as will be explained in Chapter 6. The tested surface used in this experimental part is made from a piece of acrylic and presented in Figure 3-10. It is 498 mm long, 249 mm high, and 29 mm thick, which is large to use as the contact angle measurement device (optical goniometer instrument).

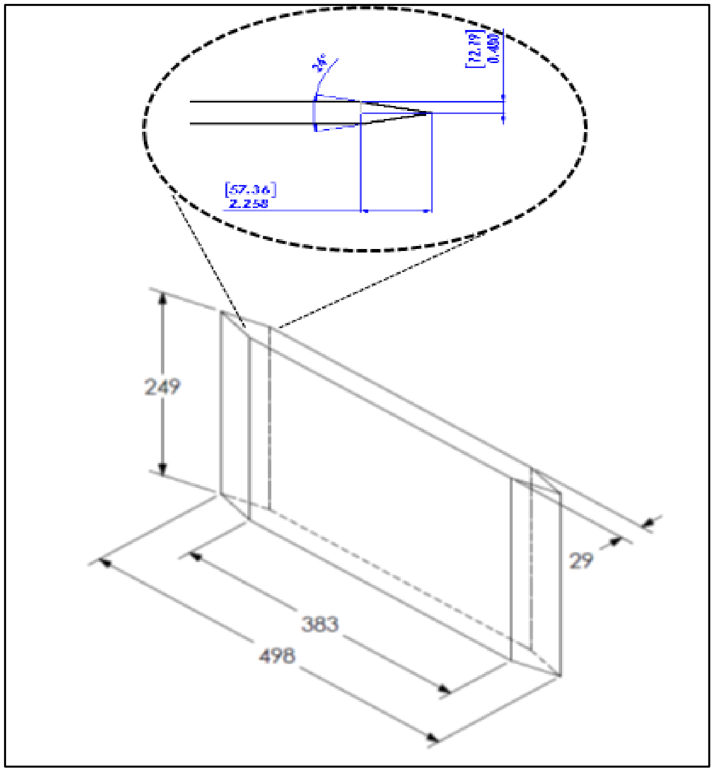

Figure 3-10 The tested surface used in the second experimental part with its original dimensions

3-4-1 Surfaces Preparation

Instead of the original tested surface, three small pieces of acrylic are used to characterize the fabricated surfaces, which are 150 mm long, 55 mm high, and 25.4 mm thick. The samples were fabricated by a spray technique, the recommended technique by the coating producers, similar to the originally tested surfaces used in this study. The samples were cleaned with acetone before the coating process and left for 72 hours to cure after applying the coatings. Three commercial SH coatings were applied using a spray technique. The SH coatings are Ultra Ever Dry (UED), FPC-800M and FlouroThane-MW from Cythonix. The PFC-M800 and FlouroThane-MW are monolayer coatings, while UED is a binary layer coating. The chemical composition of the coating ingredients of FPC-800M contains ethyl nonafluoroisobutyl ether, ethyl nonafluorobutyl and fluoropolymer. The FlouroThane-MW consists of solvent naphtha (petroleum), light aliphatic and fluorocarbons. Figure 3-11 is shown the three samples used to characterize the SHS in this work.

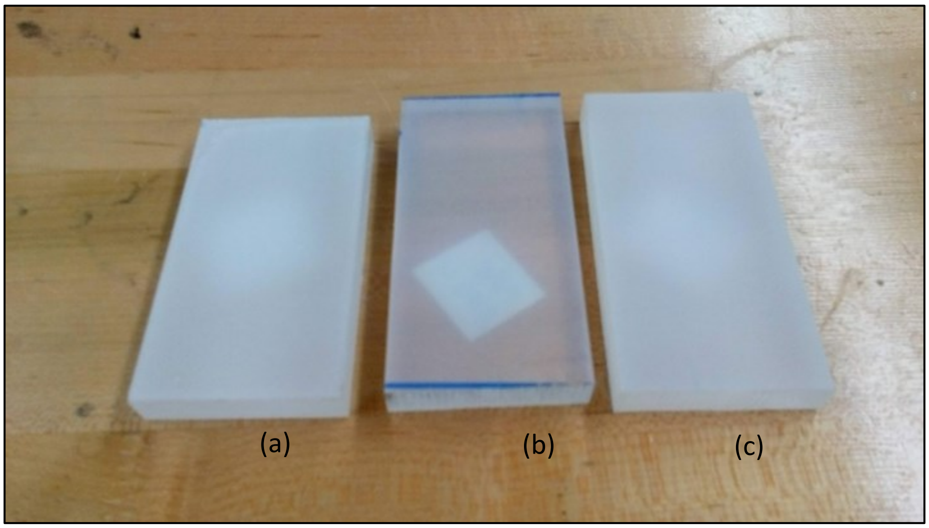

Figure 3-11 The three fabricated samples used to characterize the SH-coated surfaces a) FT-MW,(b) UED and (c) FPC-800M

3-4-2 Surfaces Characterization

The static and dynamic contact angles are used in this work to characterize the surface wettability. The tested surface in the second experimental part will be a flat surface, which makes it more difficult to determine its wetting degree.

3-4-2-1 Static Contact Angle

The static contact angle measures the wetting behaviour of a liquid on a flat surface. It is defined as the angle formed between the liquid-vapour interface and the solid surface when the liquid is in equilibrium with its vapour. Several methods can be used to measure the static contact angle of a flat surface. One common method is the sessile drop method, in which a droplet of liquid is placed on the surface, and the contact angle is measured using an optical goniometer instrument. Other methods include the pendant drop method and the spinning drop method, which involve suspending a droplet from a needle or spinning it on a flat surface. It is important to note that the static contact angle is dependent on the surface chemistry and roughness of the material, as well as the properties of the liquid being used. Therefore, it is necessary to carefully control these variables when measuring the static contact angle of a superhydrophobic surface.

The small acrylic pieces were painted with the three commercial coatings. The static contact angle (SCA- Θ_s) was measured over 20 points of each piece to characterize each used coating's average static contact angle. A 15 µL droplet of deionized water was used to calculate the contour of the droplet, which was based on the tangent fitting model for all samples. The tangent fitting model accurately captured the contour at each measurement's LH/RH static contact angles. The resulting SCA measurements show that the FPC-800M is 155˚ (±5˚) and 147˚ (±5˚) for the UED SH surface. The FlouroThane -MW surface has Θ_s of 145˚ (±5˚). The results showed acceptable SCA compared to producer specifications, as shown in Table 3-3 and Figs. 3-12.

Table 3-3 Summary of static contact angle for all tested flat surfaces; the reported errors are the standard deviations of measurements that were taken at different locations on each tested fabricated sample.

	CA(M)[°]	Uncertainty [°]	CA(L)[°]	CA(R)[°]
FT-MW	145	± 5	145.2	145.2
UED	147	± 5	147.5	147.6
FPC-800M	155	±5	154.7	155.2

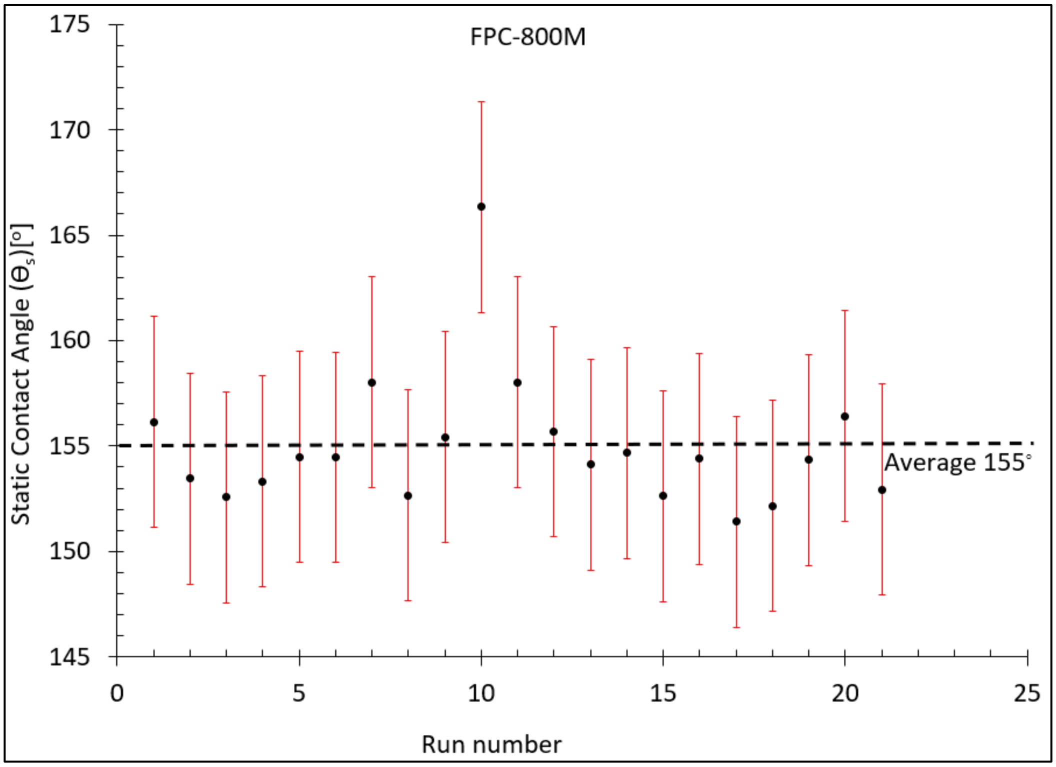
FPC-800M
Static Contact Angle (Θ_s)[°]
Average 155°
Run number
175
170
165
160
155
150
145
0
5
10
15
20
25

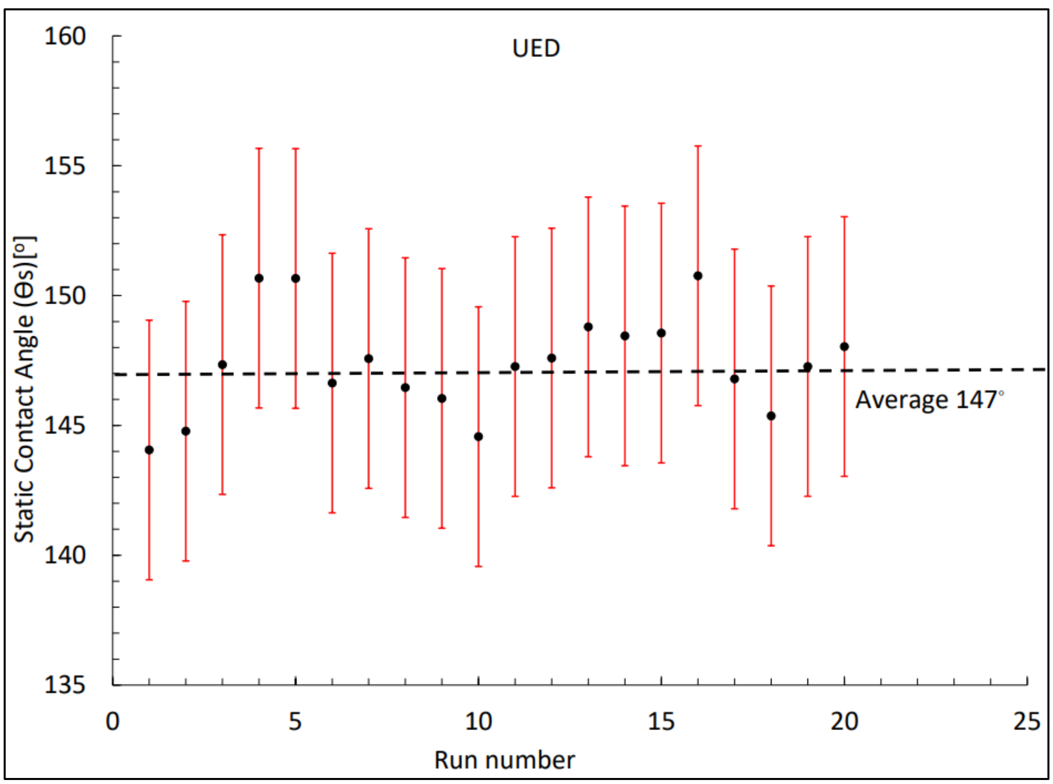
UED
Static Contact Angle (Θs)[°]
Average 147°
Run number
160
155
150
145
140
135
0
5
10
15
20
25

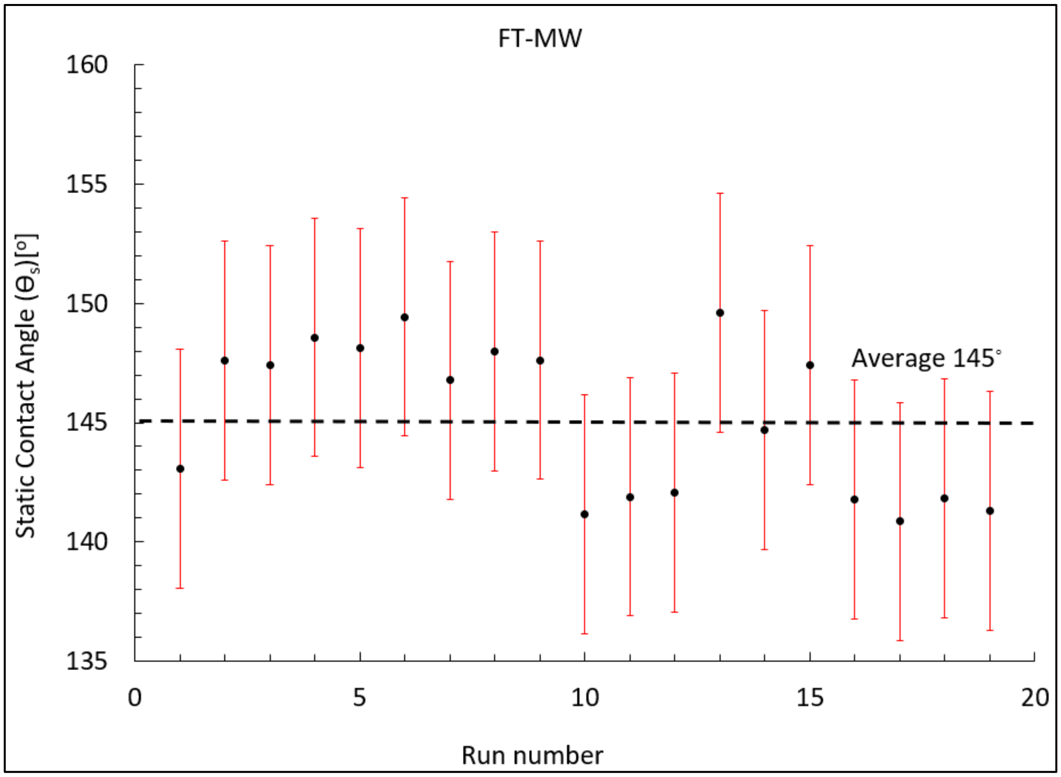

Figure 3-12 The Static contact angle measurements for all used flat surfaces, the error bars for RMS error which is ±5◦ for each measurement

3-4-2-2 Dynamic Contact Angles and Contact Angle Hysteresis

The dynamic (dynamic and receding) contact angle of a superhydrophobic surface is the angle at which a liquid droplet will make contact with the surface when it is in motion. It is an important measure of the wetting properties of a surface, as it determines how easily a liquid will spread or bead up on the surface. The contact angle hysteresis (difference between advancing and receding contact angle) is an important parameter that can be used to characterize surface wettability. Several factors, including surface chemistry, surface roughness, and the viscosity and surface tension of the liquid, influence the dynamic contact angle of a superhydrophobic surface. In general, surfaces with a more hydrophobic (water-repellent) chemistry and a higher degree of roughness will tend to have lower dynamic contact angles. The dynamic contact angle can be measured by increasing/decreasing droplet volume or applying liquid drops on a tilted surface.

In the present work, the samples are superhydrophobic, and due to the high surface none wettability degrees, it isn't easy to use the increasing/decreasing droplet volume technique. The tilt surface technique is used in this work, and a video clip is recorded using the OCA15E device and 15 μL of deionized water at ten different locations over each SH-tested sample. ImageJ software is used to post-processing the video clips to measure the tilt angle for each trial. The results showed a close tilt angle of all samples, the minimum and maximum measured angle over each piece at different locations, as illustrated in Table 3-4 and Fig.3-13. The general trend of tilt angle for all models is contrary to the SCA measurements. It could be behind this trend because the selected location to make the measurements picked up after many trials to find where the 15 μL droplet was stable on the coated surface. These locations showed low none wettability degrees.

Table 3- 4 The average tilt angle measurements for the tested samples with the standard deviation and minimum and maximum measured values.

	FT-MW	UED	FPC-800M
Mean	2.5	1.9	1.8
STDEV	0.67	1.3	0.93
Min	1.7	0.8	0.38
Max	3.4	4.1	3.2

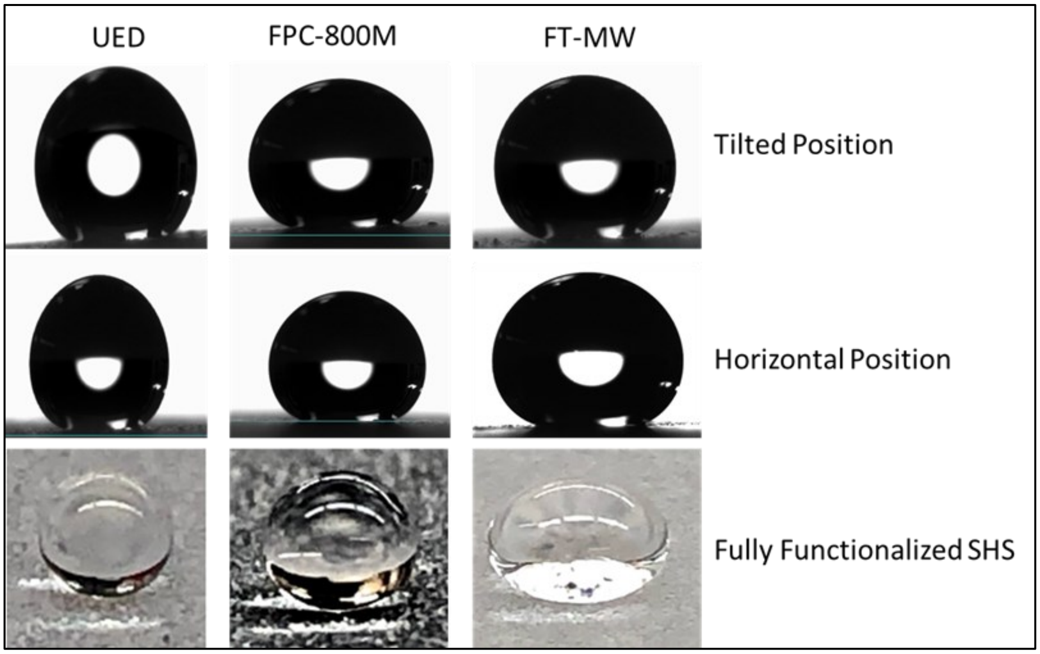

Figure 3-13 The tilt angle measurements for all tested samples of SHSs. The lower images are for the water droplet at the horizontal position, and the upper images are for the tilt angle position—the images taken from the operating software CA20E of an optical SCA device of OCA15E from DataPhysics GMBH. The zoom-in photos are taken with a magnification of 10X of a digital camera.

3-5 Summary

The details of fabrications and characterization of three curved surfaces and three other flat surfaces are presented in this chapter. The first part was conducted in a small experimental domain of TC cells. The curved surfaces were fabricated over the CDC using the dipping and spinning technique using SHBC, UED and FPC-800M SH commercial coatings. The thickness of the coating layer was determined since it is a very sensitive parameter to calculate the shear stress over these surfaces when it changes the TC cell gap. SEM images investigated the surface morphology for all fabricated samples used in this part. The SHBC and FPC-800M showed the zoom-in pictures for the nano-micro scale with a magnification of 22000X for the original spot. The SEM of the UED sample can't provide any details for the surface topography. Gray scale differences in these SEM images cannot be used to estimate surface height since the contrast is based on secondary electrons collected at the detector rather than height. The SCA and DCA for the tested samples were determined to characterize the surface wetting degree. Three different liquids were used to measure the surface wettability: water, 5 and 10 cSt silicone oil. The samples with water showed a superhydrophobic behaviour, while the case of five cSt silicone oil showed oleophobic and oleophilic with ten cSt silicone oil.

The larger experimental domain uses flat samples, which is the second part of the present work. Three samples of acrylic were used to characterize the surface wettability. The commercial coatings used in this part are UED, FT-MW and FPC-800M. The spray technique prepared the samples as recommended. The SCA of FPC-800M is the highest, then UED and FT-MW, respectively. The tilt angle was used to determine the CA hysteresis, and all samples showed a tilt angle of less than 3°.

CHAPTER IV

Chapter 4 The Influence of Curved Superhydrophobic Surfaces' Wettability on Drag Reduction in Taylor-Couette Flows of Water and Oil

This chapter investigates the effects of surface wettability on the drag-reducing performance of three hydrophobic coatings when applied to curved aluminum surfaces and uses three tested liquids with different viscosities. The main content of this chapter has been published (Alsharief, A. F. A., Duan, X., Yethiraj, A., & Muzychka, Y. (2023). "Wettability Effects of Curved Superhydrophobic Surfaces on Drags Reduction in Taylor-Couette Flows of Water and Oil." Journal of Fluids Engineering, ASME, (FE 23-1194). The author of this thesis is the first author of this paper. The first author conducted the experiments, analyzed the data, and prepared the manuscript. Prof. Duan, Prof. Yethiraj and Prof. Muzychka, as the second, third and fourth authors, provided their suggestions on experimental observation, suggestions for data analysis and revision of this paper.

4-1 Introduction

Viscous shear drag forces can significantly impact marine vessels, with approximately 50% of ships and 60% of submarine's drag being attributed to skin friction [2]. These forces can increase fuel consumption and CO2 emissions, contributing to ocean/sea pollution. Many techniques have been explored in the past to reduce viscous skin friction, including passive methods such as structured and unstructured superhydrophobic surfaces (SHSs) that alter the surface topography. Structured SHSs, which consist of microgrooves placed periodically in the flow direction, have been studied in the past, and the governing laws of slip length (b) have been examined experimentally, theoretically, and numerically. However, the high fabrication cost limits the scalability of structured SHSs for large-area applications such as submarine vehicles or internal pipeline surfaces. Unstructured SHSs with a random rough texture can be produced using inexpensive and easily scalable techniques such as spray coating, dipping-spinning, sandblasting, and chemical or electrochemical etching [63]. Research has found that many naturally occurring superhydrophobic surfaces have two key characteristics: low surface energy materials and a micro-nano or micro-micro two-level biological structure [64]. By applying the principle of bionics to create micro-nano or micro-micro structures with two levels and modifying them with low surface energy materials, it is possible to create SH surfaces with a static contact angle of 170◦and a contact angle hysteresis of fewer than 5◦ [64] [65].

Several challenges arise when attempting to use superhydrophobic surfaces (SHSs) to reduce drag in turbulent flows, as opposed to laminar flows. In strongly turbulent flows, large fluctuations in velocity and pressure can cause a wetting transition to Wenzel, in which the surface texture acts as hydrodynamic roughness and increases frictional drag [63]. This spotlights the importance of understanding the drag reduction mechanism of SHSs in all Taylor Couette flow regions. Many studies have focused on how surface morphology changes affect drag reduction [63]. It has been found that identical rough textures can yield significantly different slip length values when tested under different flow conditions due to the wetted solid fraction increasing as the air-water interface penetrates deeper into the texture [63]. A variety of design rules have been proposed in the literature to determine the optimal spacing and size of geometrical features forming the SHS. In low turbulence conditions, it is generally suggested to use random roughness surfaces (SH coating surfaces) with root mean square (r.m.s.) roughness parameters of $k+ > 1$. However, the opposite is suggested for the high Reynolds number turbulence regime: $k+ < 1$ [62]. In their study, Rajappan et al. [66] concluded that the mean autocorrelation length λ determines the randomly rough SHSs. This indicates the lateral separation of surface asperities. It is analogous to the influence of the spatial periodicity L on the slip length b in the case of regularly patterned SHSs [67]. In addition, the study established the key parameters to design scalable, randomly rough SHSs to reduce the turbulent drag. Those parameters are a large lateral spacing between roughness peaks, a small root mean square roughness, and the existence of hierarchical roughness structures.

Scalable SHSs are necessary for practical drag-reduction applications that can be applied over large areas of substrates in contact with the flow. These previous research efforts led to reported drag reduction in the range of 15% to 90% [5]. However, other studies involving identical surfaces with strong water-repellent properties did not have consistent results, with some studies even reporting drag enhancements of -90%. [62]. Researchers have used the cell setup of Taylor-Couette flow[68][69][70][71] extensively to study how drag can be reduced using various passive and active methods, including riblets [72][71][73] bubbles [62][74][75], liquid-infused surfaces [43], and textured SH surfaces [67]. Many rheometer apparatuses have been used, i.e. cone and plate, rotating disc and plate, and bespoke cells of Taylor-Couetteflow. The readings from some of these apparatuses were debated and criticized as their results are inconclusive since the achieved slip length is within the experiment uncertainty range [76].

This chapter investigates the achieved drag reduction using fabricated surfaces with different commercial SH coatings and three liquids with low to high viscosities. Although many experiments have been carried out to investigate the mechanism of drag reduction, it is yet unknown how the similar surface topography and the flows of liquids with different viscosities will impact the achieved drag reduction. To our knowledge, much research has yet to be conducted on the significant drag reduction observed on the SH surfaces, which possess similar characteristics. Additionally, the original Taylor Couette cell, which is a cylindrical apparatus used in rheometry, has yet to be frequently utilized to investigate this phenomenon. The present study intends to evaluate the wettability of different curved surfaces with SH coatings for drag reduction purposes. It will use three commercial SH coatings, and the sample surfaces were coated by the dipping and spinning technique. Using the same commercial brand SH coating assumes that the surfaces have the same topographical features. The three flow regimes inside the TC cell are laminar, laminar with Taylor vortices and turbulent [77]. Once the tested liquid has reached the first transition point, the radial pressure gradient, which increases radially, causes a secondary flow that drives the fluid from the inner to the outer wall. When this three-dimensional perturbation starts, the laminar shear flow will begin to form vortices. The flow is driven away from the inner wall since the vortices' rotation and the tangential velocity of the inner cylinder combined to cause the maximum local pressure. Vortices, which come in pairs, cause pressure distributions to show local maximums and minimums at the outer and inner walls, respectively, and that fills the gap with an alternative pressure pattern [78]. Contrary to the previous studies [66][71] [79]; and by coating the outer TC cell surface (inner surface of concentric disposal cups (CDC)), the drag reduction effect can be studied under controlled conditions, allowing for a better understanding of the mechanisms involved. Moreover, the three coatings will be investigated with three different liquids with low to high surface tensions; this will allow us to investigate how the same surface will reduce the drag when the surface energy decreases and the viscosities of the tested liquids increase.

4-2 Experimental setup and procedure

This section is organized into three subsections. The first subsection introduces all components of the flow facility that was used for Experiment 1, presented in Chapters 5 and 6. This flow facility will be called the Taylor Couette flow facility or TC cell. The second subsection of this section introduces the calibration measurements and benchmark tests used in all tested liquids in this part of my research. The third subsection describes the experimental procedure and the maximum shear rate applied for each tested liquid.

4-2-1 Experimental Setup

Rheometric torque measurements can be used as a macroscopic tool to investigate the area-averaged microscopic liquid-slip phenomena across a vast, random (and perhaps anisotropic) surface topography. However, using the original cell of the Taylor-Couette flow of the rheometer producer avoids systematic errors and eliminates uncertainties. A narrow-gap cell of Taylor-Couette flow with a radius ratio of $\eta = \frac{r_i}{r_o} = 0.92$ was used for this work, along with the CDCs and the measuring bob of model CC27 for MCR 301 Compact Rheometer from Anton Paar- GmbH. An image of the measuring system and schematic of the geometry of the Taylor-Couette flow setup is shown in Figures 4-1. The inner radius of the measuring bob ri is 13.329 mm, and the outer radius ro is 14.464 mm, which is the inner radius of the smooth surface of the base CDC. The gap length L is 39.999 mm, corresponding to a length-to-gap ratio of $\Gamma = 36.4$. The maximum shear rate used in this study was 2000 s^{-1}, performed with a maximum rotational speed of 1557 rpm. The Rheometer MCR301 has an integrated 360° capacitive normal force sensor (50 N) and high-resolution optical encoder, which allows it to have torque measurement ability from 0.5 nNm to 200 mNm. The measuring bob is connected to the head of the rheometer's spindle and is immersed in the fluid inside the present cell of Taylor-Couette flow, as shown in Figs. (4-1 a and b).

4-2-2 Rheometer calibration and benchmark test

In this part, the Rheometer MCR301 from Antoon Paar will be used after coating the CDCs with three different commercial superhydrophobic coatings (see Figure 4-1). Quality management (QM) tests were performed before each use of the MCR 301 device using the air as tested fluid and the original measuring system of cylindrical setup CC27 SN17316. The QM report was issued and considered as a calibration procedure, as seen in a sample attached in Appendix B. The QM report is available on the Anton Paar rheometer MCR 301, a tool that can evaluate the quality and repeatability of measurements taken by the instrument. It analyzes the consistency of measurements by comparing multiple sample readings and uses statistical methods to determine measurement error. The results are presented in an easily understandable format. The QM report has various applications, including optimizing measurement conditions, validating the instrument's performance, and monitoring its long-term performance. It is especially useful for ensuring the accuracy and dependability of rheological measurements, which are crucial in various industries such as cosmetics, food, pharmaceuticals, and polymers. To assess the TC cell employed in the current study, the researchers conducted benchmark tests using four liquids with established viscoelastic characteristics: water with a viscosity of one cSt, as well as silicone oils with viscosities of 5, 10, and 100 cSt. The known viscoelastic properties tested liquids showed expected behaviour at different applied shear rates using the TC cell. All tested liquids showed their viscosity value in the laminar regime, as shown in Figure 4-2(a). The laminar regime increased with an increase in the tested liquid viscosity. The linear relation of the Newotian tested liquids between the shear rate and shear stress was confirmed, as shown in Figure 4-2(b), and at the high shear rate, the tested liquids showed a change in their linear behaviour. At this point, the flow is considered to be in the early turbulence stage. The maximum shear rate used in these benchmark tests was 2000 s^{-1}, and water and 5 and 10 cSt silicone oils exhibited the change in their linear relation except the 100 cSt silicone. The applied shear rate increased to 2750 s^{-1}, the safe operating condition for the rheometer device used in the present work. The test did not present any change in the linear relation of its viscoelastic characteristics. For this reason, the 100 cSt silicone oil was excluded from this study.

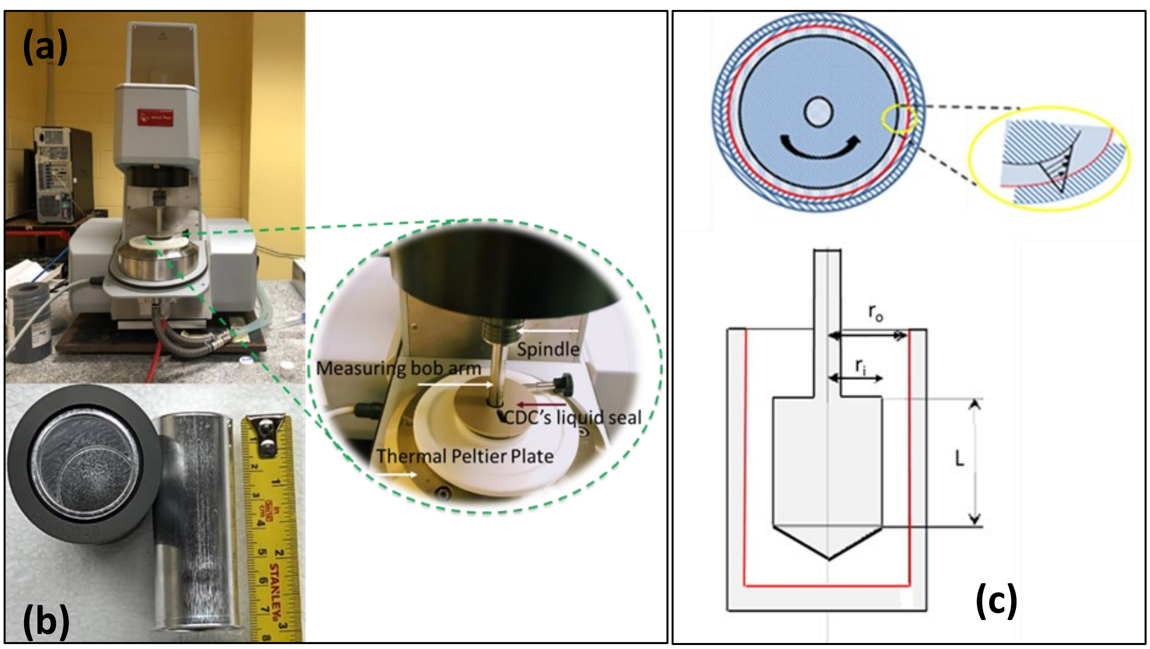

Figure 4-1 The MCR 301 modular compact rheometer device is equipped with an integrated temperature sensor to maintain constant temperature using the peltier plate and lift motor(a), concentric disposal cups with its base for measuring system setup of the CC27 model used as a Taylor-Couette cell (b), and its schematic diagram where inner radius r_i = 13.329 mm and the outer radius r_o=14.464 mm and the measuring bob length L=40 mm.

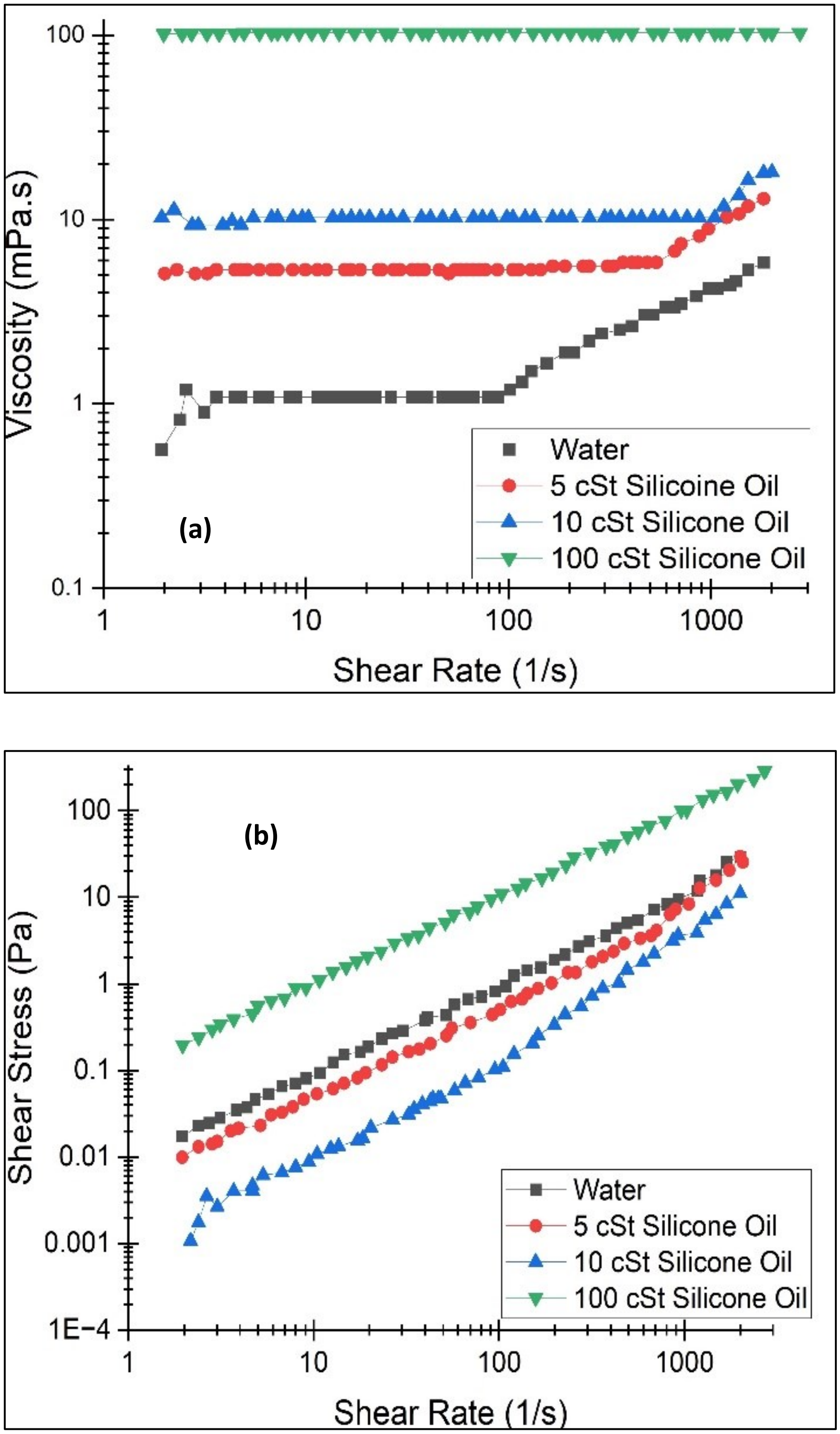

Figure 4-2 The benchmark test of all fluids used in the rheometer study under maximum shear rate.

4-2-3 Experimental procedure

The rheometric torque measurements can be used to investigate area-averaged liquid-slip phenomena across vast, random (and anisotropic) topographies. In order to avoid experimental errors and reduce measurement uncertainties, the original setup of the rheometer device was used as a Taylor-Couette cell. In the present work, a narrow-gap Taylor-Couette cell with a radius ratio of $\eta = \frac{r_i}{r_o} = 0.92$ was used along with the CDCs and the measuring bob of model CC27, as shown in Figs. 4-1b and c. The inner radius of the measuring Bob (R_i) is 13.329 mm, and the outer radius (R_o) is 14.464 mm, which is the inner radius of the baseline CDC (smooth surface). The gap length (L) is 39.999 mm, corresponding to a length-to-gap ratio of $\Gamma = 36.4$. The maximum shear rate used in this study was 2000 s^{-1}, performed with a maximum rotational speed of 1557 rpm. The rheometer is equipped with a sensitive torque sensor fixed in the measuring arm and an integrated temperature sensor to maintain constant temperature using the Peltier plate and lift motor, which offers an accurate end zero-gap setting. The rheometer's lift motor in the stand provides precise zero-gap settings and automatically compensates for gap change, and the end effect correction factor is considered to be CL =1. The time-averaged wall shear stress (τ) is calculated based on the measured torque from Equation (4-1)[54].

$$\tau = \frac{1+\Delta^2}{2000 \cdot \Delta^2} \cdot \frac{T}{2 \cdot \pi \cdot L \cdot r_i^2 \cdot C_L} \tag{4-1}$$

where T is the measured global torque, and the ratio of radii $\Delta = \frac{r_o}{r_i}$.

The shear rate ($\dot{\gamma}$) is calculated as[80]:

$$\dot{\gamma} = \omega \cdot \frac{1+\Delta^2}{\Delta^2-1} \tag{4-2}$$

where $\omega = \frac{\pi}{30} \cdot n$ is the angular velocity, and n is the rotational speed in rpm.

The drag reduction ratio (DR%) can be directly assessed for each surface as the percentage decrease in the measured global torque caused by the SH coating versus a smooth, no-slip boundary at the same Reynolds number as in Equation (4-3)

$$DR\% = \left(\frac{T_s - T_c}{T_s}\right) \cdot 100 = \left(\frac{\tau_s - \tau_c}{\tau_s}\right) \cdot 100 \tag{4-3}$$

Here, T_s, τ_s, T_c, and τc are the time-average global torque and shear stress over smooth and coated surfaces, respectively.

4-2-4 The Experimental Setup Uncertainty

The uncertainty analysis is carried out based on Kline & McClintock's theory[81], shown in the following root sum square equation:

$$\delta(DR) = \sqrt{\left[\frac{\partial(DR)}{\partial \tau_s} \cdot \delta\tau_s\right]^2 + \left[\frac{\partial(DR)}{\partial \tau_c} \cdot \delta\tau_c\right]^2} \tag{4-4}$$

where $\delta(DR), \delta\tau_s$, $\delta\tau_c$ are the uncertainty of drag reduction and shear stress with and without SH coating. Differentiating the equation of *DR* with respect to τ_s and τ_c substituting in the above equation with assuming $\delta\tau_s$=$\delta\tau_c$=$\delta\tau_{const.}$ Yields[82]:

$$\delta(DR) = \frac{\delta\tau_{const.}}{\tau_s} \cdot \sqrt{1 + \frac{\tau_c}{\tau_s}} \tag{4-5}$$

The uncertainties analysis of the drag reduction δ(DR) is presented in Appendix D. the average uncertainty of drag reduction δ(DR) is far less than the drag reduction range in the experiment. It has small values with increasing Re numbers.

4-3 Characterization of the flow regimes of the Taylor-Couette cell setup

The case of flow between two concentric cylinders in which the inner cylinder is rotating and the outer cylinder is at rest provides an example of a complicated and unstable stratification caused by centrifugal forces and curved walls. In the present work, three liquids were first selected to investigate the fabricated surfaces by increasing their kinematic viscosities to 1, 5 and 10 cSt. This selection is based on decreasing the surface tensions of the used liquids starting from water. The properties of the selected liquids are shown and summarized in Table 4-I. An analysis of experimental data using uncoated samples is performed first to investigate the flow regions in the current Taylor-Couette cell. The maximum shear rate the device could present in this work is 2750 s^{-1}, which comes from a rotational speed of 1557 rpm, and that is applied for all tested liquids. The radius ratio (η) is very high since the gap d is small, with 1.1 mm in the original setup; this reduces the maximum *Re* number that can be achieved with the current available rotational speed. The Reynolds number (*Re*) is used to characterize the flow regimes in the present Taylor-Couette flow, which is in the form [77].

$$Re = \frac{U_i \cdot d}{\nu} \geq 128 \qquad \text{(viscosity instability)} \qquad (4\text{-}6)$$

where U_i is the peripheral velocity of the inner cylinder, which U_i=($r_i \cdot \omega_i$), d is the gap distance, and ν is the kinematic viscosity.

Table 4-1 Summary of the flow parameters and the tested fluid's properties at 20° C that includes the shear rate ($\gamma^{\cdot}$), Reynolds number (Re), the density (ρ), kinematic viscosity (ν) and the surface tension force (σ)

Fluid	$\dot{\gamma}$		Re		ρ	ν	σ
	min(s^{-1})	max(s^{-1})	min	max	Kg/m^3	($x10^{-6}$) m^2/s	mN/m
Water	2	1000	2.45	1227.34	998.16	1.2	72.86
Silicone Oil (5cSt)	2	2000	0.43	425.32	923	5.8	19.81
Silicone Oil(10cSt)	2	2000	0.21	204.86	945	12	20.21

The energy transfer from the laminar flow to the unstable flow causes a large increase in the torque required for the inner measuring bob. The torque coefficient is used to determine the flow regimes in the Tayler-Couette cell flow, and it is defined as [77];

$$C_M = \frac{T_i}{\frac{1}{2} \cdot \pi \cdot \rho \cdot U_i^2 \cdot r_i^2 \cdot L} \tag{4-7}$$

The measured torque is Ti, and the height of the measuring bob is L. Based on the cell geometry of Taylor-Couetteflow, three flow regimes may be distinguished, each restricted by the Re number.

$Re < 128$: Laminar Couette flow,

$128 < Re < 900$: Laminar flow with Taylor Vortices,

$Re > 900$: Turbulent flow.

Figure 4-3 shows that water and 5 and 10 cSt silicone oils behave similarly. The 5 and 10 cSt silicone oils have two flow regimes, which are stable and unstable laminar, while water extends to the early stage of the turbulent regime, all at a critical Rec1 number of 128. However, the torque coefficient is inversely proportional to the Re number. This means increasing the viscosity causes an increase in the torque coefficient and a decrease in the Re number. For this reason, doubling the viscosity allows covering very low Re numbers (~0.2).

Water tests show an early turbulent stage, while the oils cover the laminar regime, which is governed by geometry conditions, and the work of Couette [58] proved this hypothesis. In high Re number flows, one could anticipate the specifics of the force to fade away and a universal pattern to emerge, and the global properties of the system could be expected to scale with Re number to some power [83], which more recent compared with the work of Schlichting [77]. Figure 4-3 shows the flow regimes for our experimental setup and, more specifically, using water as a tested liquid based on the work of [84]. There are five flow regimes separated by four critical Re numbers, as presented for the fixed external and rotating internal cylinders, which are circular Couette flow regime (CCF), Taylor vortex flow regime (TVF), wavy vortex flow regime (WVF), modulated wavy vortex flow regime (MWVF)and turbulent Taylor vortex flow regime (TTVF).

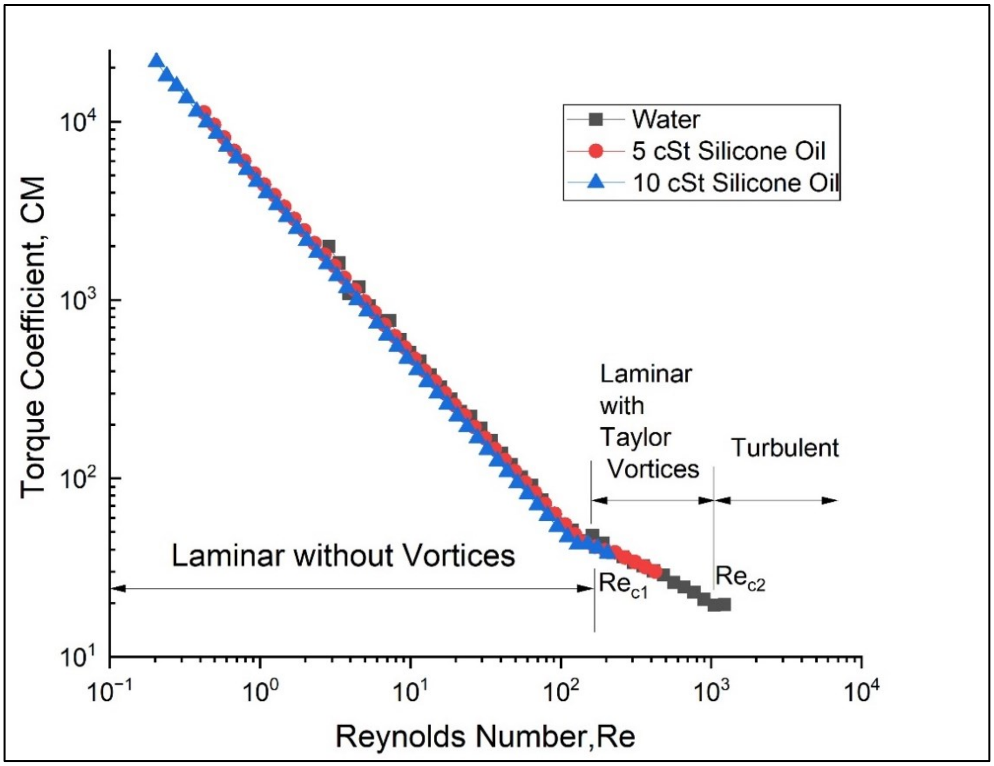

Figure 4-3 Taylor-Couette flow regimes of the used cell in terms of torque coefficient (CM) calculated using Equation (4-7) and the Reynolds number for all tested liquids in the present setup over a smooth baseline (uncoated) surface. For the present setup, Rec1=128 and Rec2=900.

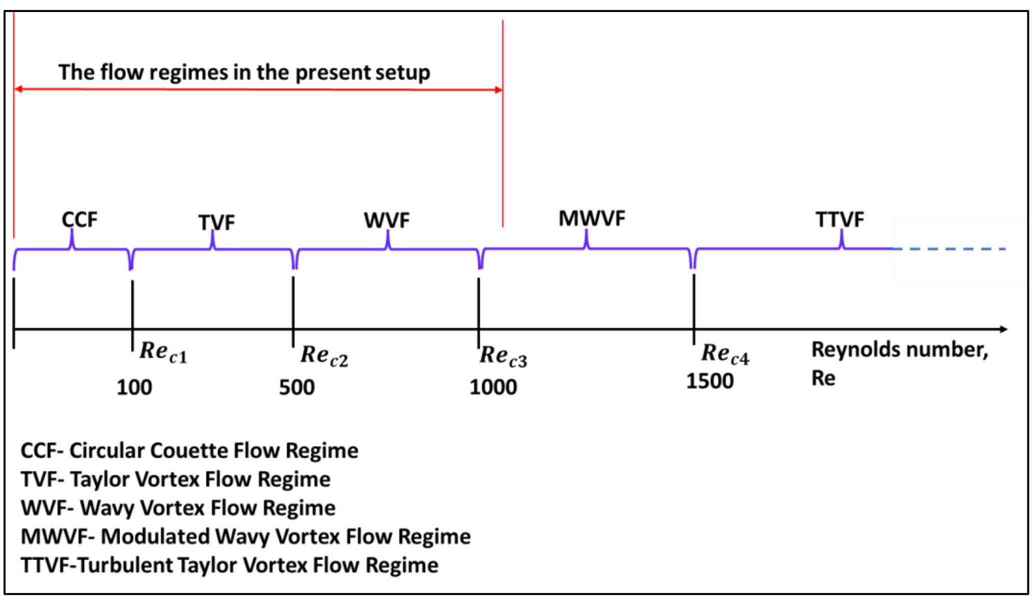

Figure 4-3 Observed rich flow structures (in an internal rotational cylinder and fixed external cylinder) phase diagram for Taylor-Couette flow adopted from [85]

The flow regimes in the TC cell used in this work were identified by the torque acting on a smooth baseline internal surface of the outer cylinder, which was measured with a maximum angular speed (n) of 1552 rpm and to compare data using deionized water. Frictional heating causes thermal effects on estimating the correct fluid viscosity, as was mentioned by Hall [72]. However, all measurements were conducted using a constant volume of deionized water of 19 ml and at a constant temperature of 20 ± 0.10 ˚C since the CDCs sit on a stress-controlled Rheometer's fixed thermal Peltier plate (Anton-Paar MRC-301)[54]. The non-dimensional toque G is given by:

$$G = \frac{\tau}{\rho \cdot \nu^2 \cdot L} \qquad (4\text{-}8)$$

where ρ and ν are the working fluid's density and kinematic viscosity, respectively. Fig. 4a shows the measured dimensionless torque versus the Re number. In the laminar range, the measurements show good agreement and are identical to the reference work of Couette [86], which adapts the following empirical Equation [57]:

$$G = \frac{4 \cdot \pi \cdot \eta \cdot Re}{[(1+\eta) \cdot (1-\eta)^2]} \qquad \text{For Re<400} \quad , \qquad (4\text{-}9)$$

where η is the radius ratio. After the critical Re number, the flow comes to the instability regimes, as described in Figure 4-3. The reference work of Wendt [87] was used to compare our results in these flow regimes. The comparison showed good agreement with Wendt's work as he fitted his measurements in this regime to the following correlation [87] [88] [71]:

$$G = 1.45 \cdot \left(\frac{\eta^{\frac{3}{2}}}{1-\eta^{\frac{7}{4}}} \right) \cdot Re, \quad \text{For } 400\text{<Re< } 104 \quad , \qquad (4\text{-}10)$$

The critical Reynolds number can be seen easily from Figure 4-4a when the intersection of both fitting correlations at Re of 82. To identify the critical Reynolds numbers or transition points for the flow regimes, we followed Lathrop et al. [88] [89]and assumed a power-law scaling torque exponent α of the torque given by:

$$G = Re^{\alpha} \tag{4-11}$$

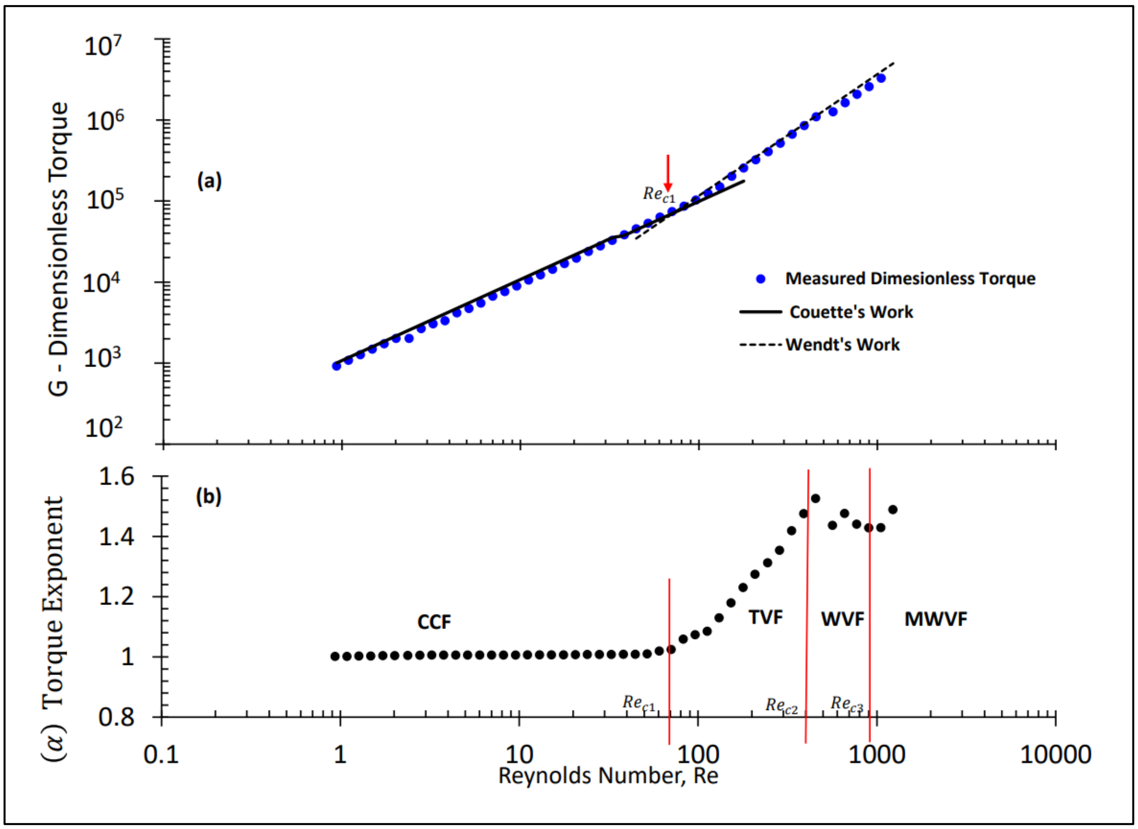

Figure 4-4 (a) The dimensionless torque of the present TC flow with a smooth surface; (b) the corresponding local torque exponent α.

The torque exponent α is computed as follows:

$$\alpha = \frac{d\, log_{10}\, G}{d\, log_{10}\, Re} \tag{4-12}$$

The measurements of the deionized water allow us to determine the local exponent α at a low Reynolds number of 2.5. The local exponent α determined from the slope of the graph. A sliding linear least square fitting technique similar to that utilized by Lathrop et al. [89] was used to compute the slope across 13 adjacent data points, which equivalent to $\log_{10} G\ vs\ \log_{10} Re$ (corresponding to a window of $\Delta \log_{10} Re = 0.8$ wide). A sliding window with an 85% overlap with the previous window was used because direct numerical differentiation emphasizes noise in the data[4,29]. The result of α calculations from data in Figure 4-4a is presented in Fig. 4b. Although the torque exponent α varies with Reynolds numbers, the torque exponent α remains reasonably constant around 1 with a torque measurement error of ± 3.5% for Re < 82. These results agree with the early work of Couette (1890) [86] for the laminar Couette flow regime, and it is similar to recently published works [71][90].

The earlier predictions by [87][89], showed that the dimensionless torque does not follow a fixed power-law scaling (i.e. G ~Re α, where α is a constant value) for flows of 800 < Re < 1.23 x 106. Here, after the CCT regime, the flow developed into transition regimes, and the flow structure depended on Reynolds numbers. The first transition regime starts with the Taylor vortex flow regime (TVF) in the Reynolds number range of 82 < Re < 455. The TVF is known as the unstable spiral axisymmetric vortices regime [85]. The torque exponent increases monotonically from 1.2 to 1.52, indicating that the flow becomes unstable but not turbulent. Subsequently, as the rotation speed is increased beyond Re > 450, the TC cell flow undergoes a new kind of instabilities known as non-axisymmetric instabilities, which lead to a state of great Spatio-temporal complexity, known as wavy vortex flow (WVF) [85]. The WVF regime in the present TC cell flow starts Re_{c2} = 455.

Although the dimensionless torque is identical to Wendt's empirical fitting correlation, the torque exponent will not be constant; it decreases beyond Re = 455 from 1.52 to 1.42 at Re_{c3}= 900, which agrees with the literature in this transition regime [71][89]. In case Re > 900, the present study has limited data, which allowed investigating up to a maximum Reynolds number of 1227. The Re_{c4} should be at α = 1.66, which indicates a flow transition from modulated wavy vortex flow Regime (MWVF) to a turbulent Taylor vortex flow regime (TTVF) at a high Reynolds number larger than 104 [66][89][71]. The present study shows an increase in α from 1.43 at Re = 900 to 1.49 at Re = 1227, which agrees with all data in the literature in the MWVF regime [66][79][88][91].

4-4 Results & Discussion

The available experimental data for DR over SH coating surfaces are sometimes inconclusive or even contradictory, as similar surfaces produced DR and enhanced the drag [92][93]. The method proposed by C. Choi & C. Kim [83], which uses a cone and plate rheometer to measure slippage for nanostructured surface, was commented on due to the experimental uncertainty [76]. Many other studies used the custom-designed cell of Taylor-Couette flow in their experimental investigation, with a simple tare correction of the end effects [67][84]. However, as mentioned earlier, this work used the original cell setup of Taylor-Couette to avoid any unknown experimental uncertainty sources and provides crucial results. The measurements using all surfaces were performed at a constant temperature of (20± 0.5) ˚C using the thermal Peltier. Experiments over the smooth and the SHS were performed at the same shear rate variation for all the CDC samples using the TC cell. This subsection presents the results from the measurements using all tested liquids in this part of the research (samples of the rheomtere measurements illustrated in Appendix C).

4-4-1 The Averaged Torque Measurements

It is preferable to measure the non-coating surface under similar flow conditions, i.e., shear strain, fluid properties, and the experimental geometry, to properly compare the drag reduction performance. In this work, the baseline global torque for the Taylor-Couette flow is obtained using a plain uncoated (smooth) surface of aluminum CDCs for all tested liquids. The shear rate systematically varied to measure the torque globally at each shear rate step for 10 sec. The global torque is measured for each sample three times, and the average value is considered in this work. The time-averaged global torque is nondimensionalized and is computed from Equation (4-8) as follows:

$$G = \frac{T}{\rho \cdot \nu^2 \cdot L} \tag{4-13}$$

Moreover, the Prandtl-von Kármán coordinates used for $Re > Re_{c1}$ allow us to verify the achieved drag in this regime. The Prandtl-von Kármán coordinates between the dimensionless shear stress is typically expressed using a skin friction coefficient as follows:

$$C_f = \frac{2 \cdot \tau}{\rho \cdot (r_i \cdot \omega)^2} \tag{4-14}$$

where ρ is the density of the working fluid, and the shear Reynolds number Re_τ defined as follows:

$$\mathrm{Re}_\tau = \mathrm{Re} \cdot \sqrt{\frac{C_f}{2}} \tag{4-15}$$

Prandtl–von Kármán coordinates are inserted in Figures 4-6,7,8 to illustrate the difference between the tested surfaces and fluids used in the present work.

The comparisons in Figures 4-6,7,8 are for water, 5 cSt and 10 cSt Silicone oil, respectively. The comparisons clarify that the global dimensionless torque generally increases monotonically with the Re number; this is for all tested liquids and SHSs. Although the curves are essentially overlapping at the laminar Couette flow regions (Re_{c1} < 128), a close examination of the results shows that all fluids' dimensionless torque measurements have a slight change with the smooth surfaces (baseline) for all tested samples and fluids. It is known that the laminar flows present an effective wall slip boundary condition due to a stable air layer within the asperities of the textured substrate [78][84][94]. This known mechanism can reduce the drag, which its magnitude is controlled by the feature-length scale and the wetted solid fraction of the surface rather than the flow features [68].

Figure 4-5 presents the dimensionless torque G over smooth and fabricated SH surfaces in water experiments. In the laminar regime, when Re < 128, the G values of fabricated SH surfaces are very close, as expected to the smooth surface value. In regimes of Re >128, the fabricated surfaces show low dimensionless torque G compared to the smooth surface. This low G means decreasing in the ratio of the torque required to derive the flow inside the TC cell. Still, the illustration does not show a large difference in performance among all SH surfaces, but a noticeable difference was observed compared to the base surface.

Figure 4-6 presents the dimensionless torque variation 5 cSt silicone oil. The increase in the viscosity reduces the difference between the smooth surface and all fabricated SH surfaces; this decrease in the dimensionless torque coefficient is observed in laminar flow

Re_{c1} <105, where all curves appear to overlap closely with a small quantitative difference data starting from Re_{c1} the last data point.

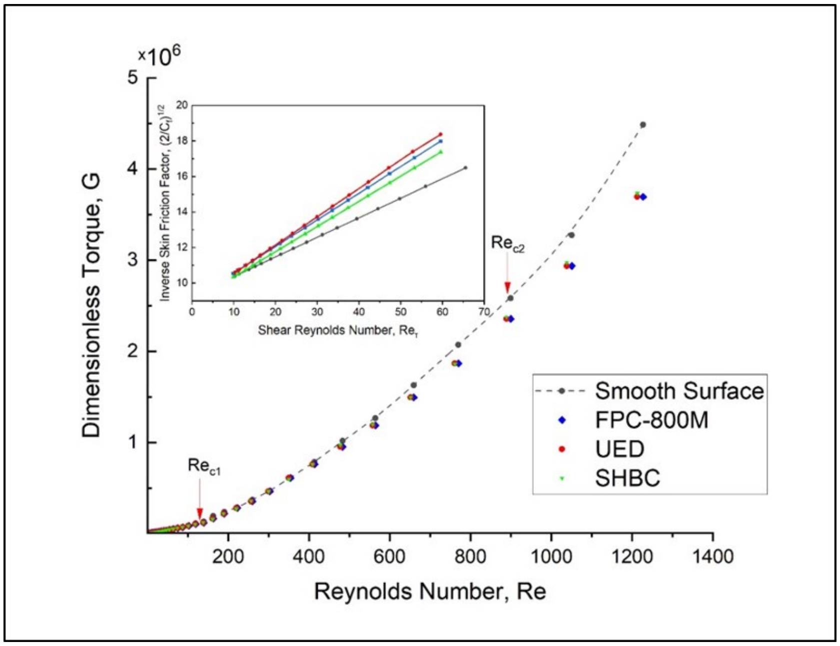

Figure 4-5 The variation of the dimensionless torque (G) against Reynolds (Re) number for all coated surfaces compared to the uncoated surfaces using water as tested liquid.

Inset: Measured skin friction plotted in Prandtl–von Kármán coordinates. The dashed black line is fit to the scaling for data starting from Rec1the last data point.

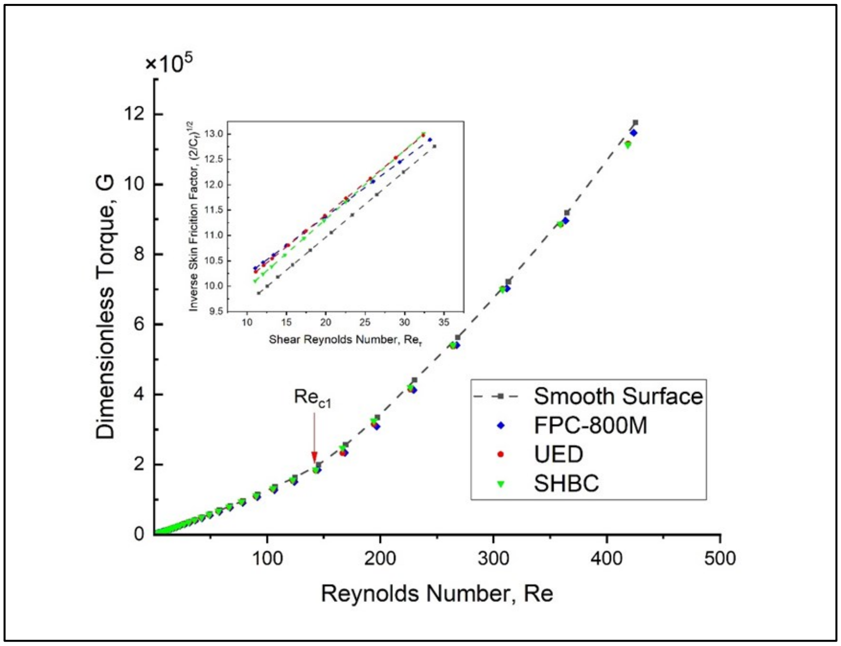

Figure 4-6 The measured dimensionless torque (G) for all coated and uncoated surfaces using 5 cSt silicon oil as a tested liquid. Inset: Measured skin friction plotted in Prandtl–von Kármán coordinates. The dashed black line is the fit to the scaling for da data starting from Rec1 the last data point.

The torque coefficient range increases with an increase in viscosity; as Figure 4-7 illustrates, the variation between the fabricated SH surfaces and the smooth surface becomes very small and difficult to distinguish in all flow regimes, especially after Re <127. The high shear rate applied can be observed more distinctly in the flow pattern that follows Re_{c1}, as there is only a slight variation in the torque coefficient among all surfaces. The maximum Re number achieved in the 10 cSt flow is 203 with a high shear rate of 2000 s^{-1}, and the flow in the early unstable laminar regime. These differences between smooth and coated surfaces decrease with increasing fluid viscosity. Using different tested fluids shows the viscous laminar flow of the used Taylor-Couette cell at a meagre Re number (minimum Re = 0.2).

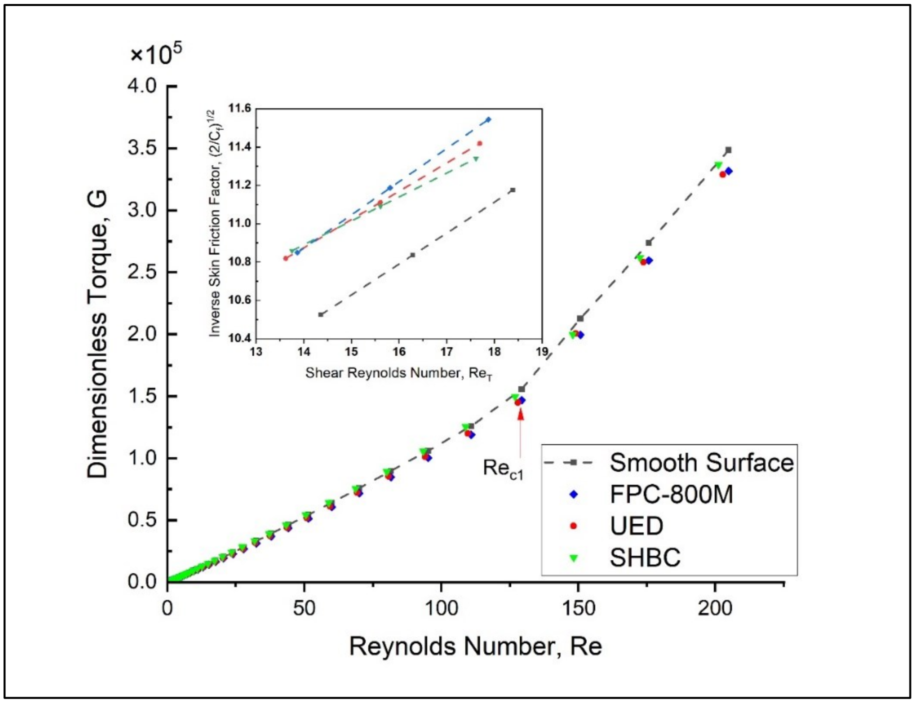

Figure 4-7 The measured dimensionless torque (G) for all coated and uncoated surfaces using 10 cSt as a tested liquid. Inset: Measured skin friction plotted in Prandtl–von Kármán coordinates. The dashed black line is fit to the scaling for the last three data points after Re_{c1}.

4-4-2 The Achieved Drag Reduction

The slip effect on the SH surface significantly reduces drag for specific flow conditions. According to the time-averaged shear stress, the computed DR using Equation (4-3) shows a similar pattern to previous experimental and computational investigations in the literature [85]. Figures 4-8,9, and 10 show the drag reduction pattern achieved over all the fabricated surfaces. With the increased flow velocity of all used liquids, all fabricated surfaces enhanced drag reduction in the laminar flow regime. As Reynolds number increases beyond the critical value, the flow becomes more unstable, and Taylor vortices form and disappear more frequently. In response to this, vortices elongate, and their size decreases, leading to a phenomenon known as vortex stretching [85] [68]. Taylor vortices induce mixing in

Taylor-Couette flow during the transitional regime. It reduces the velocity gradients and turbulence intensity, leading to a decrease in the shear stress, which is larger for smaller gaps between the cylinders and higher aspect ratios [68] [95].

The present cell setup of Taylor-Couette flow using water as the tested liquid showed a maximum experimental range of rotational speed with a Re number of 1227. The smooth, uncoated surface showed a higher torque coefficient than the three coated SH surfaces. The region of low Re number ($< Re_{c1}$), as shown in Figure 4-8, shows low drag reduction, which is expected in this region as the flow is laminar. This trend confirms the previous investigations in the literature[96] [97], where the behaviour of Taylor-Couette laminar flow is a function in geometry rather than the Re number. Drag enhancement at the starting condition is interpreted as the inhomogeneous distribution of plastron layer thickness at this early operating point. Increasing the Re number leads to an increase in the DR, as shown after the starting point. When zooming in on the laminar region of Figure 4-8, it becomes clear that the drag reduction (DR) performance for the three fabricated surfaces has a general trend of increase and is very similar to each other in its fluctuating behaviour. When following the results from Re_{c1}=128, the achieved DR converges

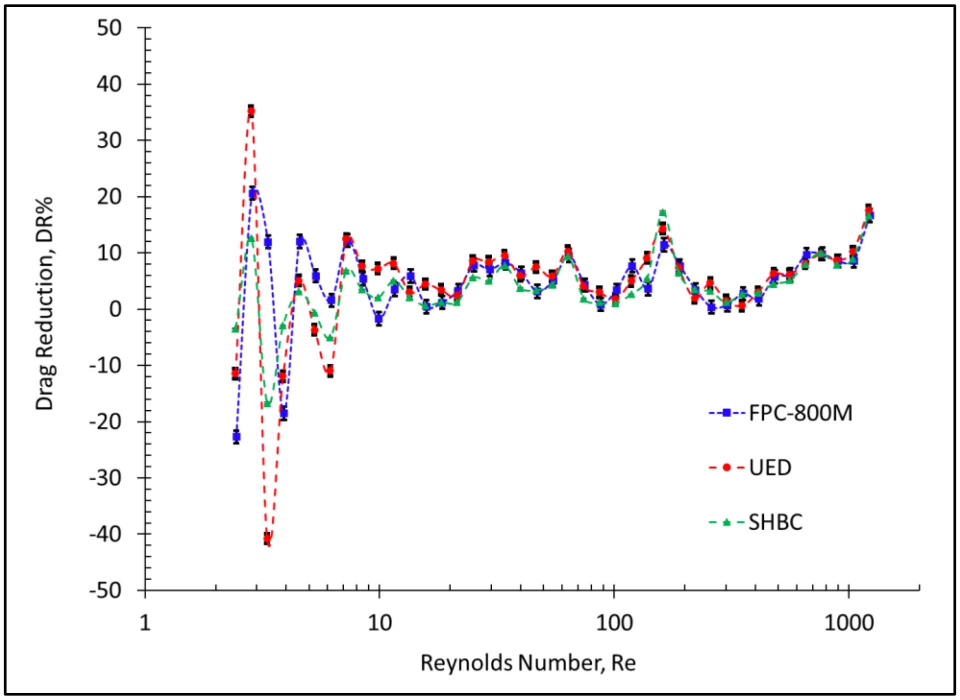

Figure 4-8 The achieved drag reduction ratio (DR%) over each surface in the experimental range of water. The error bars presented are standard deviation errors for measurements.

to a small range of 1% among all the tested surfaces. On average, all surfaces produced a DR range between 7% and 12%. It is apparent that the surface with the highest θ_s and the lowest CAH of 1° (UED) has the highest drag reduction performance compared to the FPC-800M and SBHC surfaces shown in Figure 4-8. The FPC-800M surface has the highest RMS mean value of DR% compared to the other surfaces, while the SHBC surface has the lowest achieved drag reduction. The steady rise in performance illustrates the effectiveness of the fabricated surfaces in reducing drag, which is attributed to their high surface hydrophobicity and the increase of the Reynolds number.

The results of experiments using silicone oil with a viscosity of 5 cSt are shown in Figure 4-9. As the viscosity was increased fivefold using the same cell setup of Taylor-Couette flow, the dimensionless torque G was higher than that of water, as shown in Figures 4-6 and 4-7. This decrease in the Reynolds number range resulted in a significant portion of the experiment being in the laminar flow regime. Interestingly, the experiments revealed a slight drag reduction despite the surfaces exhibiting oleophilic wetting behavior with this oil.

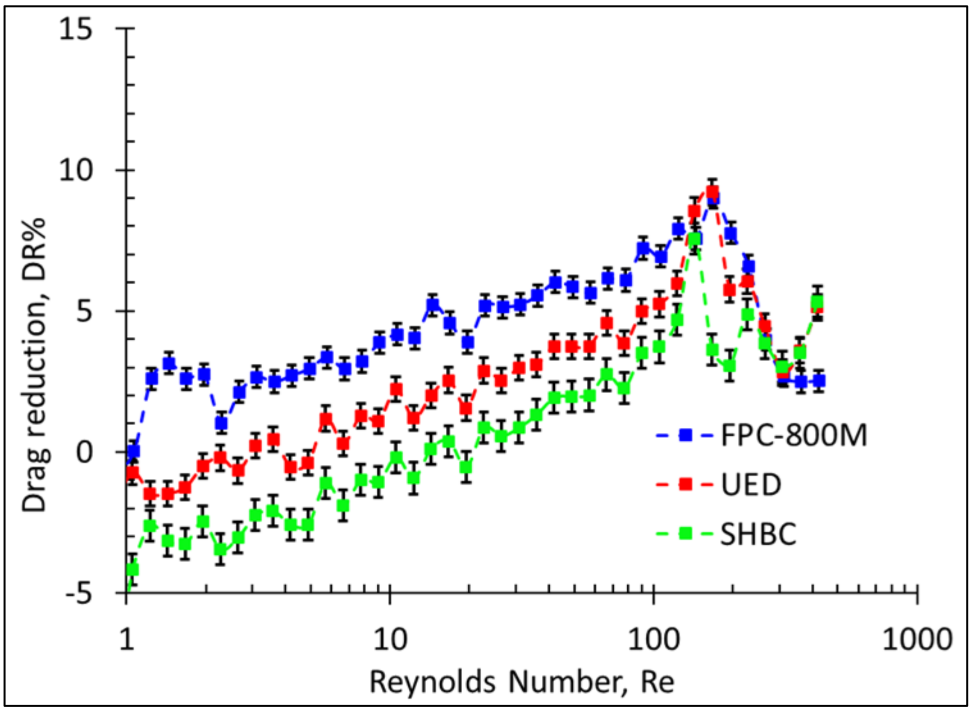

Figure 4-9 The achieved drag reduction ratio (DR%) over each surface in the experimental range of 5 cSt silicone oil. The error bars presented are standard deviation errors for measurements.

A drag reduction of around 5% was achieved with the same surfaces that showed superhydrophobic behaviour. This drag reduction percentage was observed at high Reynolds numbers (= Re_{c1}). Taylor turbulent vortices increase the energy dissipation rate at the critical Reynolds number. This increase in the energy dissipation rate significantly increases the torque required to maintain the cylinder rotation, causing the drag reduction to jump suddenly at this value. After Re_{c1}, the flow becomes unstable, and Taylor vortices start to form. The vortices induce mixing, leading to a decrease in the shear stress[68] [95]. The FPC-800M surface showed more drag reduction overall compared to the other fabricated surfaces, but the drag reduction decreased after the critical Reynolds number. The UED surface demonstrated an increasing drag reduction percentage, which was lower than that of the FPC-800M but increased at the critical Reynolds number. This trend is expected as both surfaces had a lower wetting degree compared to the SHBC surface. The SHBC surface had a high oleophobic wetting degree with a contact angle of 16°, and the average drag reduction was around 2.5%, which is less than that of the other fabricated surfaces.

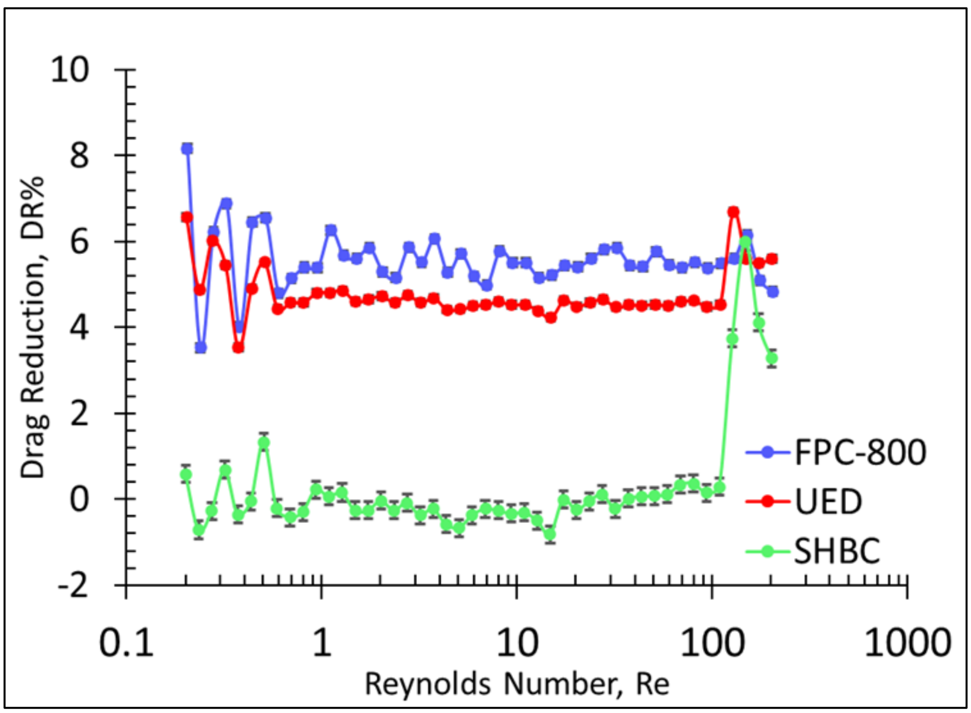

Figure 4-10 The achieved drag reduction ratio (DR%) over each surface in the experimental range of 10 cSt silicone oil. The error bars presented are standard deviation errors for measurements.

Figure 4-10 displays the drag reductions obtained using silicone oil with a viscosity of 10 cSt. It shows a smaller experimental range, with a maximum Reynolds number of 201, resulting from increasing the kinematic viscosity by a factor of ten when compared to water. This resulted in the flow being in the laminar regime. The FPC-800M and UED surfaces showed an average drag reduction of around 5% and 4%, respectively. The FPC-800M surface has a lower wetting degree (contact angle of 27 degrees) than the UED surface, which explains the slightly higher performance of the FPC-800M in reducing viscous drag. The SHBC surface (SCA of 13°) showed no drag reduction until it reached the critical Reynolds number, where a sharp spike of 6% was observed, similar to the FPC-800M and UED surfaces, which both showed 7%. A low wetting degree promotes the formation of a continuous air layer that effectively reduces the frictional resistance, resulting in a significant drag reduction effect. This is missed in the laminar regime of the SHBC. After the critical Reynolds number, the flow displayed a decreasing trend due to the transition flow regime but still had values greater than 2% for all samples. The performance of all surfaces using silicone oils with viscosities of 5 and 10 cSt is unexpected as the surfaces showed high wettability. This enhancement in the drag reduction is attributed to specific flow conditions, such as the applied high shear rate and the resultant high torque and dynamic pressure, which in turn decreases the wettability degree of the outer surface of the TC cell. These explanations are consistent with previous investigations in the literature [35][98].

4-5 Summary

In summary, it is evident from the data shown in Figures 4-9,10 and 11 that silicone oil flowing on surfaces with superhydrophobic features and low oleophilic static contact angles shows considerable drag reduction. These drag reductions achieved with the same SHSs do not correlate simply with any single measure of the surface wetting degrees using silicone oils. The achieved drag reduction can be attributed to many factors, such as increased shear rate, lower static pressure and connection of the air inside the cell to the ambient air. Increasing the applied shear rate increases the flow velocity, global torque, and dynamic pressure [68] [95] [98]. In the present work, the silicone oil's viscosity increased five and ten times compared to the deionized water. As a result, this increased shear rate within a smaller range of Reynolds numbers, ultimately resulting in a higher average global torque. The small gap width in the current TC cell contributed to an increase in dynamic pressure and a reduction in static pressure near the outer wall of the TC cell [68] [95]. The decrease in static pressure facilitates the growth of the air layer (Plastron) trapped between the tested liquid and the walls. This occurs because the air inside the cell is connected to the ambient air, as shown in Figure 4-1a. The existence of an air layer acts as a lubricant between the flowing liquid and the surrounding surfaces. The plastron thickness increases by linking the air within the Taylor-Couette flow cell to the ambient air, ensuring its integrity for an extended duration and enhancing the lubrication at the interface[40]. The air inside the cell of the Taylor-Couette flow is linked to the surrounding air, allowing air to be entrained in the plastron layer trapped between the liquid and the fabricated surface, resulting in a thicker plastron layer, which is consistent with the results of previous experimental and computational studies in the literature[62][66][79][43].

CHAPTER V

Chapter 5 Impact of Plastron Thickness and Slip Length on Drag Reduction over Superhydrophobic Surfaces in Taylor Couette Flow

This chapter studies the effects of the plastron thickness and effective slip length on the achieved drag reduction over superhydrophobic surfaces in a Taylor Couette flow. We demonstrate slippage over three fabricated SHSs in laminar and low turbulent Taylor–Couette flows. We experimentally investigate how the slip length increases with a higher Reynolds number (Re) over the tested SHSs; simultaneously, the air plastron thickness is investigated using a viscous model. The mean skin friction coefficient (C_f) can be fitted to a modified semi-empirical logarithmic law expressed in the Prandtl–von Kármán coordinate. The main content of this chapter has been published (Alsharief, A. F. A., Duan, X. & Muzychka, Y. (2023). "Evolution of Air Plastron Thickness and Slip Length over Superhydrophobic Surfaces in Taylor Couette Flows." Journal of Fluids, MDPI, 8(4), p. 133. The author of this thesis is the first author of this paper. The first author conducted the experiments, analyzed the data, and prepared the manuscript. Prof. Duan, and Prof. Muzychka, as the second and third authors, provided their suggestions on experimental observation, data analysis and revision of this paper.

5-1 Introduction

The drag forces on the walls of confined flows can reduce the fluid flow's momentum, which leads to a reduction in the efficiency of the designed system. The most practical approach used to achieve the overall viscous shear drag reduction (DR) is the passive technique (e.g., changing the wall topology) [6][7][8]. The slip over the SH coating surface could be explained as a combination of direct and indirect effects. In laminar flows, a reduction in skin friction drag can be analyzed by comparing the slip length to the characteristic length of the flow geometry [98]. Air–water interfaces on or in roughness elements are usually used to describe the effective slip length, which is the direct effect. The main forces dominating the flow region near the wall are the viscous drag force parallel to the wall and the flow's liquid pressure, which is normal to the wall. In random roughness, as hydrostatic pressure increases, the trapped air layer (plastron) becomes gradually thinner, and its dynamics can only be predicted in an average or statistical manner [98]. Thus, the slip length values in the laminar region are lower than those in turbulent flow regions. When the Reynolds number is high, shear stress and pressure fluctuation are caused by turbulence enhancing the wetting [8], which is an indirect effect. By modelling the air diffusion process of a plastron as a nonlinear oscillation system, Piao and Park [99] investigated the effects of fluctuating air–water interfaces. The study suggested that the interaction between the air compression due to fluctuating water pressure and the water impalement due to gas diffusion determines the plastron's response to the unsteady environment. In contrast to regularly structured roughness, the random roughness morphology is thought to suffer from the negative effect of the spanwise slip being identical to the streamwise slip, as well as the inability to maintain a full plastron resulting in non-uniform asperities im-paling the water [99].

The air layer trapped between the SH surface and the water is commonly called the air plastron. As a lubricator, the air plastron reduces viscous skin friction and enhances the effective slip velocity [100]. The plastron and the drag reduction effects disappear when the SH surface transits from a non-wetted Cassie–Baxter state to a wet-ted Wenzel state.

Consequently, preventing or delaying the transition to the Wenzel state is crucial since it is typically the more thermodynamically advantageous state [62]. Increasing the Laplace pressure by using small air buckets or increasing the hydrophobicity of the surface can achieve this tendency [15].

For drag reduction to be sustained, it is also necessary to minimize gas diffusion from the plastron into the liquid. This can be achieved, for example, by increasing the volume of the saturated gas in the liquid, e.g., gas or bubbles injection technique [15][101]. The gas is transported from the plastron into the liquid at an accelerated rate with higher flow velocities, giving shorter effective diffusion lengths [101]. The plastron air layer connected to ambient air showed enhancement of the achieved drag reduction compared with the same case of the isolated plastron layer. This enhancement refers to the ambient air entraining the plastron layer [79].

Only a limited number of investigations have characterized the plastron air thickness since it is challenging. Different techniques have been used to investigate the plastron layer growth at low and high Reynolds number flows. In stagnant water, Bobji et al. [101] used the total internal reflection (TIR) of light at the air–water interface to visualize air pockets over SHSs with regular and random textures. They observed that the air pockets gradually dissolved in water, and the surface became completely wet. The intensity of light reflected from the plastron and confocal microscopy to characterize the time-dependent morphology of trapped air over an SHS in stagnant water was used by Poetes et al. [58]. Initially, they observed that the SHS was covered in a complete plastron, but air diffusion into the water gradually made the plastron thinner. They observed exponential increases in diffusion rate with increasing immersion depths (static pressures) in SHS. Spherical cup-shaped bubbles are formed as the plastron reaches a critical thickness. They also dissolve in water over time. Samaha et al. [58] measured the longevity of the air pockets using an optical spectroscopy system based on the intensity of reflected light. They observed that reduction in the reflected light from the plastron over time is correlated with a decrease in both drag reduction and the contact angle of the SHS.

Few studies were performed to investigate the air plastron layer as it was subjected to the flow. Most of them were carried out in a water tunnel using TIR and high-speed camera techniques for optical observations [8][58][102]or tracer-based methods such as particle image velocimetry (PIV) technique [103]. It is challenging to visualize the plastron in large-scale flow facilities in turbulent flows. Moreover, a large volume of water with high ionicity, temperature control, and mechanical vibration of the facility also contribute to challenges [105]. The study of Ling et al. [32] showed that when the roughness elements are exposed to the turbulent flow, the Reyn-olds stresses become the main contributor to the wall shear stress, resulting in less drag reduction. In addition, the mechanical interaction between the plastron and solid pollutants in the liquid, or the tracer particles used in the intrusive measurement techniques, showed the plastron's instability; its lifetime was shortened by approximately 50% [102][59]. With the use of a cone-and-plate rheometer, Lee et al. [97] showed that a larger gas fraction at the air–water interface increases effective slip over the structured SHS, though the plastron becomes unstable. Later, they observed that an SHS's DR performance is significantly limited by the plastron's stability at high velocity.

This chapter studies the relationship between the plastron thickness, the slip length, and the wettability of various SHSs experimentally, based on the Taylor–Couette (TC) flow cell of the rheometer's measurements performed in Chapter 5 using water. In addition, a regression analysis was performed to predict the wettability effects on the achieved drag reduction (DR%). Three SHSs were used, and all of them were fabricated with commercial SH coatings on the outer surface of the TC cell. The outer surface was selected as the tested surface of the TC cell because of the high dynamic pressure compared with the inner surface [105]. This high dynamic pressure will decrease the static pressure and allow the air to entrain in the plastron layer. According to previous studies [78], this can potentially allow the plastron to last longer than it has in cases where the inner wall is coated. The surface morphology was investigated by scanning electronic microscopy; the wetting degree was characterized by measuring each sample's static and dynamic angles. The experimental data of the flow are used to calculate the slip length and the plastron thickness. The plastron thickness is calculated based on the viscous model of the slippage of water suggested by V. Olga [106]. A statistical regression method is used to analyze the experimental data and investigate the relationship between the air plastron thickness and the slip length (independent variables) and the Reynolds number, shear stress, viscous ratio, and surface hydrophobicity (dependent variables). The original TC cell with superhydrophobic surfaces enables us to study the growing plastron thickness and the achieved slip length under well-controlled conditions.

5-2 Skin Friction coefficient measurement

In this work, the baseline shear stress (τ_{ω}) for the TC cell was obtained using an uncoated surface of Aluminum CDCs, computed from Equation (5-1). The dimensionless wall shear stress is typically expressed using a skin friction coefficient. The skin friction coefficient is plotted versus Reynolds numbers to investigate the flow behaviour. The skin friction coefficient is given by the following:

$$C_f = \frac{\tau}{\frac{1}{2}\cdot\rho\cdot U_i^2} = 2\cdot\frac{u_\tau}{U_i} \tag{5-1}$$

Here, $U_i = (r_i \cdot \omega)$ is the measuring bob linear velocity for our system and $u_\tau = (\frac{\tau_\omega}{\rho})^{0.5}$ is the friction velocity. The theoretical friction coefficient of the laminar Couette flow can be expressed by [90] [107][108]

$$C_f = \left(\frac{2}{2-\frac{d}{r_o}}\right)\cdot\frac{2}{Re} \qquad \text{for Re} < 100 \tag{5-2}$$

and for turbulent flow [107][108]

$$\frac{1}{\sqrt{C_f}} = 3.52\cdot\ln\left(Re\cdot\sqrt{C_f}\right) + 4.1 \qquad \text{for Re} > 100 \tag{5-3}$$

The coefficient of friction values decreases with higher Reynolds numbers for all fabricated surfaces, as shown in Figure 5-1. However, it can be seen that the laminar Couette flow regions (Re < 82) slightly differ from the smooth surfaces (baseline) for all tested samples. This behaviour is expected since the flow in these regions is controlled by the flow geometry [108]. The standard deviation error of the measurements is 0.5%. The turbulent region can detect no difference between the fabricated and smooth surfaces.

5-3 The logarithmic friction law of slip length in turbulent regime

The method used by Panton [109] showed that the coefficient of friction in turbulent Taylor–Couette flows should obey a logarithmic friction law expressed in the form of Prandtl–von Kármán [66][34][88][108] as follows:

$$\sqrt{\frac{2}{C_f}} = M \ln\left(Re\sqrt{\frac{C_f}{2}}\right) + N \tag{5-4}$$

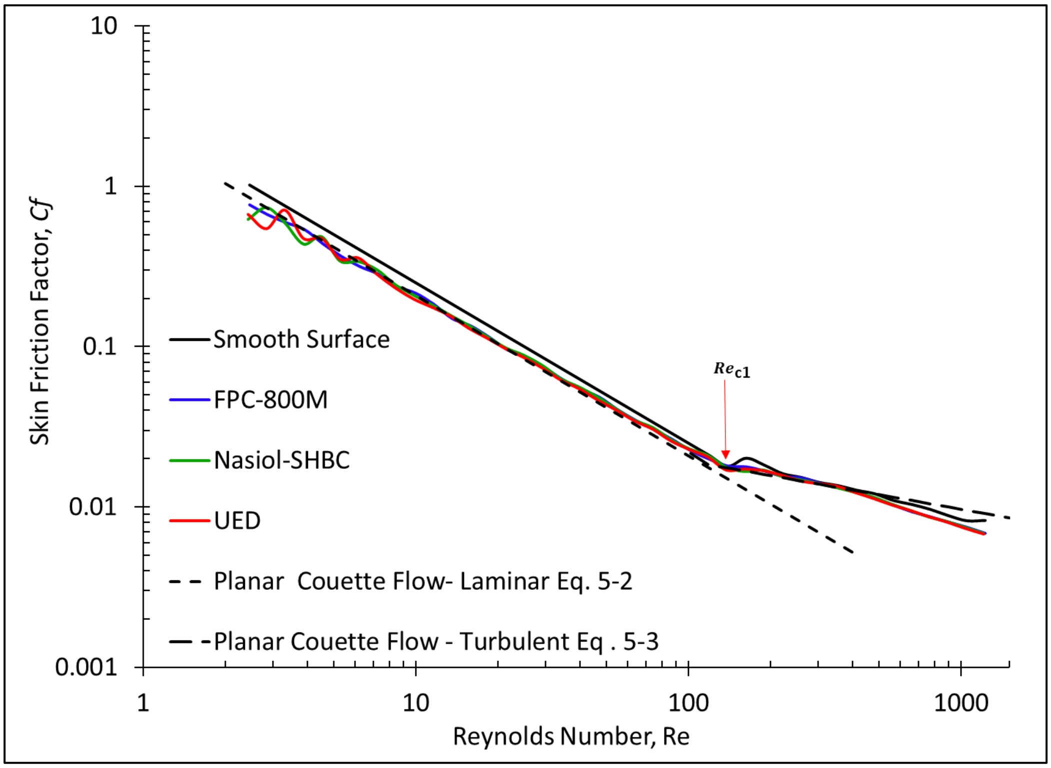

Figure 5-1 Comparison of skin friction of the experimental data in laminar and turbulent regions using all smooth and coated surfaces. The computed data using Equation (5-1), theoretical laminar data using Equation (5-2), and turbulent theoretical data using Equation (5-3).

where M and N are constants that depend on the radius ratio ($\eta = \frac{r_i}{r_o}$) of the TC cell geometry. Plotting the baseline data curve allowed us to verify that our baseline measurements conformed to this logarithmic law. The measured skin friction coefficient data for the smooth outer surface were plotted in Prandtl–von Kármán coordinates (for Re > Rec1), as seen in Figure 5-1. A least-square fit of the smooth surface data to Equation (5-4) yielded the values M = 4.37 and N = −2.1 for the present TC cell, which has η = 0.92. With superhydrophobic coating applied on the outer surface of the TC cell, these areas become almost shear-free boundaries, which allow local flow to slip. The no-slip condition is still applied to the inner surface, which is the measuring bob. Srinivasan et al. [35] determined how the Navier slip adjusts the skin friction presented in Equation (5-4) when applied on the inner surface. They applied Panton's angular momentum defect theory [109] and incorporated finite wall slips at the inner surface. The existence of the core region was verified experimentally and numerically with a weakly varying angular mo-mentum dependence, as well as thin layers near the inner and outer cylinders, which are characterized by a sharp decay in the angular momentum [35] [109] [110].

Using the defect theory, Panton [109] matches the approximately constant angular momentum in the bulk of the TC flow to that of the wall layers to derive a logarithmic friction law of the form expressed in Equation (5-4). Srinivasan et al. [35] showed that a composite boundary condition significantly affects the outer flow that imposes an "effective" spatially averaged slip length at the rough SH wall. They modified this theory by deriving a friction law, analogous to Equation (5-4), for rough SH texture applied to the inner surface of their TC cell. A similar concept was used in this work to derive the friction law for rough SH texture applied to the outer TC cell surface (a detailed description of the derivation is given in Appendix E. The obtained logarithmic friction law has the final form as follows:

$$\sqrt{\frac{2}{C_f}} = M \ln\left(Re\sqrt{\frac{C_f}{2}}\right) + N + b^{+} \tag{5-5}$$

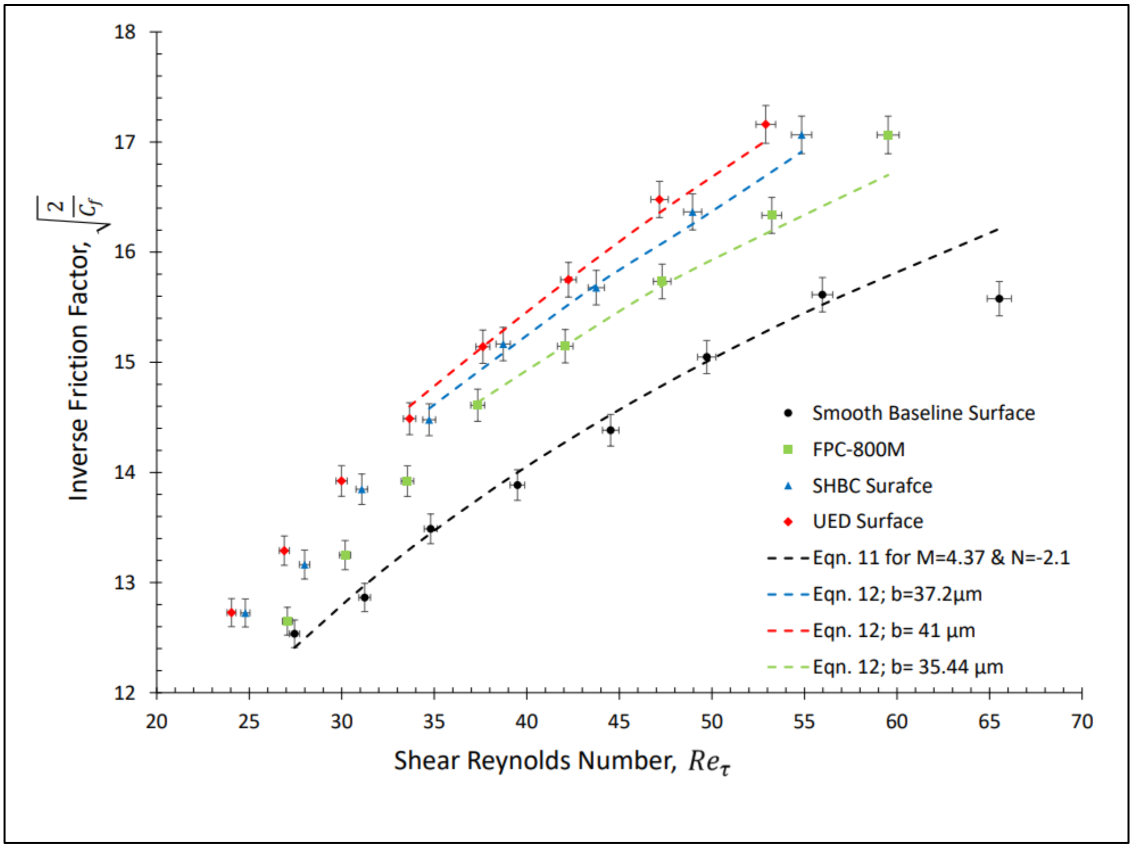

Figure 5-2 The measured skin friction plotted in Prandtl–von Kármán coordinates for all tested surfaces. The black dashed line is the smooth baseline friction curve for the Taylor–Couette fixture, given by Equation (5-4) with M = 4.37 and N = −2.1. The coloured das dash lines are least-squares fits of Equation (5-5) to data of the last five points of each tested SHS. The red dashed curve (UED) with b = 41 μm, the blue dashed line (FPC-800M) with b = 37.2 μm, and the green dashed line (SHBC) with b = 35.4 μm.

The dimensionless slip length is defined as $b^+ = \frac{b_{eff}}{\delta_\nu}$, where δ_ν is the viscous length of the turbulent flow and is introduced as $\delta_\nu = \sqrt{\frac{(\rho\nu)^2}{\tau_\omega}}$. Whereas b^+ increases with the Reynolds number, as will be shown in the next subsection. Earlier experimental and numerical works showed that the b^+ is independent of the high Re in turbulent flows [34] [66][111][112]. The effective slip length was estimated from the TC cell measurements using all fabricated SH surfaces in different flow regimes. The effective slip length is used as the characteristic parameter quantifying the drag-reducing ability of our SH surfaces.

The TC cell in this work has a high radius ratio (0.92), which limited our ability to obtain data in the fully turbulent regime. The inverse of skin friction is no longer linearly related to the shear Reynolds number ($Re_\tau = Re \cdot \sqrt{\frac{C_f}{2}}$) when plotted in Prandtl–von Kármán coordinates due to the last term of b^+ in Equation (12). A nonlinear regression for SH surfaces data using Equation (5-5) [34] [66] results in the best-fit single-constant value of b^+ for each SH surface. The experimentally measured data and corresponding fit data of Equation (5-5) are plotted in Figure 5-2. The present TC setup has a limited experimental range (limited Reynolds number), so the single value of b^+ measures the friction-reducing performance of each surface, as shown in Figure 5. It can be seen that the UED in the regime of $Re > Re_{c1}$ has a high value of the inverse friction coefficient compared to the FPC-800 and SHBC.

5-4 The achieved effective slip length

The torque measurements for the TC cell in the rheometer setup allow calculating the apparent shear stress over the SH surfaces. Navier's definition of slip velocity is

$$u_s = b_{eff} \frac{du}{dy} \tag{5-6}$$

where beff is the slip length, and $\frac{du}{dy}$ is the shear rate. This general definition is not useful to describe the slip over the superhydrophobic surface, where the slip length is related to the way the liquid contacts the engineered surfaces. An effective slip length has been introduced to estimate the slippage over the fabricated hydrophobic surfaces [96][113] [114]:

$$b_{eff} = \left(\frac{M_{woc}}{M_c} - 1\right) \cdot d \ = \left(\frac{\tau_{woc}}{\tau_c} - 1\right) \cdot d \tag{5-7}$$

where Mwoc is the measured torque without coating, and Mc is the torque with SH coatings. The ratio of these two torques can be used to find the effective slip length. Similarly, $\frac{\tau_{woc}}{\tau_c}$ is the ratio of the measured shear stresses without coating and with the SH coating, which can also be used to find the effective slip length. In the rheometer measurements, the shear stress is related to the applied torque, which is affected by the surface wettability. One can see that from Equation (5-7), the slip length is directly related to the average shear stress that is by the viscous length, which is given as $\delta_\nu = \sqrt{\frac{\rho\nu^2}{\tau_c}} = \frac{\nu}{u_\tau}$. In the laminar flow regime, the magnitude of effective slip length is governed by the surface feature-length scale and the wetted solid fraction [34]. This study calculates the effective slip length for anisotropic and random surface morphology using Equation (5-7). In Figure 5-3, the calculated values of b+ for all fabricated

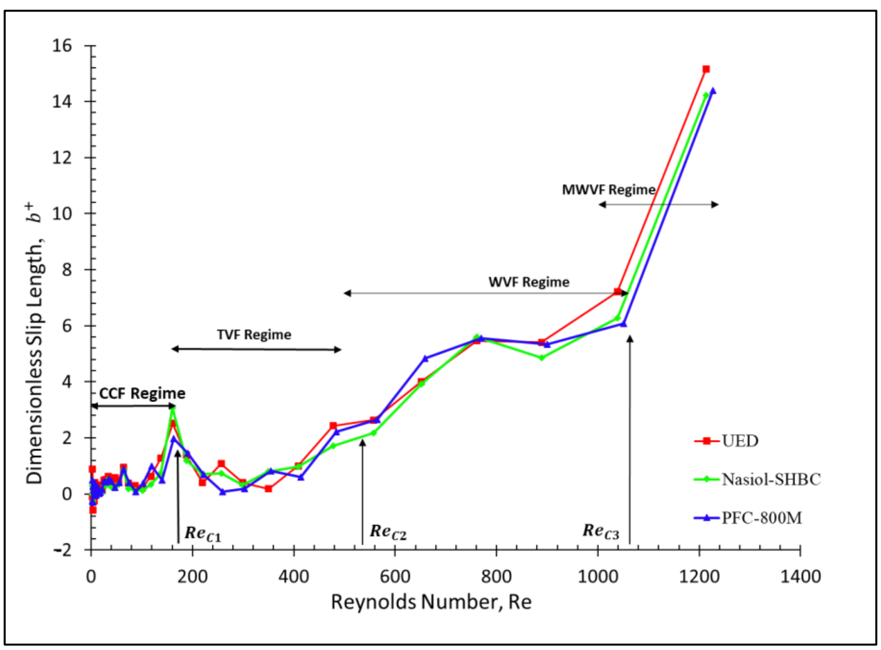

Figure 5-3 Scaling the dimensionless slip length b+, which is calculated based on the effective slip length of Equation (5-7) and normalized by the viscous length (δ ν).

surfaces are plotted against the Reynolds number. The laminar region has low slip length values, which agrees with the literature. The maximum slip length increases from the TVF regime, but a more explicit increase is seen from the WVF regime to the end of flow in the MWVF regime. The UED surface shows the highest b+ value of 16, with a mean effective slip length of beff ≈ 72 μm with a 95% upper confidence limit of 114 μm and a 95% lower confidence limit of 30 μm. The FPC-800M and SHBC showed the highest values at 14.4 and 14.2 for b+, respectively. Although the slip length varies with all surfaces through TVF and WVF regimes, the early stage of the MWVF regime shows a monotonically increase in the flow over all surfaces. The present TC cell with a high radius ratio ($\eta = 0.92$) did not allow measurement in the TTVF regime, despite a maximum rotational speed (Ω) of 1557 rpm being used.

5-5 The achieved air plastron thickness by using the viscous slippage model

Since the existence and condition of the plastron are more difficult to maintain and measure in the TC flows, it is critical to explore the impacts of random roughness morphology surface and Reynolds number on the plastron. The capillary force of the air–water interface trapped on the asperity (roughness) top counteracts the hydrostatic pressure of water, causing the concave deflection [98]. Suppose the local contact angle of water on the sidewall of roughness exceeds the advancing contact angle. In that case, the interface is depinned (released) from the asperity top and slides into the roughness, therefore initiating the wetting transition. There would be no precise critical hydrostatic pressure if the roughness were random [98]. Instead, as hydrostatic pressure increases, the plastron becomes thinner and thinner. The plastron and the DR are lost as the SH surface transitions from a non-wetted (Cassie–Baxter state) to a wetted (Wenzel) state. As the Wenzel state is often the thermodynamically more preferred state, preventing or delaying this transition is critical. Two mechanisms can accomplish this transition by using SH coatings: first, by lowering the size (spaces between nanoparticles) of the asperities in which the air is trapped in order to enhance the Laplace pressure; second, by increasing the surface's hydrophobicity (reducing the surface energy). Another thing to consider in maintaining DR is the diffusion of air from the plastron into the liquid, which may be accomplished by increasing the amount of saturated air in the liquid [62] [15] [63][50]. Many previous studies in the literature showed that in high flow velocity, the air plastron volume could be lost by the convection–diffusion mechanism [62] [66]. Flows with large velocities produce shorter effective diffusion lengths, accelerating the air plastron's dissolving into the liquid [101]. Turbulent flows with Reynolds numbers of ($5 \times 10^5 \leq Re \geq 1.5 \times 10^6$) showed steady movement and variations in the thickness of the air plastron, which was caused by the pressure fluctuations in the flow boundary layer [104].

Many previous studies were performed experimentally and analytically to determine the thickness of the air plastron [50][115]. The slippage viscous model introduced by Olga V. [116] says that if the surface is considered ideal (neglecting the roughness effect), and an average value μa characterizes the viscosity of the air plastron adjacent to the wall, the slip length due to the thickness of air plastron δ can be expressed as follows:

$$\delta = \frac{b_{eff}}{(\frac{\mu_l}{\mu_a} - 1)} \tag{5-8}$$

Although the fabricated CDCs have a 42 mL capacity in the present work, they are filled with just 19 mL of tested fluid, which means the SH surface is not fully submerged; this was implemented to create a connection between the air plastron and the ambient air in the lab (see Figure 4-1a). Based on Srinivasn's work [34], this procedure offered more drag reduction than the case where the air plastron was isolated for the same Reynolds number in their study. Figure 5-4 presents the present study's dimensionless air plastron thickness δ^+ for all fabricated surfaces versus the used Reynolds number. Although the maximum Reynolds number in the present work is lower than the turbulent Reynolds number mentioned in the literature, it can be seen that the air plastron thickness is close to being constant among each fluid flow. The results of air plastron thickness δ are directly proportional to the slip length, as shown in Figures 5-3 and 4, which have around 4.2 μm over all fabricated surfaces. The geometry of the TC setup used in the present work did not show high Reynolds number flows, which placed limitations on observing any change in the air plastron thickness over all the used surfaces.

5-6 Regression analysis for the slip length and the air plastron thickness

The rheometer data were analyzed to study the relationship between the dimensionless plastron thickness (the dependent variable) and several predictor variables: the dimensionless slip length, the ratio of the dynamic viscosity of water to air, the Reynolds number, and the advancing dynamic contact angle as a measure of wettability. Those predictors are the most important parameters that significantly impact the dependent's value. This statistical analysis aimed to understand how these predictor variables influence the dimensionless plastron thickness and to make predictions about the thickness based on known values of the predictor variables. The

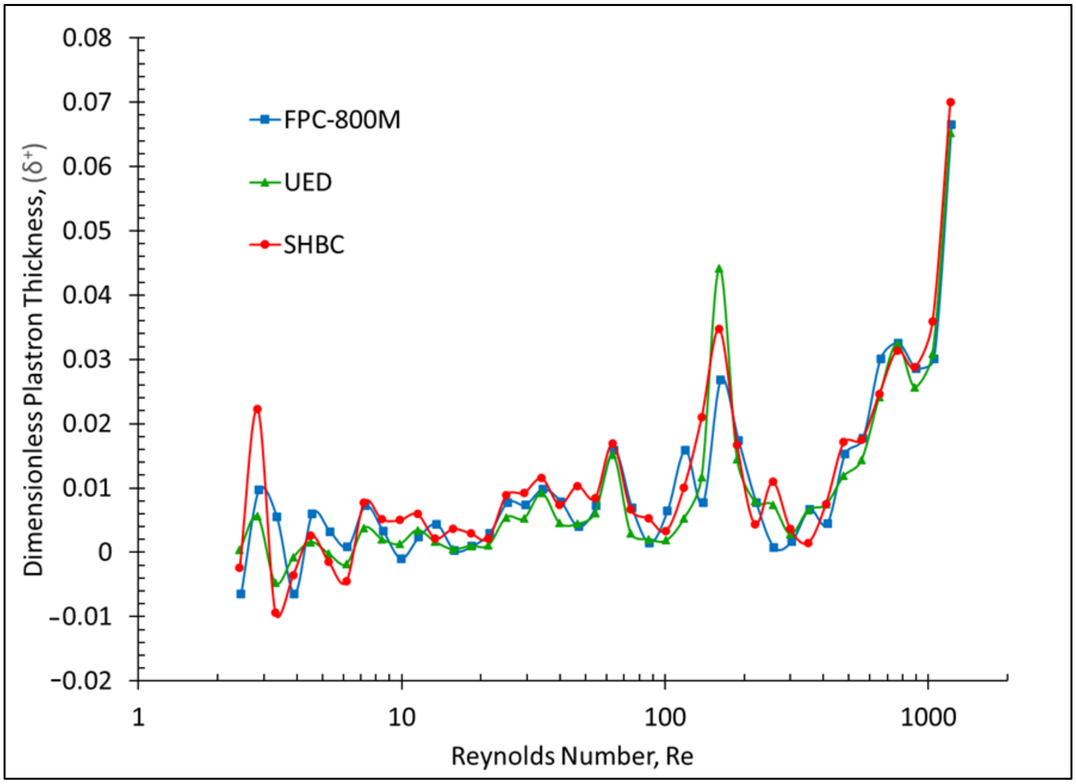

Figure 5-4 Semi-log plot for the variation of the dimensionless plastron thickness based on the viscous model of Equation (5-8) and normalized by the viscous length (δv) over the tested SHSs versus the Reynolds numbers in the present work with a maximum Reynolds number of 1227.

multiple linear regression (MLR) method was used to analyze the data using the statistical package from the IBM SPSS software. A model was statistically formulated for the predicted dimensionless air plastron thickness δ^+. Overall, 164 measured points for all 3 SH surfaces and 1 smooth surface are used; the descriptive statistics are presented in Table 5-1. Various options and preferences in the setting can be customized by the user to modify the behaviour of the SPSS software, such as data editor, output viewer, syntax editor, and general settings. These settings can be accessed and modified through the "Options" menu in SPSS. The regression model presents the impact of the predictors on the dependent δ^+, which is summarized in Equation (5-9), and the model summary is illustrated in Table 5-2 with the coefficient of determination $R^2 = 0.871$.

$$\delta^+ = 2 + 5 \cdot b^+ + 0.0358 \cdot \frac{\mu_W}{\mu_a} + 0.01066 \cdot Re + 0.0001 \cdot Cos\theta_{adv} \tag{5-9}$$

Table 5-1 Descriptive statistics of the regression model.

Parameter	Mean	STD.DEV.	N
δ+	0.008	0.013	164
Re	206.47	306.46	164
Cos Θ	0.54	0.69	164
μw/μa	0.86	50	164
b+	1.001	2.36	164

Table 5-2 . Regression model summary of the dependent variable (δ^+).

Model	R	R^2	Adjusted R^2	STD Error	Changes Statistics				
					R^2 Change	F Change	dF_1	dF_2	Sig. F Change
1	0.933 [a]	0.871	0.868	0.0045	0.871	269.39	4	159	0.0005

[a] Predictors: constant, b+, cos Θ, μw/μa, Re.

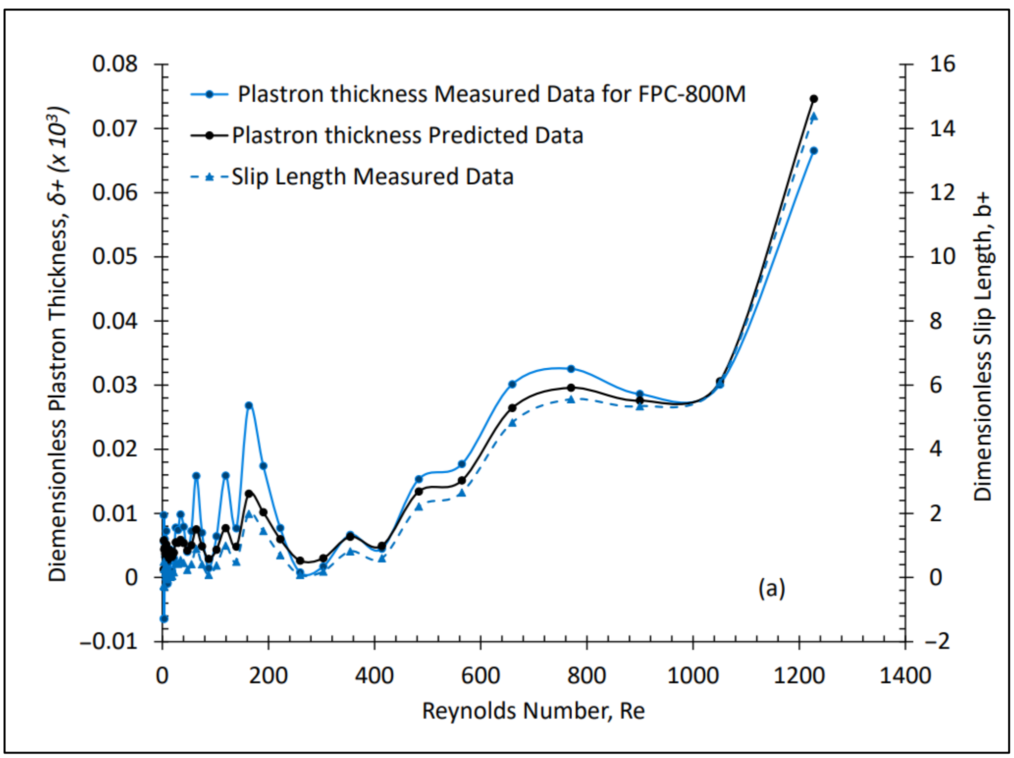

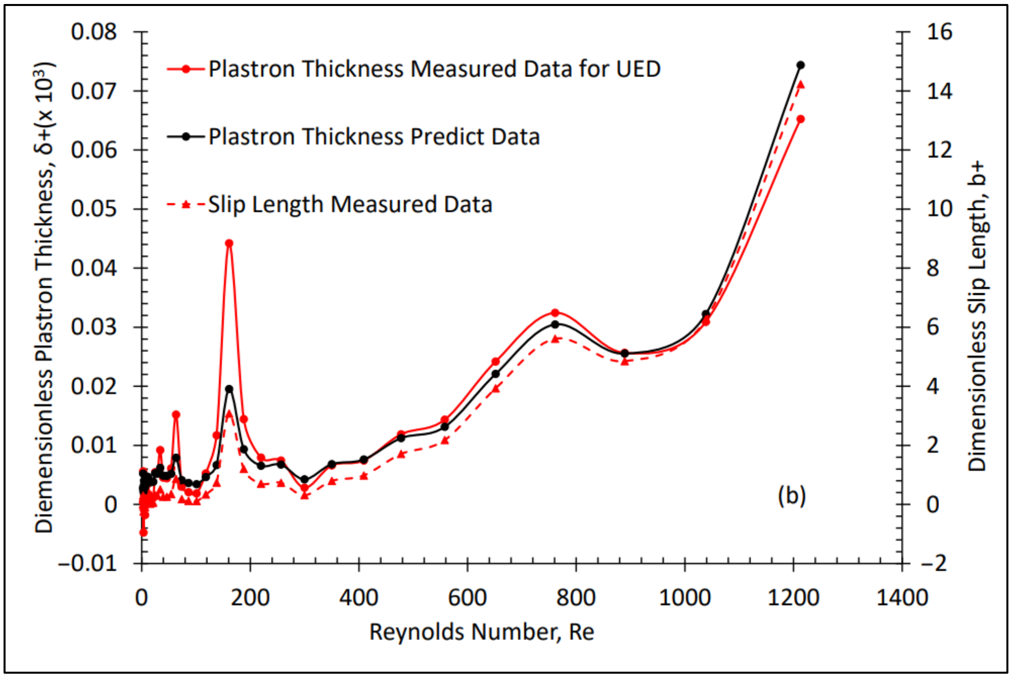

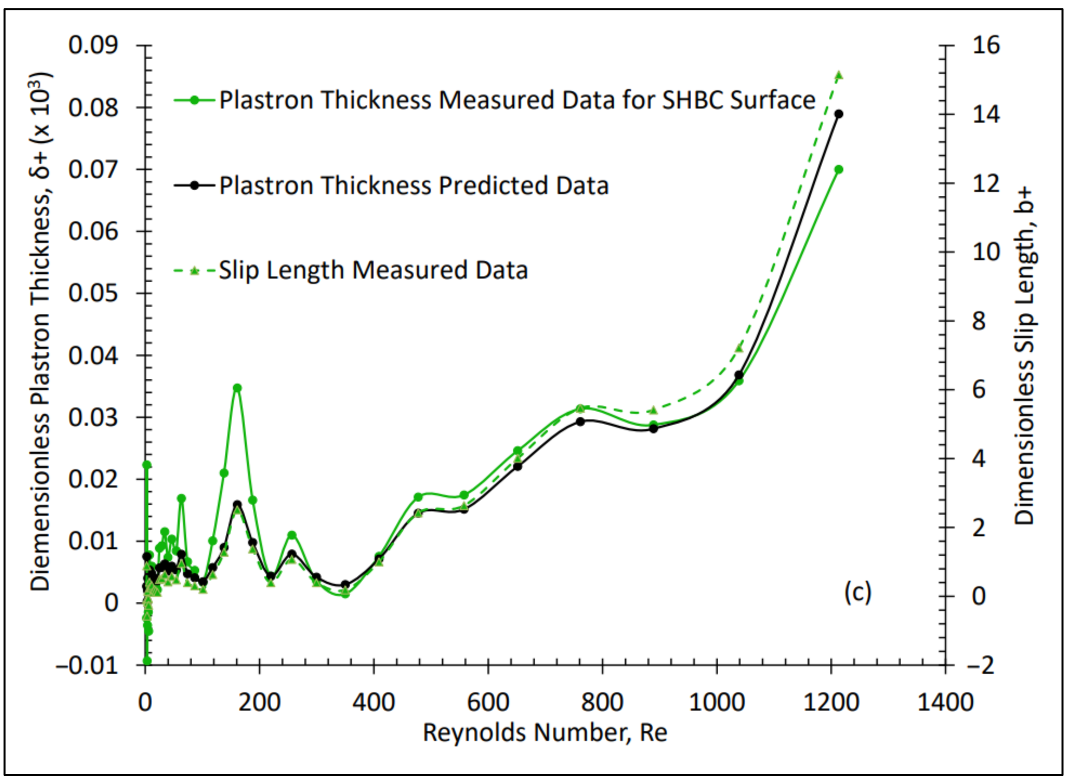

Figure 5-5 The comparison of measured data of both the dimensionless plastron thickness and the dimensionless slip length by the predicted linear regression model data of dimensionless plastron thick-ness for the tested SHSs of (a) FPC-800M, (b) UED, and (c) SHBC

The measured and predicted $\delta+$ and $b+$ are presented individually in Figure 5-5 for each tested SH surface. It was revealed from the regression analysis that all the predictors have a positive impact on the predicted δ^+. In other words, all predictors are positively associated with the predicted δ^+. The predicted and measured dimensionless air plastron thickness δ^+ for each used SH surface was compared with the achieved dimensionless slip length b^+. Figures 5-5a,b and c present the variation of the predicted and measured δ^+ versus the operating Reynolds numbers for the UED, FPC-800, and SHBC. The regression model agrees well with the measured δ^+ for all surfaces; it shows a statistically significant 95% confidence level.

Furthermore, the comparison between the achieved values and the predicted $\delta+$ and measured b^+ values showed a high level of correlation. A sensitivity analysis was performed using the stepwise method to investigate each predictor's effect and determine the most significant predictor's impact on the model. The sensitivity analysis indicates that the $b+$, Reynolds number, and dynamic viscosity ratio are the most influential parameters that affect the regression model, as illustrated in Figure 5-6. It shows the sensitivity index of all predictors, and the achieved $b+$ has the highest sensitivity index of 0.87 with the lowest RMSE of 0.005. On the contrary, the advancing dynamic contact angle (Θ_{adv}) has the lowest sensitivity index of 0.01. This small contribution of (Θ_{adv}) interprets the limited wetting degrees of the three tested samples and one plain sample used in the present work. In comparison, the b is the major predictor parameter affecting the regression model, which is expected, as introduced in the slippage viscous model of Equation (5-8).

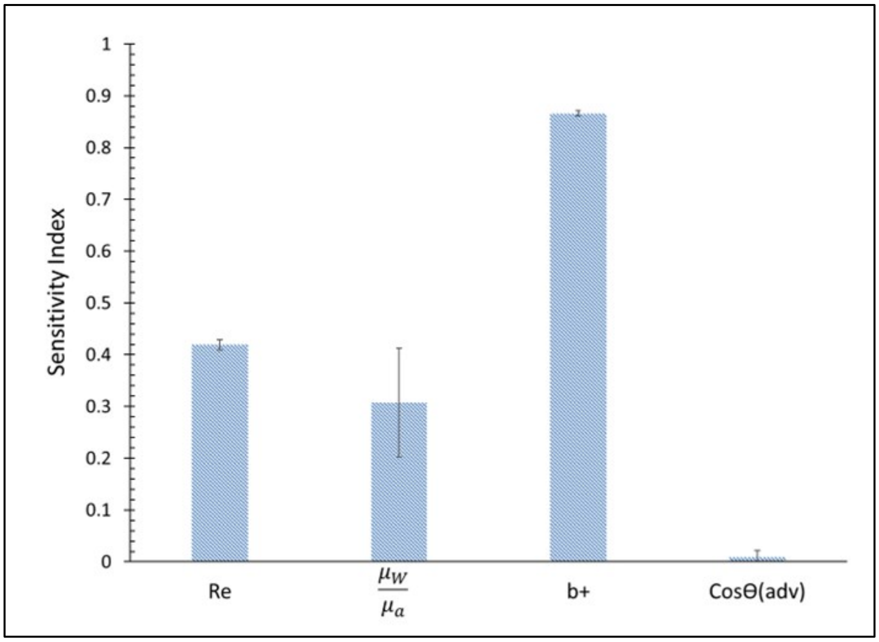

Figure 5-6 The sensitive check of the linear regression model with RMSE for each parameter.

5-4 Summary

In summary, using water as a tested liquid, the effective slip length and the plastron thickness are investigated on three SHS in a TC cell flow facility. A modified version of the Prandtl–von Kármán skin friction law was developed by applying boundary layer (angular momentum defect) theory to turbulent TC flow. The study allowed for the determination of an effective slip length, "b", that describes the non-wetting behaviour of superhydrophobic surfaces (SHS) on the outer wall of the TC cell used in WVF and MWVF regions. The findings indicate that despite having effective slip lengths of only a few micrometres, superhydrophobic surfaces can effectively decrease skin friction during the initial turbulent stages (WVT-MWVT) flows. The plastron thickness at different Reynolds numbers for all tested superhydrophobic surfaces (SHSs) is calculated using a slippage viscous model. The measurement data analysis reveals a distinct correlation between plastron thickness and slip length, with the UED surface exhibiting the highest values of δ+ and b+ among the surfaces examined. The average achieved drag reduction among the three tested surfaces is in the range of 7% to 11%. The regression model developed demonstrates a strong correlation between δ+ and b+ for all tested superhydrophobic surfaces (SHSs). The predicted data closely aligns with the measured data, indicating good agreement. Despite slight variations in wetting degree among the SHSs, the plastron thickness is directly linked to the slip length and the water/air dynamic viscosity ratio. The small number of tested surfaces had minimal influence on the accuracy of the regression model.

CHAPTER VI

Chapter 6 Comparing Study of Drag Reduction on Various Superhydrophobic Surfaces in Open Channel Turbulence: Laser Doppler Velocimetry Measurements

This chapter investigates the drag-reducing performance of three hydrophobic coatings experimentally when applied to sharp edges flat plate surfaces in an open channel facility and measured by using a Laser Doppler Velocimetry (LDV). The main content of this chapter has been submitted Physics of Fluids Journal, AIP. (Alsharief, A. F. A., Duan, X., Nyantekyi-Kwakye, B. & Muzychka, Y. (2023). "An experimental investigation of the impact of anisotropic slip-length boundary conditions on turbulent flow over superhydrophobic surfaces within an open channel". The author of this thesis is the first author of this paper. The first author conducted the experiments, analyzed the data, and prepared the manuscript. Prof. Duan, Prof. Nyantekyi-Kwakye and Prof. Muzychka, as the second, third and fourth authors, provided their suggestions on experimental observation, data analysis and revision of this paper.

6-1 Introduction

Skin friction (viscous) drag is important when designing marine vessels or pipelines. It is the force created from laminar or turbulent flow along the surface of a marine vessel or pipe, and it significantly impacts the performance and efficiency of a marine vessel. The energy consumed by propulsion or pumping systems to overcome skin friction drag increases fuel consumption, consequently increasing pollutants such as carbon dioxide and other greenhouse gases, contributing to climate change and damaging marine ecosystems [117]. The viscous friction accounts for 60-70% of the overall drag on a cargo ship and

80% on a tanker, as reported by Fukuda et al. [118]. Given that the shipping industry alone is responsible for 3.3% of CO_2 emissions, as Brostow [117] highlighted, addressing this issue has significant global implications regarding energy conservation and reducing greenhouse gas emissions. It is, therefore, crucial to reduce friction drag for external flows since it can result in power savings as well as emission reduction. These global challenges urge engineers to use various design strategies to minimize skin friction drag, eliminate its effects, and safeguard the environment.

6.1.1 Drag reduction techniques:

Skin friction drag reduction (DR) in turbulent flows, which forms a significant part of overall drag forces, has received considerable attention due to the tremendous economic and ecological interest in such flows over the last few decades. The reduction of overall viscous shear drag can be classified into three main categories: active techniques, interactive drag-reduction techniques, and passive techniques, as illustrated in Figure 1-1 [6] [7][8]. Active drag reduction includes suction, blowing, bionic jet surface, air bubbles, and heating wall. However, in most of these techniques, extra gas-providing devices or energy are essential for an effective active drag reduction, raising costs and limiting their applications. Interactive drag reduction through polymer addition has been studied extensively, but its mechanism remains a complicated task [82]. Passive drag-reduction techniques can be classified into two main approaches. The first method relies on the so-called superhydrophobic effect using unstructured surfaces [9]. It results from a combination of the hydrophobicity of the surface material (chemically hydrophobic) and surface topography (physically rough)[98]. Many biological surfaces exhibit remarkable non-wetting features, particularly in certain plant leaves [6][11]. The superhydrophobicity of lotus leaves is well known. Much attention has been drawn to the well-known superhydrophobicity of lotus leaves, which has created great interest in fundamental research and industrial applications. A lotus leaf's static contact angle and hysteresis are around 164◦ and 3◦C). By mimicking the lotus leaf structure, the superhydrophobic coating works to reduce surface energy. Surface energy quantifies the disruption of intermolecular bonds that occurs when a surface is created. When reducing the surface energy, the contact area fraction between liquid and solid surfaces also becomes a minimum since the liquid has a tendency to stick to itself more than it sticks to a given surface [13]. The second approach is structured superhydrophobic surfaces, which have two categories. The first category is the compliant wall drag reduction related to rearranging the bulk flow into properly formed surface grooves, which could be longitudinal or transverse microgrooves. Alternately, the use of extremely thin grooves with friction decreases the flow velocity inside such grooves, thus reducing the shear to which the bounding wall is exposed [6][11][12]. The challenge with this technique is that the compliant wall work is difficult to sustain over a long period of time. It will lose its drag-reduction efficiency if compliant wall hardness is achieved [6]. The second category uses riblet micro-post surfaces associated with grooves specially structured to create small separation bubbles where the fluid slows down, exposing the bounding wall to a reduced shear [6][11][12]. Although the riblet posts surfaces approach has a limited application, many researchers have proven that this method reduces frictional drag up to about 10% in water [6][11]. The last two passive DR methods are active in single-fluid systems [11]. All characteristics of the methods described above use distinctive surface topography, leading to the formation of the desired flow structures. Many examples of their applications include water repellency, self-cleaning, anti-icing, anti-biofouling, anti-corrosion, desalination, and drag reduction [13][14].

6.1.2 Superhydrophobic Coating Progress

The industry of superhydrophobic coating materials has made significant progress over the past decades, leading to the commercial availability of several products. It encountered numerous difficulties throughout its developmental stages, and each stage had limited applicability and durability [29]. However, recent advances in superhydrophobic technology have opened the door to a wide range of applications, from personal use to highly complex industrial applications [14]. The mechanism for reducing drag through coating focuses mainly on reducing drag on roughly smooth (nano-scale roughness) surfaces and surfaces with low surface energy [29]. Recent research has revealed that applying a suitable coating to the desired surface makes it possible to prevent the transition from a laminar boundary layer to a turbulent boundary layer [29]. Although remarkable progress has been made in manufacturing SH polymer nanocoatings over the past two decades, many challenges still need to be addressed for large-scale industrial applications. The present era demands the production of green, eco-friendly, superhydrophobic, low-level polymer nanocoatings with volatile organic emissions (VOCs), longer shelf life, and strong adhesion qualities [14][29][31]. Therefore, it can be argued that significant progress could be made due to the growing interest and scientific attention in this area, resulting in widespread manufacturing and commercial promotion [31][30]. Superhydrophobic coatings pioneered a new manufacturing era, presenting this coating as a commercial product in the summer of 2016.

6.1.3 The Previous experimental work and gap in turbulent channel flows:

According to what has been reported in the literature, various measurement techniques have been used to study the flow behaviour over superhydrophobic surfaces. These include using direct pressure sensors, laser doppler velocimetry (LDV) and particle image velocimetry (PIV) techniques. These techniques are utilized in specific regions of study over the SHS, such as the field of view for PIV or measurement's location for LDV, focusing on the flow behaviour of that particular area rather than the entire SHS. The fluid flow over a superhydrophobic surface is often characterized by high levels of liquid mobility and its rapid movement, resulting in the formation of a turbulent boundary layer. This layer represents an area where fluid movement becomes chaotic and irregular. On the other hand, smooth surfaces tend to have more stable and uniform liquid films with less liquid movement. Moreover, the high Re number flows over SHSs linearly increase the slip velocity in physical units [119]. This state, combined with the low-friction effect of air pockets and the lubricating action, results in reduced drag and enhanced fluid flow properties. It is important to note that the shear and Reynolds stress on a superhydrophobic surface can be complex and highly dependent on the specific surface structure and fluid parameters. Further experimental research is needed to arrive at definitive conclusions about hydrodynamic sustained drag reduction. Over the past two decades, numerous surface textures and manufacturing techniques have been created for SH surfaces. However, there hasn't been a significant focus on comprehending and creating suitable flow experiments specifically for SH drag reduction. These experiments require specific criteria not considered in conventional flow-testing facilities (e.g. pipe loop flows, duct flows).

Since the existence and condition of the plastron are more difficult to maintain persistently and complicated to measure, respectively, in turbulent flows compared with laminar flows. Investigating the effects of the surface hydrophobicity and acquired slip length on the plastron and the achieved drag reduction is essential. The limitation of the field of view of the PIV systems has compelled all previous works to focus on investigating the drag at a specific region from their experimental setup. Additionally, investigations using LDV have primarily concentrated on examining the impact of SHSs on turbulent flows in the lateral direction at a specific streamwise plane. According to the recent findings on the drag reduction of turbulent flow, this study aims to experimentally examine the turbulent flow over surfaces with a random texture. The purpose of studying the mean flow pattern and assessing the skin-friction properties of SHSs is to compare them with a hydrodynamically smooth surface. Moreover, the investigations observe the drag reduction by characterizing the mean velocity profile, turbulent intensity, shear stress, and Reynolds stresses in a turbulent flow over three fabricated SHSs. The novelty of this work is to assess how effective and applicable these SHSs are in reducing drag within an external turbulent boundary layer flows from the leading edge to the trailing edge of the tested surface.

6.2 Experimental setup & procedure

6.2.1 Open channel setup

The turbulent channel flow is obtained by submerging a sharp edges test section in a large open-top water channel (water flume) in the Laboratory of Interfacial Thermofluids and Energy at the Memorial University of Newfoundland. The closed-circuit open turbulent channel flow facility used in this work is shown in the schematic of Figure 6-1.

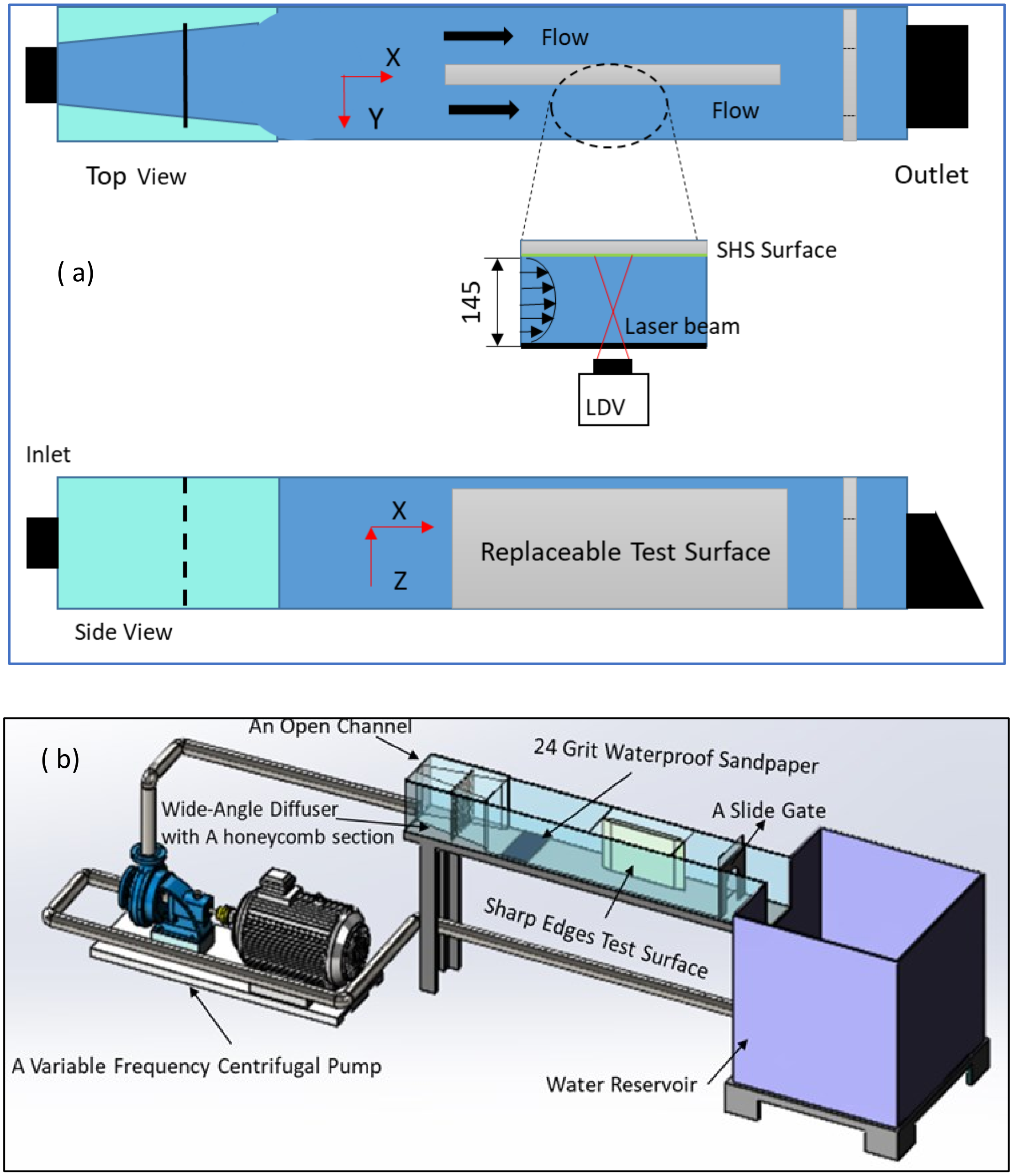

Figure 6-1 (a) Schematic of Side view photos of the test section and the LDV measurements system and (b) the fully developed turbulent flow open channel facility.

The channel flume measures 296 mm in width, 250 mm in height, and 2000 mm in length. To facilitate optical access, the sides are made of smooth plexiglass. The research uses a Cartesian coordinate system, with x representing the flow direction and y representing the distance from the wall. The water depth, h, is kept at 130 mm in the z vertical direction. The flow loop had a centrifugal pump of 5.6 kW that was controlled by a variable frequency driver (VFD). The flow was supplied to the test section from a 1,000 L open tank, and the water temperature was maintained at 12° C. The operating pump sent water to a flow conditioning section consisting of a diffuser containing a perforated honeycomb plate. The flow was initiated with a 24-grit sandpaper placed at the inlet, which spans the full width of the channel and is 50 mm long, to promote boundary layer development. The test surface was designed to insert in the location where the flow fully turbulent developed. The mean velocity was observed to be fully developed beyond a streamwise location of 640 mm. The test surface was inserted at this location, which let the distance between the test surface and the outer channel surface to 145 mm out of 296 mm, which is the complete channel width.

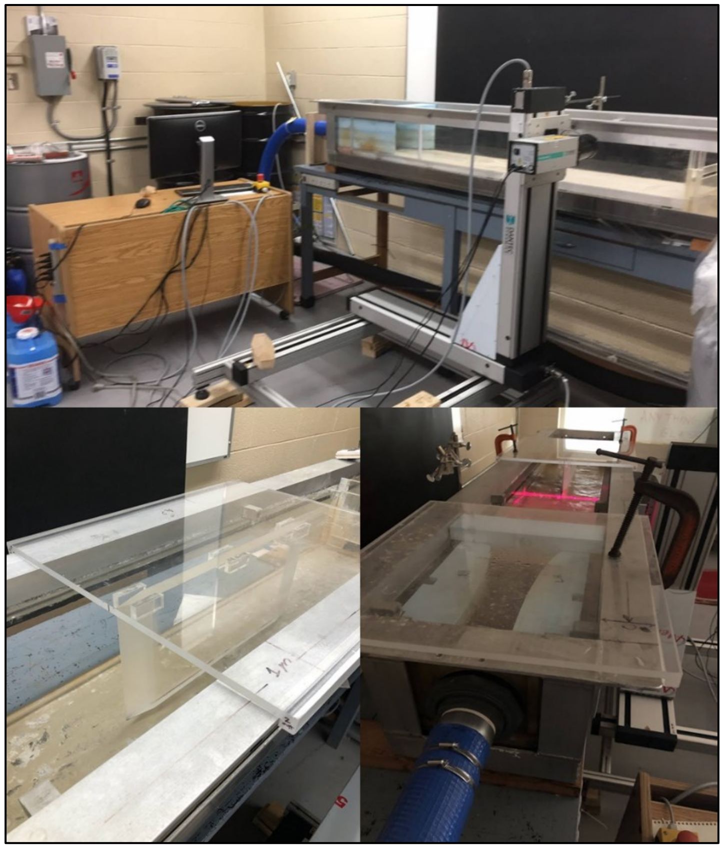

Figure 6-2 Images of the open channel flow facility, test section and the LDV system

6-2-2 Test section

The test surface, which is made from plexiglass, is designed and fabricated to have sharp leading and trailing edges with a 25 mm thickness plate, as illustrated in Section 3-4 and Figure 3-9. The test surface was inserted at 640 mm downstream in the X direction. This location let the distance between the test surface and the outer channel surface to 145 mm out of 296 mm, which is the complete channel width. The measurement points were selected along the flow direction at seven distances X = 70, 130, 200, 250, 300, 350, and 400 mm from the plate's leading edge, as illustrated in Figure 6-3. The LDV measurements were performed at 55.5, 60.5, and 65.5 mm above the channel bottom surface, avoiding wake formation and near the free surface.

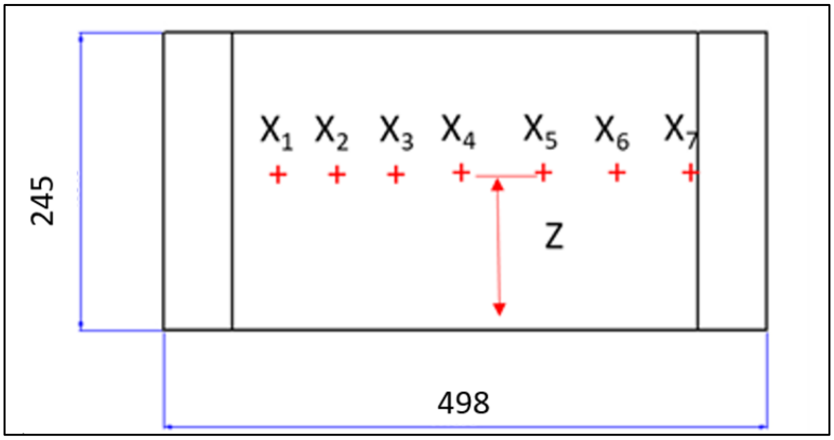

Figure 6-3 Schematic of side view for the test surface with the seven measurement locations

6-2-3 Laser Doppler Velocimetry (LDV) system

A two-dimensional (2-D) Laser Doppler Velocimetry (LDV) system was used to conduct the detailed velocity measurements in x, y, and z directions within the vicinity of the SHS. The LDV used in the present work is the FlowExplorer system, which is an optical two-component LDV from DANTEC DYNAMICS, as shown in Figure 6-4. FlowExplorer represents a groundbreaking innovation in the realm of Laser Doppler Velocimetry (LDA) for investigating turbulence. This innovation encompasses a pre-aligned and calibrated optical probe, a precise signal processor, and a comprehensive Windows software suite equipped with a wide array of tools for visually and numerically showcasing outcomes. The LDV system, in this case, acquires velocity measurements at a rate of 50 Hz on average. The flow was seeded with 10 µm diameter silver-coated hollow glass spheres with a specific gravity 1.4, enabling the capture of detailed information in the near-wall region. The laser power was 500 mW for each velocity component. The LDV is calibrated to a high degree of accuracy at the factory, with a precision of better than 0.11% for an optical lens of 300 mm front focal length, using a BSA F600 processor. The system offers 530 and 560 nm wavelengths for the first and second velocity components, resulting in a fringe distance of 20 µm. The FlowExplorer LDV system is equipped with a 3D traverse mechanism that allows for the mapping of the flow field over the test surface in multiple positions, controlled by the operating software. The data acquisition was controlled with Dantec Dynamics commercial software, BSA Flow Software. The mean velocity and turbulent intensity data in x and y were sampled for 120 S at each location. Measurements were repeated twice for each coated surface to ensure repeatability.

Figure 6-4 FlowExplorer system of the Laser Doppler Velocimetry (LDV) used as experimental measurement technique in the present turbulence open channel flow study.

The probe volume typically spans a few millimeters in length, and light intensity modulation results from the interference between laser beams, forming parallel planes known as fringes. The fringe distance (df) is determined by the laser light wavelength and the angle between the beams. This angle impacts LDV measurements, influencing the depth of the measurement volume in the near-wall region. Decreasing the angle increases sensitivity to near-wall flows, improves spatial resolution, reduces measurement depth, and mitigates wall effects. The angle of the laser beams in Laser Doppler Velocimetry (LDV) can be adjusted using optical components such as lenses. In our setup, we utilized an optical lens with a 300 mm front focal length. This specific lens was chosen for its favourable range and performance compared to others available. Due to the lack of spatial resolution, the velocity profiles consistently increase with the wall-normal distance. As a result, the present setup was unable to capture measurements at distances less than 1 mm normal to the tested superhydrophobic (SH) surface.

6-3 Inlet measurements

The test surface was positioned 640 mm downstream from the diffuser in the center of the channel. Despite the pump's wide operating range with the variable frequency switch, numerous tests were conducted to prevent the formation of the waves and the wakes near the interface surface and to minimize their impact in both the streamwise and spanwise directions. The water depth in the experimental setup was kept at 130 mm using a sliding gate, and the LDV measurements at the test section entrance were conducted along the vertical Z direction. Further, LDV measurements were conducted in the spanwise (Y) direction at 55.5, 60.5 and 65.5 mm elevations after introducing the test surface to guarantee a uniform velocity distribution. These elevations were selected after confirming the approaching Reynolds number flows with no wake formations in the viscous layer starting from the channel bottom. The approaching Reynolds number is calculated based on a characteristic length of the hydraulic diameter, as follows:

$$Re = \frac{u_{avg} * D_h}{\nu} \tag{6-1}$$

u_{avg} is the averaged measured velocity, ν is the kinematic viscosity of the water (at 12 ˚C). The hydraulic diameter $D_h = \frac{d \cdot y}{2 \cdot z + d}$, where d is the channel width of 296 mm, and z is the high of the water depth, which is constant and equal to 130 mm. Although the pump has various operational ranges, certain flow rates can be used with the current geometry of the used open channel facility. The measurements were conducted to ascertain suitable operational parameters at varying approaching Re numbers of 30500, 33800, 34200, 41000, and 49000, respectively. The measurements were done before inserting the test surface into the test section location.

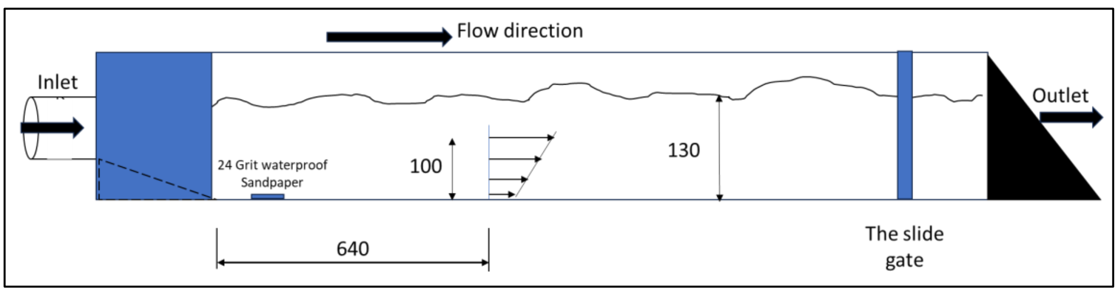

Figure 6-5 Schematic diagram of the inlet test section and measurement locations in the open channel facility, all dimensions in mm.

6-3-1 Inlet velocity measurements at different Reynolds Numbers

The region of interest would be 640 mm downstream in the X-direction, as shown in Fig. (6-5); at this point, the test surface will insert that to perform the measurements in a spanwise direction (Y-axis). The inlet velocity profiles were measured at X = 640 mm and Y =145 mm in the vertical Z direction for 100 mm from the channel bottom to avoid any wake or wave interface effect. Figure (6-6) presents all data measured using the mentioned

Re numbers. The experimental data were fitted and normalized to illustrate the velocity profiles at the entrance test section. The data were fitted with a power law to describe the velocity profiles within a fully developed turbulent boundary layer near a solid surface. The measurements showed that the fitted velocity profiles have a power range of $\frac{1}{4}$ th to $\frac{1}{6}$ th. However, it's important to note that the $\frac{1}{7}$ th power law is an approximation and may not be accurate in all situations. Turbulent boundary layers can exhibit variations due to surface roughness and flow conditions. Another tool has been used by dimensional analysis of the flow near a solid boundary to understand and analyze the turbulent flow, which is known as the Law of the Wall. The law of the wall is a fundamental principle in fluid dynamics that describes the behaviour of the velocity profile near a solid surface in a turbulent flow. It provides a mathematical relationship between the velocity of the fluid and the distance from the surface. It is conventing to define the shear or friction velocity u_τ, which equals [120][121]:

$$u_\tau = \left(\frac{\tau_w}{\rho}\right)^{\frac{1}{2}} \tag{6-2}$$

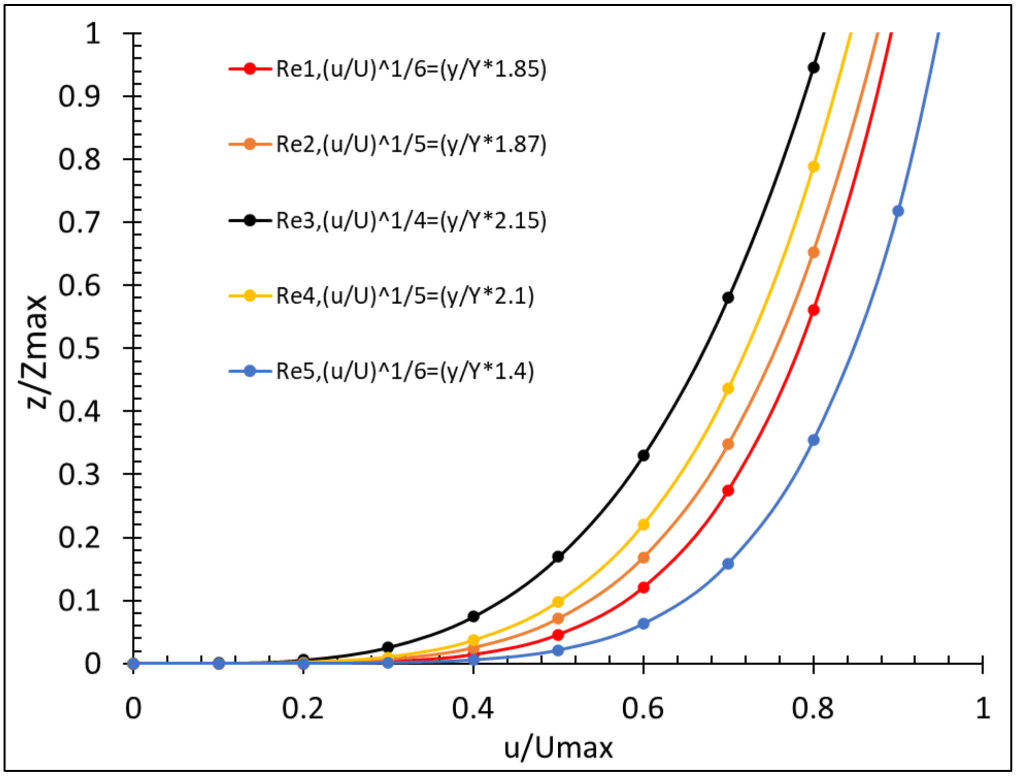

Figure 6-6 Normalized Inlet Velocity Profiles (power curve fitting of experimental data) at Different Approaching Re numbers

Where τ_w is the wall friction shear stress, and ρ the fluid density. The friction velocity u_τ can be determined experimentally as a fraction (˜10-20%) of the maximum mean velocity[120]. Then the dimensional analysis yields two dimensionless quantities, namely a dimensionless length and equal to [121]:

$$y^* = \frac{u_\tau * y}{\nu} \tag{6-3}$$

Where y is the vertical distance from the wall, and ν is the kinematic velocity. According to the coordinate system for our setup, y* will be in the Z direction for the inlet flow analysis. The second dimensionless quantity is a dimensionless velocity and is equal to [120][121]:

$$u^* = \frac{\overline{U}}{u_\tau} \tag{6-4}$$

Where $\overline{U}$ is the average of the measured velocity at y.

The logarithmic law of the wall provides a relationship between the velocity of the fluid and the distance from the wall within the logarithmic layer of the boundary layer. It is valid in the logarithmic region of the turbulent boundary layer, which is located above the viscous sublayer and below the outer region of the boundary layer. The law describes a logarithmic increase in velocity with distance from the wall, indicating that the velocity profile becomes less steep as the distance from the wall increases. It provides valuable insights into the distribution of velocities within turbulent boundary layers and is a fundamental component of the understanding of Turbulence in fluid dynamics. The logarithmic law of the wall is typically expressed as [120][121]:

$$\frac{u}{u^*} = \frac{1}{k}\ln\left(\frac{y * u^*}{\nu}\right) + C \tag{6-5}$$

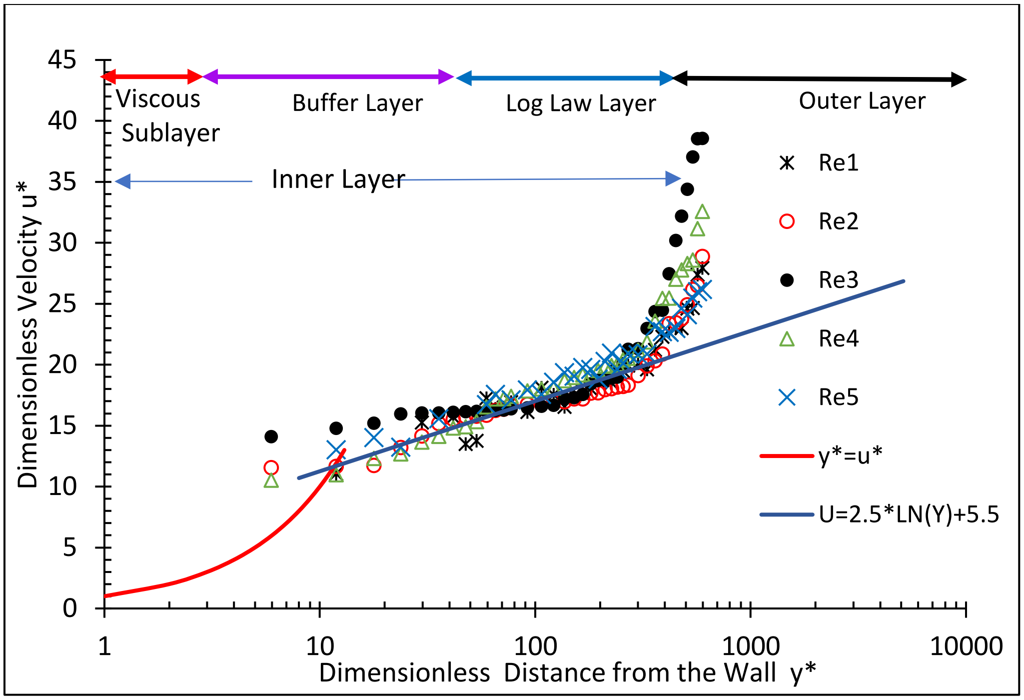

Figure 6-7 Linear and log law of the wall velocity profiles as a function of the dimensionless length y* (in vertical direction Z) at the inlet of the test section for Re numbers 30500, 33800, 34200, 41000, and 49000, respectively.

Where k is the Van-Kármán constant (=0.395 – 0.415), C is the smooth wall constant. The best numbers for these constants in the present case are 0.4 and 5.5, respectively[120][121]. The final form of the logarithmic law of the wall is:

$$\frac{u}{u^*} = 2.5\ln\left(\frac{y_* u^*}{\nu}\right) + 5.5 \tag{6-6}$$

a laminar flow near the wall will necessarily be a simple shear flow, which is defined as simple to:

$$u^* = y^* \tag{6-7}$$

Figure 6-7 shows the law of the wall velocity profiles. The Figure illustrates measurements conducted in the viscous sublayer, the log region, and the outer region of the flow for all

Re numbers. The system did not capture any details in the viscous sublayer since the seeding particles are very light and floating away from this layer. The law of the wall analysis determined the elevations of the lateral (spanwise) measurements. All elevations of the used Re numbers at 55.5, 60.5, and 65.5 mm above the channel bottom surface, and this avoids wake formation near the free surface.

6-3-2 Spanwise velocity measurements evaluation over the smooth surface at different Re Numbers

The test surface was designed to be inserted in the location where the flow fully turbulent developed, as shown in Figure 6-6. In order to investigate the uniformity of velocity distribution in the spanwise direction, three points were selected to conduct the measurements in the lateral direction, which were X_2, X_3, and X_4, as shown in Figure 6-3. The test surface is an acrylic plate with sharp leading and trailing edges, which is non-coated from our experimental work for this step. Three points at 130, 200 and 250 mm had been selected to investigate the uniformity of velocity profiles with all Re numbers used since the secondary boundary layer will generate over the test surface and the boundary layers on both sides of the open channel facility, as shown in Figure 6-8.

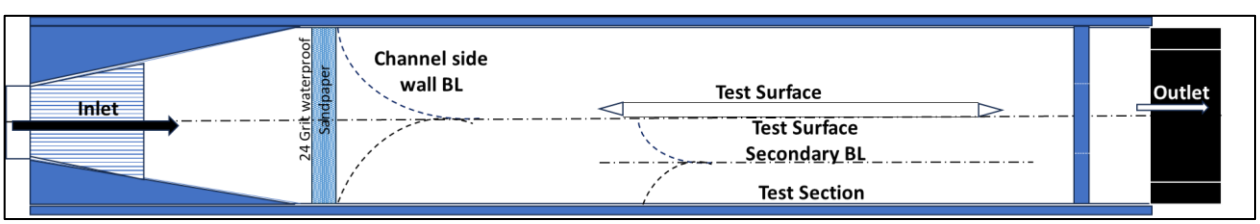

Figure 6-8 Schematic diagram of boundary layer development scenario over the test surface and the outer surfaces of the open channel

The velocity distribution and the boundary layer along the channel's side, determined from the inlet measurements, exhibit uniformity. Despite the flow's characteristic of having the highest velocity at the center of the channel width, coinciding with the test surface's location, several Reynolds numbers demonstrated a delay in the full development of the boundary layer on the uncoated test surface, as depicted in Figures 6-9 to 6-13. This delay is attributed to the constraints of the experimental setup utilized. Consequently, a range of Reynolds numbers was explored to identify a solution that addresses this non-uniform boundary layer development.

It is clear that the flow at Re number 34200 only shows a fully developed boundary layer on both sides of the test surface and side-channel wall, as illustrated in Figure 6-11. This operation condition is selected in this study, in addition to expanding the measurements in the spanwise direction from the leading edge at X_1 to the trailing edge at X_7.

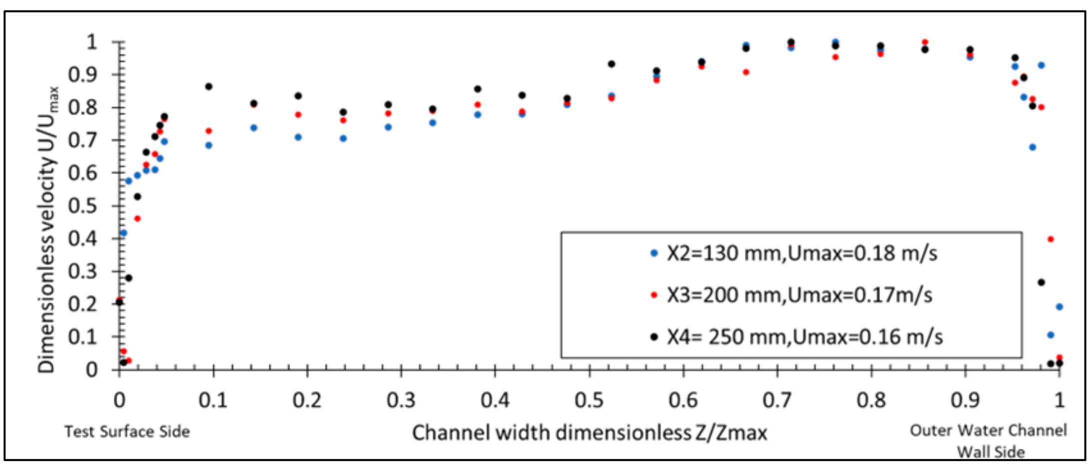

Figure 6-9 Normalized Velocity Profiles at Re number of 30500 measured at X_2, X_3 and X_4 locations.

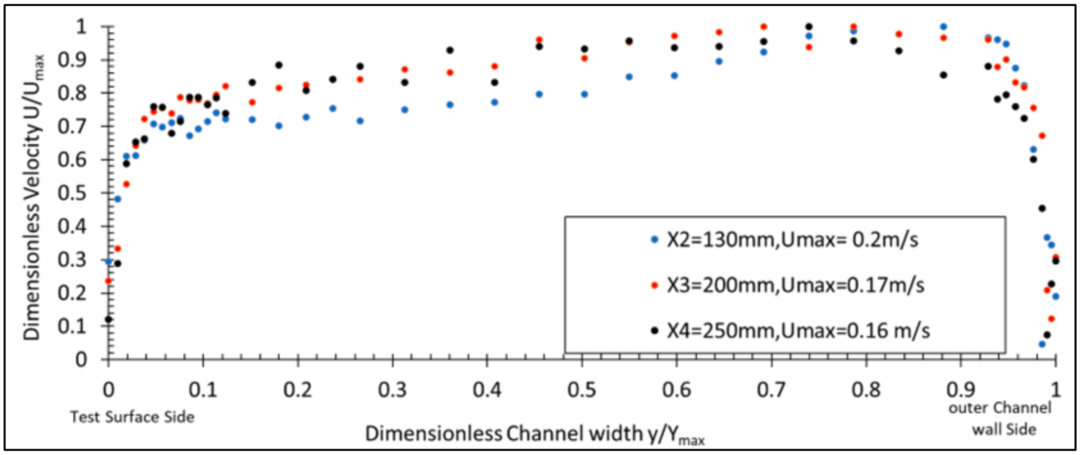

Figure 6-10 Normalized Velocity Profiles at Re number of 33800 measured at X_2, X_3 and X_4 locations.

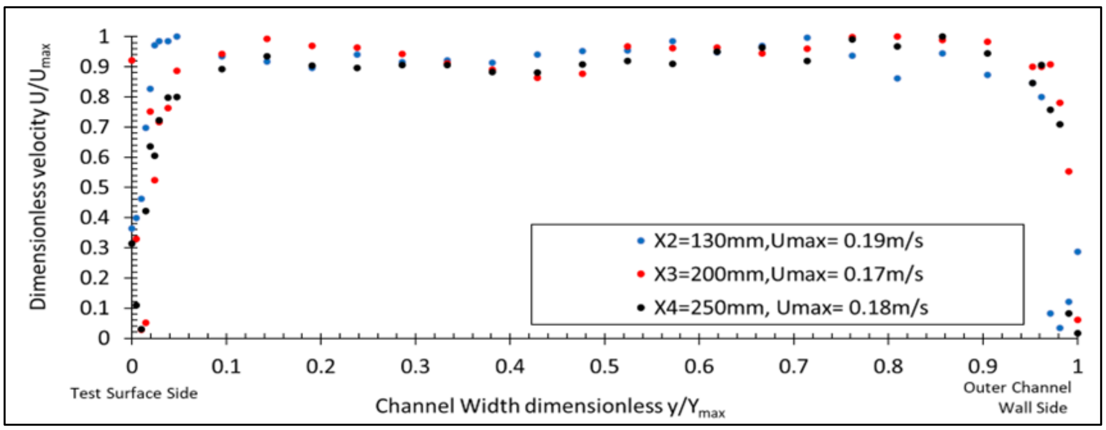

Figure 6-11 Normalized Velocity Profiles at Re number of 34200 measured at X_2, X_3 and X_4 locations

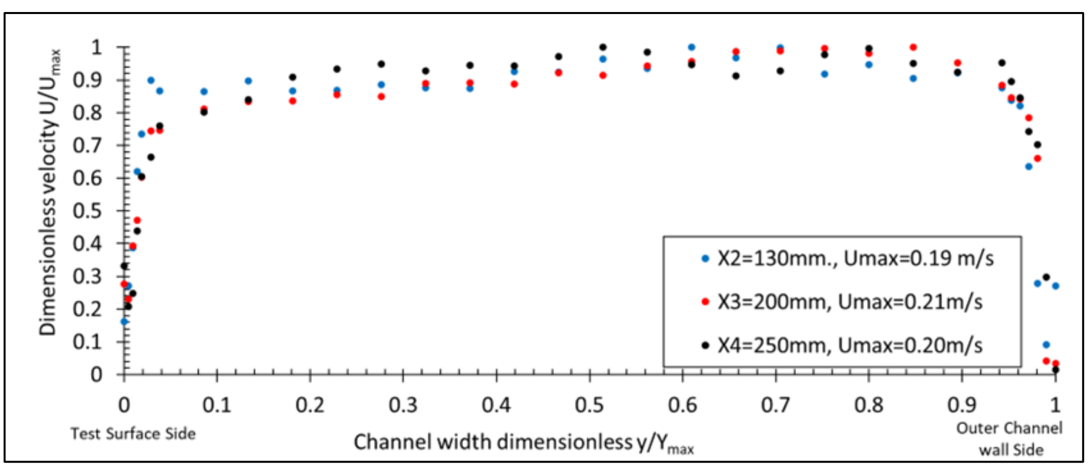

Figure 6-12 Normalized Velocity Profiles at Re number of 41000 measured

at X_2, X_3 and X_4 locations.

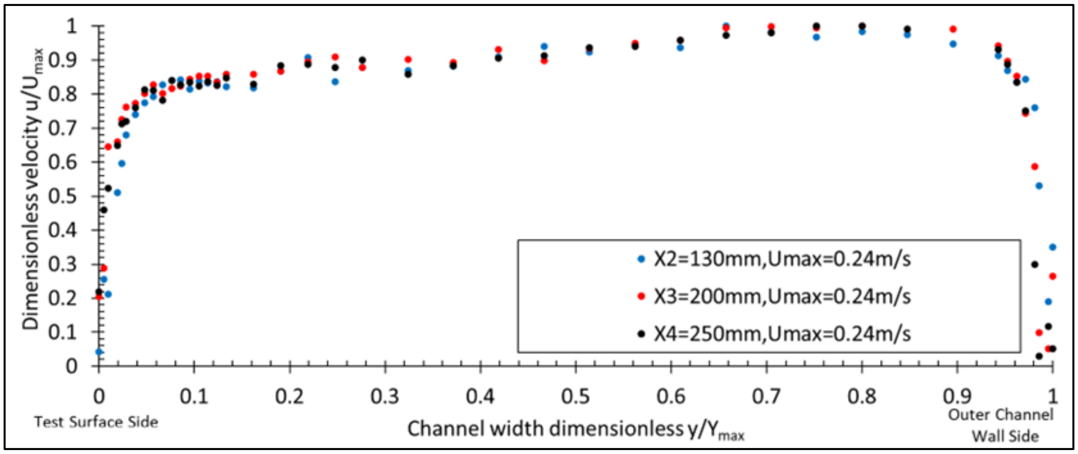

Figure 6-13 Normalized Velocity Profiles at Re number of 49000 measured at X_2, X_3 and X_4 locations

6-4 Uncertainty evaluation

This section outlines the evaluation of uncertainties in LDV measurements. Among the key error sources in LDV measurements, determining the frequency of each burst signal holds significant uncertainty. Furthermore, calculating the beam spacing introduces another substantial potential error source. Additionally, the sample size (N) influences the uncertainty in statistical measures. Yanta and Smith [122] as well as Schwarz et al. [123] established a technique for assessing uncertainty in LDV measurements. Tachie [124] and Faruque [125] developed and outlined this methodology. A 95 percent confidence level is assumed in the uncertainty analysis, and most of the interests include streamwise mean velocity, turbulence fluctuation and streamwise normal shear stress. To determine the uncertainty associated with different parameters, the subsequent relationships were applied:

The uncertainty in the streamwise component of the mean velocity:

$$\frac{\sigma_u}{U} = \left[(\sigma_o)^2 + \frac{1}{N}\left(\frac{u}{U}\right)^2\right]^{\frac{1}{2}} \tag{6-8}$$

The uncertainty in the streamwise components of turbulence fluctuation:

$$\frac{\sigma_u}{u} = \left[(\sigma_o)^2 \left(\frac{\langle uv\rangle}{u^2}\right)^2 + \frac{1}{2N}\right]^{\frac{1}{2}} \tag{6-9}$$

The corresponding expression for the streamwise normal shear stress are:

$$\frac{\sigma_{\langle uu\rangle}}{\langle uv\rangle} = \left[(\sigma_o)^2 \left(1 + \frac{u^2}{\langle uv\rangle}\right)^2 + \frac{1}{N}\left(\frac{2}{R}\right)^2\right]^{\frac{1}{2}} \tag{6-10}$$

Here σ_o is the error to uncertainty in the determination of the beam-crossing angle. Following [123], a value of 0.4 is considered for σ_o. N is the number of samples, and R is the shear stress correlation coefficient. The uncertainties for each surface used in this work and at the all seven measurement locations are illustrated in Appendix F.

6-5 Results & Discussion

6-5-1 Spanwise velocity measurements evaluation over superhydrophobic surfaces

The following section discusses the velocity profiles and the achieved drag ratio over the tested surfaces and at all seven measurement points. Compare these results and observe the performance of each surface at the same operating condition. The measurements were repeated twice to confirm the repeatability of the results, which found no change could be noticed. The measured streamwise mean velocities from the smooth and SH walls to the center of the channel after the test surface was inserted into the open channel at the selected location and normalized by the maximum velocity are shown in Figure (6-14). The experimental data are fitted to the power curves The Re number at all measurement locations is calculated based on the average bulk velocity and distance from the leading edge as the characteristic length, this gives 10250, 18600, 29000, 33000, 41000, 49500 and 58000, respectively. The velocity profiles exhibit different behaviours for all SH surfaces in comparison to the smooth surface, particularly in the near-wall region. The performance of the FPC-800M surface shows a high-velocity profile at all measurement points. The UED and FlouroThane-MW surfaces show heterogenic performance at all points. The increase in the mean velocity is likely due to the presence of the plastron layer interface and indicates that the SH surface has high-repellant water features. These features were maintained from the leading edge to trialling edge, most notably for the FPC-800M, more than the other two tested surfaces in the near wall region. The results from determining uncertainty estimates for all measurement locations and tested surfaces can be averaged for the mean streamwise velocity component. This average amounts to 0.4% of the positive U_m. Due to its small magnitude, it is not depicted as error bars in Figure (6-14).

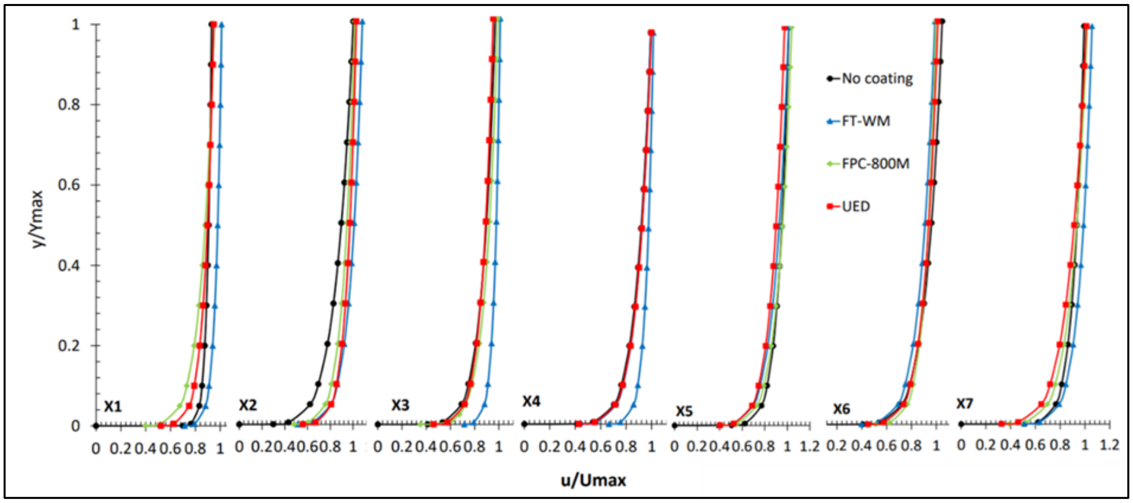

Figure 6-14 Mean streamwise velocity profiles over the smooth baseline and all SHS normalized by the corresponding maximum velocity; the fitted lines are only shown for clarity.

6-5-2 Turbulence over superhydrophobic surfaces

This section aims to study the effect of the SHS on turbulence intensity and Reynolds stress. Statistical characterization of the turbulent flow is presented over the superhydrophobic surface (denoted SHS) and the sharp edges acrylic test surface (denoted smooth). The velocity measurements in this work are used to understand the mechanism of the skin-friction reduction over SHSs and its effects on the achieved drag. The utilization of superhydrophobic surfaces in open channel flows has sparked significant attention because of its unique characteristics that impact turbulent intensity. Research has indicated that the efficiency of superhydrophobic surfaces in turbulent boundary layers depends on the combined and interactive anisotropic effects originating from surface geometry. The presence of an air layer and low surface energy creates slip effects that can considerably diminish surface drag in a turbulent flow. The root mean square (rms) of streamwise velocity fluctuation normalized with the mean velocity at seven different locations over the test surface.

The normalized turbulence intensities of the tested surfaces are plotted versus the normalized spanwise axis by the water depth; this shows a complete picture of the behaviour of each surface in both inner and outer flow regions in the global coordinates. All locations in the downstream direction show a good collapse of the turbulence intensity in the outer region, where the profile descends from a sharp peak, levels off, and then drops again to a minimum in the channel center. In the inner region, the tested smooth surface illustrates a burst of turbulence intensity in the early viscous sublayer near-wall region. In contrast, the fabricated SH surfaces exhibit higher turbulence intensity in the buffer layer.

In order to evaluate each surface turbulence structure in the near-wall region, the axes were rescaled by the average of the bulk mean velocity value at each measurement location as a function in the dimensionless wall distance y^+. This axis rescaling shows how the turbulence intensity of the fabricated surfaces is higher than the smooth surface, as shown in Figure (6-15). The turbulence intensities over SHS are high in y^* between 10 to 40; these high turbulence intensities are due to their ability to alter the flow dynamics at the surface-fluid interface. Moreover, the existence of a plastron layer within the surface textures can enhance turbulent mixing as the fluid traverses across them. The smooth surface at a distance of $y^* < 10$ showed some high turbulence intensities due to the irregularities and roughness of the surface texture, which disrupts the flow and leads to increased turbulence. It can be seen that the FT-MW surface shows a high turbulence intensity and decays at y^+, ranging between 40-50. The exhibited turbulence intensity by

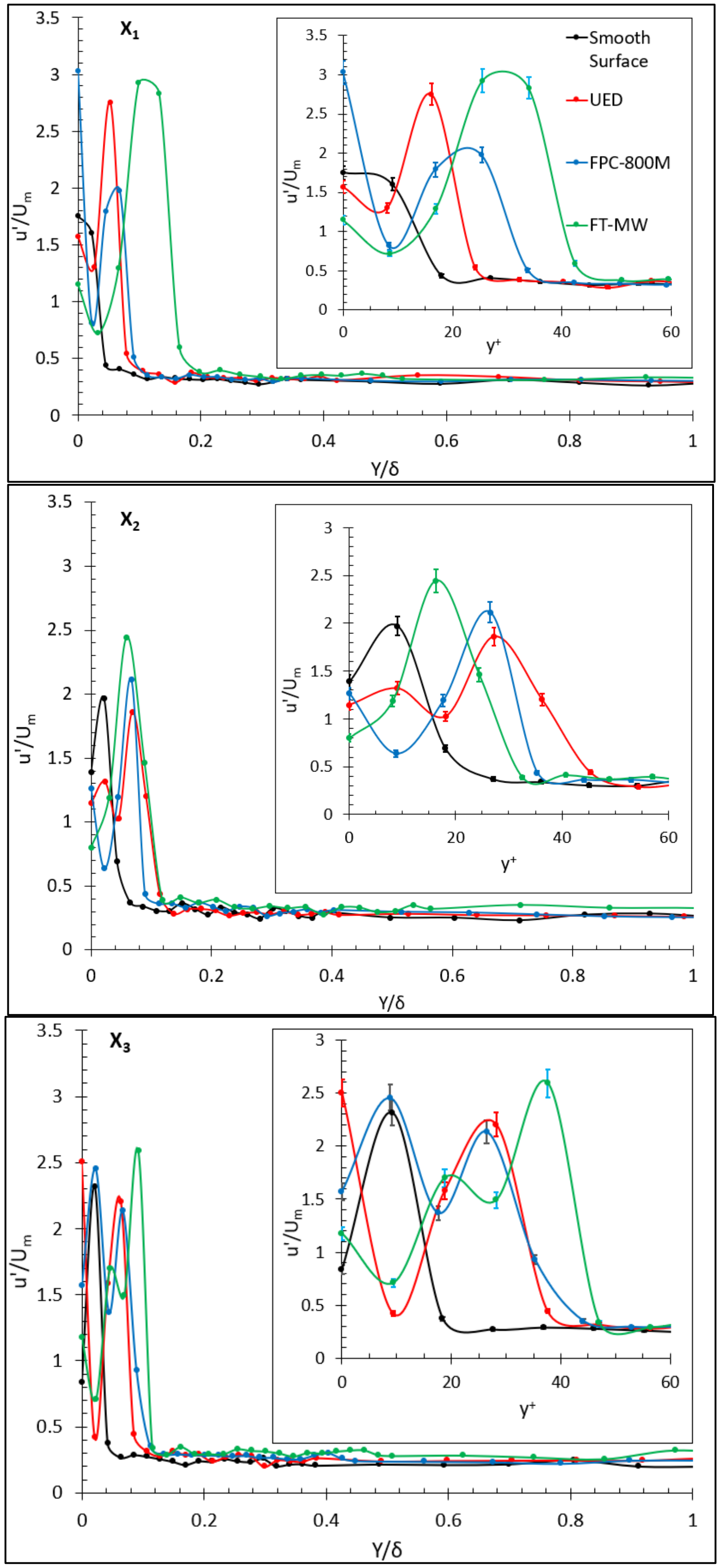

X1
u'/Um
Y/δ
Smooth Surface
UED
FPC-800M
FT-MW
y+
X2
X3

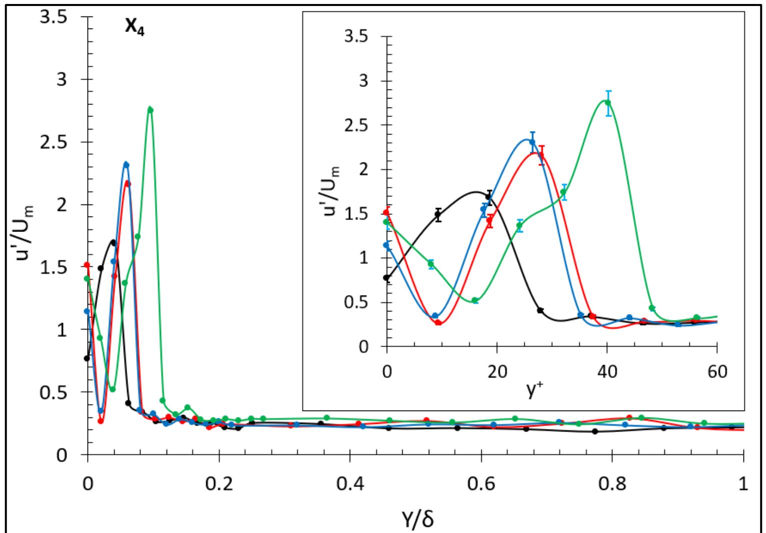
X4
u'/Um
Y/δ
u'/Um
y+

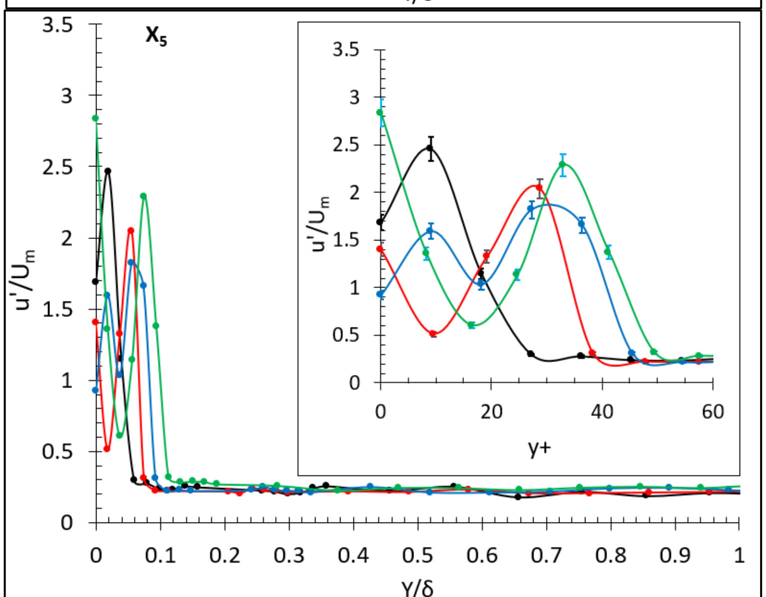
X5
u'/Um
Y/δ
u'/Um
y+

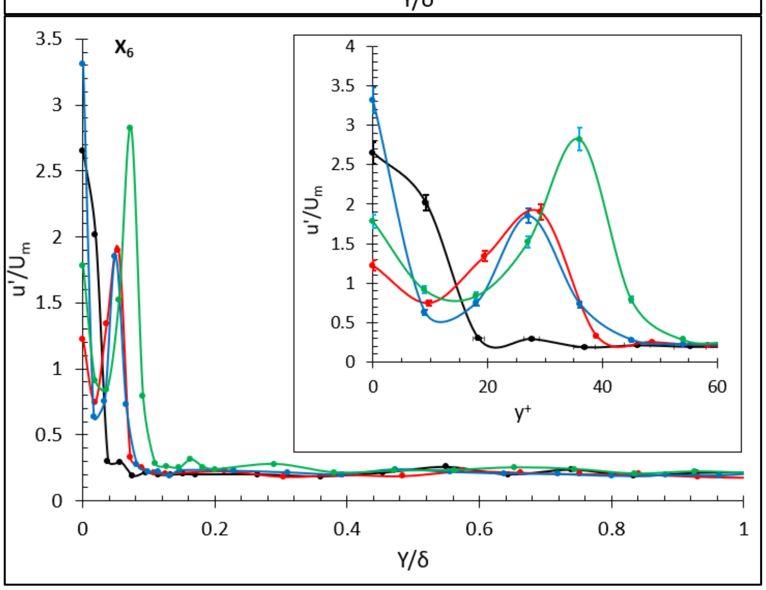
X6
u'/Um
Y/δ
u'/Um
y+

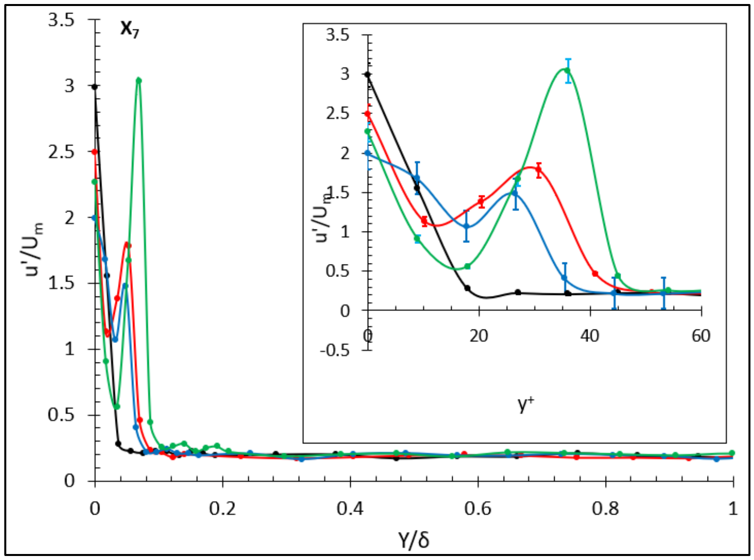

Figure 6-15 The turbulence intensity at all measurement planes from X_1 to X_7 on the tested surfaces, including the smooth baseline and three superhydrophobic coatings; the insert figure is a zoom-in near-wall region for each measurement plane. The error bar for the bar for the uncertainty is calculated based on equation (6-9)

the UED and FPC-800M surfaces is higher than the smooth surface. The plots presented the first measured point for the fabricated surfaces 0.5 mm from the smooth baseline surface.

The streamwise component of normal Reynolds stress $\frac{\grave{u}\grave{u}}{U_m}$ obtained from the LDV measurements and shown in Figure (6-16) to evaluate its distribution across the mid-channel. The streamwise normal shear stress in the global coordinates shows a good collapse in the near wall region, as shown in Figure (6-16). Using all tested surfaces, the outer region presents almost zero value for all seven measurement locations, which confirms the fully developed state of the turbulent channel flow. But the zoom-in near wall region coordinates show that the SH surfaces have a high variation for the streamwise normal shear stress ($\frac{\grave{u}\grave{u}}{u_\tau}$) compared to the smooth baseline surface, and the peak occurs in the early buffer region. The peak value of streamwise normal shear stress also indicates the skin-friction drag [126][127], and its high values over the fabricated tested SH surfaces indicate the drag reduction achieved. The zoom-in streamwise normal shear stress profiles of SH surfaces maintain this high variation at all measurement locations except the last location (X_7) when the streamwise normal shear stress starts to decay after the peak immediately and shows a trend less than the smooth baseline surface. The latter decreases gradually from the SHS value to that of the smooth baseline wall as the boundary layer develops with a streamwise distance. Many previous studies interpreted that the level of the increase in the streamwise normal shear stress depends on the relative roughness of the SHS, as discussed by [32] and [126]. These observations should presumably refer to the height of the SCA (θ_s) and its effects on the air layer thickness since the SCA and the DCA measurements showed these variations, as discussed earlier. The observed increase in the streamwise normal shear stress in the near wall region over the fabricated SH surfaces is consistent with recent numerical simulations [128] and [129]. The collapse of the streamwise normal shear stress in the outer region of the log layer is also consistent with the boundary layer being under fully developed flow conditions.

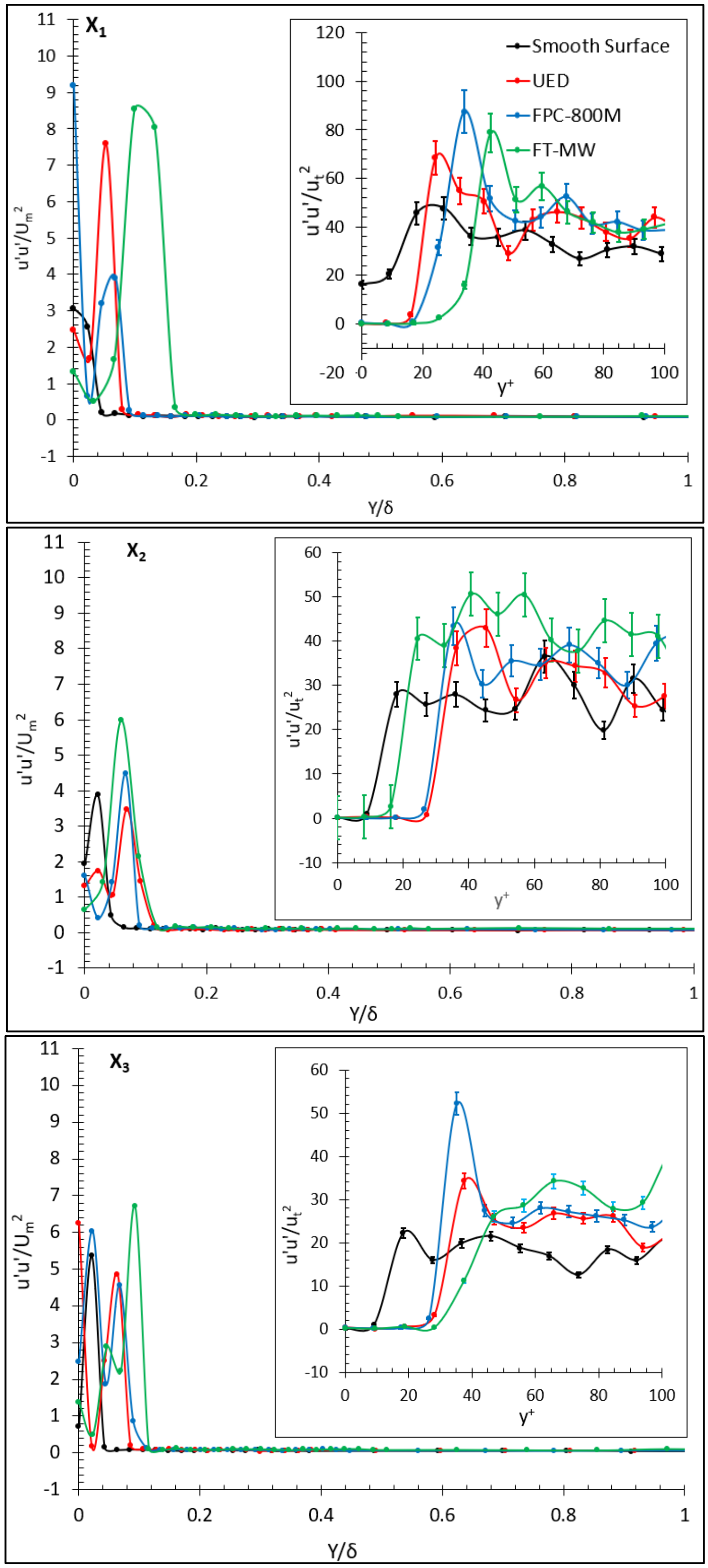
X1
X2
X3
Smooth Surface
UED
FPC-800M
FT-MW
u'u'/U_m^2
u'u'/u_t^2
Y/δ
y+

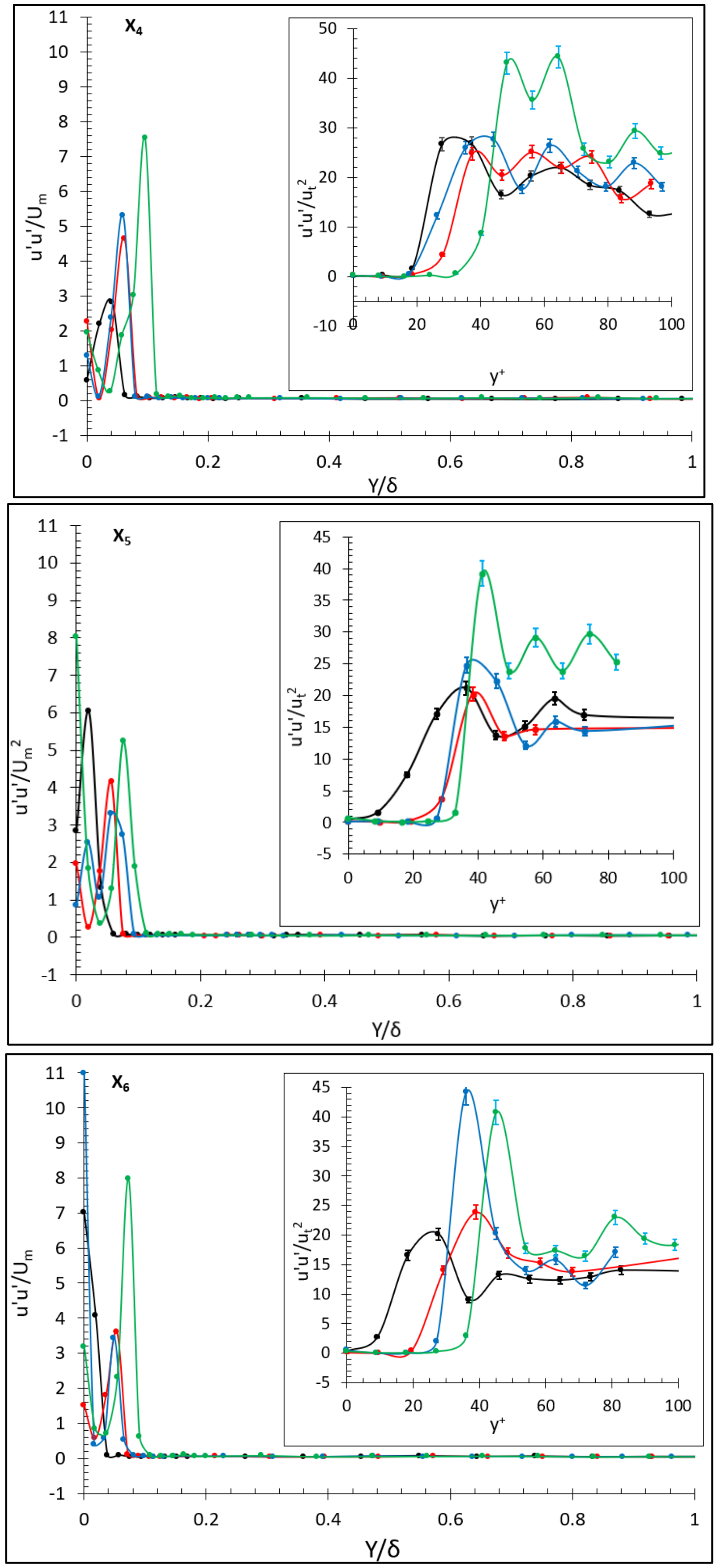
X4
u'u'/U_m
Y/δ
u'u'/u_t^2
y+
X5
u'u'/U_m^2
Y/δ
u'u'/u_t^2
y+
X6
u'u'/U_m
Y/δ
u'u'/u_t^2
y+

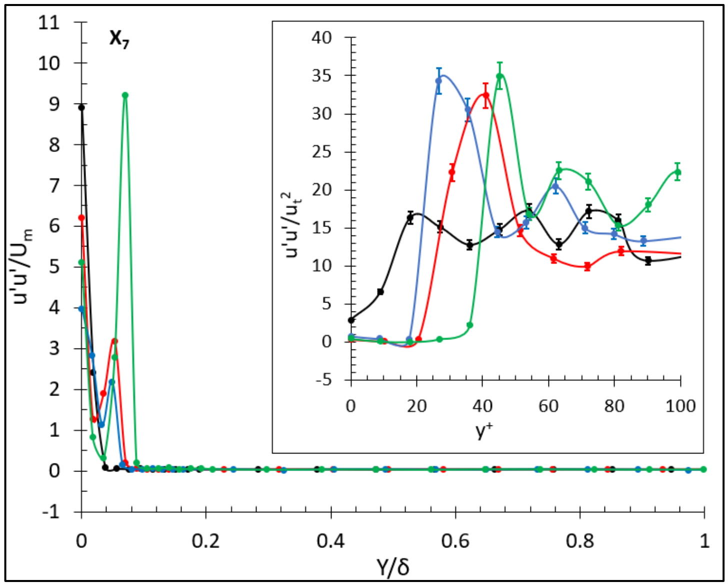

Figure 6-16 The streamwise normal shear stress (SNSS) normalized by the average velocity at all measurement planes from X_1 to X_7 on the tested surfaces, including the smooth baseline and three superhydrophobic coatings; the insert figure is a zoom-in near-wall region for each measurement plane, and the SNSS normalized using friction velocity. The error bar for the uncertainty is calculated based on equation (6-10)

6-5-3 The Achieved drag estimation over various superhydrophobic surfaces

The wall shear stresses at the seven measurement locations of all tested surfaces are calculated based on equation (6-2) and illustrated in Figure (6-17). It can be seen that the FPC-800M surface shows low wall shear stress (τ_ω) compared with the smooth baseline surface, and it maintains this low τ_ω from leading to the trailing edge. The UED surface has a maximum low (τ_ω) near the leading edge, this difference gradually decreases, and the wall shear stress becomes greater than the smooth baseline surface at the trailing edge at locations X_6 and X_7. The interpretation of this τ_ω increasing at the trailing edge refers to losing the air layer and increasing the roughness of the tested surfaces. The FT-MW shows low (τ_ω) at the first half of the tested wall and after the center, a significantly high τ_ω and to be greater than that of a smooth baseline surface in the second half to the trailing edge.

The FT-MW surface lost the air layer, which is the lubricator, and its roughness plays the main role in increasing the shear stress (τ_{ω}).

According to the wall shear stress (τ_{ω}) over the tested surfaces in Figure (6-17), the drag reduction rate ($DR\%$) can be calculated in this study using the following formula for all measurement locations and each fabricated SH surface[61];

$$DR\% = \frac{\tau_{\omega(Sm)} - \tau_{\omega(Sh)}}{\tau_{\omega(Sm)}} \times 100 \tag{6-11}$$

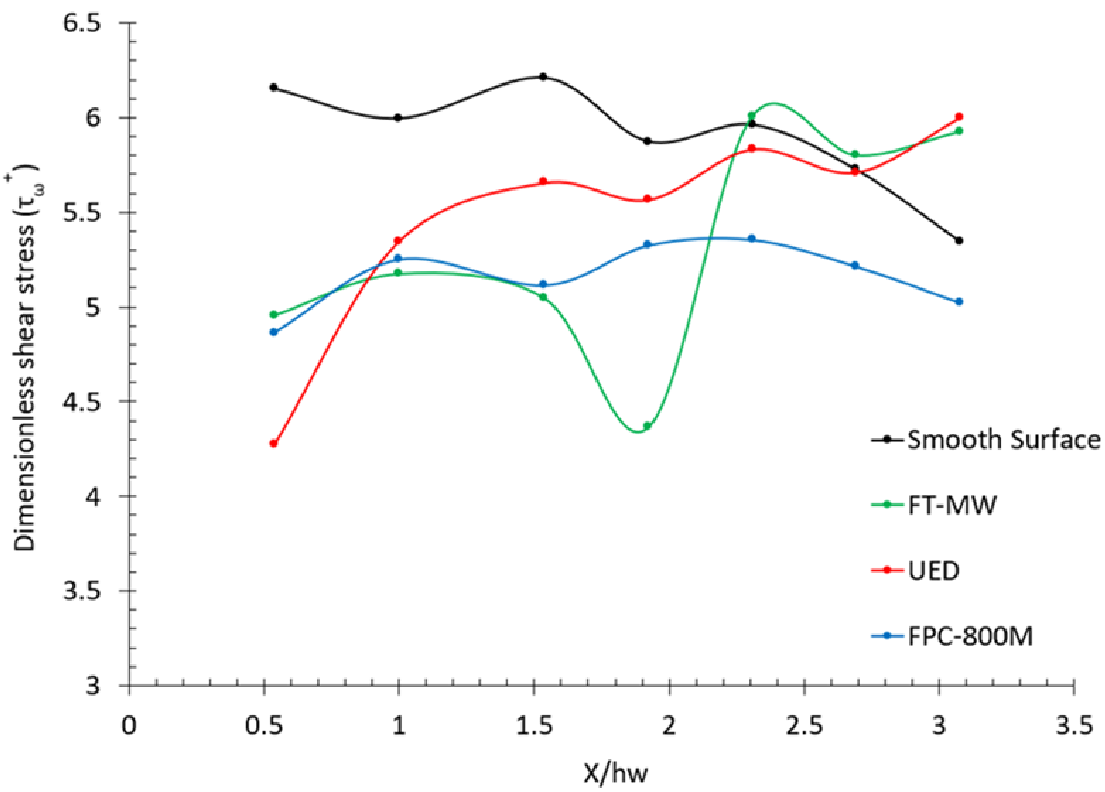

Figure 6-17 The measured shear stress along streamwise direction for each tested surface

Where $\tau_{\omega(Sm)}$ and $\tau_{\omega(Sh)}$ are the wall shear stress of the smooth baseline surface and the tested superhydrophobic surfaces, respectively. The FPC-800M shows acceptable consistency and low shear stress along the test surface, but the UED gradually decreases, while the FlouroThane-MW shows a sharp decrease in the shear stress after X_4. The drag reduction is consistent with the shear stress results, as illustrated in Figure (6-18), and it can be seen that the FPC-800M shows a drag reduction at all measurement planes in a streamwise direction. The UED surface shows a high drag reduction ratio at the leading edge of 31% that gradually decreases, resulting in a drag enhancement with a ratio of -15%. The FT-MW shows a divergent drag reduction performance from the leading edge to the center with a maximum ratio of 23%, followed by sudden drag enhancement in the second half of the tested surface to the trailing edge.

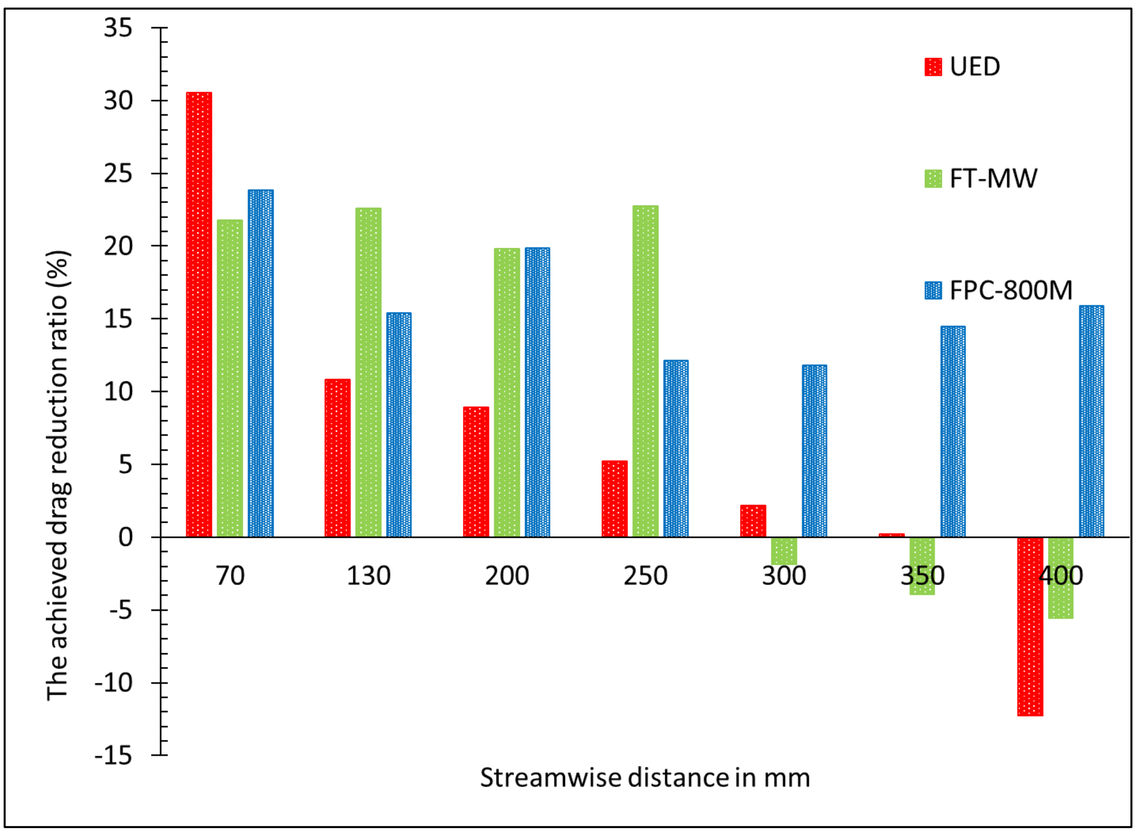

Figure 6-18 The achieved drag over all tested surfaces

6-6 Summary

In the present work, hydrodynamic drag reduction of large-area superhydrophobic sharp-edge flat plates was experimentally studied using a single approaching flow speed that cover the flows from leading to the trailing edge. Unlike previous studies that mainly focused on one plane over the tested surface, the experiments covered a broad range of flow planes at seven locations in streamwise and spanwise directions. Moreover, while previous studies were mainly performed on internal flows (e.g., channel flows), the current study has been performed in the category of external flows (boundary layer flows) covering full-turbulence regimes, which raised doubts about the drag reduction capabilities and sustainability of superhydrophobic surfaces. The outcomes unequivocally validate that superhydrophobic (SH) surfaces effectively reduce viscous drag in turbulent flows, showcasing an average reduction of 18% for FPC-800M, 11% for FT-MW, and 8% for UED. The findings indicate greater drag reduction in the turbulent boundary layer is achieved with a superhydrophobic surface exhibiting elevated static and dynamic contact angles. The fabricated superhydrophobic (SH) surfaces led to reductions observed in streamwise and spanwise turbulence intensity and the streamwise normal shear stress. These suppressions were prominent in the near-wall region, where their influence extended. Notably, the Reynolds stresses in streamwise and spanwise directions surpassed the no-slip surface within this region. However, as one moves away from the wall, the suppressions in Reynolds stresses diminish, signifying turbulence attenuation and the attainment of fully developed flow. The observations concerning all the surfaces tested raise inquiries regarding the achieved slip velocity and slip length and the interpretation of the observed scenarios. Additionally, there is a need to understand the factors contributing to the drag enhancement at the trailing edge of the tested surfaces that exhibited this scenario.

CHAPTER VII

Chapter 7 Assessing Theoretical Slip Length Prediction Model on Superhydrophobic Surfaces in Open Channel Flow

This chapter evaluates the theoretical prediction model to calculate the slip velocity and slip length over various superhydrophobic surfaces. The main content of this chapter has been submitted as a part of (Alsharief, A. F. A., Duan, X., Nyantekyi-Kwakye, B. & Muzychka, Y. (2023). "An experimental investigation of the impact of anisotropic slip-length boundary conditions on turbulent flow over superhydrophobic surfaces within an open channel". Physics of Fluids Journal, AIP. The author of this thesis is the first author of this paper. The first author conducted the experiments, analyzed the data, and prepared the manuscript. Prof. Duan, Prof. Nyantekyi-Kwakye and Prof. Muzychka, as the second, third and fourth authors, provided their suggestions on experimental observation, data analysis and revision of this paper.

7.1 Introduction

In superhydrophobicity, the surface is characterized by a combination of microscale or nanoscale roughness and low surface energy, which can lead to a thin layer of air (plastron) trapped between the liquid and the surface. This trapped air layer reduces the solid-liquid contact area and enhances the slipperiness over the fabricated surface. Increasing the plastron thickness leads to improved slip velocity and, correspondingly, provides a reduction in friction. The slip velocity is a phenomenon where the fluid near the superhydrophobic surface exhibits reduced resistance or slippage compared to the bulk fluid. Rare studies were conducted to measure and calculate the slip velocity, as mentioned in Table 2-2. Many techniques used to measure slip velocity involved assessing the speed difference between the fluid in contact with the superhydrophobic surface and the free-flowing bulk fluid. The slip velocity was calculated based on Navier's definition of the slip velocity, as mentioned in earlier chapters.

The slip length is a characteristic parameter that describes the slipperiness of a fluid-solid interface. It represents the distance over which a fluid slips past a solid surface before reaching the no-slip condition, where the fluid velocity matches the velocity of the solid surface. In other words, it quantifies the extent to which a fluid can slide along a solid surface without experiencing significant viscous resistance. Determining the slip length experimentally can be challenging, but that depends on the measured slip velocity, as explained in the literature [49, 52, 60, 61].

A theoretical prediction model of friction drag reduction in turbulent flow by superhydrophobic surfaces was suggested by Fukagata, Kasagi and Koumoutsakos [130] and used in this work to calculate the slip velocity over the tested SHSs. While significant research efforts have been dedicated to understanding drag reduction in laminar flows, the effects induced by hydrophobic surfaces on turbulent flow were poorly understood until the early direct numerical simulation "DNS" performed by Min and Kim [131]. By analyzing turbulence statistics and vorticity patterns, they identified the fundamental physical mechanisms linked to changes in drag. However, the available computational capabilities in current technology, expanding direct numerical simulation (DNS) to high Reynolds numbers suitable for real-world applications, exceeds the computational cost. This highlights the necessity to derive a formula that can forecast the drag reduction efficiency achieved with a specific slip length across various Reynolds numbers. The concept presented by Fukagata, Kasagi, and Koumoutsakos [130] builds upon the drag augmentation/attenuation mechanisms introduced by Min and Kim [131].

This study will use this concept to calculate the slip velocity over the tested SHSs in the open channel flow using the data collected by the LDV measurements, which allows us to predict the anisotropic slip length conditions combined with the achieved drag reduction investigated in the previous chapter.

7.2 Slip Velocity Theoretical Prediction Model

The theoretical predicted model of Fukagata, Kasagi, and Koumoutsakos [130] focuses solely on the streamwise slip, i.e., ($\boldsymbol{b}$ = 0). In terms of slip flow's wall units, the average slip velocity ($\boldsymbol{u_s}$)is represented as follows:

$$u_s^+ = b^+ \frac{du^+}{dy^+} |_{wall} \tag{7-1}$$

According to its definition, the mean wall shear in wall units consistently equals one. Hence, the relationship between $\boldsymbol{u_s}$ and $\boldsymbol{b}$ can be expressed as follows:

$$u_s^+ = b^+ \tag{7-2}$$

The normal velocity gradient at the measurement locations is calculated by dividing the measured ($\boldsymbol{\tau_\omega}$) by the known water viscosity [55]. As shown in Figure 7-1, the mean velocity profile of the slip flow, characterized by a bulk mean velocity of ($\boldsymbol{U_b}$), can be envisioned as a combination of ($\boldsymbol{u_s}$) and the velocity profile of a no-slip flow at a reduced or effective bulk mean velocity, ($\boldsymbol{U_{be}}$). The slip velocity ($\boldsymbol{u_s}$) is calculated based on the approach suggested by Fukagata et al. [55], and by using the present formula:

$$u_s = U_b - U_{be} \tag{7-3}$$

where $\boldsymbol{U_b}$ is the bulk mean velocity of the flow for the smooth baseline surface, and $\boldsymbol{U_{be}}$ is the bulk mean velocity of the flow for the superhydrophobic surface.

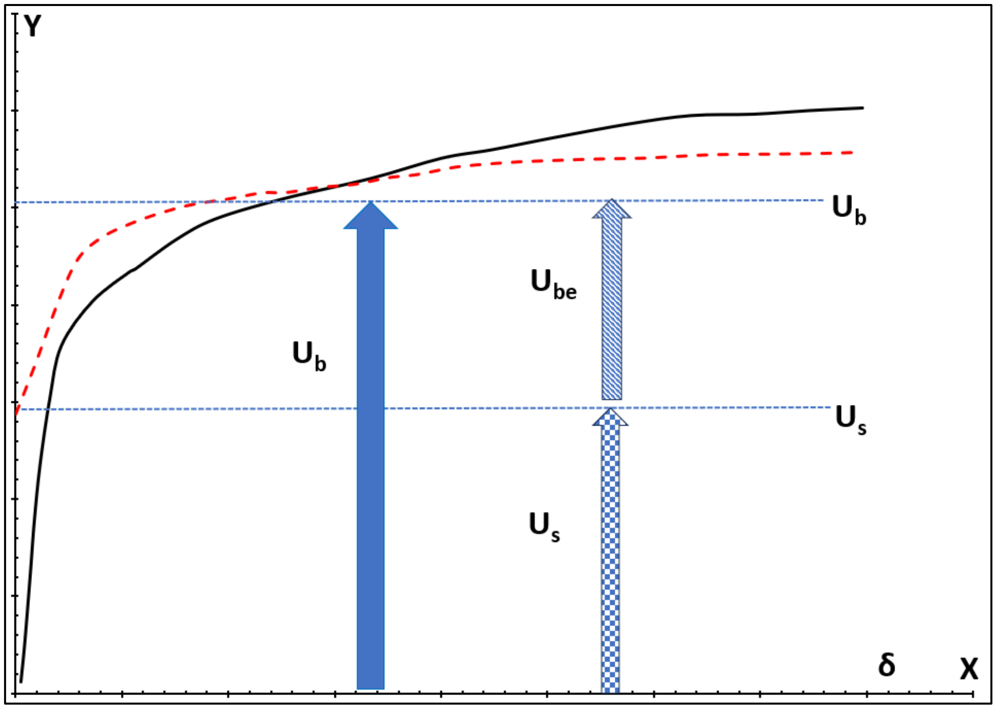

Figure 7-1 Schematics of the drag decrease mechanism and the effective bulk mean velocity (U_{be}) and δ is the boundary layer thickness (adopted from [130])

7.3 Slip Length Calculations

In superhydrophobic surfaces, for example, microstructures or textures can create an air layer (plastron) between the liquid and the surface, reducing friction. This reduced friction is often quantified through an effective slip length, which is a parameter that characterizes how much the flow behaves as if there is slippage at the surface. It is interesting to understand the drag reduction demonstrated for all measurement locations of all tested surfaces in terms of an effective slip length (b). The effective slip length b for a superhydrophobic surface is given by Navier's hypothesis as follows:

$$b = \frac{u_s}{\frac{du}{dy}|_{s=0}} \tag{7-4}$$

Where ($\boldsymbol{u_s}$) is the slip velocity and $\frac{du}{dy}|_{s=0}$ is the normal velocity gradient evaluated at the superhydrophobic surface. The wall shear stresses at the seven measurement locations of all tested surfaces are calculated based on equation 6-2 and illustrated in Figure 6-17. The effective slip length (b) relates the slip velocity at the surface to the shear stress at the surface. It's used in mathematical models to describe how fluid flows over such modified surfaces and how the presence of texture or microstructures influences the overall drag and flow behaviour.

7.4 Results and Discussion

Based on the discussion of Figure 6-17 and as illustrated in the dimensionless Figure 7-2, the FPC-800M surface shows low wall shear stress (τ_ω) compared with the smooth baseline surface, and it maintains this low τ_ω from leading to the trailing edge. The UED surface has the lowest (τ_ω) near the leading edge; this difference gradually decreases, and the wall shear stress becomes greater than the smooth baseline surface at the trailing edge. The interpretation of this τ_ω increasing at the trailing edge refers to losing the air layer and increasing the roughness of the tested surfaces. The FT-MW shows low (τ_ω) at the first half of the tested wall and, after the center, a significantly high τ_ω and to be greater than that of a smooth baseline surface in the second half to the trailing edge. The FT-MW surface lost the air layer, which is the lubricator, and its roughness plays the main role in increasing the shear stress (τ_ω). The calculated slip velocity based on equation 7-3 is presented in Table 7-1.

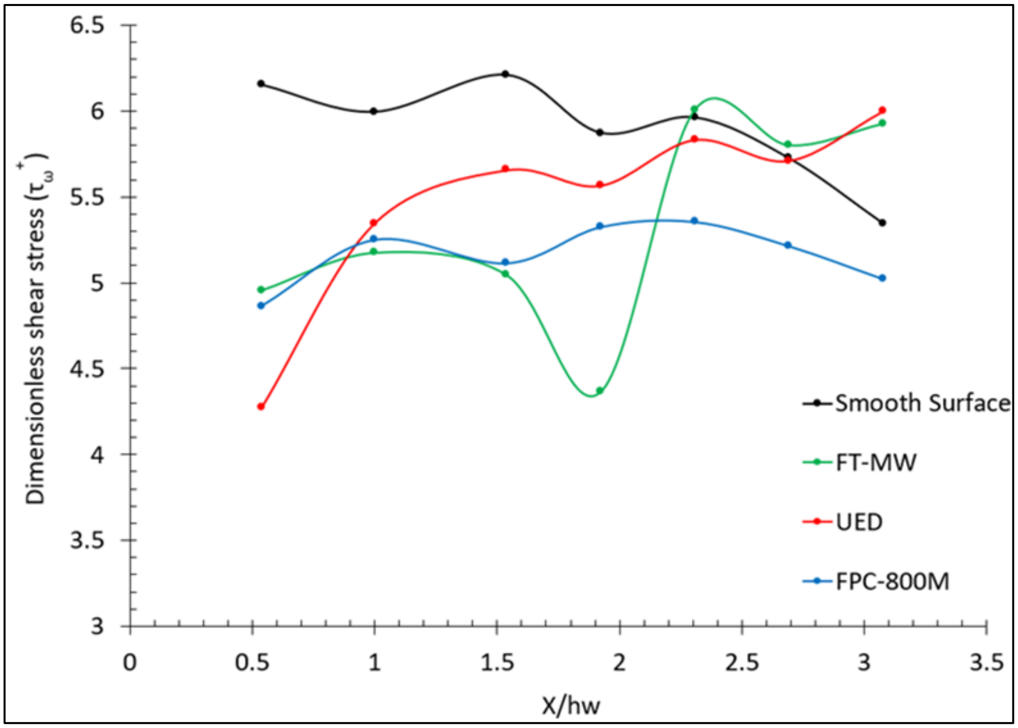

Figure 7-2 The measured shear stress along a streamwise direction for each tested surface

Table 3-1 The calculated streamwise slip velocity using equation (7-3) over the fabricated SH surfaces.

	UED	FPC-800M	FT-MW
X1	0.028	0.028	0.021
X2	0.016	0.018	0.02
X3	0.011	0.028	0.019
X4	0.008	0.012	0.019
X5	0.008	0.012	-0.0005
X6	0.003	0.016	-0.0009
X7	-0.002	0.015	-0.001

It can be seen that the slip velocity starts high for all tested surfaces and decreases in the streamwise direction. The FPC-800M maintains positive values and decreases gradually to the last location, and the UED has a similar trend till the last location, which has negative slip velocity. A similar trend for the FT-MW surface with the last three locations, and these negative values are not true physically. Figure (7-3) presents the slip length calculated at all locations for all tested surfaces in the present work. There is a strong correlation between the slip length and the wall shear stress (τ_{ω}) across all surfaces that were tested. Furthermore, the locations where a negative slip velocity is observed exhibit a negative slip length on the same scale as the coating thickness of commercially available brands, as confirmed in our prior research [132].

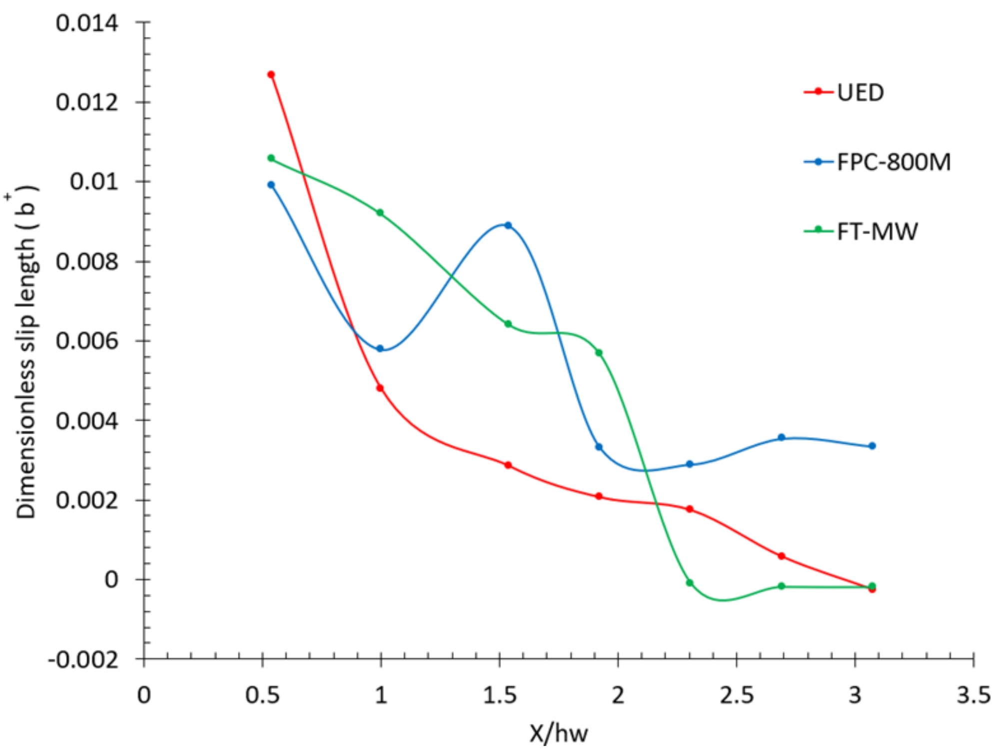

Figure 7-3 The slip length over all tested SH surfaces in the flow direction, which presented as positive values, The negative values presented for the SH surface thickness.

7.5 Summary

In Chapter 7, a proposed theoretical predicted model by Fukagata, Kasagi, and Koumoutsakos [2006] has been introduced and calibrated using the present experimental data. This model assumes that significant drag reduction can be achieved using a hydrophobic surface even at Reynolds numbers within the practical range of 10^5 to 10^6, which induces a slip length on the order of ten wall units or more using direct numerical simulation data and shows good agreement. The model used in the current work to predict the slip velocity near the wall of the fabricated superhydrophobic surfaces and the achieved slip length is based on the Navier hypothesis. The slip velocity was calculated and showed 10% to 15% of the maximum velocity with negative values in regions where the measurements showed drag enhancement. The slip length results showed identical agreement compared to the shear stress measurements. The high values of the slip length are calculated near the leading edge. For the FPC-800M surface, maintain the slip length with a slight decrease to the trailing edge with average slip length of 275 μm. The FT-MW surface achieved a high constant slip length till the center of the tested surface, then decayed to the order of the coating layer thickness of 10 μm. The UED surface showed the highest slip length among the tested surfaces at the leading edge of ~ 500 μm. The slip length gradually decreased till the last tested location, X_7, when it became in order of 10 μm and close to the coating layer thickness. These results agree with the discussed drag reduction in Chapte 6, highlighting the importance of investigastion of the plastron layer over superhydrophobic surfaces.

CHAPTER VIII

Chapter 8 Conclusions and Recommendations for Further Work

This chapter summarizes the key discoveries from Chapters 4-7 and provides an overview of the accomplishments presented in this Ph.D. thesis. The content is organized to align with the information presented in the corresponding chapters. Additionally, a section discusses potential directions for future research that upcoming researchers may pursue.

8.1 Conclusion

8.1.1 Conclusion of Taylor-Couette Flow Study

This study seeks to assess how changes in surface wettability impact the effectiveness of drag reduction in a Taylor–Couette flow cell, involving nine differently coated CDC samples. This analysis also encompasses an examination of surface morphology, coating layer thickness, contact angles, and flow experiments. The sample surfaces were created using three superhydrophobic (SH) coatings through dip and spin techniques. Various liquids, including water and silicon oils, were used to test these fabricated surfaces. The SEM images revealed that surfaces coated with FPC-800M and SHBC exhibited a nanoporous sponge-like structure, whereas the UED-coated surface did not provide valuable morphology information. The coating thickness of all samples fell within the 4–27 μm range. UED-coated samples were positioned in the middle of this range, while SHBC-coated samples displayed the highest thickness, averaging 20 μm. Moreover, This research focuses on the experimental and statistical exploration of the relationship between plastron thickness and slip length over the prepared three superhydrophobic surfaces (SHSs). conducted at a maximum Reynolds number of 1227 for water, 475 for 5 cSt silicone oil, and 250 for 10 cSt silicone oil. The study involved the measurement of θ_s, θ_{adv} and contact angle hysteresis CAH. The main findings and objectives accomplished in this thesis can be summarized as follows:

- Despite minor variations among the tested surfaces, the UED demonstrated the highest static and advanced dynamic contact angles. The used TC cell showed limited turbulence due to its high radius ratio of 0.92, which enabled the flow structure phase diagram to reach the MWVF region at a high rotational speed provided by the rheometer before entering the TTVF region.
- A modified version of the Prandtl–von Kármán skin friction law was developed by applying boundary layer (angular momentum defect) theory to turbulent TC flow. The study allowed for the determination of an effective slip length, "b", that describes the non-wetting behaviour of superhydrophobic surfaces (SHS) on the outer wall of the TC cell used in WVF and MWVF regions. The results demonstrate that even though super hydrophobic surfaces typically exhibit effective slip lengths of only a few micrometres, they are capable of reducing skin friction in the early turbulent stages (WVT-MWVT) flows.
- A slippage viscous model is used to calculate the plastron thickness at each Reynolds number for all tested SHSs. The comparisons of all the measurement data show a clear relationship between the plastron thickness and the slip length; the UED surface has the highest values of $\delta +$ and $b +$ among the tested surfaces.
- The attainable drag reduction in TC flows with the three fabricated SHSs is in the range of 7 to 11%.

- The UED surfaces showed poor wettability for water, with a high SCA (158 deg) and a low CAH (1 deg). The 5 and 10 cSt silicone oils have very close surface tensions, and both showed convergent characteristics using all fabricated surfaces. FPC800M and UED surfaces showed oleophilic behaviour for the 5 cSt silicone oil, while SHBC exhibited superoleophilic properties for silicone oil of 10 cSt, with low Θ_s (of 13 deg).
- The results showed no coating thickness effects on the achieved drag reduction. Although the UED surfaces (with a 15.5 µm average coating thickness) showed the highest maximum drag reduction for all tested liquids, the FPC800M surfaces (with a 4.5 µm average thickness) exhibited a high average drag reduction. In comparison, low drag reduction was observed using all SHBC surfaces (with 20.2 µm average coating thickness).
- Despite the common use of the static contact angle (Θ_s) to describe the wetting degree, the advancing contact angle (Θ_{adv}) measurements clearly correlate with the achieved drag reduction in water flows. The UED surface had the highest (Θ_{adv}) of 156 deg, and the surface showed a maximum drag reduction.
- The difference in the CAH was small between all three SH surfaces by 1 deg in the case of using water as the tested liquid. Generally, FPC-800M presented a high RMS value of the drag reduction using all tested liquids, as shown in Fig. (8-1).
- Measuring the (Θ_{adv}) of silicone oils was challenging. Still, the achieved drag reduction ratios matched with the measured Θ_s for all surfaces, where FPC-800M surfaces had high Θ_s compared with SHBC surfaces which had low Θ_s. The high drag reduction achieved using UED is attributed to its highest contact angles and nano-scale surface structures. The SHBC Measuring the (Θ_{adv}) of silicone oils was challenging. Still, the achieved drag reduction ratios matched with the measured Θ_s for all surfaces, where FPC-800M surfaces

had high Θ_s compared with SHBC surfaces which had low Θ_s. The high drag reduction achieved using UED is attributed to its highest contact angles and nano-scale surface structures. The SHBC surface has a high degree of wetting for silicone oils. As the viscosity of the oil increases, the wetting degree also increases. This can result in drag enhancement of the surface in the case of 10 silicone oils because the flow is in the laminar regime, where the surface topography and flow geometry primarily influence the flow.

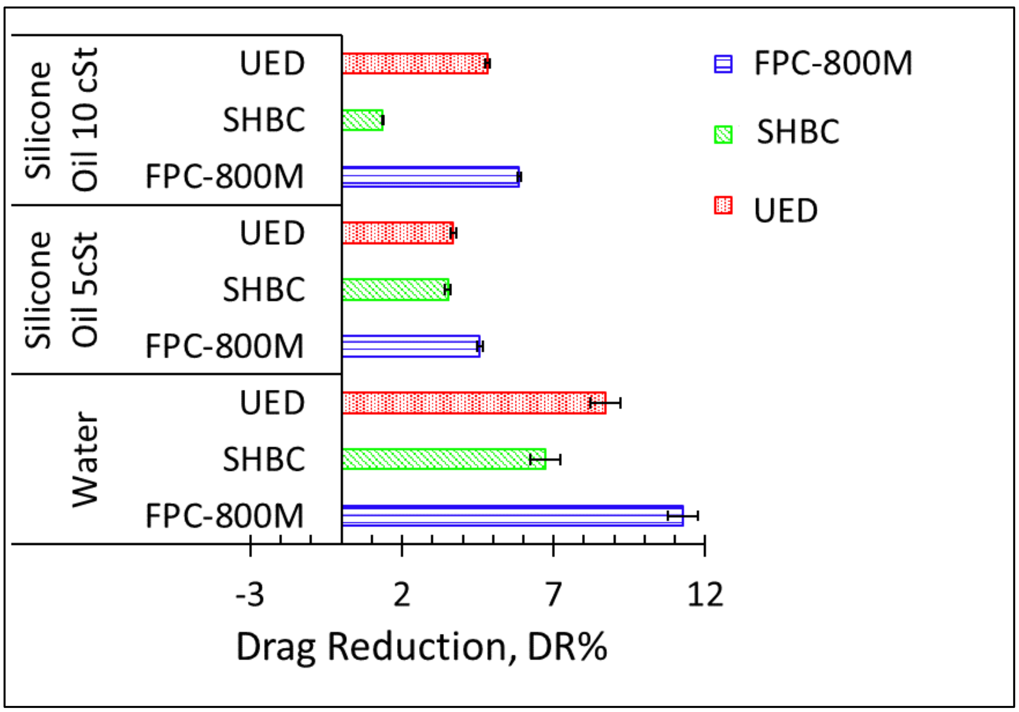

Figure 8-1 Comparison of the RMS value of the achieved drag reduction ratio (DR%) using the tested liquids and all fabricated surfaces for the Taylor–Couette flow cell. The error bars presented are the uncertainty of the measurements.

8.1.2 Conclusion of Open Channel Study

In this part of the study, we conducted experimental investigations on the hydrodynamic drag reduction achieved by superhydrophobic flat plates. Unlike prior studies that primarily concentrated on a single plane above the tested surface, our experiments encompassed a comprehensive assessment of flow conditions at seven locations spanning both streamwise and spanwise directions. Furthermore, while earlier research predominantly dealt with internal flows, our present study falls within the realm of external flows, specifically boundary layer flows, encompassing a wide spectrum of turbulence. The outcomes of this study serve to dispel uncertainties regarding the efficacy and durability of drag reduction offered by superhydrophobic surfaces. The following conclusion can be drawn from the findings of this research:

- Assisted by direct and comparative measurements of viscous drag and a genuine plastron in place during all flow tests, the results have positively confirmed that the SH surfaces reduce the viscous drag in turbulent flows in an average ratio of 18% for FPC-800M and 11% for FT-MW, and 8% for UED.
- The results show that a superhydrophobic surface with higher static and dynamic contact angles is more beneficial to drag reduction in the turbulent boundary layer, and otherwise, the air layer (plastron) is susceptible to the high wall shear rate in the turbulent boundary layer flow and is prone to be depleted. Consequently, the surface becomes wet with water, and the roughness of the superhydrophobic surface patterns increases; an increase is seen in the viscous drag (e.g., FT-MW and UED surfaces).

- Incisive evaluation for the theoretical prediction model of the slip velocity and the slip length is examined, and the model shows that the slip length is in the order of the coating thickness when the plastron depletes. Then, the roughness increases compared to the uncoated baseline surface. These are new insights gained by this experimental study.
- Suppressions induced by the fabricated SH surfaces were observed in the streamwise and spanwise turbulence intensity and the Reynolds stresses. In the near wall region where the suppressions occur and expand and the streamwise and spanwise Reynolds stresses were larger than the Reynolds stresses of near uncoated surface. However, the suppressions of the Reynolds stresses collapsed farther away from the wall, indicating turbulence attenuation and the flow became fully developed.
- In contrast, when the Reynolds stresses were normalized using the corresponding friction velocity and plotted versus the non-dimensionalized distance y+, it evaluates the near wall region with more details. It can be seen that the suppressions of SH surfaces indicate a faster increase in SHS Reynolds stresses in the vicinity of the wall compared with the smooth uncoated surface. This is in general due to the increasing slip velocity at the interface layer. In down streamwise, the Reynolds stresses of the superhydrophobic surfaces (SHSs) become reduced compared to those of the smooth surface. This is primarily attributed to the dampening of turbulence caused by the partial slip at the wall.
- The slip velocities over the tested SH surfaces showed high values in the upstream, and each surface showed a different scenario to the last measurement in the downstream direction. The FPC-800M maintains higher values compared to the UED and FT-MW surfaces. These scenarios agree with the achieved slip length and drag reduction. The negative slip velocity measurements in the last measurement locations over the UED and

FT-MW surfaces resulted in negative slip lengths. These slip lengths are in order of the thickness of the SH coating layer, as confirmed in our prior study.

8.2 Recommendations and Future Work

The passive drag reduction over various SHSs has been investigated in Taylo-Couette cell and over a flat plate in an open channel facility that using three different liquids. Further investigations are suggested to be considered and addressed in future work to cover the following research areas:

- Further investigations could entail conducting experiments to measure the DR% under various SH surfaces with different witting degrees to gain insight into the drag reduction mechanism.
- Further investigation into increasing the plastron thickness and the effective slip length is recommended to understand better the drag reduction mechanism over SH surfaces in Taylor–Couette flows and how that will work with Poiseuille flows.
- The influence of the surface roughness on the turbulent DR performance and the longevity of the plastron of the fabricated SHSs should be considered for large area of the tested surfaces, which would be the main focus in practical scenarios where long-term, consistent DR performance is needed.
- The accumulation of these data would enable the creation of a statistical model utilizing regression analysis to determine the effect of the predicted parameters on the plastron thickness relative to the present setup.
- A flow visualization study would be desirable to investigate the plastron over the tested SHSs in the open channel flow from the leading to trailing edge at different approaching Re numbers.

- Experimental investigations are recommended to be conducted in a closed pipe loop to examine drag reduction in Poiseuille flow. This involves using partial differential pressure sensors initially and later modifying the loop to include a test section for Laser Doppler Velocimetry (LDV) measurements. These measurements have to be performed over various superhydrophobic surfaces (SHSs) and at different flow rates. This allows to use two phase oil /water flows and investigates the impact of surface topology modification on the viscous shear resistance.
- Numerical simulations using a computational fluid dynamic code to investigate the flow behaviour over the SHSs used in Taylor-Couette flows and Open Channel flows. This may also unveil additional insights into the flow mechanism and the achieved darg over the tested surfaces in both experimental works in the present study, which might be challenging to obtain using experimental methods.

References

[1] W. Brostow, “Drag reduction in flow: Review of applications, mechanism and prediction,” *Journal of Industrial and Engineering Chemistry*, vol. 14, no. 4. pp. 409–416, 2008, doi: 10.1016/j.jiec.2008.07.001.

[2] M. Perlin and S. Ceccio, *Mitigation of Hydrodynamic Resistance-Methods to Reduce Hydrodynamic Drag*. World Scientific Co Pte. Ltd, 2015.

[3] J. M. F. A. Mohammadi, “A spectral algorithm for the analysis of flows in grooved channels,” *Int. J. Numer. Methods Fluids*, vol. 69, no. 27 april, pp. 606–638, 2012, doi: 10.1002/fld.2577.

[4] M. Z. Hossain and J. M. Floryan, “Drag reduction in a thermally modulated channel,” *J. Fluid Mech.*, vol. 791, pp. 122–153, 2016, doi: 10.1017/jfm.2016.42.

[5] B. Dean and B. Bhushan, “Shark-skin surfaces for fluid-drag reduction in turbulent flow: A review,” *Philos. Trans. R. Soc. A Math. Phys. Eng. Sci.*, vol. 368, no. 1929, pp. 4775–4806, 2010, doi: 10.1098/rsta.2010.0201.

[6] Y. F. Fu, C. Q. Yuan, and X. Q. Bai, “Marine drag reduction of shark skin inspired riblet surfaces,” *Biosurface and Biotribology*, vol. 3, no. 1. pp. 11–24, 2017, doi: 10.1016/j.bsbt.2017.02.001.

[7] K. R. Sreenivasan and C. M. White, “The onset of drag reduction by dilute polymer additives, and the maximum drag reduction asymptote,” *J. Fluid Mech.*, vol. 409, pp. 149–164, 2000, doi: 10.1017/S0022112099007818.

[8] M. A. Samaha, H. V. Tafreshi, and M. Gad-el-Hak, “Superhydrophobic surfaces:

From the lotus leaf to the submarine," *Comptes Rendus - Mec.*, vol. 340, no. 1–2, pp. 18–34, 2012, doi: 10.1016/j.crme.2011.11.002.

[9] J. P. Rothstein, "Slip on superhydrophobic surfaces," *Annu. Rev. Fluid Mech.*, vol. 42, pp. 89–109, 2010, doi: 10.1146/annurev-fluid-121108-145558.

[10] C. Lee, C. H. Choi, and C. J. Kim, "Superhydrophobic drag reduction in laminar flows: a critical review," *Exp. Fluids*, vol. 57, no. 12, 2016, doi: 10.1007/s00348-016-2264-z.

[11] Y. Luo, L. Wang, L. Green, K. Song, L. Wang, and R. Smith, "Advances of drag-reducing surface technologies in turbulence based on boundary layer control," *J. Hydrodyn.*, vol. 27, no. 4, pp. 473–487, 2015, doi: 10.1016/S1001-6058(15)60507-8.

[12] A. Mohammadi and J. M. Floryan, "Mechanism of drag generation by surface corrugation," *Phys. Fluids*, vol. 24, no. 1, 2012, doi: 10.1063/1.3675557.

[13] J. T. Simpson, S. R. Hunter, and T. Aytug, "Superhydrophobic materials and coatings: A review," *Reports Prog. Phys.*, vol. 78, no. 8, 2015, doi: 10.1088/0034-4885/78/8/086501.

[14] S. Das, S. Kumar, S. K. Samal, S. Mohanty, and S. K. Nayak, "A Review on Superhydrophobic Polymer Nanocoatings: Recent Development and Applications," *Ind. Eng. Chem. Res.*, vol. 57, no. 8, pp. 2727–2745, 2018, doi: 10.1021/acs.iecr.7b04887.

[15] P. Zhang and F. Y. Lv, "A review of the recent advances in superhydrophobic

surfaces and the emerging energy-related applications," *Energy*, vol. 82, pp. 1068–1087, 2015, doi: 10.1016/j.energy.2015.01.061.

[16] M. Z. Hossain, D. Floryan, and J. M. Floryan, "Drag reduction due to spatial thermal modulations," *J. Fluid Mech.*, vol. 713, no. October, pp. 398–419, 2012, doi: 10.1017/jfm.2012.465.

[17] E. Lauga, "Apparent slip due to the motion of suspended particles in flows of electrolyte solutions," *Langmuir*, vol. 20, no. 20, pp. 8924–8930, 2004, doi: 10.1021/la049464r.

[18] E. Lauga, M. Brenner, and H. Stone, "Microfluidics: The no-slip boundary condition," *Springer Handbooks*, pp. 1219–1240, 2007, doi: 10.1007/978-3-540-30299-5_19.

[19] D. Maynes, K. Jeffs, B. Woolford, and B. W. Webb, "Laminar flow in a microchannel with hydrophobic surface patterned microribs oriented parallel to the flow direction," *Phys. Fluids*, vol. 19, no. 9, 2007, doi: 10.1063/1.2772880.

[20] N. J. Lund, "Effective Slip Lengths for Stokes Flow over Rough, Mixed-Slip Surfaces," 2015, [Online]. Available: http://hdl.handle.net/10063/4162.

[21] X. P. Zhang, N. J. Lund, and S. C. Hendy, "Effective slip length: Some analytical and numerical results," *ANZIAM J.*, vol. 57, no. 1, pp. 79–88, 2015, doi: 10.1017/S1446181115000127.

[22] R. S. Voronov, D. V. Papavassiliou, and L. L. Lee, "Review of fluid slip over superhydrophobic surfaces and its dependence on the contact angle," *Ind. Eng.*

Chem. Res., vol. 47, no. 8, pp. 2455–2477, 2008, doi: 10.1021/ie0712941.

[23] A. Busse, N. D. Sandham, G. McHale, and M. I. Newton, “Change in drag, apparent slip and optimum air layer thickness for laminar flow over an idealised superhydrophobic surface,” *J. Fluid Mech.*, vol. 727, pp. 488–508, 2013, doi: 10.1017/jfm.2013.284.

[24] Z. G. and F. Yang, *Surfaces and Interfaces of Biomimetic Superhydrophobic Materials*, vol. 1st, no. July. 2018.

[25] K.-Y. Law and H. Zhao, *Surface Wetting*. 2016.

[26] A. CarrÉ and K. L. Mittal, “Superhydrophobic surfaces,” *Superhydrophobic Surfaces*, pp. 1–509, 2009, doi: 10.1515/jmbm-2012-0022.

[27] J. C. E. P. I. Russell, *Superhydrophobic Surfaces*, vol. 7, no. 2. 2017.

[28] K. Y. Law and H. Zhao, *Surface wetting: Characterization, contact angle, and fundamentals*. 2015.

[29] G. Yunqing, L. Tao, M. Jiegang, S. Zhengzan, and Z. Peijian, “Analysis of Drag Reduction Methods and Mechanisms of Turbulent,” *Appl. Bionics Biomech.*, vol. 2017, 2017, doi: 10.1155/2017/6858720.

[30] S. E. Shima Soleimani, “A review of drag reduction and heat transfer enhancement by riblet surfaces in closed and open channel flow _ Elsevier Enhanced Reader.pdf.” 2020.

[31] L. jiang Cumming Yu, Mengfei Liu, Chunhui Zhang, Hao Yan, Minghui Zhang, Quingshan Wu, Mingjie Liu, “Bio-inspired drag reduction_ From nature organisms

to artificial functional surfaces _ Elsevier Enhanced Reader.pdf," *Giant*, vol. 2, no. 100017, p. 112, 2020, doi: 10.1016/j.giant.2020.100017.

[32] H. Ling, S. Srinivasan, K. Golovin, G. H. McKinley, A. Tuteja, and J. Katz, "High-resolution velocity measurement in the inner part of turbulent boundary layers over superhydrophobic surfaces," *J. Fluid Mech.*, vol. 801, no. September, pp. 670–703, 2016, doi: 10.1017/jfm.2016.450.

[33] M. S. Naim and M. F. Baig, "Turbulent drag reduction in Taylor-Couette flows using different super-hydrophobic surface configurations," *Phys. Fluids*, vol. 31, no. 9, 2019, doi: 10.1063/1.5116316.

[34] S. Srinivasan, J. A. Kleingartner, J. B. Gilbert, R. E. Cohen, A. J. B. Milne, and G. H. Mckinley, "Sustainable Drag Reduction in Turbulent Taylor-Couette Flows by Depositing Sprayable Superhydrophobic Surfaces," vol. 014501, no. JANUARY, pp. 1–5, 2015, doi: 10.1103/PhysRevLett.114.014501.

[35] G. Srinivasan, Siddarth; Kleingartner, Justin; Gilbert, Jonathan; Milne, Andrew; Cohen, Robert; McKinley, . "Sustainable Drag Reduction in Turbulent Taylor-Couette Flows using Sprayable Superhydrophobic Surfaces.," *APS Div. Fluid Dyn.*, vol. H8-005.

[36] G. I. Taylor, "Two Rotating Cylinders .," *Philos. Trans. rhe R. Soc. London. Ser. A, Contain. Pap. a Math. or Phys. Character*, vol. 223, no. 1923, pp. 289–343, 1923.

[37] S. Grossmann, D. Lohse, and C. Sun, "High – Reynolds Number Taylor-Couette Turbulence," 2016, doi: 10.1146/annurev-fluid-122414-034353.

[38] F. Physik, “between independently rotating cylinders,” vol. 581, pp. 221–250, 2007, doi: 10.1017/S0022112007005629.

[39] C. Choi and C. Kim, “UCLA Large Slip of Aqueous Liquid Flow over a Nanoengineered Superhydrophobic Surface,” 2006, doi: 10.1103/PhysRevLett.96.066001.

[40] K. Watanabe, T. Takayama, S. Ogata, and S. Isozaki, “Flow between two coaxial rotating cylinders with a highly water-repellent wall,” *AIChE J.*, vol. 49, no. 8, pp. 1956–1963, 2003, doi: 10.1002/aic.690490805.

[41] L. I. Jian, Z. Ming, C. A. I. Lan, Y. E. Xia, and Y. Run, “On the measurement of slip length for liquid flow over super-hydrophobic surface,” no. 2006039, 2009, doi: 10.1007/s11434-009-0577-5.

[42] B. R. Solomon, K. S. Khalil, and K. K. Varanasi, “Drag Reduction using Lubricant-Impregnated Surfaces in Viscous Laminar Flow,” 2014.

[43] B. J. Rosenberg, T. Van Buren, M. K. Fu, A. J. Smits, and A. J. Smits, “Turbulent drag reduction over air- and liquid- impregnated surfaces impregnated surfaces,” vol. 015103, no. September 2015, 2016.

[44] T. Van Buren and A. J. Smits, “Substantial drag reduction in turbulent flow using liquid-infused surfaces,” pp. 448–456, 2017, doi: 10.1017/jfm.2017.503.

[45] R. J. P. H. Xu, C. R. Crick, “Evaluating the resilience of superhydrophobic materials using the slip-length concept,” *J. Mater. Chem.*, vol. 6, pp. 4458–4465, 2018, doi: 10.1039/c7ta10510j.

[46] A. Rajappan, K. Golovin, B. Tobelmann, V. Pillutla, and W. Choi, "Influence of textural statistics on drag reduction by scalable , randomly rough superhydrophobic surfaces in turbulent flow Influence of textural statistics on drag reduction by scalable , randomly rough superhydrophobic surfaces in turbulent flow," vol. 042107, 2019, doi: 10.1063/1.5090514.

[47] C. Peguero and K. Breuer, "On Drag Reduction in Turbulent Channel Flow over Superhydrophobic Surfaces," pp. 233–236, 2009, doi: 10.1007/978-3-642-03085-7.

[48] C. J. B. Salil Gogte, Peter Vorobieff, Richard Truesdell, and Andrea Mammoli, Pratik Shah, "Effective slip on textured superhydrophobic surfaces Effective slip on textured superhydrophobic surfaces," vol. 051701, no. April 2005, 2009, doi: 10.1063/1.1896405.

[49] C. Henoch *et al.*, "Turbulent drag reduction using superhydrophobic surfaces," *Collect. Tech. Pap. - 3rd AIAA Flow Control Conf.*, vol. 2, no. June, pp. 840–844, 2006, doi: 10.2514/6.2006-3192.

[50] Z. Jia-peng, D. U. Xiang-dang, and S. H. I. Xiu-hua, "Experimental research on friction-reduction with super-hydrophobic surfaces," vol. 6, no. 3, pp. 58–61, 2007.

[51] R. J. Daniello, N. E. Waterhouse, and J. P. Rothstein, "Drag reduction in turbulent flows over superhydrophobic surfaces," *Phys. Fluids*, vol. 21, no. 8, pp. 1–26, 2009, doi: 10.1063/1.3207885.

[52] B. Woolford, J. Prince, D. Maynes, and B. W. Webb, "Particle image velocimetry characterization of turbulent channel flow with rib patterned superhydrophobic walls," *Phys. Fluids*, vol. 21, no. 8, 2009, doi: 10.1063/1.3213607.

[53] B. Bhushan, “Biomimetic Structures for Fluid Drag Reduction in Laminar and Turbulent Flows,” no. January 2010, 2014, doi: 10.1088/0953-8984/22/3/035104.

[54] and C.-H. C. Elias Aljallis, Mohammad Amin Sarshar, Raju Datla, Vinod Sikka, Andrew Jones, “"Experimental study of skin friction drag reduction on superhydrophobic flat plates in high Reynolds number boundary layer flow,” *Phys. Fluids*, vol. 25, no. 7, 2013, doi: 10.1063/1.4816362.

[55] R. A. Bidkar, L. Leblanc, A. J. Kulkarni, V. Bahadur, S. L. Ceccio, and M. Perlin, “Skin-friction drag reduction in the turbulent regime using random-textured hydrophobic surfaces,” *Phys. Fluids*, vol. 26, no. 8, 2014, doi: 10.1063/1.4892902.

[56] H. Park, G. Sun, and C. J. Kim, “Superhydrophobic turbulent drag reduction as a function of surface grating parameters,” *J. Fluid Mech.*, vol. 747, pp. 722–734, 2014, doi: 10.1017/jfm.2014.151.

[57] J. Zhang, H. Tian, Z. Yao, P. Hao, and N. Jiang, “Mechanisms of drag reduction of superhydrophobic surfaces in a turbulent boundary layer flow,” *Exp. Fluids*, vol. 56, no. 9, pp. 1–13, 2015, doi: 10.1007/s00348-015-2047-y.

[58] B. V. Hokmabad and S. Ghaemi, “Turbulent flow over wetted and non- wetted superhydrophobic counterparts with random structure,” vol. 015112, no. May 2015, 2016, doi: 10.1063/1.4940325.

[59] J. W. Gose *et al.*, “Characterization of superhydrophobic surfaces for drag reduction in turbulent flow,” *J. Fluid Mech.*, vol. 845, pp. 560–580, 2018, doi: 10.1017/jfm.2018.210.

[60] W. Abu Rowin, J. Hou, and S. Ghaemi, “Turbulent channel flow over riblets with superhydrophobic coating,” *Exp. Therm. Fluid Sci.*, vol. 94, no. July 2017, pp. 192–204, 2018, doi: 10.1016/j.expthermflusci.2018.02.001.

[61] W. A. Rowin and S. Ghaemi, “Streamwise and spanwise slip over a superhydrophobic surface,” *J. Fluid Mech.*, vol. 870, pp. 1127–1157, 2019, doi: 10.1017/jfm.2019.225.

[62] P. A. Bullee *et al.*, “Bubbly drag reduction using a hydrophobic inner cylinder in Taylor-Couette turbulence,” *J. Fluid Mech.*, vol. 883, 2019, doi: 10.1017/jfm.2019.894.

[63] H. Aziz and H. V. Tafreshi, “Role of particles spatial distribution in drag reduction performance of superhydrophobic granular coatings,” *Int. J. Multiph. Flow*, vol. 98, pp. 128–138, 2018, doi: 10.1016/j.ijmultiphaseflow.2017.09.006.

[64] Y. Li, Y. Pan, and X. Zhao, “Measurement and quantification of effective slip length at solid-liquid interface of roughness-induced surfaces with oleophobicity,” *Appl. Sci.*, vol. 8, no. 6, 2018, doi: 10.3390/app8060931.

[65] M. Liravi, H. Pakzad, A. Moosavi, and A. Nouri-Borujerdi, “A comprehensive review on recent advances in superhydrophobic surfaces and their applications for drag reduction,” *Progress in Organic Coatings*, vol. 140. 2020, doi: 10.1016/j.porgcoat.2019.105537.

[66] A. Rajappan *et al.*, “Influence of textural statistics on drag reduction by scalable, randomly rough superhydrophobic surfaces in turbulent flow,” *Phys. Fluids*, vol. 31, no. 4, 2019, doi: 10.1063/1.5090514.

[67] D. Panchanathan, A. Rajappan, K. K. Varanasi, and G. H. McKinley, “Plastron Regeneration on Submerged Superhydrophobic Surfaces Using in Situ Gas Generation by Chemical Reaction,” *ACS Appl. Mater. Interfaces*, vol. 10, no. 39, pp. 33684–33692, 2018, doi: 10.1021/acsami.8b12471.

[68] S. Grossmann, D. Lohse, and C. Sun, “High-Reynolds Number Taylor-Couette Turbulence,” *Annu. Rev. Fluid Mech.*, vol. 48, no. 2016, pp. 53–80, 2016, doi: 10.1146/annurev-fluid-122414-034353.

[69] K. Avila and B. Hof, “High-precision Taylor-Couette experiment to study subcritical transitions and the role of boundary conditions and size effects,” *Rev. Sci. Instrum.*, vol. 84, no. 6, 2013, doi: 10.1063/1.4807704.

[70] D. P. M. Van Gils, G. W. Bruggert, D. P. Lathrop, C. Sun, and D. Lohse, “The Twente turbulent Taylor-Couette (T3C) facility: Strongly turbulent (multiphase) flow between two independently rotating cylinders,” *Rev. Sci. Instrum.*, vol. 82, no. 2, 2011, doi: 10.1063/1.3548924.

[71] S. Raayai Ardakani, “Geometry Mediated Drag Reduction Using Riblets and Wrinkled Surface Textures,” *ProQuest Diss. Theses*, no. 2011, 2018, [Online]. Available: https://login.proxy.library.msstate.edu/login?url=https://www.proquest.com/dissertations-theses/geometry-mediated-drag-reduction-using-riblets/docview/2067997902/se-2?accountid=34815%0Ahttps://resolver.ebscohost.com/openurl?ctx_ver=Z39.88-2004&ctx_enc=inf.

[72] T. Hall and D. Joseph, “Rotating cylinder drag balance with application to riblets,” *Exp. Fluids*, vol. 29, no. 3, pp. 215–227, 2000, doi: 10.1007/s003489900075.

[73] A. J. Greidanus, R. Delfos, S. Tokgoz, and J. Westerweel, “Turbulent Taylor–Couette flow over riblets: drag reduction and the effect of bulk fluid rotation,” *Exp. Fluids*, vol. 56, no. 5, pp. 1–13, 2015, doi: 10.1007/s00348-015-1978-7.

[74] T. H. Van Den Berg, S. Luther, D. P. Lathrop, and D. Lohse, “Drag reduction in bubbly Taylor-Couette turbulence,” *Phys. Rev. Lett.*, vol. 94, no. 4, pp. 4–7, 2005, doi: 10.1103/PhysRevLett.94.044501.

[75] K. Sugiyama, E. Calzavarini, and D. Lohse, “Microbubbly drag reduction in Taylor - Couette flow in the wavy vortex regime,” *J. Fluid Mech.*, vol. 608, pp. 21–41, 2008, doi: 10.1017/S0022112008001183.

[76] L. Bocquet, P. Tabeling, and S. Manneville, “Comment on ‘large slip of aqueous liquid flow over a nanoengineered superhydrophobic surface,’” *Phys. Rev. Lett.*, vol. 97, no. 10, 2006, doi: 10.1103/PhysRevLett.97.109601.

[77] H. Schlichting, *Boundary - Layer Theory*, 7th Editio. McGrae-Hill Book Company, 1979.

[78] P. Reinke, M. Schmidt, and T. Beckmann, “The cavitating Taylor-Couette flow,” *Phys. Fluids*, vol. 30, no. 10, 2018, doi: 10.1063/1.5049743.

[79] S. Srinivasan, J. A. Kleingartner, J. B. Gilbert, R. E. Cohen, A. J. B. Milne, and G. H. McKinley, “Sustainable drag reduction in turbulent Taylor-Couette flows by depositing sprayable superhydrophobic surfaces,” *Phys. Rev. Lett.*, vol. 114, no. 1,

pp. 1–5, 2015, doi: 10.1103/PhysRevLett.114.014501.

[80] A.-P. Inc., *MCR 301e Manuel and Guideline*. 2015.

[81] M. F. Kline S, "Describing uncertainties in single-sample experiments. Mech Eng 75:," *Mech. Eng.*, no. 75, pp. 3–8, 1953.

[82] X. Zhang, X. Duan, and Y. Muzychka, "New mechanism and correlation for degradation of drag-reducing agents in turbulent flow with measured data from a double-gap rheometer," *Colloid Polym. Sci.*, vol. 296, no. 4, pp. 829–834, 2018, doi: 10.1007/s00396-018-4300-4.

[83] C. H. Choi and C. J. Kim, "Large slip of aqueous liquid flow over a nanoengineered superhydrophobic surface," *Phys. Rev. Lett.*, vol. 96, no. 6, 2006, doi: 10.1103/PhysRevLett.96.066001.

[84] M. S. J. Hashmi, *Comprehensive Materials Processing*, vol. 13, no. 1. 2017.

[85] H. L. Swinney, "Flow regimes in a circular Couette system with independently rotating cylinders," *J. Fluid Mech.*, vol. 164, no. 1986, pp. 155–183, 1986, doi: 10.1017/S0022112086002513.

[86] Maurice Frédéric Alfred Couette, "Études sur le frottement des liquides," 1890.

[87] V. F. Wendt, "Turbulente Stromungen zwischen zwei rotierenden," vol. 97, no. 6, 1932.

[88] D. P. Lathrop, J. Fineberg, and H. L. Swinney, "Transion to shear driven turbulence in couette taylor flow," vol. 46, no. 10, 1992.

[89] D. P. Lathrop, J. Fineberg, and H. L. Swinney, "turbulent flow between concentric

rotating cylinder at large Re," vol. 68, no. 10, pp. 1515–1519, 1992.

[90] A. Tong, P.; Goldburg, W.I; Huaang, J.S.; Witten, "Anisotropy in Turbulent Drag Reduction," *Phys. Rev. Lett.*, vol. 65, no. 22, p. 1238, 1990, doi: 10.1038/2071238d0.

[91] H. J. Aydin, E M; Leutheusser, "Plane-Couette flow between smooth and rough walls," *Expermental in Fluids*, vol. 312, pp. 302–312, 1991.

[92] K. B. Golovin, J. Gose, M. Perlin, S. L. Ceccio, and A. Tuteja, "Bioinspired surfaces for turbulent drag reduction," *Philos. Trans. R. Soc. A Math. Phys. Eng. Sci.*, vol. 374, no. 2073, 2016, doi: 10.1098/rsta.2016.0189.

[93] B. Vajdi Hokmabad and S. Ghaemi, "Turbulent flow over wetted and non-wetted superhydrophobic counterparts with random structure," *Phys. Fluids*, vol. 28, no. 1, 2016, doi: 10.1063/1.4940325.

[94] H. L. Swinney, "Flow regimes in a circular Couette system with independently rotating cylinders," *J. Fluid Mech.*, vol. 164, pp. 155–183, 1986, doi: 10.1017/S0022112086002513.

[95] M. Schrimpf, J. Esteban, H. Warmeling, T. Färber, A. Behr, and A. J. Vorholt, "Taylor-Couette reactor: Principles, design, and applications," *AIChE J.*, vol. 67, no. 5, pp. 1–24, 2021, doi: 10.1002/aic.17228.

[96] C. H. Choi, U. Ulmanella, J. Kim, C. M. Ho, and C. J. Kim, "Effective slip and friction reduction in nanograted superhydrophobic microchannels," *Phys. Fluids*, vol. 18, no. 8, pp. 1–8, 2006, doi: 10.1063/1.2337669.

[97] C. Lee, C. H. Choi, and C. J. Kim, “Structured surfaces for a giant liquid slip,” *Phys. Rev. Lett.*, vol. 101, no. 6, pp. 1–4, 2008, doi: 10.1103/PhysRevLett.101.064501.

[98] H. Park, C. H. Choi, and C. J. Kim, “Superhydrophobic drag reduction in turbulent flows: a critical review,” *Exp. Fluids*, vol. 62, no. 11, 2021, doi: 10.1007/s00348-021-03322-4.

[99] L. Piao and H. Park, “Two-Dimensional Analysis of Air-Water Interface on Superhydrophobic Grooves under Fluctuating Water Pressure,” *Langmuir*, vol. 31, no. 29, pp. 8022–8032, 2015, doi: 10.1021/acs.langmuir.5b01847.

[100] J. Ou, B. Perot, and J. P. Rothstein, “Laminar drag reduction in microchannels using ultrahydrophobic surfaces,” *Phys. Fluids*, vol. 16, no. 12, pp. 4635–4643, 2004, doi: 10.1063/1.1812011.

[101] Y. Xiang, S. Huang, P. Lv, Y. Xue, Q. Su, and H. Duan, “Ultimate Stable Underwater Superhydrophobic State,” *Phys. Rev. Lett.*, vol. 119, no. 13, pp. 1–5, 2017, doi: 10.1103/PhysRevLett.119.134501.

[102] B. V. Hokmabad and S. Ghaemi, “Effect of Flow and Particle-Plastron Collision on the Longevity of Superhydrophobicity,” *Sci. Rep.*, vol. 7, no. October 2016, pp. 1–10, 2017, doi: 10.1038/srep41448.

[103] J. Seo and A. Mani, “Effect of texture randomization on the slip and interfacial robustness in turbulent flows over superhydrophobic surfaces,” *Phys. Rev. Fluids*, vol. 3, no. 4, pp. 1–15, 2018, doi: 10.1103/PhysRevFluids.3.044601.

[104] D. Reholon and S. Ghaemi, "Plastron morphology and drag of a superhydrophobic surface in turbulent regime," *Phys. Rev. Fluids*, vol. 3, no. 10, pp. 1–21, 2018, doi: 10.1103/PhysRevFluids.3.104003.

[105] M. Perlin and S. Ceccio, "Mitigation of hydrodynamic resistance: Methods to reduce hydrodynamic drag," *Mitig. Hydrodyn. Resist. Methods to Reduce Hydrodyn. Drag*, no. November, pp. 1–152, 2014, doi: 10.1142/9789814612265.

[106] O. I. Vinogradova, "Drainage of a thin liquid film confined between hydrophobic surfaces," no. 1, pp. 2213–2220, 1995.

[107] B. J. Rosenberg, T. Van Buren, M. K. Fu, and A. J. Smits, "Turbulent drag reduction over air- and liquid- impregnated surfaces," *Phys. Fluids*, vol. 28, no. 1, 2016, doi: 10.1063/1.4939272.

[108] A. J. Greidanus, R. Delfos, S. Tokgoz, and J. Westerweel, "Turbulent Taylor–Couette flow over riblets: drag reduction and the effect of bulk fluid rotation," *Exp. Fluids*, vol. 56, no. 5, 2015, doi: 10.1007/s00348-015-1978-7.

[109] R. L. Panton, "Panton 1992-Scaling laws for the angular momentum of a completely turbulent couette flow.pdf." C. R. Acad. Sci, serie II, Paris, t. 315, pp. 1467–1473, 1992.

[110] G. S. Lewis and H. L. Swinney, "Velocity structure functions, scaling, and transitions in high-Reynolds-number Couette-Taylor flow," *Phys. Rev. E - Stat. Physics, Plasmas, Fluids, Relat. Interdiscip. Top.*, vol. 59, no. 5, pp. 5457–5467, 1999, doi: 10.1103/PhysRevE.59.5457.

[111] D. Paghdar, S. Jogee, and K. Anupindi, "Large-eddy simulation of counter-rotating Taylor–Couette flow: The effects of angular velocity and eccentricity," *Int. J. Heat Fluid Flow*, vol. 81, no. October 2019, p. 108514, 2020, doi: 10.1016/j.ijheatfluidflow.2019.108514.

[112] J. Seo and A. Mani, "On the scaling of the slip velocity in turbulent flows over superhydrophobic surfaces," *Phys. Fluids*, vol. 28, no. 2, 2016, doi: 10.1063/1.4941769.

[113] S. Srinivasan, W. Choi, K. C. Park, S. S. Chhatre, R. E. Cohen, and G. H. McKinley, "Drag reduction for viscous laminar flow on spray-coated non-wetting surfaces," *Soft Matter*, vol. 9, no. 24, pp. 5691–5702, 2013, doi: 10.1039/c3sm50445j.

[114] C. T. Fairhall, N. Abderrahaman-Elena, and R. García-Mayoral, "The effect of slip and surface texture on turbulence over superhydrophobic surfaces," *J. Fluid Mech.*, vol. 861, pp. 88–118, 2019, doi: 10.1017/jfm.2018.909.

[115] Y. Xue, P. Lv, H. Lin, and H. Duan, "Underwater superhydrophobicity: Stability, design and regulation, and applications," *Appl. Mech. Rev.*, vol. 68, no. 3, 2016, doi: 10.1115/1.4033706.

[116] O. I. Vinogradova, "Slippage of water over hydrophobic surfaces," *Int. J. Miner. Process.*, vol. 56, no. 1–4, pp. 31–60, 1999, doi: 10.1016/S0301-7516(98)00041-6.

[117] X. Qi and D. P. Song, "Minimizing fuel emissions by optimizing vessel schedules in liner shipping with uncertain port times," *Transp. Res. Part E Logist. Transp. Rev.*, vol. 48, no. 4, pp. 863–880, 2012, doi: 10.1016/j.tre.2012.02.001.

[118] K. Fukuda, J. Tokunaga, T. Nobunaga, T. Nakatani, T. Iwasaki, and Y. Kunitake, "Frictional drag reduction with air lubricant over a super-water-repellent surface," *J. Mar. Sci. Technol.*, vol. 5, no. 3, pp. 123–130, 2000, doi: 10.1007/s007730070009.

[119] R. J. Daniello, N. E. Waterhouse, and J. P. Rothstein, "Drag reduction in turbulent flows over superhydrophobic surfaces," *Phys. Fluids*, vol. 21, no. 8, 2009, doi: 10.1063/1.3207885.

[120] S. B. Pope, "Turublent Flows." Cambridge University Press, Cambridge UK, p. 773, 2001.

[121] B. Nyantekyi-Kwakye, E. E. Essel, K. Dow, S. P. Clark, and M. F. Tachie, "Hydraulic and turbulent flow characteristics beneath a simulated partial ice-cover," *J. Hydraul. Res.*, no. 2015, 2020, doi: 10.1080/00221686.2020.1780493.

[122] W. YANTA and R. SMITH, "Measurements of turbulence-transport properties with a laser Dopplervelocimeter," 1973.

[123] A. C. Schwarz, M. W. Plesniak, and S. Murthy, "Turbulent Boundary Layers Subjected to Multiple Strains," *28th Fluid Dyn. Conf.*, vol. 121, no. September, 1997, doi: 10.2514/6.1997-1874.

[124] M. F. Tachie, R. Balachandar, and D. J. Bergstrom, "Open channel boundary layer relaxation behind a forward facing step at low reynolds numbers," *J. Fluids Eng. Trans. ASME*, vol. 123, no. 3, pp. 539–544, 2001, doi: 10.1115/1.1383971.

[125] M. Faruque and A. Al, "Smooth and rough wall open channel flow including

effects of seepage and ice cover," 2009.

[126] W. Abu Rowin, J. Hou, and S. Ghaemia, "Inner and outer layer turbulence over a superhydrophobic surface with low roughness level at low Reynolds number," *Phys. Fluids*, vol. 29, no. 9, 2017, doi: 10.1063/1.5004398.

[127] J. S. Paschkewitz, Y. Dubief, and E. S. G. Shaqfeh, "The dynamic mechanism for turbulent drag reduction using rigid fibers based on Lagrangian conditional statistics," *Phys. Fluids*, vol. 17, no. 6, pp. 1–18, 2005, doi: 10.1063/1.1925447.

[128] S. H. Lee and H. J. Sung, "Direct numerical simulation of the turbulent boundary layer over a rod-roughened wall," *J. Fluid Mech.*, vol. 584, pp. 125–146, 2007, doi: 10.1017/S0022112007006465.

[129] N. Saito and D. I. Pullin, "Large eddy simulation of smooth-rough-smooth transitions in turbulent channel flows," *Int. J. Heat Mass Transf.*, vol. 78, pp. 707–720, 2014, doi: 10.1016/j.ijheatmasstransfer.2014.06.088.

[130] K. Fukagata, N. Kasagi, and P. Koumoutsakos, "A theoretical prediction of friction drag reduction in turbulent flow by superhydrophobic surfaces," *Phys. Fluids*, vol. 18, no. 5, pp. 16–20, 2006, doi: 10.1063/1.2205307.

[131] T. Min and J. Kim, "Effects of hydrophobic surface on skin-friction drag," *Phys. Fluids*, vol. 16, no. 7, pp. 3–6, 2004, doi: 10.1063/1.1755723.

[132] A. F. A. Alsharief, X. Duan, and Y. S. Muzychka, "Evolution of Air Plastron Thickness and Slip Length over Superhydrophobic Surfaces in Taylor Couette Flows," *Fluids*, vol. 8, no. 4, 2023, doi: 10.3390/fluids8040133.

[133] D. C. M. De Nicola F, Castrucci P, Scarselli M, Nanni F, Cacciotti I, "Super-hydrophobic multi-walled carbon nanotube coatings for stainless steel," *Nanotechnology*, vol. 14, p. 16:26, 2015.

[134] Z. X. Zhu X, Zhang Z, Ge B, Men X, "Fabrication of a superhydrophobic carbon nanotube coating with good reusability and easy repairability," *Colloids Surfaces A Physicochem. Eng. Asp.*, vol. 444, no. 5, pp. 252–258.

[135] Y. C. Zhang HF, Teo MK, "Superhydrophobic carbon nanotube/polydimethylsiloxane composite coatings.," *Mater. Sci. Technol. (United Kingdom)*, vol. 31, no. 14, pp. 1745–1753, 2014.

[136] L. G. Yang Z, Wang L, Sun W, Li S, Zhu T, Liu W, "Superhydrophobic epoxy coating modified by fluorographene used for anti-corrosion and self-cleaning.," *Appl. Surf. Sci.*, vol. 401, no. 145, p. 55.

[137] S. H. Lin Y, Ehlert GJ, Bukowsky C, "Superhydrophobic functionalized graphene aerogels," *ACS Appl. Mater. interfaces.*, vol. 7, no. 3, pp. 2200–2203.

[138] Y. H. Junaidi MU, Azaman SH, Ahmad NN, Leo CP, Lim GW, Chan DJ, "Superhydrophobic coating of silica with photoluminescence properties synthesized from rice husk ash," *Prog. Org. Coatings.*, vol. 111, no. 1, pp. 29–37.

[139] X. X. Meng J, Lin S, . "Preparation of breathable and superhydrophobic coating film via spray coating in combination with vapor-induced phase separation.," *Prog. Org. Coatings.*, vol. 107, no. 1, pp. 29–36.

[140] E. B. Caldona, A. C. C. De Leon, P. G. Thomas, D. F. Naylor, B. B. Pajarito, and R.

C. Advincula, “Superhydrophobic Rubber-Modified Polybenzoxazine/SiO2 Nanocomposite Coating with Anticorrosion, Anti-Ice, and Superoleophilicity Properties,” *Ind. Eng. Chem. Res.*, vol. 56, no. 6, pp. 1485–1497, 2017, doi: 10.1021/acs.iecr.6b04382.

[141] C. F. Liao CS, Wang CF, Lin HC, Chou HY, . “Fabrication of patterned superhydrophobic polybenzoxazine hybrid surfaces,” *Langmuir*, vol. 25, no. 6, pp. 3359–62, 2009.

[142] C. Z. Cao D, Zhang Y, Li Y, Shi X, Gong H, Feng D, Guo X, Shi Z, Zhu S, . “Fabrication of superhydrophobic coating for preventing microleakage in a dental composite restoration.,” *Mater. Sci. Eng.*, vol. 78, no. C, pp. 333–40.

[143] P. D. Sparks BJ, Hoff EF, Xiong L, Goetz JT, “Superhydrophobic hybrid inorganic–organic thiol-ene surfaces fabricated via spray-deposition and photopolymerization,” *ACS Appl. Mater. interfaces.*, vol. 5, no. 5, pp. 1811–1818.

[144] X. Q. Chen J, Zhang L, Zeng Z, Wang G, Liu G, Zhao W, Ren T, “Facile fabrication of antifogging, antireflective, and self-cleaning transparent silica thin coatings,” *A Physicochem. Eng. Asp.*, vol. 509, pp. 149–157.

[145] W. T. Jiang C, Zhang Y, Wang Q, “Superhydrophobic polyurethane and silica nanoparticles coating with high transparency and fluorescence,” *J. Appl. Polym. Sci.*, vol. 129, no. 5, pp. 2959–65.

[146] L. E. Steele A, Bayer I, “Inherently superoleophobic nanocomposite coatings by spray atomization,” *Nano Lett.*, vol. 9, no. 1, pp. 501–506.

[147] C. C. Wang CF, Tzeng FS, Chen HG, "Ultraviolet-durable superhydrophobic zinc oxide-coated mesh films for surface and underwater–oil capture and transportation," *Langmuir*, vol. 28, no. 26, pp. 10015–10024.

[148] S. S. Zhang J, Pu G, "Fabrication of zinc oxide/polydimethylsiloxane composite surfaces demonstrating oil-fouling-resistant superhydrophobicity.," *ACS Appl. Mater. Interfaces.*, vol. 2, no. 10, pp. 2880–2883.

[149] C. Z. Lai Y, Tang Y, Gong J, Gong D, Chi L, Lin C, "Transparent superhydrophobic/superhydrophilic TiO 2-based coatings for self-cleaning and anti-fogging.," *J. Mater. Chem.*, vol. 22, no. 15, pp. 7420–7426, 2012.

[150] L. M. Holtzinger C, Niparte B, Wächter S, Berthomé G, Riassetto D, "Superhydrophobic TiO2 coatings formed through a non-fluorinated wet chemistry route.," *Surf. Sci.*, vol. 617, pp. 141–149.

[151] L. A. Xu QF, Liu Y, Lin FJ, Mondal B, "Superhydrophobic TiO2–polymer nanocomposite surface with UV-induced reversible wettability and self-cleaning properties," *ACS Appl. Mater. interfaces.*, vol. 5, no. 18, pp. 8915–24.

[152] L. E. Bayer IS, Steele A, Martorana PJ, . "Fabrication of superhydrophobic polyurethane/organoclay nano-structured composites from Cyclomethicone-in-water emulsions.," *Appl. Surf. Sci.*, vol. 257, no. 3, pp. 823–829.

[153] L. E. Steele A, Bayer I, Yeong YH, De Combarieu G, Lakeman C, Deglaire P, "Adhesion strength and superhydrophobicity in polyurethane/organoclay nanocomposites," in *InNanotech Conference Expo*, 2011, pp. 13–16.

[154] C. K. Lee SG, Ham DS, Lee DY, Bong H, “Transparent superhydrophobic/translucent superamphiphobic coatings based on silica–fluoropolymer hybrid nanoparticles,” *Langmuir.*, vol. 29, no. 48, pp. 15051–7.

[155] T. P. de Francisco R, Hoyos M, García N, “Transparent superhydrophobic/translucent superamphiphobic coatings based on silica–fluoropolymer hybrid nanoparticles,” *Langmuir*, vol. 6, no. 13, pp. 10014–21.

[156] X. C. Wang D, Zhang Z, Li Y, “Highly transparent and durable superhydrophobic hybrid nanoporous coatings fabricated from polysiloxane,” *ACS Appl. Mater. Interfaces*, vol. 6, no. 13, pp. 10014–21.

[157] H. C. Zhou X, Kong J, Sun J, Li H, “Stable superhydrophobic porous coatings from hybrid ABC triblock copolymers and their anticorrosive performance,” *ACS Appl. Mater. interfaces.*, vol. 9, no. 35, pp. 30056–63.

[158] G. F. Amigoni S, Taffin de Givenchy E, Dufay M, “Covalent layer-by-layer assembled superhydrophobic organic-inorganic hybrid films,” *Langmuir*, vol. 25, no. 18, pp. 11073–7.

[159] M. J. Zhang L, Xue CH, Cao M, Zhang MM, Li M, “Highly transparent fluorine-free superhydrophobic silica nanotube coatings,” *Chem. Eng. J.*, vol. 320, no. 1, pp. 244–52.

[160] Z. Wang, X. Chen, Y. Gong, B. Zhang, and H. Li, “Superhydrophobic nanocoatings prepared by a novel vacuum cold spray process,” *Surf. Coatings Technol.*, vol. 325, pp. 52–57, 2017, doi: 10.1016/j.surfcoat.2017.06.044.

Appendices

Appendix A

Table I: Recent studies on superhydrophobic surface fabrication, materials, characterizations and application

Authors	***Coating materials (based SH coating)***	***Coating Method/technique***	***Substrate***	***Contact angle***	***Coating layer thickness***	***Application***
De, N. et al. [133]	multiwalled carbon nanotube (MWCNT)	chemical vapor deposition (CVD)	Stain steels (flat plate)	154° ±4°	1.6 ± 0.8 µm	Corrosion and fouling and also imparts low friction and drag reduction properties.
Zhu, X. et al. [134]	multiwalled carbon nanotube (MWCNT)	Spraying followed by surface floatation	Many substrates (flat plate)	163° (a sliding angle =3°)	-	Practical applications with high abrasion strength.
Zhang, HF. et al. [135]	carbon nanotube/polydimethylsiloxane (CNT/ PDMS)	spray suspension technique	various kinds of solid substrates	166° (a sliding angle of <5°)	(Diameter 30–50 nm, length 10–20 mm, purity .95 wt-%)	fabricate SH coatings with suitability for engineering applications
Yang, Z. et al. [136]	epoxy coatings modified by fluorographene/ or graphene oxide	dip-coating method + FG powder was dispersed	Cupper substrate (flat plate)	154°	3.5 nm	self-cleaning properties, mechanical abrasion resistance, and chemical stability

Lin, Y. et al. [137]	graphene aerogels with a silane surface modification	Hummers' method+ Aqueous dispersions	-	160°	0.52 nm	Lightweight self-cleaning and anticorrosive materials.
Junaidi, MU et al. [138]	rice husk ash (RHA)	Spray method	glass slide (flat plate) + The concrete cubes	157.7°	-	Practical use in construction and building.
Meng, J. et al. [139]	the polymer solution+ inorganic nanoparticles of SiO2	Combining the spraying technique and non-solvent VIPS	clean glass substrate (flat plate)	>150°	-	preparing waterproof but breathable textile
Caldona et al. E.B. [140]	PR, PRS25, PRS30, PRS35, and PRS50	dip-coated	Impact-resistant carbon steel (CS) sheets	158° ± 1	-	anticorrosion and anti-ice tests + Glass micro slides (GS)
Liao C.S. et al. [141]	polybenzoxazine hybrid surfaces reinforced with SiO2 nanoparticles	a direct (UV) assisted replica moulding method	polybenzoxazin e hybrid surface	161.1° (a sliding angle of <3°)	-	It served as a mechanical hand to transfer water droplets from a SHS to a hydrophilic one.
Cao, D. et al. [142]	photo-crosslinked polyurethane (PU) and organic fluoro group-functionalized SiO2 nanoparticles	Soaked + immersion	resin composite (dental body)	160.1°), low sliding angle (<1°)	113.5 nm	a dental composite restoration.
Sparks, B.J. et al. [143]	inorganic-organic thiol-ene which consist of pentaerythritol tetra (PETMP), triallyl isocyanurate (TTT),	sequential spray-deposition and photo-polymerization	a variety of substrate surfaces including glass, paper, stone,	(>150°), low roll-off angles (<5°)	-	Scalable for treatment of large-area substrates and has the potential to provide an

	tetravinylcyclotetrasiloxane (TMTVSi), and hydrophobic fumed silica nanoparticles		and cotton fabric.			economical route to SHS for textiles and other industrial applications.
Chen, J. et al. [144]	hydrolysis process of TEOS and silica nanoparticles thin	the one-step chemical vapor deposition method	Glass slides	CAH(5.3°, 4.9°, 4.9°, 2.2° and 4.8° at 0.5s, respectivel y	20 ± 5 nm & 50 ± 5 nm	self-cleaning and the antifogging property
Jiang, C. et al. [145]	Trimethylsiloxa-ne suspension onto a precoated polyurethane	Spin coating	the bare glass substrate	154.7°-163.1°	240 nm	waterproof light-emitting devices, solar cell panels, window treatments
Steele, A. et al. [146]	casting suspensions of ZnO nanoparticles onto polymers (a hierarchical nanotextured surface)	spray-coating method	Almost any surface (glass substrate used)	157° & 168°,	-	The coatings can be applied to large and/or flexible substrates.
Wang, C.F. et al. [147]	Nonfluorinated zinc oxide-coated mesh films	Hydrothermal process	steel substrates	(>150°)	(mesh films having a pore size of appro. 38 & 600 µm	This surface can be used for under water− oil capturing.
Zhang, J. et al. [148]	nonfluorinated zinc oxide/ polydimethylsiloxane	Casting method	PDMS Substrate-polymeric substrate	(160° ± 2°), roll-off angles 3°	-	The anti-oil-fouling performance is the swelling of the

						underlying PDMS substrate
Lai, Y. et al. [149]	The TNBs, functionalized titanium dioxide nanobelts	electrophoretic deposition	glass substrate	(>160°)	600 nm	self-cleaning and anti-fogging
Holtzinger, C. et al. [150]	polystyrene spheres grafted with hexadecyl trimethoxysilane	deposited by spin-coating	silicon substrates	160°	-	a facile route used to produce strongly rough TiO2 coatings
Xu, Q.F. et al. [151]	the multifunctional TiO2 high-density polyethylene (HDPE)	A lamination templating method	polymer substrate	158 to 156°	from microscale to nanoscale	To produce an antimicrobial material
Bayer, I. S. et al. [152]	polyurethane−organoclay nanocomposites coating	spray-coating method	aluminum substrates	155°	-	Specific biomedical applications.
Steel, A. et al. [153]	Polyurethane coatings	Spray-airbrush atomizer method	aluminum substrate	>160°	-	investigating the substrate adhesion
Lee, S. G. et al. [154]	Silica-fluoropolymer hybrid nanoparticles	spray-coating method	Glass, steel, polymers substrates	151°, 163°, 150° for all substrate	-	highly transparent superhydrophobic/ superamphiphobic coatings
De Franciso, R. et al. [155]	polyfluorene/organosilica (PFO/Si)	sprayed method	glass, Whatman paper, and cellulose-based substrates	165°± 2	444, 465, and 496 nm	Easy adaptation to use in industrial applications
Wang, D. et al. [156]	(PSO) + (PDMS)	spin-coated + solidification-induced	glass substrate	155°	Between 2 and 7 μm	Safety goggles, windshields, solar cell panels, and

						windows for electronic devices.
Zhou, X. et al. [157]	triblock copolymers (PDMS–PS–PiBuPOSSMA)	the solution-casting(Deposition) method	stainless-steel cylinder substrates	137.5°±15 to 158.9 °± 1°	4.5 ± 1.1 µm to 33.2 ± 0.5 µm	Anticorrosive paints for metal protection application
Amigoni, S. et al. [158]	assembling covalently different layers of amino- and epoxy-functionalized silica nanoparticles	Layer by layer technique	Sloid substrate	150°	-	Antibacterial activities.
Zhang, L. et al. [159]	silica nanotubes + polymethylsiloxane + multiwalled carbon nanotubes	spraying a dispersion process	glass substrate	higher (WCA) of 165°, SA lower than 3°	-	Outdoor self-cleaning properties & a protective cover over solar cells
Wang, Z. et al. [160]	Oleic acid (OA)-modified TiO2 nanoparticles.	Vacuum cold spray (ceramic coating technology)	Aluminum substrate	a CA of 151.2°and a SA of 1.2°	70–80 µm	Characterization of hydrophobicity

Appendix B

Company:
Street:
City:

QM Report

Test | Info Air Check
c529744e-f660-4399-9822-7a7f2bd674ff

Test created by operator: rheometer
Test creation date: 5/12/2021 10:25:59 AM

Origin of project: RoutineAdjustments
2352f277-34af-4e42-b04f-57a2646ce9f2

-

Measuring Set | Info

Configuration:
ay default configuration
Device:
MCR 301 SN80520801
Measuring cell:
C-PTD200 SN80521112
Measuring system:
CC27 SN17316

-

Precision Air Check

Measuring point [first] | Torque precision value:
Measuring point [last] | Torque precision value: 0.004586 µN·m
Arithmetic mean of residual torque (precision value): 0µNm +/- 0.0151 µN·m

-

Quick Air Check

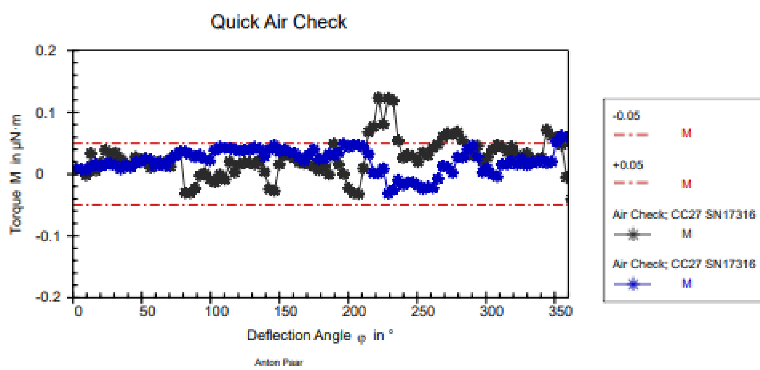

Measurement success state: OK
Project approval status: Project is created from unapproved template
Timestamp of printout: 5/12/2021 10:52:01 AM

Signature of operator: ____________ Name: Date:

Signature of approver: ____________ Name: Date:

Page 1 of 1

Company:
Street:
City:

QM Report

Test | Info

	Air Check 735b241c-9526-41eb-8765-21b864c881e5
Test created by operator:	rheometer
Test creation date:	5/20/2021 11:49:12 AM
Origin of project:	RoutineAdjustments 2352f277-34af-4e42-b04f-57a2646ce9f2

-

Measuring Set | Info

Configuration:
ay default configuration
Device:
MCR 301 SN80520801
Measuring cell:
C-PTD200 SN80521112
Measuring system:
CC27 SN17316

-

Precision Air Check

Measuring point [first] | Torque precision value:	-0.02443 μN·m
Measuring point [last] | Torque precision value:	-0.02244 μN·m
Arithmetic mean of residual torque (precision value):	0μNm +/- 0.02169 μN·m

-

Quick Air Check

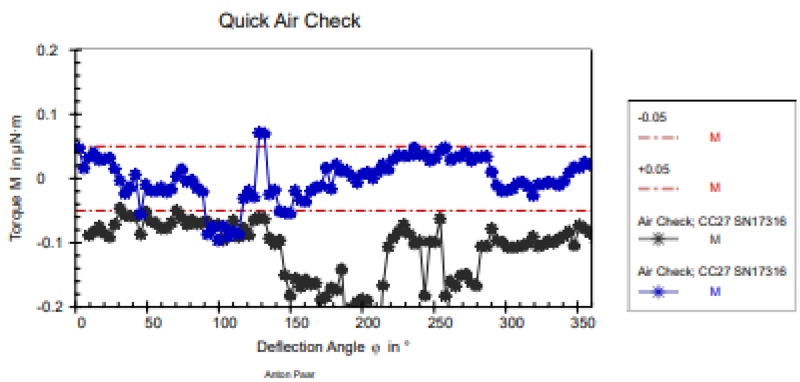

Measurement success state:	OK
Project approval status:	Project is created from unapproved template
Timestamp of printout:	5/20/2021 12:06:04 PM

Signature of operator: ____________________ Name: Date:

Signature of approver: ____________________ Name: Date:

Page 1 of 1

Appendix C

Rheometer measurements output sample using water

Project: Flow Curve | DESKTOP-K6DAQI5, 5/7/2021 | 1

Test: Water-FPC-800M-3rd trial

Result: Viscosity curve 1

Interval and data points: 1 41

Interval data: Point No.	Shear Rate	Shear Stress	Viscosity	Temperature	Torque	Rotational Speed	Status
	[1/s]	[Pa]	[mPa·s]	[°C]	[mN·m]	[1/min]	
1	2	0.0018428	0.92161	20	9.79E-05	1.5567	Dy_auto
2	2.34	0.0025491	1.0913	20	0.0001354	1.8185	Dy_auto
3	2.73	0.0029565	1.0835	20	0.00015704	2.1244	Dy_auto
4	3.19	0.0035135	1.1023	20	0.00018663	2.4815	Dy_auto
5	3.72	0.0037298	1.0018	20	0.00019812	2.8987	Dy_auto
6	4.35	0.0042928	0.98704	20	0.00022802	3.3859	Dy_auto
7	5.08	0.0048533	0.95536	20	0.00025779	3.955	Dy_auto
8	5.93	0.0058576	0.98713	20	0.00031114	4.6198	Dy_auto
9	6.93	0.0068463	0.98772	20	0.00036366	5.3963	Dy_auto
10	8.1	0.0084102	1.0387	20	0.00044673	6.3033	Dy_auto
11	9.46	0.0098293	1.0393	20	0.0005221	7.3628	Dy_auto
12	11	0.010846	0.98181	20	0.00057612	8.6004	Dy_auto
13	12.9	0.013222	1.0247	20	0.00070234	10.046	Dy_auto
14	15.1	0.015607	1.0354	20	0.00082898	11.735	Dy_auto
15	17.6	0.017363	0.98616	20	0.00092226	13.707	Dy_auto
16	20.6	0.021375	1.0393	20	0.0011354	16.011	Dy_auto
17	24	0.025024	1.0417	20	0.0013292	18.702	Dy_auto
18	28.1	0.029296	1.0441	20	0.0015561	21.846	Dy_auto
19	32.8	0.034172	1.0426	20	0.0018151	25.518	Dy_auto
20	38.3	0.041848	1.093	20	0.0022229	29.807	Dy_auto
21	44.7	0.047871	1.0704	20	0.0025428	34.817	Dy_auto
22	52.2	0.056446	1.0806	20	0.0029983	40.669	Dy_auto
23	61	0.066855	1.0956	20	0.0035511	47.505	Dy_auto
24	71.3	0.079886	1.1208	20	0.0042433	55.489	Dy_auto
25	83.3	0.092607	1.1123	20	0.004919	64.816	Dy_auto
26	97.2	0.11003	1.1315	20	0.0058446	75.711	Dy_auto
27	114	0.138	1.2148	20	0.0073302	88.437	Dy_auto
28	133	0.18627	1.4038	20	0.009894	103.3	Dy_auto
29	155	0.23748	1.5322	20	0.012614	120.67	Dy_auto
30	181	0.29881	1.6505	20	0.015872	140.95	Dy_auto
31	211	0.40522	1.9162	20	0.021524	164.64	Dy_auto
32	247	0.51708	2.0933	20	0.027466	192.31	Dy_auto
33	289	0.64667	2.2412	20	0.034349	224.64	Dy_auto
34	337	0.82868	2.4587	20	0.044017	262.4	Dy_auto
35	394	1.0434	2.6502	20	0.055421	306.5	Dy_auto
36	460	1.3025	2.8324	20	0.069186	358.01	Dy_auto
37	537	1.5963	2.9718	20	0.084791	418.2	Dy_auto
38	627	2.0631	3.2881	20	0.10958	488.48	Dy_auto
39	733	2.583	3.5244	20	0.1372	570.59	Dy_auto
40	856	3.2695	3.819	20	0.17367	666.5	Dy_auto
41	1.00E+03	4.0826	4.0826	20	0.21686	778.53	Dy_auto

Project: Flow Curve | DESKTOP-K6DAQI5, 5/7/2021 | 1

Test: Water-UED-3rd trial

Result: Viscosity curve 1

Interval an	1	41						
Interval da	Point No.	Shear Rate	Shear Stre:	Viscosity	Temperatu	Torque	Rotational	Status
		[1/s]	[Pa]	[mPa·s]	[°C]	[mN·m]	[1/min]	
	1	2	0.001848	0.92413	20	9.8153E-0!	1.5567	Dy_auto
	2	2.34	0.001917	0.8208	20	0.000102	1.8185	Dy_auto
	3	2.73	0.002992	1.0963	20	0.000159	2.1244	Dy_auto
	4	3.19	0.00332	1.0415	20	0.000176	2.4815	Dy_auto
	5	3.72	0.004192	1.1258	20	0.000223	2.8987	Dy_auto
	6	4.35	0.004035	0.92785	20	0.000214	3.3859	Dy_auto
	7	5.08	0.005407	1.0643	20	0.000287	3.955	Dy_auto
	8	5.93	0.00614	1.0347	20	0.000326	4.6198	Dy_auto
	9	6.93	0.006695	0.96588	20	0.000356	5.3963	Dy_auto
	10	8.1	0.007822	0.9661	20	0.000415	6.3033	Dy_auto
	11	9.46	0.009462	1.0005	20	0.000503	7.3628	Dy_auto
	12	11	0.011076	1.0026	20	0.000588	8.6004	Dy_auto
	13	12.9	0.012928	1.0019	20	0.000687	10.046	Dy_auto
	14	15.1	0.015514	1.0292	20	0.000824	11.735	Dy_auto
	15	17.6	0.018071	1.0264	20	0.00096	13.707	Dy_auto
	16	20.6	0.021985	1.069	20	0.001168	16.011	Dy_auto
	17	24	0.025721	1.0707	20	0.001366	18.702	Dy_auto
	18	28.1	0.028499	1.0156	20	0.001514	21.846	Dy_auto
	19	32.8	0.034977	1.0671	20	0.001858	25.518	Dy_auto
	20	38.3	0.041184	1.0757	20	0.002188	29.807	Dy_auto
	21	44.7	0.047329	1.0583	20	0.002514	34.817	Dy_auto
	22	52.2	0.054945	1.0518	20	0.002919	40.669	Dy_auto
	23	61	0.067545	1.107	20	0.003588	47.505	Dy_auto
	24	71.3	0.076519	1.0736	20	0.004065	55.49	Dy_auto
	25	83.3	0.091645	1.1008	20	0.004868	64.817	Dy_auto
	26	97.2	0.11523	1.1849	20	0.006121	75.711	Dy_auto
	27	114	0.13172	1.1596	20	0.006997	88.437	Dy_auto
	28	133	0.18207	1.3721	20	0.009671	103.3	Dy_auto
	29	155	0.23943	1.5448	20	0.012718	120.67	Dy_auto
	30	181	0.30319	1.6746	20	0.016104	140.95	Dy_auto
	31	211	0.39063	1.8472	20	0.020749	164.64	Dy_auto
	32	247	0.51476	2.0839	20	0.027343	192.31	Dy_auto
	33	289	0.66888	2.3181	20	0.035529	224.64	Dy_auto
	34	337	0.81718	2.4246	20	0.043406	262.39	Dy_auto
	35	394	1.0336	2.6255	20	0.054902	306.49	Dy_auto
	36	460	1.2922	2.8099	20	0.068636	358.02	Dy_auto
	37	537	1.6199	3.0157	20	0.086045	418.19	Dy_auto

Project: Flow Curve | DESKTOP-K6DAQI5, 5/7/2021 | 1

Test: Water-Nasiol SHBC-3rd trial

Result: Viscosity curve 1

Interval and data points: 1 41

Interval data:	Point No.	Shear Rate	Shear Stress	Viscosity	Temperature	Torque	Rotational Speed	Status
		[1/s]	[Pa]	[mPa·s]	[°C]	[mN·m]	[1/min]	
	1	2	0.01816	9.0817	20.00	0.00096459	1.5567	Dy_auto
	2	2.34	0.018052	7.7284	20.00	0.0009589	1.8185	Dy_auto
	3	2.73	0.020853	7.6423	20.00	0.0011077	2.1244	Dy_auto
	4	3.19	0.019791	6.2091	20.00	0.0010512	2.4815	Dy_auto
	5	3.72	0.020608	5.5351	20.00	0.0010947	2.8987	Dy_auto
	6	4.35	0.021295	4.8965	20.00	0.0011311	3.3859	Dy_auto
	7	5.08	0.02355	4.6357	20.00	0.0012509	3.955	Dy_auto
	8	5.93	0.023178	3.9059	20.00	0.0012311	4.6198	Dy_auto
	9	6.93	0.023983	3.46	20.00	0.0012739	5.3963	Dy_auto
	10	8.1	0.025102	3.1003	20.00	0.0013333	6.3033	Dy_auto
	11	9.46	0.027464	2.904	20.00	0.0014588	7.3628	Dy_auto
	12	11	0.030094	2.7242	20.00	0.0015985	8.6004	Dy_auto
	13	12.9	0.031853	2.4685	20.00	0.0016919	10.046	Dy_auto
	14	15.1	0.034135	2.2647	20.00	0.0018132	11.735	Dy_auto
	15	17.6	0.037322	2.1198	20.00	0.0019824	13.707	Dy_auto
	16	20.6	0.0409	1.9888	20.00	0.0021725	16.011	Dy_auto
	17	24	0.044944	1.8709	20.00	0.0023873	18.702	Dy_auto
	18	28.1	0.049651	1.7695	20.00	0.0026373	21.846	Dy_auto
	19	32.8	0.04859	1.4825	20.00	0.002581	25.518	Dy_auto
	20	38.3	0.042412	1.1078	20.00	0.0022528	29.807	Dy_auto
	21	44.7	0.051113	1.1429	20.00	0.002715	34.817	Dy_auto
	22	52.2	0.059689	1.1426	20.00	0.0031705	40.669	Dy_auto
	23	61	0.071311	1.1687	20.00	0.0037879	47.505	Dy_auto
	24	71.3	0.083033	1.165	20.00	0.0044105	55.49	Dy_auto
	25	83.3	0.10076	1.2102	20.00	0.0053519	64.817	Dy_auto
	26	97.2	0.12087	1.2429	20.00	0.0064205	75.711	Dy_auto
	27	114	0.1357	1.1946	20.00	0.0072081	88.437	Dy_auto
	28	133	0.17187	1.2953	20.00	0.009129	103.3	Dy_auto
	29	155	0.24574	1.5855	20.00	0.013053	120.66	Dy_auto
	30	181	0.31159	1.7211	20.00	0.016551	140.95	Dy_auto
	31	211	0.39447	1.8653	20.00	0.020953	164.64	Dy_auto
	32	247	0.5089	2.0602	20.00	0.027031	192.31	Dy_auto
	33	289	0.66349	2.2995	20.00	0.035243	224.64	Dy_auto
	34	337	0.85248	2.5293	20.00	0.045281	262.39	Dy_auto
	35	394	1.0883	2.7644	20.00	0.057808	306.49	Dy_auto
	36	460	1.3403	2.9145	20.00	0.071192	358.02	Dy_auto
	37	537	1.6493	3.0705	20.00	0.087609	418.19	Dy_auto
	38	627	2.0145	3.2106	20.00	0.107	488.48	Dy_auto
	39	733	2.5482	3.4769	20.00	0.13535	570.59	Dy_auto
	40	856	3.2205	3.7618	20.00	0.17106	666.49	Dy_auto
	41	1E+03	4.1067	4.1068	20.00	0.21814	778.53	Dy_auto

Project: Flow Curve | DESKTOP-K6DAQI5, 5/7/2021 | 1

Test: Water-W/O-C 3rd Trial

Result: Viscosity curve 1

Interval and data points: 1 41

Interval data:

Point No.	Shear Rate	Shear Stress	Viscosity	Temperature	Torque	Rotational Speed	Status
	[1/s]	[Pa]	[mPa·s]	[°C]	[mN·m]	[1/min]	
1	2	0.0018267	0.91355	20.00	9.7029E-05	1.5567	Dy_auto
2	2.34	0.0027553	1.1796	20.00	0.00014635	1.8185	Dy_auto
3	2.73	0.0023011	0.84328	20.00	0.00012223	2.1244	Dy_auto
4	3.19	0.0029623	0.92937	20.00	0.00015735	2.4815	Dy_auto
5	3.72	0.0034852	0.93605	20.00	0.00018512	2.8987	Dy_auto
6	4.35	0.0041676	0.95827	20.00	0.00022137	3.3859	Dy_auto
7	5.08	0.0047708	0.93912	20.00	0.00025341	3.955	Dy_auto
8	5.93	0.0059445	1.0018	20.00	0.00031576	4.6198	Dy_auto
9	6.93	0.0066093	0.95353	20.00	0.00035107	5.3963	Dy_auto
10	8.1	0.0078353	0.96774	20.00	0.00041619	6.3033	Dy_auto
11	9.46	0.0096291	1.0182	20.00	0.00051147	7.3628	Dy_auto
12	11	0.010679	0.96671	20.00	0.00056725	8.6005	Dy_auto
13	12.9	0.012778	0.99024	20.00	0.00067872	10.046	Dy_auto
14	15.1	0.0147	0.97529	20.00	0.00078084	11.735	Dy_auto
15	17.6	0.017164	0.97486	20.00	0.00091169	13.707	Dy_auto
16	20.6	0.021439	1.0425	20.00	0.0011388	16.011	Dy_auto
17	24	0.025118	1.0456	20.00	0.0013342	18.702	Dy_auto
18	28.1	0.027888	0.99385	20.00	0.0014813	21.846	Dy_auto
19	32.8	0.034028	1.0382	20.00	0.0018075	25.518	Dy_auto
20	38.3	0.040871	1.0675	20.00	0.0021709	29.807	Dy_auto
21	44.7	0.046362	1.0367	20.00	0.0024626	34.817	Dy_auto
22	52.2	0.053522	1.0246	20.00	0.0028429	40.669	Dy_auto
23	61	0.066279	1.0862	20.00	0.0035206	47.505	Dy_auto
24	71.3	0.075393	1.0578	20.00	0.0040047	55.49	Dy_auto
25	83.3	0.089038	1.0695	20.00	0.0047295	64.817	Dy_auto
26	97.2	0.11312	1.1632	20.00	0.0060088	75.711	Dy_auto
27	114	0.13342	1.1746	20.00	0.007087	88.437	Dy_auto
28	133	0.18936	1.4271	20.00	0.010058	103.3	Dy_auto
29	155	0.23623	1.5241	20.00	0.012548	120.67	Dy_auto
30	181	0.29587	1.6343	20.00	0.015716	140.95	Dy_auto
31	211	0.3911	1.8494	20.00	0.020774	164.64	Dy_auto
32	247	0.52073	2.108	20.00	0.027659	192.31	Dy_auto
33	289	0.66292	2.2975	20.00	0.035212	224.64	Dy_auto
34	337	0.83864	2.4883	20.00	0.044546	262.39	Dy_auto
35	394	1.057	2.6848	20.00	0.056143	306.5	Dy_auto
36	460	1.2903	2.8057	20.00	0.068535	358.02	Dy_auto
37	537	1.6078	2.9932	20.00	0.085404	418.2	Dy_auto
38	627	2.0037	3.1935	20.00	0.10643	488.48	Dy_auto
39	733	2.562	3.4956	20.00	0.13608	570.59	Dy_auto
40	856	3.1222	3.647	20.00	0.16584	666.49	Dy_auto
41	1E+03	3.901	3.901	20.00	0.20721	778.53	Dy_auto

Appendix D

Uncertainty evaluation

The measurement uncertainties are evaluated here using Eq. (5-5) and presented in Table IV. Due to the consistent occurrence of $\delta\tau_c$ being smaller than $\delta\tau_s$ in drag reduction experiments, the τ_c/τ_s ratio is below 1. In such experimental scenarios, the minimum value of τ_s is around 1 mN·m, and the uncertainty ($\delta\tau$) in the rheometer used is approximately 0.001 mN·m. The maximum uncertainty of drag reduction δ(DR) is 2, which happens at the first measurement point (first Re number). The high uncertainty levels observed in the rheometer measurements using superhydrophobic surfaces can be attributed to several factors. One of the main reasons is the presence of the plastron layer or trapped air pockets on the superhydrophobic surface. These trapped air pockets can cause fluctuations in the test fluid flow at the beginning of the measurement, leading to inconsistencies in the measured torque.

Additionally, the random nature of the textured superhydrophobic surfaces can contribute to the uncertainty. These surfaces' roughness and nano, micro-scale structures create an uneven flow profile, leading to inconsistent shear rates and increased uncertainty in the measurements. The plastron layer becomes more homogeneous with increased shear rate and increases in thickness [40], thus causing a reduction in the uncertainty at high Re numbers in transition and turbulent flow regimes. The minimum uncertainty of drag reduction δ(DR) evaluated in the present study ranges from 0.0007 to 0.005, significantly smaller than the range of drag reduction observed in the experiment. Error bars are not shown in the Figures of results for better readability. The minimum, maximum and average uncertainties of drag reduction δ(DR) for all the measurements are illustrated in Table I, and the uncertainties of all measurements are illustrated in Table II.

Table I summary of the uncertainties of drag reduction δ(DR) from all measurements.

Liquid	δ(DR)	FPC-M	UED	SHBC	Re number
Water	Min	0.005045	0.005043	0.005021	1227
	Max	2.014969	1.788956	1.85877	2.5
	Average	0.227554	0.220968	0.222646	-
5 cSt	Min	0.001334	0.001299	0.001296	0.419
	Max	1.724218	1.93445	1.68213	418
	Average	0.394896	0.425101	0.398954	-
10 cSt	Min	0.000728	0.000725	0.000733	205
	Max	1.264896	1.274552	1.312821	0.205
	Average	0.196506	0.197091	0.202145	-

Table II The uncertainties of drag reduction δ(DR) from all measurements of water

Water			
Smooth	FPC-800M	UED	SHBC
1.8004	2.0150	1.7890	1.8588
0.9856	0.8898	0.9252	0.8303
0.8968	0.8448	0.8406	0.9194
0.9779	1.0719	0.9568	0.9981
0.6528	0.6147	0.6423	0.6361
0.6132	0.5952	0.5760	0.5837
0.5435	0.5392	0.5570	0.5738
0.3963	0.3729	0.3827	0.3723
0.3734	0.3634	0.3667	0.3593
0.3227	0.3254	0.3191	0.3111
0.2631	0.2585	0.2564	0.2525
0.2313	0.2246	0.2287	0.2278
0.1990	0.1986	0.1983	0.1946
0.1700	0.1690	0.1688	0.1670
0.1464	0.1440	0.1454	0.1446
0.1142	0.1098	0.1110	0.1094
0.0974	0.0940	0.0949	0.0934
0.0839	0.0805	0.0806	0.0800
0.0723	0.0700	0.0709	0.0701

0.0613	0.0603	0.0602	0.0590
0.0527	0.0514	0.0516	0.0512
0.0430	0.0410	0.0410	0.0409
0.0380	0.0372	0.0376	0.0372
0.0334	0.0333	0.0332	0.0329
0.0280	0.0276	0.0279	0.0278
0.0221	0.0213	0.0218	0.0216
0.0187	0.0184	0.0182	0.0179
0.0127	0.0120	0.0117	0.0118
0.0103	0.0099	0.0100	0.0099
0.0085	0.0084	0.0084	0.0085
0.0066	0.0066	0.0065	0.0065
0.0052	0.0052	0.0052	0.0052
0.0040	0.0039	0.0039	0.0040
0.0031	0.0031	0.0031	0.0031
0.0024	0.0023	0.0024	0.0023
0.0019	0.0019	0.0019	0.0019
0.0015	0.0014	0.0014	0.0014
0.0012	0.0011	0.0011	0.0011
0.0010	0.0009	0.0009	0.0009
0.0008	0.0007	0.0007	0.0007
0.0005	0.0005	0.0005	0.0005

Table III The uncertainties of drag reduction δ(DR) for all measurements of 5 & 10 cSt silicone oil

5 cSt Silicone oil				10 cSt Silicone oil			
Smooth	FPC-800M	UED	SHBC	Smooth	FPC-800M	UED	SHBC
1.8702	1.7395	1.9302	1.7742	1.3177	1.2649	1.2746	1.3128
1.7369	1.6175	1.7266	1.6504	1.1624	1.1419	1.1338	1.1656
1.6037	1.4956	1.6160	1.5266	0.9720	0.9421	0.9427	0.9726
1.4704	1.3736	1.4814	1.4027	0.8329	0.8046	0.8101	0.8294
1.4094	1.2516	1.4198	1.2789	0.7294	0.7149	0.7163	0.7301

1.2219	1.1296	1.2317	1.1551	0.6139	0.5944	0.5988	0.6136
1.0385	1.0383	1.0417	1.0597	0.5234	0.5065	0.5089	0.5195
0.8760	0.8646	0.8821	0.8870	0.4558	0.4449	0.4455	0.4559
0.7487	0.7369	0.7539	0.7601	0.3897	0.3798	0.3807	0.3902
0.6440	0.6356	0.6477	0.6543	0.3335	0.3246	0.3258	0.3337
0.5504	0.5428	0.5515	0.5569	0.2849	0.2773	0.2780	0.2843
0.4772	0.4747	0.4775	0.4853	0.2429	0.2354	0.2371	0.2427
0.4058	0.4014	0.4069	0.4117	0.2089	0.2030	0.2038	0.2086
0.3456	0.3411	0.3451	0.3493	0.1794	0.1744	0.1753	0.1795
0.2966	0.2928	0.2957	0.2995	0.1536	0.1491	0.1499	0.1536
0.2547	0.2513	0.2553	0.2579	0.1319	0.1284	0.1287	0.1318
0.2180	0.2148	0.2183	0.2207	0.1133	0.1104	0.1106	0.1133
0.1851	0.1820	0.1839	0.1860	0.0965	0.0937	0.0942	0.0965
0.1594	0.1570	0.1591	0.1608	0.0830	0.0807	0.0811	0.0831
0.1356	0.1335	0.1347	0.1362	0.0708	0.0687	0.0692	0.0709
0.1157	0.1135	0.1150	0.1163	0.0611	0.0595	0.0597	0.0612
0.0983	0.0962	0.0971	0.0983	0.0522	0.0507	0.0510	0.0523
0.0843	0.0826	0.0838	0.0847	0.0448	0.0436	0.0437	0.0448
0.0712	0.0694	0.0705	0.0712	0.0383	0.0374	0.0374	0.0383
0.0609	0.0595	0.0601	0.0607	0.0326	0.0317	0.0319	0.0326
0.0524	0.0513	0.0519	0.0525	0.0280	0.0272	0.0273	0.0280
0.0440	0.0429	0.0434	0.0438	0.0239	0.0232	0.0233	0.0239
0.0376	0.0366	0.0371	0.0375	0.0205	0.0199	0.0200	0.0205

0.0319	0.0311	0.0315	0.0318	0.0175	0.0171	0.0171	0.0176
0.0271	0.0263	0.0266	0.0269	0.0148	0.0144	0.0145	0.0148
0.0229	0.0222	0.0224	0.0226	0.0127	0.0123	0.0124	0.0127
0.0194	0.0189	0.0191	0.0192	0.0108	0.0105	0.0105	0.0108
0.0165	0.0160	0.0162	0.0163	0.0091	0.0089	0.0089	0.0091
0.0139	0.0135	0.0136	0.0137	0.0078	0.0076	0.0076	0.0078
0.0118	0.0115	0.0116	0.0117	0.0066	0.0065	0.0065	0.0066
0.0099	0.0095	0.0096	0.0097	0.0056	0.0055	0.0055	0.0056
0.0084	0.0081	0.0081	0.0082	0.0048	0.0046	0.0047	0.0048
0.0070	0.0067	0.0068	0.0068	0.0041	0.0039	0.0040	0.0040
0.0057	0.0055	0.0055	0.0055	0.0034	0.0033	0.0033	0.0034
0.0044	0.0042	0.0042	0.0044	0.0029	0.0028	0.0028	0.0029
0.0034	0.0033	0.0033	0.0033	0.0025	0.0024	0.0024	0.0024
0.0026	0.0025	0.0025	0.0025	0.0021	0.0020	0.0020	0.0021
0.0020	0.0020	0.0020	0.0020	0.0017	0.0016	0.0016	0.0016
0.0016	0.0016	0.0016	0.0016	0.0012	0.0012	0.0012	0.0012
0.0012	0.0012	0.0012	0.0012	0.0009	0.0009	0.0009	0.0009
0.0010	0.0010	0.0009	0.0009	0.0007	0.0007	0.0007	0.0007

Appendix E
Defect Theory Derivation of the Outer Wall of Taylor-Couette Cell Flow

Using the defect theory, Panton [109] matches the approximately constant angular momentum in the bulk of the TC flow to that of the wall layers.

$$\langle \gamma \rangle = r \cdot \langle V_\theta \rangle \quad \text{(E-1)}$$

In the outer bulk region, the angular momentum in his theory is expressed as:

$$\langle \gamma \rangle = \langle \gamma_o \rangle + \langle \frac{u_\tau}{V_i} \rangle \langle \gamma_1 \rangle \quad \text{(E-2)}$$

Where $V_i = \Omega \cdot r_i$ is the inner rotor velocity (measuring bob) $\langle \gamma_o \rangle$ is the constant angular velocity; $\langle \gamma_1 \rangle$ is a first-order correction

V_θ is the circumferential velocity, and a time average is indicated by $\langle \quad \rangle$

- In the limit of Re $\longrightarrow \infty$, the ratio of the rotor velocity $\langle \frac{u_\tau}{V_i} \rangle \to 0$.

Therefore, it is the introduction of the defect term $\langle \gamma_1 \rangle$ that facilitates matching with the wall layer.

On the inner wall, the angular momentum decreases as $(r_i V_i) - \langle \gamma \rangle$, where the $(r_i V_i)$ is the angular momentum, which is induced by wall motion.

Upon scaling with friction velocity u_τ and the viscous length scale δ_ν , the scaled angular momentum $\langle \gamma^+ \rangle$ can be defined as a function of the scaled wall distance $y^+ = \frac{(r - r_i)}{\delta_\nu}$ as follows:

$$\gamma^{+}{}_{(y^{+})} = \frac{r_i V_i - \langle\gamma\rangle}{r_i \cdot u_\tau} \tag{E-3}$$

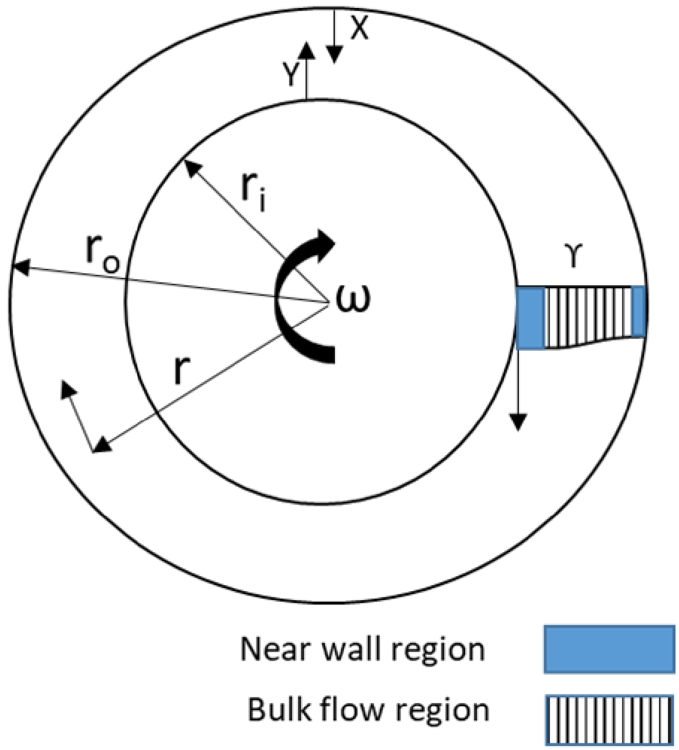

Figure E-1 Taylor – Couette flow with the inner cylinder rotating and the outer fixed cylinder

As Panton [109] suggested, the most important results come from mathematically matching the angular momentum laws of the core and wall regions. There is an overlap region where both the wall representation $\gamma^{+}{}_{(y^{+})}$ and the core representation $\Gamma_{(Y)}$ are valid. Where $\Gamma_o = \frac{\langle\gamma_o\rangle}{(r_i \cdot V_i)}$, and $\Gamma_{1(Y)} = \frac{\langle\gamma_1\rangle}{(r_i \cdot V_i)}$.

Matching these values in the overlap region leads to:

$$(\gamma^{+})\left(\frac{u_\tau}{V_i}\right) = 1 - \Gamma_o - \left(\frac{u_\tau}{V_i}\right) \cdot \Gamma_{1(Y)} \tag{E-4}$$

where Γ_1 is a function of the outer variable $Y = \frac{(r-r_i)}{d}$ while γ^+ is a function of

$$y^+ = \frac{(r-r_i)}{\delta_\nu}$$

Proceeding according to Panton [1], differentiating both sides of Equation (E-3) by Y in the overlap region and using the relation

$\frac{y^+}{Y} = \frac{\Delta r}{\delta_\nu}$ results in the relation:

$$y^+ \frac{d\gamma^+}{dy^+} = -Y \frac{d\Gamma_1}{dY} \equiv \frac{1}{\alpha} \tag{E-5}$$

where α is a constant independent of Y and y^+.

Panton [109] suggested that for a boundary layer in the Taylor Couette cell, α should reduce to the universal von Karman constant K in the zero curvature limit. Solving this expression results in the identical set of the equation of ϒ+ and Γ 1 that Panton [109] obtains as:

$$\Gamma_1 = \frac{-1}{\alpha} \cdot \ln Y + C_1 \qquad \longrightarrow \qquad Y \tag{E-6}$$

$$\gamma^+ = \frac{1}{\alpha} \cdot \ln(y^+) \qquad y^+ \rightarrow \infty \tag{E-7}$$

However, the substitution of Eq. (E-6) and Eq. (E-7) into our modified form of Eq. (4) gives

Where $Re_\tau = \frac{u_\tau \cdot d}{\nu}$

Repeating the same calculation at the coated stationary outer wall surface in the X direction with:

$$\gamma^+ = \frac{\left(r_o \cdot V_{Slip} - \langle \gamma \rangle\right)}{r_i \cdot u_\tau} \tag{E-8}$$

First, considering the existence of an overlap region where both representations are valid, Eq. (1) can be substituted into Equation (E-8). Then, using the modified theory of Srinivasan's work [34] by introducing a finite averaged slip velocity $\langle V_{slip} \rangle$ that is related to the local viscous stress at the outer CDC's wall by the Navier slip hypothesis as $\langle V_{Slip} \rangle = b \cdot \left(\frac{dV_\theta}{dX}\right)_{X=0}$, where b is the effective slip length due to the superhydrophobic coating and $\left(\frac{dV_\theta}{dX}\right)_{X=0}$ is the time-averaged velocity gradient at the wall.

The distance away from the outer (coated) wall expressed in wall units is

$$X^+ = \frac{(r_o - r)}{\delta_\nu} \tag{E-9}$$

If the velocity in the viscous sublayer close to the outer wall is shifted by a constant value, according to Min & Kim [96], so that $\langle V_\theta^+ \rangle = X^+ + b^+$ and $\frac{d\langle V_\theta \rangle^+}{dX^+} = 1$, the Navier slip hypothesis upon scaling reduces to :

$$V_{Slip}^+ = b^+ \tag{E-10}$$

where $V_{Slip}^+ = \frac{V_{Slip}}{u_\tau}$ and $b^+ = \frac{b_{eff}}{\delta_\nu}$

There is an overlap region where both the wall representation $(\gamma)_{(X)}^+$ and the core representation $\Gamma(X)$ are valid.

Matching the values in this region yields:

$$(\gamma^+ + b^+) = 1 - \Gamma_o - \frac{u_\tau}{V_i} \tag{E-11}$$

Repeating the argument given in the Y direction for the coated wall layer on the outer cylinder gives two more overlaps laws $(X = r_o - r), X = \frac{X}{d}$

$$X^+ = x \cdot \frac{u_\tau}{\nu} = XRe_\tau \; and \; \gamma^+ = \frac{\langle \gamma \rangle}{(r_o u_\tau)}$$

This leads to the following matched expression

$$\Gamma_1 = \frac{1}{\beta} ln(X) + C_3 \qquad X \to 0 \tag{E-12}$$

$$\gamma^+ = \frac{1}{\beta} ln(X^+) + C_4 \qquad X \to \infty \tag{E-13}$$

Substitute (13) and (14) in Equation. (12) leads to another friction velocity relation

$$\Gamma_o \frac{V_i}{u_\tau} = \frac{1}{\beta} lnRe_\tau + C_3 + C_4 + b^+ \tag{E-14}$$

Finally, Equations (8) and (15) are added together to eliminate Γ_o and using

$$\frac{V_i}{u_\tau} = \left(\frac{C_f}{2}\right)^{\frac{-1}{2}}$$

We obtain the modified skin friction law in the presence of slip that is used as eqn (15)

$$\sqrt{\frac{2}{C_f}} = M \cdot ln(Re_\tau) + N + b^+ \tag{E-16}$$

where, $M = \left(\frac{1}{\alpha} + \frac{1}{\beta}\right)$, and N=C_1+C_2+C_3+C_4 are constants that depend only on the curvature of the TC cell. These constants can be determined from friction measurements with non-coated surfaces and plotted in Prandtl-von Karman coordinates.

Appendix F

Measurement Uncertainty at X_1`

	Smooth			UED			FPC-800M			FT-MW		
Y+	Um	u'	<u'u'>	Um	u'	<u'u'>	Um	u'	<u'u'>	Um	u'	<u'u'>
0.00	2.95	3.99	8.41	0.40	0.53	0.01	0.40	0.39	0.91	0.40	0.57	1.02
8.45	0.40	11.96	3.10	0.40	0.53	0.01	0.40	0.69	0.79	0.40	0.47	0.99
16.90	0.42	6.34	9.51	0.40	0.42	0.02	0.40	0.49	0.83	0.40	0.38	1.23
25.35	0.43	5.04	10.71	0.43	3.21	0.81	0.40	0.68	1.84	0.40	1.50	4.15
33.80	0.42	5.96	10.25	0.43	3.86	1.17	0.40	1.92	5.35	0.40	1.55	4.21
42.25	0.42	5.48	10.36	0.45	4.49	1.61	0.40	2.09	5.82	0.48	1.65	4.61
50.69	0.42	5.68	10.15	0.43	4.40	1.53	0.40	2.24	6.25	0.46	1.66	4.62
59.14	0.42	5.84	10.13	0.45	4.46	1.59	0.40	2.38	6.65	0.47	2.41	6.77
67.59	0.42	5.79	10.34	0.44	4.45	1.58	0.40	2.28	6.38	0.47	2.44	6.86
76.04	0.42	4.99	11.14	0.42	3.87	1.19	0.40	2.22	6.21	0.58	2.43	6.85
84.49	0.42	5.23	10.31	0.43	4.31	1.48	0.40	2.45	6.86	0.58	2.73	7.69
92.94	0.41	5.89	9.81	0.42	3.98	1.26	0.40	2.37	6.61	0.59	2.81	7.92
101.39	0.41	5.48	10.17	0.43	4.02	1.28	0.40	2.27	6.35	0.66	2.71	7.65
109.84	0.41	5.43	10.67	0.43	4.08	1.32	0.40	2.36	6.60	0.68	2.92	8.23
118.29	0.41	5.70	10.43	0.43	4.34	1.50	0.40	2.33	6.49	0.66	2.88	8.13
126.74	0.42	5.37	10.14	0.43	4.22	1.42	0.40	2.49	6.98	0.70	2.90	8.19
135.19	0.42	4.75	11.06	0.42	3.88	1.20	0.40	2.46	6.90	0.68	3.00	8.44
177.43	0.41	5.40	10.17	0.43	4.19	1.40	0.40	2.22	6.20	0.69	2.80	7.90
219.68	0.41	5.80	10.18	0.42	3.87	1.20	0.40	2.32	6.49	0.70	2.67	7.52
261.92	0.41	5.37	9.99	0.43	4.18	1.39	0.40	2.29	6.40	0.65	2.79	7.87
304.17	0.41	5.95	9.34	0.42	3.78	1.14	0.40	2.36	6.62	0.64	2.54	7.17
346.42	0.41	6.26	9.34	0.41	3.48	0.96	0.40	2.29	6.39	0.66	2.61	7.34
388.66	0.41	5.48	9.66	0.41	3.36	0.90	0.40	2.18	6.11	0.60	2.63	7.41
430.91	0.41	6.38	8.92	0.41	3.22	0.82	0.40	2.15	6.03	0.60	2.41	6.78
473.15	0.41	6.44	8.54	0.41	3.07	0.75	0.40	2.08	5.81	0.61	2.32	6.52
515.40	0.41	6.45	8.51	0.40	2.94	0.69	0.40	2.09	5.85	0.56	2.40	6.75
557.64	0.40	7.04	7.68	0.40	2.85	0.65	0.40	2.09	5.84	0.54	4.49	12.68

Measurement's Uncertainty at X_2

	Smooth			UED			FPC-800M			FT-MW		
Y+	Um	u'	u'u'	Um	u'	u'u'	Um	u'	u'u'	Um	u'	u'u'
0.00	0.40	0.00	0.00	0.41	0.52	0.94	0.40	1.41	3.74	0.40	0.79	1.66
9.02	0.40	2.94	8.27	0.40	0.50	1.15	0.40	0.75	0.75	0.40	0.54	0.76
18.03	0.43	0.97	2.54	0.40	0.51	1.15	0.40	0.59	0.75	0.40	0.39	0.75
27.05	0.43	3.38	9.49	0.40	3.20	9.02	0.40	0.43	0.75	0.40	0.96	2.58
36.06	0.42	3.80	10.68	0.46	3.84	10.85	0.41	2.50	6.95	0.41	2.60	7.26
45.08	0.42	3.64	10.23	0.46	4.49	12.67	0.41	2.77	7.75	0.41	3.11	8.75
54.10	0.42	3.68	10.34	0.43	4.39	12.38	0.41	3.02	8.49	0.41	3.14	8.83
63.11	0.42	3.59	10.12	0.44	4.46	12.60	0.41	3.07	8.62	0.41	3.09	8.70
72.13	0.42	3.60	10.11	0.44	4.45	12.55	0.41	3.13	8.79	0.41	3.18	8.94
81.14	0.43	3.67	10.32	0.43	3.86	10.91	0.41	3.10	8.70	0.41	3.16	8.88
90.16	0.42	3.95	11.12	0.43	4.31	12.15	0.41	3.10	8.70	0.41	3.19	8.97
99.18	0.42	3.65	10.28	0.43	3.98	11.23	0.41	3.18	8.93	0.41	3.08	8.66
108.19	0.41	3.48	9.79	0.43	4.02	11.33	0.41	3.20	9.02	0.41	3.34	9.38
117.21	0.42	3.61	10.15	0.43	4.08	11.50	0.41	3.06	8.60	0.41	3.20	8.99
126.22	0.42	3.78	10.65	0.43	4.34	12.24	0.41	3.12	8.76	0.41	3.18	8.94
135.24	0.41	3.69	10.41	0.43	4.22	11.92	0.41	3.04	8.53	0.41	3.09	8.68
144.26	0.42	3.59	10.11	0.42	3.88	10.94	0.41	3.14	8.84	0.41	3.23	9.08
153.27	0.42	3.92	11.03	0.43	4.19	11.84	0.41	3.15	8.86	0.41	3.17	8.90
162.29	0.41	3.60	10.15	0.42	3.88	10.94	0.41	3.22	9.07	0.41	3.17	8.92
207.37	0.41	3.61	10.16	0.42	4.18	11.79	0.41	2.98	8.38	0.41	3.08	8.66
252.45	0.41	3.54	9.96	0.42	3.78	10.68	0.41	3.08	8.66	0.41	3.09	8.70
297.53	0.41	3.32	9.31	0.42	3.48	9.80	0.41	3.04	8.54	0.41	2.98	8.36
342.61	0.41	3.31	9.31	0.41	3.37	9.50	0.40	2.84	7.96	0.41	2.77	7.78
387.69	0.41	3.42	9.63	0.41	3.22	9.08	0.40	2.68	7.51	0.40	2.80	7.85
432.77	0.41	3.16	8.89	0.41	3.07	8.67	0.40	2.72	7.61	0.40	2.77	7.77
477.84	0.41	3.03	8.51	0.41	2.94	8.30	0.40	2.52	7.06	0.40	2.66	7.46
522.92	0.40	3.02	8.48	0.40	2.86	8.04	0.40	2.59	7.25	0.42	4.59	12.94
568.00	0.40	2.72	7.64	0.40	2.84	7.99	0.40	2.39	6.69	0.40	2.45	6.85
613.08	0.95	2.73	7.65	0.40	2.80	7.89	0.40	2.30	6.43	0.40	2.30	6.43

Measurement's Uncertainty at X_3

	Smooth			UED			FPC-800M			FT-MW		
Y+	Um	u'	u'u'	Um	u'	u'u'	Um	u'	u'u'	Um	u'	u'u'
0.00	0.41	2.11	5.83	0.40	0.98	2.66	0.40	0.68	1.71	0.40	0.56	0.75
9.20	0.40	5.38	15.18	0.40	0.81	1.03	0.40	0.44	0.75	0.40	0.36	0.85
18.41	0.40	5.99	16.92	0.40	0.45	0.86	0.40	0.53	1.08	0.40	0.70	1.91
27.61	0.40	4.99	14.09	0.40	0.47	1.17	0.40	0.43	0.82	0.40	0.58	0.75
36.82	0.47	5.20	14.69	0.47	4.45	12.54	0.41	1.99	5.52	0.41	0.56	1.36
46.02	0.46	5.21	14.73	0.45	4.96	13.98	0.41	3.30	9.25	0.41	2.98	8.31
55.23	0.47	5.50	15.54	0.46	5.38	15.17	0.42	3.97	11.17	0.42	3.53	9.91
64.43	0.49	5.46	15.41	0.51	6.03	17.04	0.41	3.56	10.02	0.42	3.68	10.36
73.63	0.47	4.97	14.03	0.47	5.62	15.87	0.42	4.05	11.40	0.42	3.85	10.85
82.84	0.47	5.24	14.81	0.48	5.62	15.87	0.42	3.76	10.59	0.42	3.94	11.08
92.04	0.46	5.75	16.24	0.45	5.57	15.72	0.42	3.86	10.85	0.43	4.00	11.26
101.25	0.45	4.98	14.06	0.46	5.52	15.58	0.42	3.89	10.97	0.42	4.04	11.40
110.45	0.47	5.90	16.69	0.46	5.23	14.76	0.41	3.67	10.35	0.42	3.94	11.10
119.66	0.45	5.29	14.93	0.46	5.44	15.35	0.41	3.68	10.35	0.42	3.88	10.93
128.86	0.43	4.95	13.99	0.43	5.52	15.58	0.42	3.95	11.12	0.42	3.99	11.24
138.06	0.45	5.02	14.16	0.46	5.69	16.07	0.41	3.73	10.49	0.42	3.83	10.79
147.27	0.44	5.23	14.77	0.45	5.42	15.30	0.41	3.75	10.55	0.42	3.88	10.93
156.47	0.45	5.61	15.83	0.45	5.49	15.49	0.42	3.79	10.68	0.42	3.82	10.76
165.68	0.44	5.02	14.16	0.44	5.03	14.19	0.42	3.71	10.45	0.42	3.84	10.81
211.70	0.44	5.24	14.81	0.44	5.35	15.09	0.41	3.60	10.15	0.43	3.93	11.08
257.72	0.43	4.70	13.27	0.43	4.88	13.78	0.41	3.81	10.73	0.42	4.05	11.42
303.74	0.43	4.61	13.02	0.43	4.93	13.91	0.41	3.68	10.36	0.42	3.84	10.81
349.76	0.42	4.45	12.57	0.43	4.67	13.17	0.41	3.62	10.17	0.42	3.87	10.90
395.79	0.42	4.65	13.13	0.42	4.51	12.71	0.41	3.37	9.47	0.41	3.78	10.65
441.81	0.42	4.31	12.18	0.42	4.10	11.56	0.41	3.34	9.38	0.41	3.55	9.97
487.83	0.41	4.03	11.37	0.41	4.02	11.34	0.41	3.20	9.00	0.41	3.38	9.51
533.85	0.41	3.68	10.37	0.41	3.94	11.11	0.41	3.29	9.24	0.41	3.44	9.69
579.87	0.41	3.75	10.57	0.41	3.73	10.53	0.40	2.92	8.21	0.41	3.30	9.27

Measurement's Uncertainty at X_4

	Smooth			UED			FPC-800M			FT-MW		
Y+	Um	u'	u'u'	Um	u'	u'u'	Um	u'	u'u'	Um	u'	u'u'
0.00	17.14	19.62	55.47	0.40	0.48	0.94	0.40	0.50	0.81	0.40	0.77	1.94
9.30	0.41	0.62	0.75	0.40	1.37	2.37	0.40	1.01	0.76	0.40	0.62	0.75
18.61	0.45	0.40	0.84	0.40	0.47	0.75	0.40	0.44	0.75	0.40	0.63	0.97
27.91	0.51	5.71	16.12	0.40	0.53	1.26	0.40	0.89	2.38	0.40	0.38	1.03
37.21	0.46	6.05	17.09	0.46	4.97	14.01	0.41	3.39	9.52	0.40	0.50	0.75
46.52	0.47	6.45	18.19	0.48	5.91	16.67	0.43	4.23	11.92	0.40	0.46	1.11
55.82	0.45	5.91	16.67	0.50	6.05	17.09	0.42	4.45	12.53	0.42	3.43	9.63
65.13	0.45	6.08	17.15	0.50	6.36	17.97	0.43	4.50	12.68	0.42	3.90	10.98
74.43	0.44	6.55	18.49	0.51	6.26	17.68	0.42	4.28	12.07	0.44	4.21	11.87
83.73	0.44	5.31	15.00	0.46	6.17	17.41	0.42	4.49	12.66	0.42	4.27	12.02
93.04	0.45	6.05	17.09	0.48	6.21	17.55	0.43	4.47	12.61	0.42	4.22	11.90
102.34	0.44	6.44	18.19	0.44	5.29	14.91	0.42	4.35	12.27	0.42	4.23	11.94
111.64	0.44	5.83	16.44	0.44	5.26	14.83	0.42	4.25	11.98	0.43	4.67	13.17
158.16	0.43	5.79	16.33	0.43	4.71	13.28	0.41	4.18	11.77	0.43	4.31	12.16
204.68	0.42	5.27	14.87	0.43	4.86	13.71	0.42	4.33	12.22	0.42	4.28	12.07
251.20	0.43	5.64	15.92	0.42	4.46	12.58	0.41	3.79	10.68	0.42	4.09	11.53
297.72	0.43	4.99	14.08	0.43	4.29	12.11	0.41	3.68	10.35	0.41	3.84	10.81
344.23	0.42	4.85	13.68	0.41	4.17	11.75	0.41	3.62	10.19	0.41	3.64	10.24
390.75	0.41	4.35	12.25	0.41	9.73	11.05	0.41	9.53	9.34	0.41	3.62	10.21
437.27	0.42	4.43	12.48	0.41	9.99	10.48	0.41	9.80	10.05	0.41	10.34	9.54
483.79	0.41	4.41	12.43	0.41	10.02	9.41	0.41	9.77	8.93	0.41	11.01	9.56
530.31	0.41	4.13	11.63	0.41	10.42	9.57	0.40	9.25	8.32	0.41	10.39	8.89
576.82	0.41	4.11	11.57	0.41	10.54	9.30	0.40	9.39	8.39	0.41	10.49	8.71

Measurement's Uncertainty at X_5

	Smooth			UED			FPC-800M			FT-MW		
Y+	Um	u'	u'u'	Um	u'	u'u'	Um	u'	u'u'	Um	u'	u'u'
0.00	1.07	4.62	13.01	0.40	0.43	0.75	4.08	10.55	29.82	0.40	0.41	0.75
9.07	0.40	0.55	1.32	0.40	0.76	0.77	0.40	0.45	0.75	0.40	0.40	0.75
18.14	0.40	0.51	1.66	0.40	0.55	0.75	0.40	0.40	0.88	0.40	0.63	0.78
27.20	0.51	6.22	17.56	0.40	0.56	1.38	0.40	0.40	0.75	0.40	0.40	0.82
36.27	0.50	6.26	17.70	0.46	5.09	14.37	0.42	1.44	4.02	0.40	0.39	0.75
45.34	0.47	6.12	17.29	0.46	6.06	17.09	0.44	4.02	11.33	0.40	1.17	3.32
54.41	0.50	6.85	19.35	0.46	6.17	17.42	0.46	5.04	14.23	0.42	3.64	10.26
63.48	0.46	5.71	16.14	0.45	5.83	16.45	0.46	5.06	14.27	0.42	4.12	11.65
72.55	0.48	6.29	17.76	0.44	5.61	15.82	0.45	4.94	13.95	0.44	4.69	13.24
117.89	0.46	5.91	16.68	0.47	6.10	17.22	0.44	4.46	12.59	0.43	4.55	12.86
126.96	0.49	6.75	19.09	0.46	6.14	17.35	0.44	4.27	12.06	0.44	5.00	14.13
136.02	0.44	5.75	16.24	0.46	5.97	16.85	0.44	4.55	12.85	0.43	4.84	13.66
145.09	0.45	5.85	16.52	0.44	5.73	16.18	0.44	4.65	13.12	0.41	4.16	11.74
154.16	0.45	5.47	15.45	0.44	5.52	15.58	0.44	4.63	13.06	0.42	4.11	11.61
163.23	0.47	5.95	16.81	0.43	5.18	14.63	0.43	4.44	12.52	0.42	4.20	11.85
208.57	0.47	6.24	17.63	0.45	5.82	16.45	0.45	4.57	12.90	0.41	3.81	10.73
253.91	0.46	5.77	16.30	0.42	4.60	12.97	0.43	4.36	12.30	0.41	3.60	10.14
299.25	0.42	5.00	14.13	0.42	4.66	13.14	0.43	4.34	12.23	0.41	3.60	10.17
344.59	0.44	5.65	15.99	0.41	4.26	12.01	0.42	4.07	11.47	0.41	3.48	9.82
389.94	0.42	5.15	14.53	0.41	4.11	11.58	0.42	3.62	10.21	0.41	3.49	9.86
435.28	0.42	4.91	13.86	0.41	4.07	11.47	0.42	3.73	10.54	0.41	3.31	9.33
480.62	0.42	4.84	13.66	0.41	3.58	10.08	0.41	3.50	9.88	0.40	3.11	8.78
525.96	0.42	4.48	12.66	0.40	3.40	9.57	0.41	3.53	9.94	0.40	2.94	8.30
571.30	0.41	3.97	11.21	0.40	3.30	9.29	0.41	3.57	10.08	0.40	2.77	7.79

Measurement's Uncertainty at X_6

	Smooth			UED			FPC-800M			FT-MW		
Y+	Um	u'	u'u'	Um	u'	u'u'	Um	u'	u'u'	Um	u'	u'u'
0.00	0.43	0.48	0.75	0.40	0.23	0.75	0.40	0.42	0.75	0.40	0.42	0.78
9.21	0.40	0.69	0.77	0.40	0.27	0.85	0.40	0.64	0.75	0.40	0.57	0.75
18.42	0.59	5.93	16.74	0.40	0.23	0.75	0.40	0.67	0.75	0.40	0.61	1.51
27.63	0.55	6.39	18.06	0.40	0.77	2.24	0.40	2.45	6.87	0.40	0.47	0.75
36.83	0.55	6.22	17.55	0.45	4.85	13.73	0.47	4.91	13.87	0.40	0.39	0.85
46.04	0.53	7.12	20.11	0.46	5.74	16.24	0.44	4.98	14.04	0.41	2.07	5.76
55.25	0.49	5.91	16.68	0.47	6.40	18.12	0.43	5.26	14.83	0.42	4.02	11.31
64.46	0.49	5.97	16.85	0.46	6.18	17.48	0.43	5.22	14.71	0.43	4.74	13.31
73.67	0.51	6.78	19.17	0.46	6.06	17.16	0.42	4.85	13.68	0.43	4.69	13.22
82.88	0.49	6.52	18.42	0.44	5.77	16.34	0.43	5.13	14.48	0.44	4.58	12.92
128.92	0.46	6.08	17.16	0.43	5.35	15.13	0.43	4.60	12.97	0.43	4.66	13.14
174.96	0.46	5.93	16.73	0.42	4.98	14.08	0.42	4.43	12.48	0.43	4.74	13.37
221.01	0.45	5.53	15.63	0.42	4.67	13.24	0.41	3.91	11.00	0.42	4.25	12.00
267.05	0.44	5.34	15.10	0.42	4.78	13.53	0.41	4.28	12.05	0.41	4.18	11.77
313.09	0.44	5.30	14.96	0.41	4.24	12.01	0.41	4.11	11.57	0.41	4.08	11.50
359.14	0.44	5.06	14.30	0.41	4.16	11.78	0.41	3.69	10.39	0.41	3.86	10.87
405.18	0.44	5.07	14.30	0.41	4.15	11.76	0.41	3.53	9.95	0.41	3.54	9.98
451.22	0.43	4.44	12.54	0.41	3.70	10.49	0.41	3.55	9.97	0.41	3.43	9.65
497.27	0.43	4.40	12.42	0.41	3.32	9.43	0.41	3.41	9.56	0.41	3.41	9.59
543.31	0.43	4.67	13.17	0.40	3.12	8.85	0.40	3.32	9.33	0.41	3.25	9.13
589.35	0.42	4.00	11.29	0.40	3.17	8.98	0.40	3.00	8.42	0.40	3.29	9.25

Measurement's Uncertainty at X_7

	Smooth			UED			FPC-800M			FT-MW		
Y+	Um	u'	u'u'	Um	u'	u'u'	Um	u'	u'u'	Um	u'	u'u'
0.00	0.40	5.66	0.75	0.40	0.46	0.75	0.40	0.38	0.75	0.40	0.46	0.75
9.02	0.40	3.99	1.34	0.40	0.39	1.03	0.52	2.66	7.51	0.40	0.49	0.89
18.04	0.54	10.62	19.52	0.40	0.44	0.75	0.40	0.42	0.75	0.40	0.65	1.51
27.06	0.45	9.62	16.56	0.42	1.58	4.40	0.42	1.88	5.26	0.40	0.46	0.75
36.08	0.48	10.30	19.07	0.49	4.74	13.37	0.43	3.65	10.27	0.40	0.47	0.80
45.09	0.49	10.05	18.82	0.45	5.73	16.17	0.43	4.96	13.97	0.42	3.33	9.35
54.11	0.48	10.04	18.19	0.46	6.19	17.48	0.45	5.75	16.23	0.42	4.38	12.34
63.13	0.48	10.78	20.10	0.44	5.93	16.73	0.45	5.50	15.53	0.44	4.90	13.81
72.15	0.48	10.28	18.65	0.50	7.30	20.63	0.44	5.66	15.97	0.45	5.03	14.18
81.17	0.46	9.87	17.22	0.44	5.91	16.67	0.43	5.33	15.04	0.43	5.13	14.48
90.19	0.47	10.09	18.99	0.43	5.68	16.02	0.42	4.98	14.04	0.43	4.94	13.94
135.28	0.46	10.06	18.26	0.43	5.50	15.53	0.43	5.27	14.87	0.43	4.78	13.49
180.38	0.45	9.62	17.22	0.43	5.31	15.00	0.42	5.11	14.40	0.43	4.95	13.97
225.47	0.43	9.59	16.33	0.42	4.87	13.74	0.42	4.66	13.14	0.42	4.65	13.11
270.56	0.43	9.40	16.17	0.42	4.71	13.28	0.42	4.66	13.14	0.42	4.78	13.49
315.66	0.43	9.36	15.08	0.41	4.38	12.36	0.41	4.45	12.53	0.42	4.44	12.51
360.75	0.44	9.65	15.53	0.41	4.44	12.51	0.41	4.57	12.89	0.41	4.33	12.20
405.85	0.43	9.14	15.39	0.41	4.11	11.59	0.41	4.21	11.87	0.41	4.02	11.33
450.94	0.42	9.17	14.36	0.41	3.99	11.26	0.41	4.03	11.37	0.41	3.96	11.15
496.03	0.42	9.09	14.33	0.40	3.61	10.15	0.41	3.80	10.70	0.41	3.82	10.76
541.13	0.41	8.88	13.08	0.40	3.45	9.71	0.41	3.82	10.76	0.41	3.55	9.98
586.22	0.41	8.43	11.96	0.40	3.14	8.84	0.41	3.70	10.43	0.41	3.43	9.64
631.32	0.41	8.63	11.55				0.40	3.23	9.09	0.40	3.29	9.23
676.41	0.41	8.65	11.61				0.40	3.04	8.55	0.40	3.08	8.66